Ocean and laboratory observations on waves over topography

Waarnemingen, op zee en in het laboratorium,
van golven boven een hellende bodem

Ocean and laboratory observations on waves over topography

Waarnemingen, op zee en in het laboratorium, van golven boven een hellende bodem

(met een samenvatting in het Nederlands)

Proefschrift

ter verkrijging van de graad van doctor aan de Universiteit Utrecht op gezag van de rector magnificus, prof. dr. W. H. Gispen, in gevolge het besluit van het college voor promoties in het openbaar te verdedigen op woensdag 24 januari 2007 des middags te 2.30 uur

door

Frans Peter Alexander Lam

geboren op 12 april 1968 te Ede

Promotor: Prof. dr. J.T.F. Zimmerman

Co-promotoren: Dr. L.R.M. Maas
               Dr. T. Gerkema

aan mijn broer Dennis

'Ik schrijf geen proefschrift.'

. . . Maarten lachte. 'Ik heb de pest aan mensen die een proefschrift schrijven alleen om de titel. Als je wat te vertellen hebt, kun je dat ook wel zonder proefschrift. En ik heb niets te vertellen.'

'En wat vindt je vrouw daarvan?'

'Ik ben het daarmee eens hoor', zei Nicolien. 'Ik zou niet willen dat hij een proefschrift schreef.' Ze lachte zenuwachtig.

Haar antwoord verbaasde Beerta zichtbaar. Hij trok zijn wenkbrauwen op en keek haar even aan voor hij zich opnieuw tot Maarten wendde. 'Ik heb mijn hele leven nog nooit één origineel idee gehad', zei hij met nadruk, 'en toch heb ik een proefschrift geschreven. Wat laat, en ik denk ook niet dat iemand het gelezen heeft, behalve mijn promotor natuurlijk, maar ik ben Onze Lieve Heer nog iedere dag dankbaar dat ik het af heb mogen maken.'

J. J. Voskuil,
Het Bureau 1, Meneer Beerta, 1996

Summary

This thesis addresses the observation, analysis and dynamics of waves as being trapped, generated and focused by sloping topography. Three different phenomena are described and are introduced in the introduction (chapter 1).

Chapter 2: shelf waves with diurnal tidal frequency off Greenland

Tidal analysis has been carried out on current measurements at a "cross-shelf" transect off Greenland at $71°N$. The diurnal tides manifest themselves mainly as a barotropic continental shelf wave, travelling southward along the shelf slope. This follows from the amplitude distribution of the diurnal tidal components and from the rotation sense of the tidal ellipses at different cross-slope locations, as calculated with simple two-dimensional models. The well organized cross-slope pattern of the velocity amplitudes is absent in observations further north near $75°N$.

These observations suggest that the local vanishing of the group velocity, which is caused by topography, is of importance for the existence and local amplification of these continental shelf waves with diurnal tidal frequency.

Chapter 3: tidal and residual currents near the shelf break in Biscay

Theoretical and laboratory models show that internal-wave energy in continuously stratified fluids propagates in the vertical plane, at an angle set by the wave, buoyancy and Coriolis frequencies. Repeated Acoustic Doppler Current Profiler observations on three transects, crossing the shelf edge, now directly reveal this beam-wise propagation of internal tides in the Bay of Biscay. This confirms previous suggestions based on observations sampled more sparsely in space. The present observation is made by bin-wise harmonic analysis of horizontal currents, leading to the spatial resolution of barotropic and baroclinic semi-diurnal tidal and (time-averaged) residual flows.

The observed barotropic tide has a cross-slope mass flux that is roughly constant. Its fast along-slope phase variations can only in part be explained by the spring-neap tidal cycle. The observed baroclinic tide compares favourably to that produced by a two-dimensional numerical model. The observations reveal details of the internal

7

tidal beam, including its spatial amplitude distribution, presence of amphidromes and direction of phase propagation. The cross-isobath structure of the along-slope barotropic mean flow shows a localized maximum near the shelf break. Over two transects it agrees in sign and magnitude with a theoretical tidally-rectified flow. The baroclinic, cross-isobath mean flow shows a strong near-bottom downwelling flow, compensated by an on-shelf directed flow in the upper part. The along-shelf mean flow displays subsurface-intensification attributed here to frictional modification of a tidally-rectified flow that is bottom-trapped due to stratification.

Chapter 4: internal wave focusing revisited

An experiment which discussed the appearance of an internal wave attractor in a uniformly-stratified, free-surface fluid (Maas et al. 1997) is revisited. This is done in order to give a more detailed and more accurate description of the underlying focusing process. Evolution of the attractor can now be quantified. For the tank with one sloping sidewall, and for the parameter regime (density stratification, forcing frequency) studied, the inverse exponential growth rate determined at several locations in the fluid turns out to be 122 seconds always. Only the start and duration of the growth differs: away from the attractor region it appears later and is of shorter duration. Here, these features are interpreted by employing a new theoretical basis that incorporates an external forcing via a surface boundary condition (an infinitesimal barotropic seiche) and that describes the solution in terms of propagating waves.

Contents

Chapter 1

Introduction

1.1 Waves and topography in the ocean

Waves are a fascinating phenomenon. Everybody is familiar with waves of different kinds. Of all waves, water waves are the most familiar. In this thesis I will discuss those ocean waves that you cannot see directly (as a wave): tides and internal waves. These relatively small (or medium) scale processes are important for chemical and biological processes and appear to present an important link in the global circulation and in climate modelling (Garrett 2003). The title of this thesis emphasizes that many waves are influenced by topography, but have widely varying length scales. They are addressed in order of decreasing magnitude:

- continental shelf waves (wavelength up to 500 km) as observed East of Greenland, chapter 2,

- internal tides (wavelength of the order of 10 km) as observed in the Bay of Biscay, chapter 3, and

- internal waves and internal wave attractors as observed in the laboratory (wavelength of several centimetres, chapter 4).

For all three topics topography is essential, but in a different way: as a mechanism of trapping, generation and focusing of the waves, respectively.

1.1.1 Observing waves in the ocean

In a sense, the title of this thesis also reflects the different ways in which fluid motion can be observed. In the ocean, this can be done either with moored instruments (typically for one year), or from a ship. In the laboratory, fluid motion can be studied by following dye patterns. These methods are used in chapters two, three and four, respectively. As this thesis illustrates, it is the combination and interaction of these
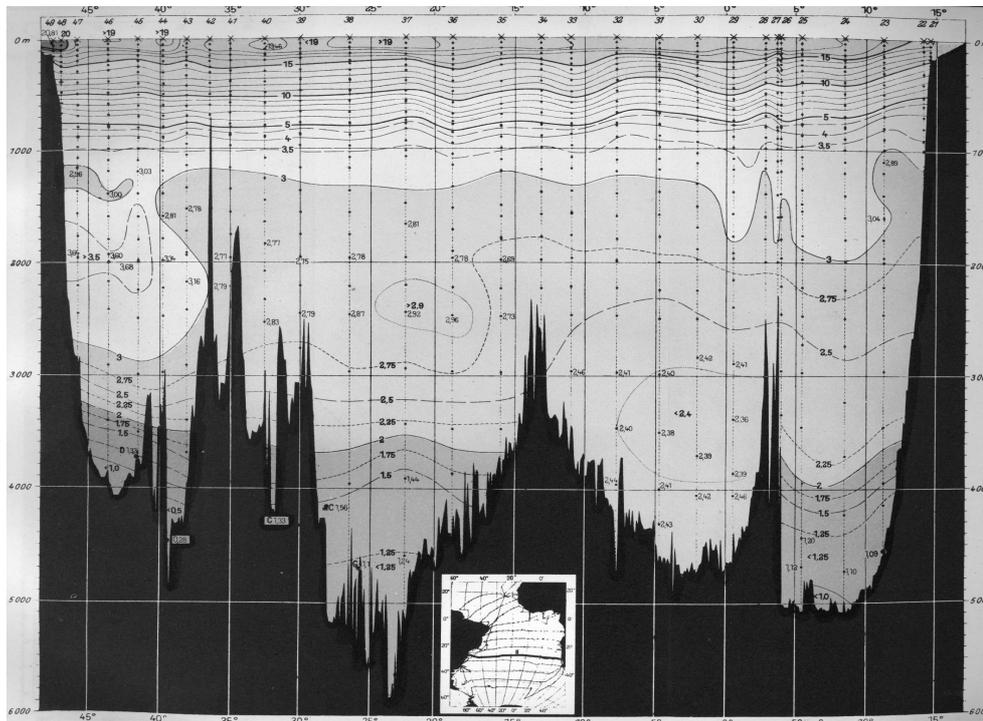
Figure 1.1: See figure C.1 for a full colour version. Temperature cross section of the South Atlantic ocean ($\sim 30°S$), resulting from the Meteor expedition 1925-1927 (Wüst and Defant 1936). Temperatures are depicted by three tones of blue and red, for temperatures below 2°, 3°, 5° and above 5°, 10°, 15° C, respectively. Note the difference in scale between the vertical (6 km) and the horizontal (over 6000 km) directions.

perspectives that is most fruitful. At sea, every observation is a superposition of all processes present at that location at that time. Moreover, and especially in the deep sea, it is hard to gather sufficient detail of these processes, both in time and space. For these reasons it is very important to have for each experiment a well designed observational strategy, based on previous experience, and on assumptions originating from results of theoretical analysis and laboratory experiments.

1.1.2   The ocean's bathymetry: the continental slope

First some general characteristics of topography in the ocean are highlighted. Figure 1.1 shows a temperature cross section of the South Atlantic Ocean. This is a quite arbitrary example, though historically interesting. It is the result of one of the transects of the German Research Vessel *Meteor* during its exploration of the South Atlantic from 1925 to 1927. This picture is intended to show details of the temper-
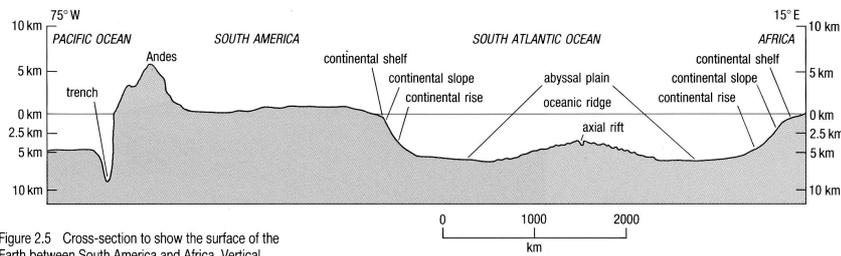
Figure 2.5   Cross-section to show the surface of the Earth between South America and Africa. Vertical exaggeration ×100.
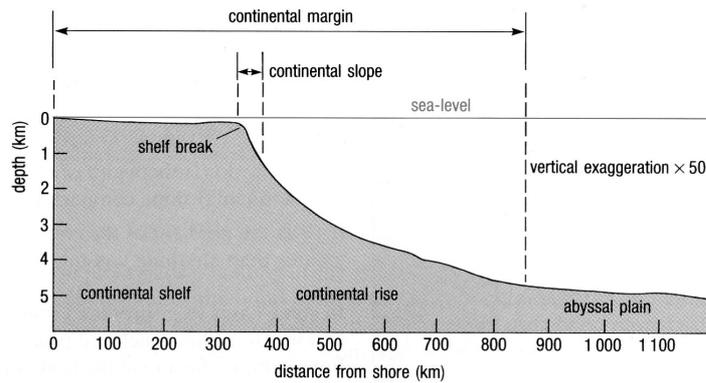
Figure 1.2: Top: Sketch of topography; zonal cross section on both sides of South America. Bottom: sketch of continental shelf and slope. (pictures from Open University course team (1989))

ature distribution in this part of the world ocean. I will come back to temperature, salinity and density in section 1.3. At this stage I focus on the topographic features in the image. We see several ridges (although the meridional extent of the ridges can not be seen from this image) between the African and South American continents. In the middle we see the Mid-Atlantic ridge, and to the east (west) we see the Walvis Ridge (Rio Grande Rise). On either side of the picture we see the steep slopes of the bordering continents. Above that, in the two upper corners of the image, we see a slight flattening of the topography. This depicts shelf seas of about 200 m of depth that border the continents.

In figure 1.2 (top) we see a more generic and schematic profile of a similar cross section, also for the South Atlantic and including South America and part of the (Eastern) Pacific. This picture shows different phenomena in a useful perspective. It illustrates that the Atlantic Ocean does not have any deep trenches, like the Peru-Chile trench in the Pacific to the west of the Andes. The continental slopes we deal with in this thesis are similar to those sketched in figure 1.2 (bottom).

In general, in the Atlantic the continental shelf next to the coast is relatively wide, although there are considerable differences in this width. Compare e.g. the Por-

tuguese shelf (typically 50 km wide) with the shelf surrounding Ireland and Scotland (up to 300 km wide). The continental shelf is an important link between the coastline and the ocean. At the outer rim of the shelf we find the shelf break. Beyond this, there is often a relatively narrow and steep transition, the continental slope and rise, to the abyssal plain. For most regions, the shelf break (or shelf edge) is taken to be along the 200 m isobath. As we will see in chapter 2, the shelf East of Greenland is deeper: up to 400 m.

From the above it can be concluded that prominent topographic features, like sea mountains and steep continental slopes, are a key element of the shape of the ocean's basin. This thesis addresses possible consequences for ocean waves. In particular, wave trapping, internal tide generation and focusing are discussed.

1.2   Wave trapping at the slope: Continental Shelf Waves

Waves in the ocean can be trapped by topography in several ways. This results in different wave classes: shelf waves, Kelvin waves and edge waves. These wave classes are distinguished by their frequency being *sub-inertial*, *hybrid*, and *super-inertial*, respectively. This classification refers to the frequency of the wave being either below or above the frequency f of inertial motion; both are allowed for the hybrid Kelvin wave. Here, the Coriolis parameter $f = 2\Omega \sin \varphi$ is related to the Earth's rotation vector, with Ω the rotation frequency of the Earth (that is: 2π radians each Sidereal day) and φ latitude (positive northward). This division also refers to the restoring mechanism of the waves: gravity for edge waves, and (conservation of potential) vorticity for shelf waves. Historically, at the end of the 19th century, in attempts to solve the well known Laplace Tidal Equations, the waves were distinguished as waves of the *first class* (gravity waves) and *second class* (vorticity waves), respectively. This was separately identified by Lamb, Margules and Hough; see Cartwright (1999, ch.7) and Platzman (1968, sec.5). Waves of the first class normally have two nearly symmetrical solutions, for waves travelling in opposite directions. Waves of the second class have a single solution, where the direction of propagation is defined by the Earth's rotation.

The first type of waves to be addressed in detail in this thesis (chapter 2) are Continental Shelf waves (CSWs) with diurnal tidal frequency as observed East of Greenland. CSWs are an example of topographic Rossby waves. They are sometimes referred to as double Kelvin waves for reasons to be discussed below. I will first briefly introduce (subsection 1.2.1) the classical Kelvin wave which is trapped by the coast. I will come back to (internal) gravity waves in sections 1.3 and 1.4, but not in a 'trapped' context. Edge waves are not discussed in the remainder of this thesis. For a more complete overview of trapping mechanisms I refer to review papers by Mysak (1980), Hendershott (1981) and Huthnance (1975, 1981b). See also LeBlond and Mysak (1978) for a more general treatment of the Coriolis force.
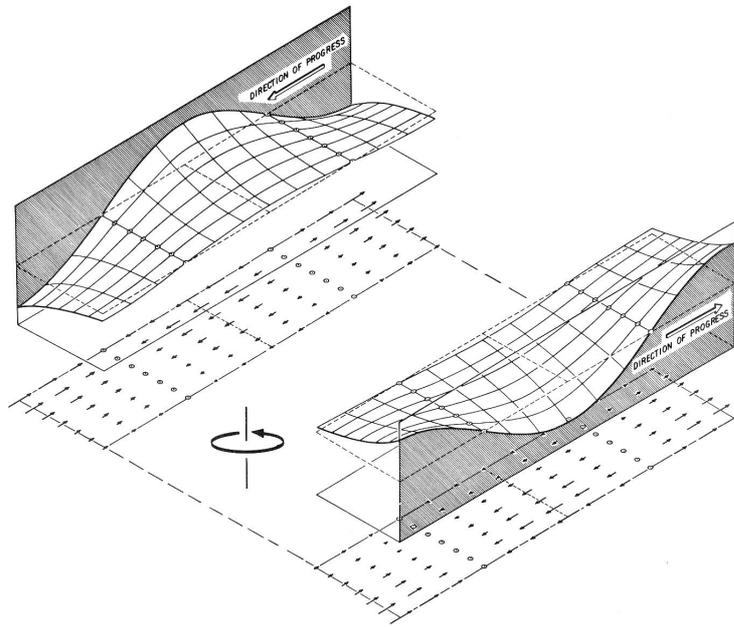
Figure 1.3: Kelvin wave characteristics (Thomson 1879) for northern hemisphere along two coastal walls. Associated linear water motion is projected on the plane below the wave (Gill 1982).

1.2.1   Kelvin waves

The simplest and also the most common appearance of a tidal wave travelling along a coast is that of a Kelvin wave. The Kelvin wave is a semi-geostrophic solution of the linearized shallow water equations for a homogeneous fluid (to be introduced in chapter 2) for a flat sea floor and a vertical coastal wall. See figure 1.3 for a sketch of the solution, as originally presented by Lord Kelvin (Thomson 1879).

The fluid motion supporting a Kelvin wave is rectilinear; the motion perpendicular to the coast equals zero; $u=0$, if we align the coast along the y–axis. In the cross-coastal direction x the forces are in *geostrophic balance:* the pressure gradient — caused by the exponentially decaying surface elevation— is balancing the Coriolis-force ($fv = g\,\partial\eta/\partial x$). Here v is the along-coastal velocity, g the acceleration due to gravity, and η the surface elevation. However, the balance in the along-coastal direction ($\partial v/\partial t = -g\,\partial\eta/\partial y$) does not depend on the Earth's rotation. This explains the hybrid (semi-geostrophic) character of the wave: it is partly influenced by rotation, partly not. The latter is even more apparent when we combine the above with the (reduced) continuity equation: $\partial\eta/\partial t = -H\partial v/\partial y$.
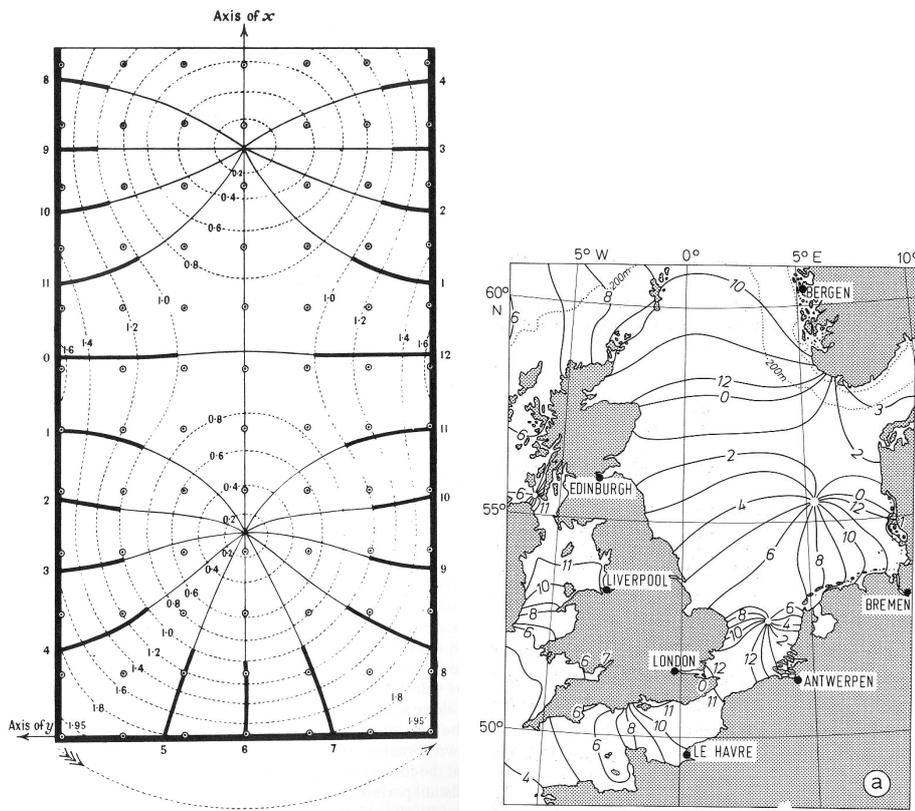
Figure 1.4: Left: famous solution of Taylor (1920) for a semi-enclosed channel (like the North Sea): reflected Kelvin wave in combination with Poincaré waves 'to make the turns'. Solid lines depict phase, dotted lines amplitudes. The incoming (reflected) Kelvin wave propagates along the left (right) wall. Right: M_2 co-tidal lines (hours) in the North Sea (Dietrich et al. 1975). Asymmetry in the observed pattern is due to friction, not included in the Taylor solution.

By assuming the wave is described as: $\sim \exp(i(ky - \omega t))$, it follows that the resulting dispersion relation is identical to that of long gravity waves: $\omega = k\sqrt{gH}$. Here $\omega \equiv 2\pi/T$ and $k \equiv 2\pi/\lambda$ are the frequency and the wave number of the wave, respectively, defined in terms of period and wavelength of the wave. The phase speed c of the wave then is $c = \lambda/T = \omega/k = \sqrt{gH}$, the square root of gravity times the (constant) water depth. Although the numerical value for the phase propagation is identical to that of long gravity waves, for the Kelvin wave there is only one direction of propagation possible: with the coast to the right when looking in the propagation direction. This is for the northern hemisphere. The wave has the coast to its left on the southern hemisphere.

The exponential decay of the amplitude of the wave off the coast is defined by what is called the *barotropic Rossby radius of deformation*:

$$R = \sqrt{gH}/|f|. \tag{1.1}$$

This radius has a typical value of 200 km for a shelf sea like the North Sea ($H = 40$ m) and 2000 km for the ocean ($H = 4000$ m) at moderate latitudes ($f = 10^{-4}$ s^{-1}).

The Kelvin wave solution does not allow for any perpendicular coast blocking the fluid motion. Therefore, the wave can only be applied to a wave travelling along a coast or canal of infinite length. Kelvin compared the situations for the English and Irish Channels, both with an incoming wave, and a reflected wave (with lower amplitude) travelling back along the opposite coastline. In a famous paper by G.I. Taylor (1920), the actual reflection of such a wave in a semi-enclosed basin was mathematically solved. This was done by adding *Poincaré waves*, which are rotationally modified gravity waves that are standing in the cross-channel direction. Details of this solution are not discussed here. In his paper, Taylor showed a numerical example and corresponding graph for parameters that suit the North Sea (see figure 1.4). This is one of the many examples showing similarity of observed tidal waves travelling along a coastline with typical characteristics of a Kelvin wave.

Before discussing double Kelvin waves and CSWs in more detail, I conclude with a remark. For a sloping sea floor, the simple Kelvin wave model should be extended. This is not trivial, and mostly skipped in standard textbooks. However, also for non-flat topography a similar *hybrid* solution can generally be found. This is not addressed any further here. It is important to realize that for non-flat topography the water motion accompanying the (modified) Kelvin wave is no longer purely alongshore.

1.2.2 Double Kelvin waves and (continental) shelf waves

Potential vorticity

Vorticity waves can be considered in terms of conservation of (linearized) *potential vorticity*.

$$\Pi = \frac{\zeta + f}{h}. \tag{1.2}$$

Here $\zeta = \partial v/\partial x - \partial u/\partial y$ is the vertical component of relative vorticity. For vertically uniform horizontal motion the other components of vorticity ($\nabla \times \vec{u}$) vanish. The Coriolis parameter f is defined as before, and it is assumed that surface elevation is small compared to the total water depth: $\eta \ll h$. Potential vorticity remains constant for any homogeneous rotating (inviscid) fluid (Pedlosky 1984). In particular, the conservation of potential vorticity is valid for Kelvin's linearized shallow water equations, referred to in the previous subsection; see e.g. Gill (1982, sec.7.2.1).

Equation (1.2) is very helpful in understanding the restoring mechanism for Rossby waves. The basic mechanism is most easily understood for *planetary* Rossby
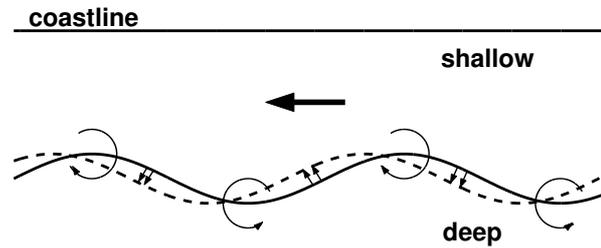
Figure 1.5: Top view of the restoring mechanism of a topographic Rossby wave. In this example, on the northern hemisphere, the CSW is travelling along the coast towards the left, as indicated by the large arrow. The circular arrows depict the restoring mechanism of the wave (full line) to maintain its potential vorticity by adjusting the relative vorticity to the modified depth. With this, the wave is driven to its new position (dashed line). Picture after Gill (1982, fig.10.18).

waves that arise over water of constant depth where f varies with latitude. The so-called β–plane, $f(y) = f_0 + \beta y$, along some reference mid-latitude $y=0$ is assuming that f varies linearly with meridional co-ordinate. The resulting Rossby waves along moderate latitudes in the atmosphere are the most well known examples.

For *topographic* Rossby waves we can take f constant over some area not too large. According to (1.2), changes in depth now imply changes in relative vorticity ζ. This is illustrated in figure 1.5. This figure shows that this topographic Rossby wave or continental shelf wave travels with the shallow water and coast on its right side (looking forward and for the northern hemisphere), just like the Kelvin wave. Historically, since their 'discovery' (Hamon 1962, 1963) many different bottom shapes have been studied mathematically; mostly two-dimensional and for most cases including a coastline (see e.g. Mysak (1980) for a review). However, shelf waves do not need a coast per se, although their dynamics is modified by the presence of a nearby coast, where no normal flow is required.

What's in a name

In the above, the mechanism of topographic Rossby waves is illustrated in terms of vorticity. In the previous subsection, it was already pointed out that these vorticity waves are also known as waves of the second class. The most common and the most significant depth transition in the ocean is at the continental slope. For this reason the associated topographic Rossby wave is called a Continental Shelf Wave (CSW), or shelf wave. This name was first suggested by Robinson (1964). The waves are also called *double Kelvin waves*, but this name, after its introduction by Longuet-Higgins(1968a, 1968b), appears to have become extinct. Originally, the name double Kelvin wave was chosen, because of the double exponential decay for a CSW travelling along a continental shelf modelled as a step topography (Longuet-Higgins 1968a).
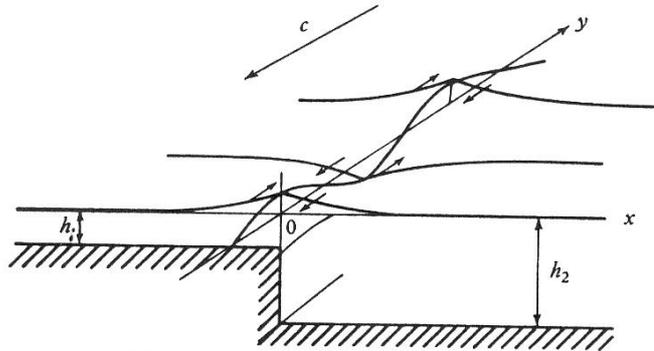
FIGURE 1. Sketch of physical situation.

Figure 1.6: Original figure of Longuet-Higgins (1968a) showing double Kelvin wave characteristics for a northern hemisphere example. The wave travels along the negative y–axis; that is: along the 'shelf break' with the shallow 'shelf' at its right (looking forward). This is similar to a Kelvin wave travelling with the coast to its right. Contrary to the ordinary Kelvin wave the associated water currents are circularly polarized (see figure 2.8 later); clockwise on the shallow shelf, and anticlockwise in the deeper basin. In the picture the rectilinear and shearing motion is sketched with arrows at the crests and throughs of the wave. In between (not shown), the flow is towards the deep basin (shallow shelf) after passage of the crest (trough).

An example: step topography

The simplest case of a CSW is that of a step-like topography (Longuet-Higgins 1968a). As stated above, this wave is also called a double Kelvin wave. The case is treated in more detail in section 2.4.3. Here the example, given without proof, is used to illustrate the main characteristics of a CSW. The relative frequency ω of this (free) wave is defined by the depth difference ($h_2 > h_1$) of the step:[1]

$$\frac{\omega}{f} = -\frac{(h_2 - h_1)}{(h_2 + h_1)}. \tag{1.3}$$

From this equation, it is clear that the frequency of the wave and the Coriolis parameter have opposite signs. This means that the wave travels with the shallow water to its right (left) in the northern (southern) hemisphere, just like Kelvin waves travelling along a coast. A sketch of the wave solution is shown in figure 1.6. Typical phase speed is several metres per second, and the wavelength is typically 50 to 500 km for tidal frequencies, as discussed below and in chapter 2. From (1.3) it is also clear that CSWs can only exist for $|\omega/f| < 1$: they are *sub-inertial*.

---

[1]The equation is derived under the assumption of a small divergence parameter ϵ, see chapter 2. Effectively this parameter is the (squared) ratio of the slope width and the Rossby radius of deformation, as defined in (1.1).

For very long waves, like planetary Rossby waves, frequency is often assumed to be low: $|\omega/f| \ll 1$. The tides can provide a forcing mechanism for CSWs. However, then the wave frequency and the Coriolis parameter can have the same order of magnitude: $|\omega/f| \lesssim 1$. The so-called critical latitude for the K_1 tide[2] is at 30°, then $|\omega(K_1)/f(\varphi = 30°)| = 1$, while for the semi-diurnal species M_2 and S_2 this is 74° and 86°, respectively. Below these critical latitudes the tidal frequencies are *super-inertial*. As demonstrated in chapter 2, CSWs with diurnal tidal frequency can, in fact, be driven resonantly when the tidal frequency *matches* the double Kelvin wave frequency, as enforced by the topographic depth difference according to (1.3).

Because Rossby waves are often studied with the assumption of low frequency, $|\omega/f| \ll 1$, it could be anticipated that tidal frequencies are too high for topographic resonance. However, for high latitudes the tidal frequency is in fact too low for typical shelf slopes. For example, the relative frequency $|\omega(K_1)/f|$ near Greenland equals about 0.5 (chapter 2), while a shelf step from 200 m to 4000 m describes a matching frequency of about 0.9 with (1.3). It is the combination of latitude and topography configuration that can give rise to topographic resonance.

A smoother transition of the continental slope supports higher *CSW-modes*, having more nodes. In chapter 2 this is analysed in detail for current measurements east of Greenland, including more general topography, and the influence of the nearby coastline and changing features along the shelf of Greenland. It is also discussed why CSWs with tidal frequency are not observed more often.

1.3   Wave generation at the slope: internal tides

The second way in which topography influences wave motion, addressed in chapter 3, is by facilitating a conversion of surface tides into internal tides. The latter owe their existence to stratification in the ocean. Internal tides are internal waves with tidal frequency. Internal waves are defined as waves that have their maximum displacement in the interior of a fluid. The principal restoring force of the waves is provided by the buoyancy of the density stratification, which in the ocean are typically caused by temperature or salinity stratification (or both); the Coriolis force also acts as a restoring force. We therefore speak of *inertio–gravity waves*.

Instead of trapping a wave, a sloping topography now causes the conversion of surface (barotropic) motion into internal (baroclinic) motion. This process is particularly effective at the shelf break, as is illustrated below by observations of the generation of the internal tide in the Bay of Biscay. Below, some basic features of stratification in the ocean are illustrated. Next, internal wave properties are discussed in terms of modes and beams, respectively. Then, finally, the internal tide generation at the shelf slope is addressed.

---

[2]Tidal theory, including the introduction of all tidal species, is not repeated here. Period of the K_1 tide is 23.93 hours and 12.42 and 12.00 hours for M_2 and S_2 respectively. See e.g. Defant (1961) for details.
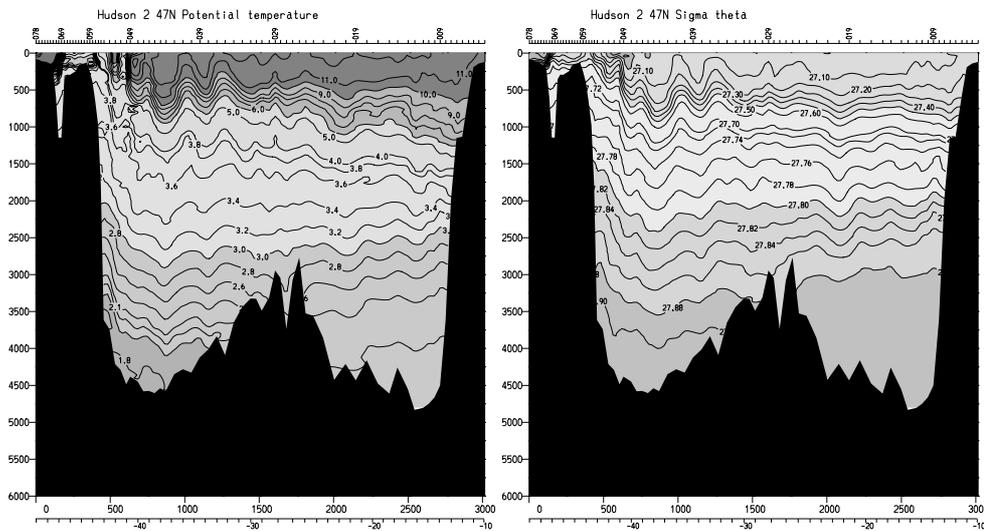
Figure 1.7: See figure C.2 for a full colour version. Cross-sections of one of the many WOCE transects, (see e.g. Siedler et al. (2001)) along $\sim 47°$ N for potential temperature (left) and potential density anomaly (σ_θ, right) for a reference depth of 0 m. Potential density is σ_θ+1000 kg/m^3. Length of the transect is 3000 km, total depth 6000 m. A similar image (not shown) is available for salinity. Note that the deeper isopleths, roughly below 1000 m, have smaller increments: 0.2° instead of 1.0° below 4° Celsius. For potential density this is: 0.02 instead of 0.10 above 27.70 kg/m^3. Source: WOCE, see e.g. Talley (2006).

1.3.1   Stratification in the ocean

In the previous subsection on continental shelf waves, the fluid was regarded as homogeneous. Now, in discussing internal tide generation, density differences in the water column are of importance. We return to figure 1.1, where we see the large scale temperature structure along a transect crossing the South Atlantic during the Meteor expedition. Recently, the World Ocean Circulation Experiment (WOCE) delivered similar graphs, more accurate and from all over the world; see e.g. Siedler et al. (2001). In figure 1.7 we see zonal cross sections for the North Atlantic, approximately along $47°$N from New Foundland to the northern Bay of Biscay. Along this plane, potential temperature and potential density anomaly are shown. At present, large international programmes (like WOCE), together with the development of new technology (remote sensing by satellites, buoys, floats, moorings, gliders, etc.), provide many new details of the ocean, and insight into its dynamics as part of the climate system.

Figures 1.1 and 1.7 illustrate that the Atlantic Ocean is density stratified. The deep ocean, below 1000 m, has an approximately constant gradient. Just above 1000 m there is a steeper gradient: the *permanent pycnocline*, and *permanent thermocline* for
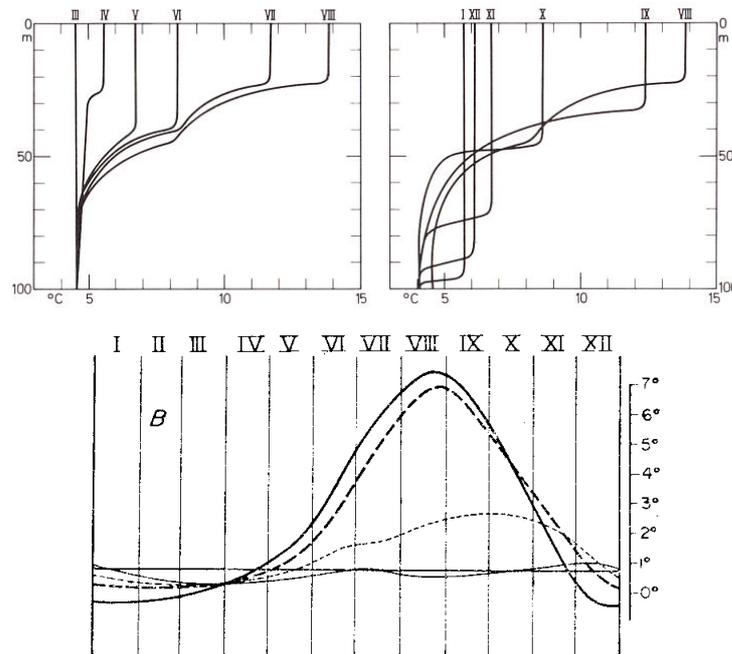
Figure 1.8: Top: variation of seasonal thermocline for a Pacific station; weather station "P" at 50°N 145°W in 1956 (Dietrich et al. 1975). Bottom: similar seasonal variation in the Bay of Biscay, but visualized differently (Defant 1961). Here five lines display the temperature in time for five different depths: 0, 25, 50, 100 and 200m. Changes in temperature decrease with depth. An interesting detail is the lagging of warming-up in summer at 50 m depth, as compared to the upper 25 m of the water column. In all three frames, months of the year are denoted by roman numbers. Note that due to the scaling, the upper two figures gives the misleading impression that temperature is constant below 100 m. The fact that temperature is not constant in the deep sea can for example be seen in figures 1.1 and 1.7.

temperature, usually taken at depths ranging from 200 m to 1000 m, or below. The top layer, with a thickness of several tens of metres, is mixed, depending on seasonal influences; see figure 1.8 for an example. The steep gradient just below this *surface mixed layer*, when present in summer or autumn, is called the *seasonal pycnocline* or *seasonal thermocline*. Depending on the season, this layer typically is from 20–40 m up to 100 m deep.

Stratification is normally expressed in terms of the *stability frequency N* (also called *buoyancy frequency* or *Brunt-Väisälä frequency*, Apel (1987, sec. 5.3)):

$$N^2 = -g(\frac{1}{\rho}\frac{\mathrm{d}\rho}{\mathrm{d}z} + \frac{g}{c_s{}^2}). \tag{1.4}$$

Here, c_s is the local speed of sound in sea water.[3] ρ is the *in-situ* density, and not the potential density of figure 1.7. For a stable stratification, that is: $N^2 > 0$, the stability frequency N is the natural radian frequency at which a water parcel will oscillate after being vertically displaced from its original position and for the density given. It is also the upper limit of free internal waves, see below. In the deep ocean the stability frequency is about 10^{-4} to 10^{-3} rad/s. For the seasonal thermocline values of the order 10^{-2} rad/s are typically found.

In figure 1.8 we see the seasonal variation of the surface mixed layer. In late summer, the water column can be approximated by two layers of constant potential densities (in each of which N=0). This is a usual —and successful— way of describing the essential dynamics of the density interface, but it is limited to the interface dynamics only.

1.3.2   Internal waves in a continuously stratified fluid

For the moment, we ignore the seasonal thermocline of the upper 100 m of the water column, and concentrate on internal (inertio–gravity) waves in the deep sea. In figures 1.1 and 1.7 it is already observed that in the ocean's interior, roughly below 1 km depth, the stratification is more or less constant. For this situation, there are two ways of describing internal waves: modes vs. rays (Turner 1973).

Internal wave modes

For a fluid over a flat bottom, motion in horizontal and vertical direction can mathematically be split and free internal waves can be described in terms of standing vertical modes. In this modal description, internal waves were called *cellular* waves, see e.g. Defant (1961). An example is given in figure 1.9 (left) for constant stratification (N=constant). In this simple case both the horizontal as well as the vertical direction can be solved in terms of sines and cosines.

For arbitrary $N(z)$ the vertical modes can in general also be solved, either analytically or numerically. See figure 1.9 (right) for an example with typical thermocline stratification. In this example the thermocline is modelled as a uniformly stratified layer of finite thickness. Roberts (1975) presents an overview of analytical solutions for several stratifications $N(z)$. A numerical method for arbitrary $N(z)$ was first employed by Fjeldstad (1933). The above mentioned example is based on this method.

A historical example from the Snellius expedition (1929–1930)

In figure 1.10 the method of Fjeldstad is applied to measurements at anchor station $253a$ of the *Snellius expedition*. The Snellius expedition (van Riel 1937, 1938) took place in 1929–1930 in order to improve hydrographic knowledge of the Indonesian

---

[3]The last term of the equation is important in deep water but is often neglected. A full derivation of the stability equation, taking into account all aspects of thermodynamics, can be found in Vallis (2005).
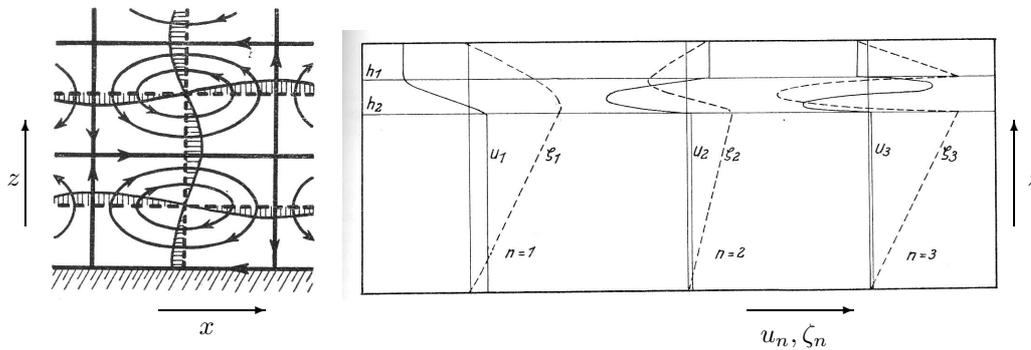
Figure 1.9: Left: Displacements (horizontal and vertical bars) and streamlines for a *cellular* standing internal wave in a fluid with constant stratification N and flat bottom (Defant 1961). See also Turner (1973). Right: Vertical distributions of velocity (u_n) and displacement (ζ_n) for the first three modes (n= 1, 2, 3) in a fluid with a stratified layer (N= constant for $h_2 < z < h_1$) between two homogeneous (N= 0) layers. Picture taken from Krauss (1973), after Fjeldstad (1933).

waters, with acoustic echo sounders that were introduced at the time. The expedition had a wide scientific scope. For physical oceanography the mapping of the Indonesian throughflow was the main target. See also van Aken (2005), for a recent historical perspective.

From the repeated measurements at the anchor station, vertical displacements of water levels were estimated at four different depths (figure 1.10, top left). In this example semi-diurnal and diurnal motion are combined. Note the maximum total vertical displacement of about 63 m from the reference level at 250 m depth. In the bottom frame of figure 1.10 for the semi-diurnal motion, the first four vertical modes are displayed (left) employing the method of Fjeldstad (1933). The observed tidal elevations at different reference depths are decomposed into these functions, based on the observed density profile, which provides $N(z)$. The neighbouring figure on the right demonstrates that this decomposition into four modes was successful.

Lek (1938a, 1938b) demonstrated that part of the independent measurements of the tidal currents at the anchor station were in line with this modal description. From this early example it is clear that internal waves with tidal frequency are present, and, due to the relatively small density differences, have large amplitudes.

Internal wave beams

For a mathematical description of the *generation* of internal waves and their propagation over uneven topography, internal wave beams are more appropriate than vertical modes. By using methods of characteristics, Magaard and Baines were the first to develop mathematical tools for the generation and bottom reflection of internal wave beams (Magaard 1962,1968; Baines,1971a,b, 1973, 1974).
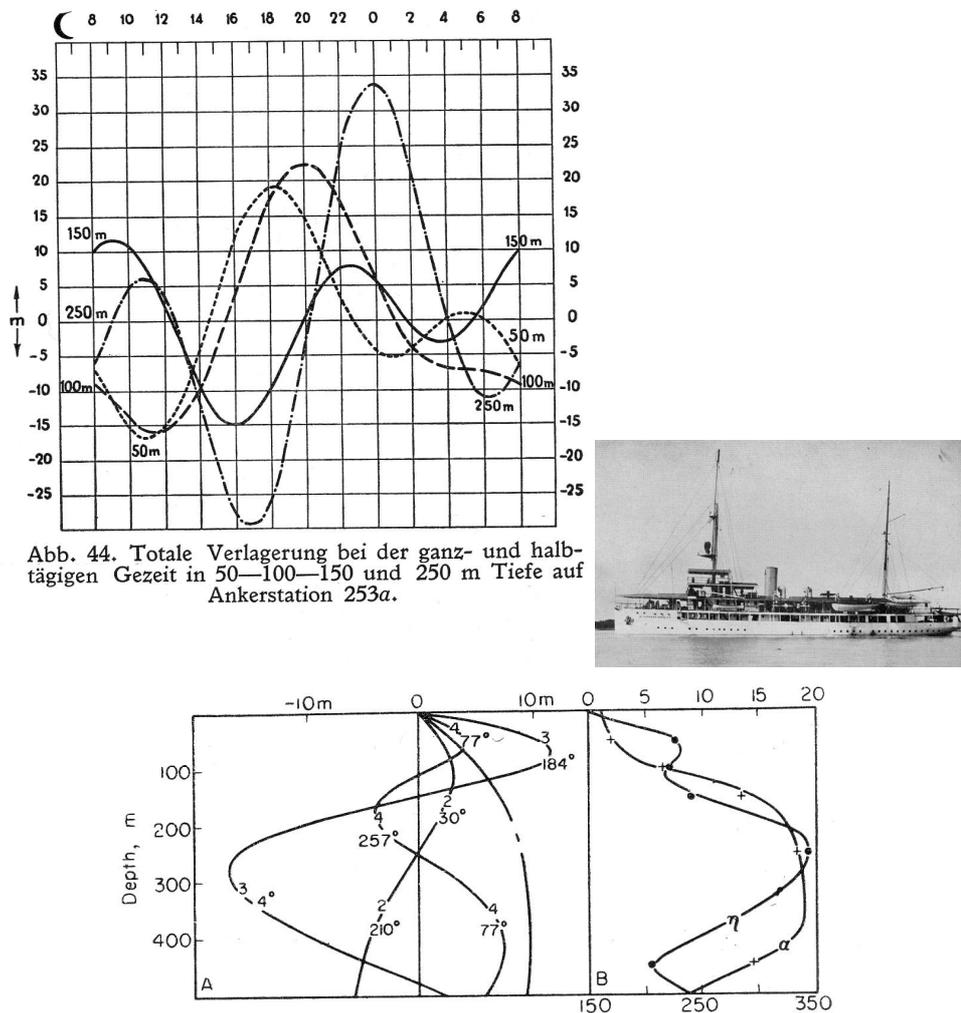
Abb. 44. Totale Verlagerung bei der ganz- und halb-
tägigen Gezeit in 50—100—150 und 250 m Tiefe auf
Ankerstation 253a.

Figure 1.10: Top: Combined diurnal and semi-diurnal vertical displacements at four different reference depths (50, 100, 150 and 250 m) for anchor station $253a$ of the Snellius expedition, 23 to 27 April 1930. These elevations are calculated from repeated temperature and salinity measurements every 1.5 hours at five different depths. At the top of the graph, the horizontal axis is labelled with lunar hours. Picture taken from Lek (1938b). Middle: picture of the ship *H.M. Willebrord Snellius* (Pinke 1938). Bottom left: Vertical distribution of amplitudes of semi-diurnal vertical displacement for four vertical modes, as decomposed for observed measurements at station $253a$. Corresponding phase is indicated for each mode. Only the upper 500 m is shown; total water depth is 1800 m. Note the large amplitude for the third mode. Bottom right: Comparison of the measured amplitude η (•, m) and phase a (+, degrees) of semi-diurnal vertical displacement with calculated curves from the combination of four modes as shown on the left. Lower picture taken from Defant (1961).
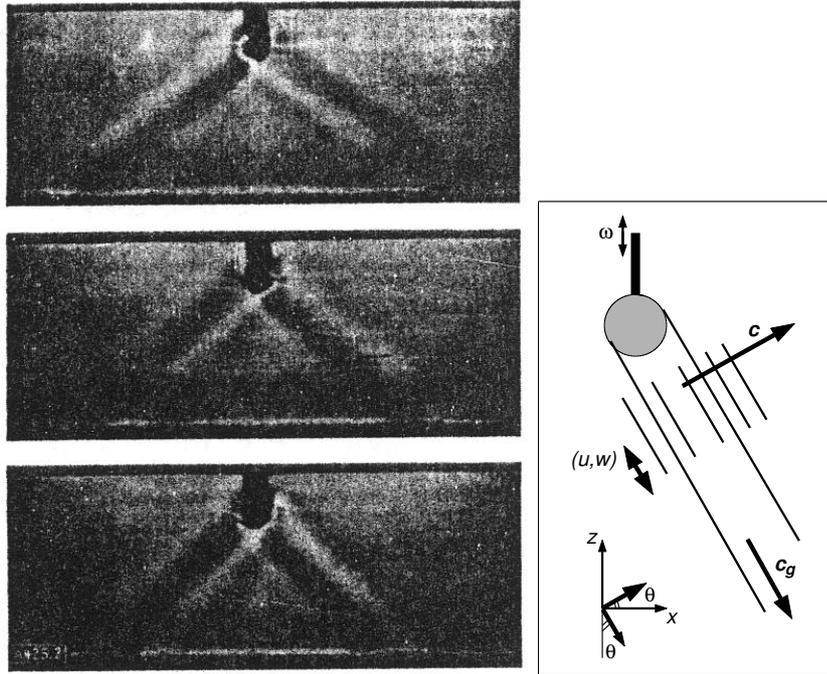
Figure 1.11: Shadowgraphs (left) of internal waves for different frequencies ranging from low (top), intermediate (middle) to high (bottom). Pictures taken from Görtler (1943). Right: sketch of internal wave characteristics in the vicinity of a vertically oscillating cylinder. Directions of oscillation, $\vec{u} = (u, w)$, and propagation of phase $\vec{c}$ and energy (group velocity $\vec{c}_g$) are indicated with arrows. Only one downward beam is sketched, while for the oscillating cylinder beams in four directions normally occur.

Typical features of these internal wave beams will be illustrated by two examples from the laboratory. These experiments were performed for the first time by Görtler (1943), see also Mowbray and Rarity (1967). Despite the poor quality of the images, it is educational to have a look at the original results of Görtler. Note that in the examples shown, all motion is two-dimensional in the xz–plane, with $\partial/\partial y = 0$. In figure 1.11 (left frames) we see internal beams emanating from the oscillating plate at the upper centre of each image. The three images are for different oscillation frequencies, increasing from top to bottom. This illustrates a typical property of monochromatic internal waves: the wave direction only depends on wave frequency (ω), stratification rate (N), and Coriolis frequency (f) according to the dispersion relation:

$$\omega^2 = N^2 \cos^2 \theta + f^2 \sin^2 \theta, \tag{1.5}$$

with θ the angle that the wave vector makes with the *horizontal* (Turner 1973). The

slope of the wave vector is given by:

$$\tan\theta = \sqrt{\frac{N^2 - \omega^2}{\omega^2 - f^2}}. \tag{1.6}$$

Here the general form for a rotating fluid is given. The non-rotating case can easily be obtained by setting the Coriolis parameter to zero ($f = 0$). For a fluid in hydrostatic equilibrium, as in chapter 3 and in Maas and Lam (1995), equation (1.5) can be approximated by taking $\omega^2 \ll N^2$, and reduces to: $\omega^2 = N^2 \cot^2\theta + f^2$.

In section 1.2 it was already noted that gravity waves are super-inertial. Equation (1.5) also implies the existence of an upper bound for the frequency of (free) internal waves, defined by the (local) stratification, $|f| < \omega < N$ (Groen 1948). Another property that follows from the dispersion relation is illustrated in the right image of figure 1.11: the group velocity (c_g) and particle motion are both perpendicular to the phase velocity $\vec{c}$,

$$\vec{c_g} \perp \vec{c}, \quad \vec{u} \perp \vec{c}, \quad \vec{u} \parallel \vec{c_g}. \tag{1.7}$$

The last property can be derived from the continuity equation for an incompressible fluid, $\nabla \cdot \vec{u} = 0$. It follows that vertical components of $\vec{c_g}$ and $\vec{c}$ are always of opposite sign.[4] In the sketch of figure 1.11 (right) the beam going to the right and downward, has upward phase propagation. This feature is most clearly demonstrated in movies of internal waves.

In general, for flat or infinitesimal topography, internal wave beams can be approximated with sufficient vertical modes; see e.g. Gerkema (2001). However, for arbitrary finite (non flat) topography, and near a generation region, an internal wave description in terms of beams is more appropriate.

1.3.3   Internal tide generation

We now return to internal waves with tidal frequency in the ocean. Here the basic features of the internal tidal beams at the continental slope of the Bay of Biscay are addressed. We will see how these beams are generated and get affected by varying stratification $N(z)$.

Internal tide generation at the continental slope

In the ocean, internal waves are not generated by an oscillating plate or cylinder. Over steep topography like the continental slope in the Bay of Biscay, horizontal tidal currents are deflected vertically, causing isopycnal excursions at tidal frequencies. From this region of large excursions, the internal waves propagate in a manner

---

[4]For inertial (gyroscopic) waves, that arise in a rotating homogeneous fluid, the dispersion relation similarly relates frequency only to the direction of the wave number vector. Here, however, the vertical components of $\vec{c_g}$ and $\vec{c}$ point in the same direction, while their horizontal components are in opposition.
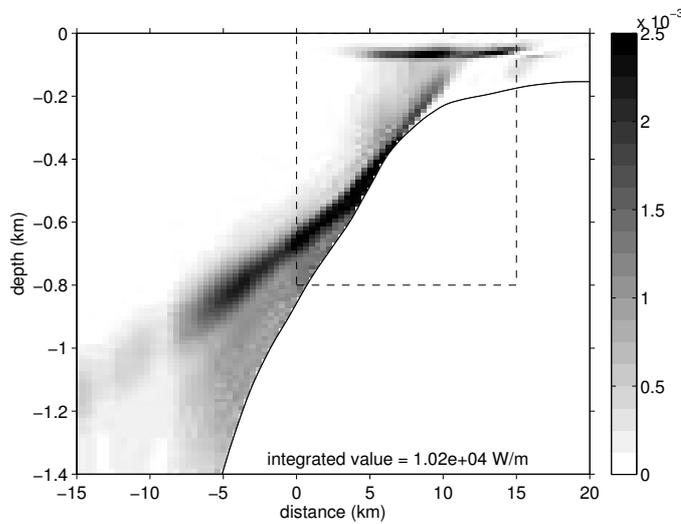
Figure 1.12: See figure C.3 for a full colour version. Conversion rate (greyscale of legend in W m^{-3}) for transect in Bay of Biscay (summer stratification). Two major generation regions for internal tidal energy can be identified: the deep stratification region at the steep slope, and the seasonal pycnocline above the shelf break. The dashed box near the shelf break refers to the observation area of chapter 3. The integrated value in W/m, as indicated at the bottom of the image, is for the entire cross-section. Picture from Gerkema et al. (2004).

similar to that of figure 1.11: the *internal tide beams*. Here the strong forcing is due to strong (cross-slope) currents of the surface tide, strong stratification, and indeed a very steep continental slope. Quantification of these three components of internal tide generation will be presented in chapter 3 (e.g. figures 3.4 and 3.5). In figure 1.12 the resulting conversion rate —of wave energy from surface tide into internal tide— is presented along a cross-shelf transect in the Bay of Biscay for an early summer stratification. The high intensity regions (dark grey) in this picture are the analogues of the oscillating cylinder or plate in laboratory experiments. The deep region of high conversion rate is caused by the permanent pycnocline in combination with the steep topography. As we will see in chapter 3, the profile $N(z)$ has a relatively deep maximum in this area. The upper region of high conversion rate is mostly dominated by the seasonal thermocline. The position of this region is caused by the shallowest part of the slope; the deeper part of the slope is further from the seasonal thermocline, while closer to the coast the steepness of the slope vanishes.

The conversion rate of the previous figure is actually based on the modelled internal tide as determined with a numerical linear hydrostatic model (Gerkema et al. 2004), to be discussed in chapter 3. Two examples computed with this model are displayed in figure 1.13, clearly showing the internal tide beam emanating from the shelf break. The result is similar to the internal wave beam as generated by an oscil-
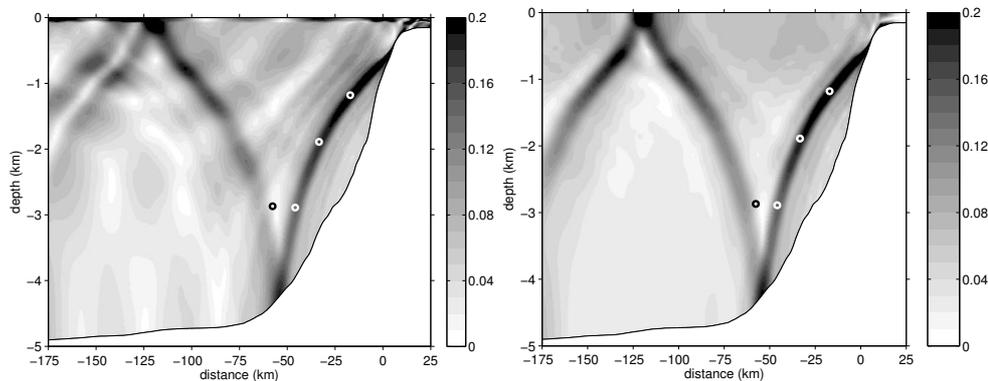
Figure 1.13: Internal tide (cross-slope current amplitudes in m/s) as calculated for the continental margin in the Bay of Biscay. Both early summer situation (left) as well as winter situation (right; without seasonal pycnocline) are shown. Here the beams are slightly curved due to the vertical variation in stratification $N(z)$. Circles indicate the location of the main beam as observed by Pingree and New (1991). Picture from Gerkema et al. (2004).

lating plate or cylinder in the laboratory (figures 1.11 and 1.17). It can be recognized that the beam gets steeper at deeper locations, where stratification is weaker. Experimental evidence of the existence of this beam in the Bay of Biscay was earlier reported by Pingree and New (1991), and is depicted by circles in figure 1.13. The right panel of the figure shows the resulting internal tide amplitudes for the winter situation, without seasonal thermocline. Comparison of these two cases immediately makes clear that, for the summer situation, the beam gets more distorted while propagating into the ocean. Also the response at the seasonal thermocline (-100 m $< z < 0$ m) is different. Gerkema et al. (2004) discuss the observed differences in more detail. It was concluded that the spatial pattern is significantly different for the two seasons, but that the overall tidal conversion rate is only marginally affected. This is due to the dominant contribution of the deeper stratification of the permanent pycnocline and below.

Internal tide observation in the Bay of Biscay

In comparing ocean and laboratory observations we observe that in the ocean there is neither an oscillating plate generating the waves, nor a camera observing them. Instead, the observations are performed with a ship at the surface. As compared with the Snellius expedition of 1929–1930 (figure 1.10 and subsection 1.3.2), in the Bay of Biscay (see figure 3.1), tidal currents are observed here with different equipment. An example of key instruments employed for both expeditions is given in figure 1.14. By towing an acoustic current profiler in the Bay of Biscay, the three-dimensional currents could be measured over the upper 800 m of the water column in bins that are 8 m thick. By sailing up and down along the cross-slope transect in the Bay of
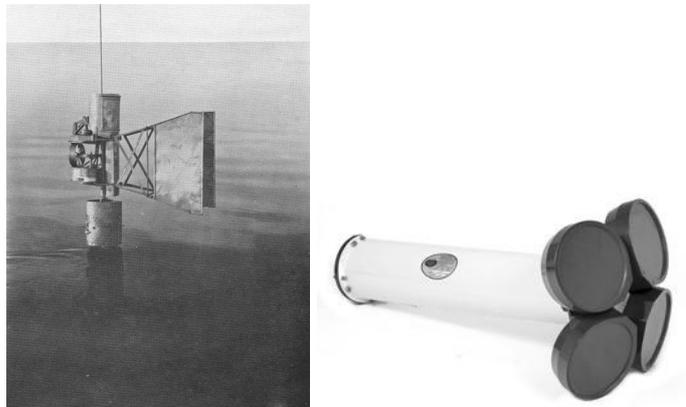
Figure 1.14: Left: mechanical, propeller based, Ekman current meter used during Snellius expedition 1929-1930. Right: ADCP current meter (RD Instruments, 75 kHz). This instrument measures the three-dimensional water flow at several depths by the reflected Doppler shift in different directions. In June 1993 it was towed (looking downward) behind the ship *R.V. Pelagia* and collected *snapshots* of the upper 800 m of the water column, as described in the text.

Biscay, it was possible to collect *snapshots* of the water flow in the upper part the water column. With these snapshots —about ten in two tidal periods— the tidal movement could be estimated for the three sampled xz–planes, each about 15 km long and 800 m deep. The sampled plane is indicated by a dashed box in figure 1.12 for one of the three transects. Apart from the tidal current amplitudes and phases, also the mean flow across and along the shelf edge could be estimated for these xz–planes. These observations are compared with numerical results of the linear model in chapter 3.

It is for the first time that part of the generated internal wave beam is observed in such (spatial) detail in the ocean. As mentioned before, the generation of powerful internal tides propagating obliquely through the deep sea along beams is of interest to the functioning of the ocean circulation, in that waves may provide a source for mixing of density stratified fluid elsewhere. However, the fate of such internal tidal beams is in general not captured well in our numerical models. Employing a three-dimensional ocean general circulation model, Drijfhout and Maas (2006) provide an exploratory study in which such internal tidal beams are recognized. They find that topography can indeed have a profound effect on their trapping.

Intermezzo: internal solitary waves

This subsection is concluded with the illustration of another type of wave that is present in the Bay of Biscay. In discussing (1.5), it was already mentioned that the frequency of internal waves has an upper bound given by N. As a consequence,

high frequency waves exist at the seasonal thermocline, that are not 'allowed' in deeper regions with smaller N: they are *trapped* at the thermocline. Like the internal tide, they are generated at the shelf break by the cross-slope horizontal currents of the surface tide. From the shelf break, they propagate in two directions along the thermocline: coastward and oceanward. Due to nonlinear and dispersion effects, they develop as so-called *internal solitary waves*, and appear as solitary wave *trains* (Gerkema 1994, 1996).

An example with measurements at both sides of the shelf break is presented in figure 1.15. Observed temperature profiles in two successive years (1995, 1996) at two positions on a cross section of the continental margin are displayed (Lam et al. 1999). These measurements were part of the *TripleB* programme, studying oceanography in the Bay of Biscay with *RV Pelagia*, see van Aken (2000). On the shelf, the passage of the internal solitary wave train (figure 1.15, bottom) looks similar to that predicted by a two-layer model.[5] Note the downward displacement of the thermocline of about 40 m. This is typical for this region; displacements up to 100 m have been reported (Pingree and Mardell 1985). The measurements at the deeper side of the shelf edge (figure 1.15, top) look different as compared to the 'predicted' shape of the thermocline from the two-layer model. It looks as if more *packages* are interfering at this position. This suggests three-dimensional influences as were also observed by New (1988) with Synthetic Aperture Radar (SAR) imagery in August 1978 about one degree further east of this observation.

Internal solitary waves can also occur further offshore. Modelling results of Gerkema (2001) confirmed that the surface reflection of the main internal tide beam, at -120 km in figure 1.13, causes the local generation of internal solitary waves. These *remote* internal solitary wave packages in the central Bay of Biscay were earlier reported by New and Pingree (1990, 1992). There is much more to say about these phenomena and their observations. Here I will not go into any further detail of internal solitary waves, as this is outside the scope of this thesis.

1.4 Focusing at the slope: internal wave attractors

While we have seen that internal tides can be generated by the surface tide near the shelf edge and over continental slopes, it remains unclear what happens to them. We anticipate that they might contribute to mixing 'elsewhere'; see also Munk and Wunsch (1998) for a discussion. Here we present theoretical and experimental evidence that yet another property of the topography plays a key role in determining that mixing 'hot spots' may, surprisingly, be quite predictable. This role is played by the focusing that internal waves experience when reflecting from a sloping boundary.

---

[5] The modelling results for this particular cross-section of the shelf slope can be found in Lam et al. (1999). This transect is actually the middle transect of figure 3.1 in chapter 3.
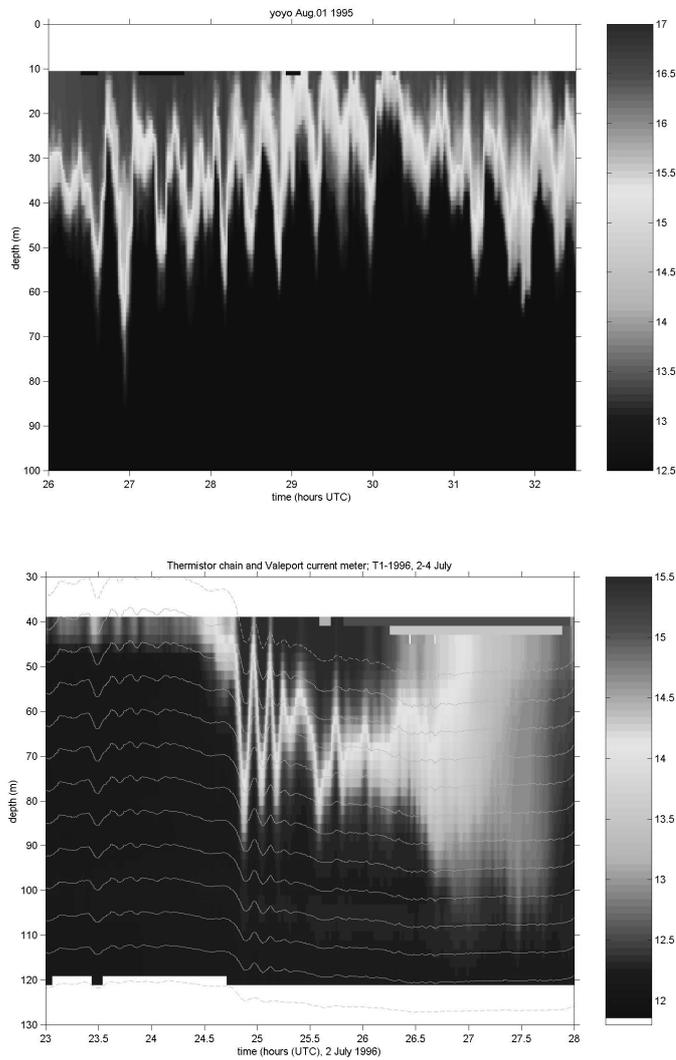
Figure 1.15: See figure C.4 for a full colour version. Measured temperature profile halfway along the slope (top), and on the shelf (bottom) 32 km coastward. The temperature profile of the upper 100 m (130 m) is shown over 6.5 hours (5 hours) in the upper (lower) image. Temperature values (°C) are as indicated in the corresponding legends. The upper image is obtained by measuring temperature (and salinity, not shown) of the upper 100 m of the water column (CTD casts; 'yoyo-station') from the ship. The lower image is retrieved by correcting 'drifting depth' of thermistors along a partly broken mooring. Corrected thermistor depth vs. time (using interpolated values of pressure sensors on both ends of the thermistor chain) is visualized by white (light grey, hardly visible) lines. The horizontal bars at the upper right of the graph are artefacts of the interpolation algorithm used. Pictures taken from Lam et al. (1999)

Figure 1.16: Subcritical (left) and supercritical (right) single focusing reflection for two pairs of internal wave rays (side view). Note: reversing the direction of the incoming rays changes the examples from focusing to defocusing.

1.4.1   Internal wave reflections

As the sketch in figure 1.16 shows, internal waves focus or defocus upon reflection from a sloping boundary. The reason is that, according to (1.5), upon reflection, the angle which the beams make with respect to the direction of gravity remains fixed and, as a result, the beams converge or diverge. When the boundary is steeper than the internal wave beam, the slope is called *supercritical*; upon reflection the wave reverses its horizontal propagation direction. The slope is called *subcritical* if it is less steep than the internal wave beam and waves continue in the same horizontal direction. In between, for *critical* bottom slope, the slope equals that of the internal wave beam and forms a separate interesting case (Eriksen 1982), not discussed in this thesis.

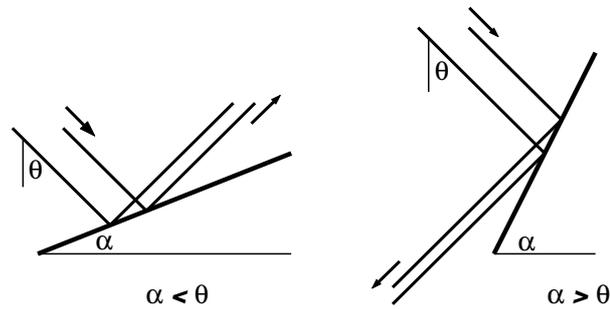The left image of figure 1.17 illustrates this process by means of a fluid experiment. Here internal waves are generated by oscillating a horizontal cylinder vertically. As can be seen from the extracted beams in the neighbouring image, after reflections at the surface and at the left boundary, the internal wave beam extends downward and to the right. After reflection at the sloping boundary (position A), the beam *brightens up*, illustrating the focusing (converging of wave energy) by the supercritical slope, just as in the right image of the sketch in figure 1.16. Following the beam clockwise, upon subsequent reflections at bottom, left wall and surface of the tank, the energy of the internal wave beam is weakened by viscous dissipation. However, after a full cycle, the beam brightens up once more upon a second focusing reflection at the sloping wall in the upper right corner of the tank (position B).

This fluid experiment convincingly shows basic properties of internal waves in a stratified fluid that are even better appreciated when viewed in movie animations. These clearly demonstrate the phase propagation and focusing characteristics of a sloping topography.
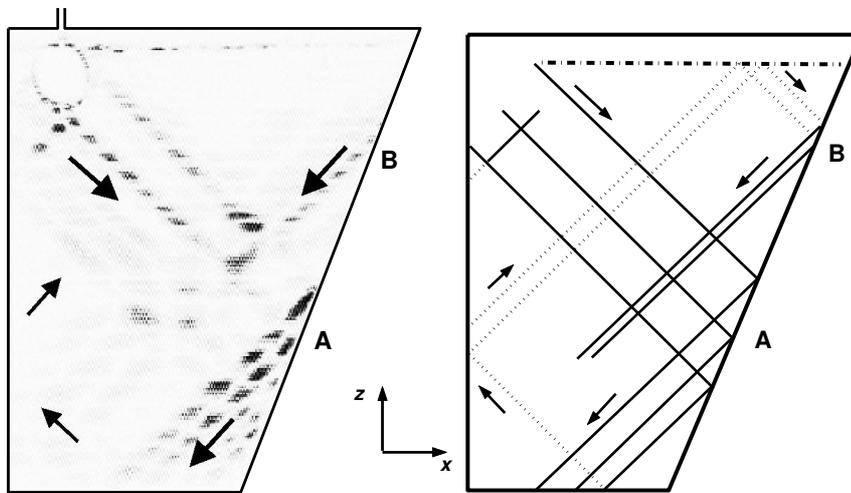
Figure 1.17: See figure C.5 for a full colour version. Internal wave experiment performed by the author in 1996 at DAMTP, Cambridge. The tank is about 380 mm high and 100 mm thick. The water is density stratified with a linear salt concentration ($N = 1.5$ rad/s). In this example, the cylinder (radius 22 mm) in the upper left corner is vertically oscillating with a frequency $\omega = 0.942$ rad/s, and an amplitude of 4 mm. In the figure at the right, the identified internal wave beams from the left image are shown. Lines not visible in the left image are dotted. The horizontal dash–dotted line near the surface is the pycnocline present in the tank. Energy propagates along the indicated arrows, similar to figure 1.11, with phase lines propagating perpendicular to the beam. Two regions of subsequent focusing reflections can be identified, regions A and B, respectively. The horizontal interruptions of the beam are caused by the *synthetic Schlieren* technique, that is used for visualization. This technique makes use of the changing refraction index in the fluid; the virtually displaced background (horizontal stripes) reveals the internal wave patterns (Dalziel et al. 1998; Sutherland et al. 2000).

1.4.2   Internal wave attractors

It is interesting to follow internal wave beams (rays) upon multiple reflections, assuming that no absorption is involved. This is similar to playing the 'internal wave billiards'. For a classical billiard, a ray's angle of reflection equals its angle of incidence, relative to the bottom normal. In that case rays diverge for most basin shapes (Berry 1981). For the internal wave billiard, however, the ray's angle relative to the vertical (gravity) is preserved. As a consequence, internal wave beams end up on a limit cycle, called a *wave attractor* (Maas and Lam 1995). It appears that this limit cycle is ultimately approached by every characteristic, no matter what the starting point of the characteristic is. Two examples for different starting positions of a characteristic (thin solid and dashed lines) are given in figure 1.18a. This attractor, with only one surface and one sidewall reflection, was defined as an attractor with *period*
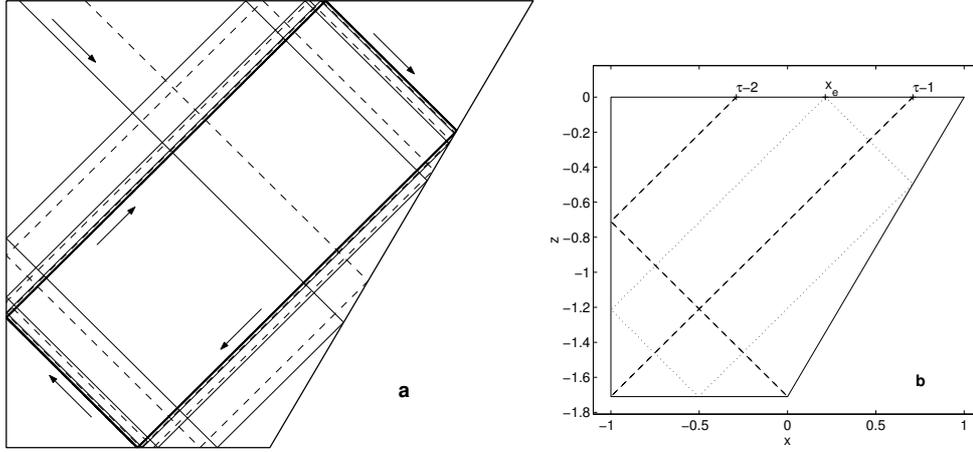
Figure 1.18: (a) Example of internal wave ray focusing (thin solid and dashed) and wave attractor (thick solid) in a trapezoidal geometry with the bottom at $z = -\tau$; $\tau = 1.71$. (b) Positions of special points at the surface, defining primary fundamental intervals: $x \in [-1, \tau - 2]$ and $[\tau - 1, 1]$ for the same tank with sloping sidewall. The position of the attractor with surface reflection at $x_e = \tau^2 - \tau - 1$ is depicted with dotted lines.

equal to one (Maas and Lam 1995). This period of the limit cycle was counted by the number of surface reflections of the limit cycle. This terminology is introduced in accordance with its usage in dynamical systems. Note that this period of the attractor is not to be confused with the internal wave period. This attractor has also been referred to as the $(m, n)=(1, 1)$–attractor, enumerating the number of reflections of the attractor at the surface (m) and the vertical side wall (n).

These attractors persist over a finite wave frequency interval. The frequency dependence of the attractor can best be expressed in terms of a scaled wave period or depth τ, defined below. By incorporating equation (1.6), the vertical co-ordinate z can be stretched, so that for any single frequency ω the angle of the internal wave vector equals $\pm 45°$ (Maas and Lam 1995). The scaled, dimensionless depth of a basin of depth D and width $2L$ then becomes:

$$\tau = \sqrt{\frac{N^2 - \omega^2}{\omega^2 - f^2}} \frac{D}{L} \,. \tag{1.8}$$

The $(1, 1)$–attractor of figure 1.18 persists over nondimensional bottom depths $1 \leq \tau \leq 2$. The single surface reflection of this attractor is at $x_e = \tau^2 - \tau - 1$; the shape of the attractor changes gradually within the indicated τ–interval (Maas et al. 1997).

For a shallow *parabolic* basin, having partly supercritical sidewalls, figure 1.19 gives an overview of all asymptotic (final) surface reflections, each having n=1 (that is: $1/2 \leq \tau \leq 1$). Here, for every depth τ, the last 200 of 1100 surface reflections of
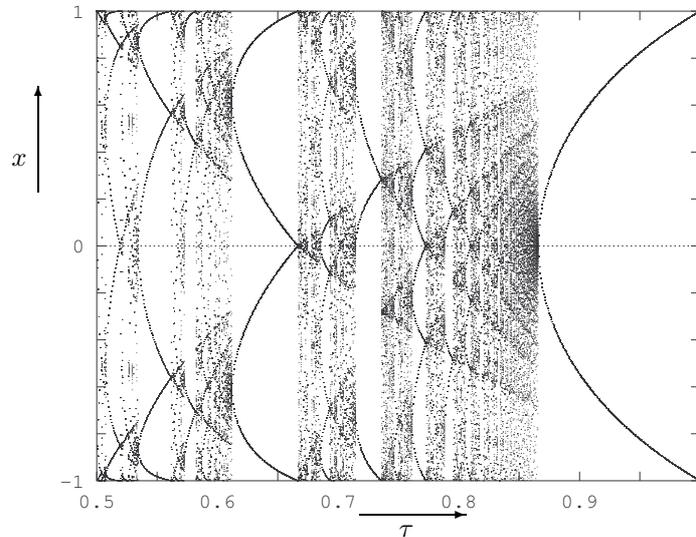
Figure 1.19: Surface reflections of attractors in a basin with parabolic cross-section. Last 200 surface reflections (of 1100 total) for a ray starting at the surface x_0=0.123456789 in positive direction. All depths for $1/2 \leq \tau \leq 1$ are plotted. Picture taken from Maas and Lam (1995).

a ray are depicted. In this example, for each τ the ray starts (arbitrary) at surface position x_0=0.123456789 in rightward direction. The fractal properties of this image are discussed in Maas and Lam (1995). From this picture it is clear that intervals of low period attractors alternate with intervals containing complex high period attractors. The lowest order periods (m=2,3,4,...) have the widest intervals for τ, like $\sqrt{3}/2 \leq \tau \leq 1$ for m=2. It can also be shown, in terms of Lyapunov exponents that measure the asymptotic convergence rate of two neighbouring rays, that the lowest order attractors have the highest convergence rate.

1.4.3   Standing modes

Although the appearance of attractors is generic, multiple periodic pathways of the reflected characteristics are incidently found for particular parameter values and for particular geometries. For two-dimensional systems, these standing modes occur when for every pathway, along a sloping segment of the boundary each focusing reflection is compensated by a defocusing reflection: all rays fold back upon themselves. The simplest (non-rectangular) case occurs for the (m,n)=$(1,2)$ standing mode for a basin with one sloping sidewall, deeper than in figure 1.18: each ray now describes roughly the pattern of a distorted figure eight (8) (Manders 2003, fig.3.2).

These standing modes are similar to the cellular modes for a non-tilted rectangular basin of rational aspect ratio, in which each characteristic also folds back upon itself. However, for rectangular basins, there is no focusing or defocusing, whereas

for sloping topography focusing is balanced by defocusing. The corresponding solution of the stream function is similar to (topographically) modified versions of the cellular modes of figure 1.9 (left), and can be related to *internal seiches* in lakes with a continuously stratified density. For a rectangular basin this has been addressed by Münnich (1996). The standing modes do not exist over extended parameter intervals for τ (basin depth or internal wave frequency), but only for very specific values of τ. Due to their sensitivity to the specific parameter setting, these internal seiches are therefore not likely to occur in nature for basins of arbitrary shape.

For a rectangle, the solution can be obtained by separation of variables. This is in general not possible for basins with sloping walls, since the boundary conditions at the slope contain both dimensions.[6] With the help of characteristics, stream function patterns can in fact be found for arbitrary geometry, as will be discussed below.

1.4.4 General solutions for the stream function

Because the two-dimensional fluid motion is incompressible, a stream function Ψ can be introduced:

$$u = -\frac{\partial \Psi}{\partial z}, \quad w = \frac{\partial \Psi}{\partial x}.$$

(1.9)

It is assumed that we will look at monochromatic waves only:

$$\Psi(x, z, t) = Re[\psi(x, z)e^{-i\omega t}].$$

(1.10)

For attractors, the corresponding solution of the spatial stream function field $\psi(x, z)$ is quite different from the *cellular* shape, described above and in figure 1.9. An example is given in figure 1.20. The stream function has 'cells' of smaller size, closer to the attractor position. The spatial structure of the stream function field of the monochromatic internal wave field is, in dimensionless form, and in stretched coordinates, described by the following hyperbolic equation:

$$\frac{\partial^2 \psi}{\partial x^2} - \frac{\partial^2 \psi}{\partial z^2} = 0.$$

(1.11)

that, for free waves, needs to be solved subject to the requirement that the boundary is a streamline ($\psi = 0$). General solutions for (1.11) can be written as:

$$\psi = f(x - z) - g(x + z).$$

(1.12)

Here the characteristics $x \pm z$ can be recognized, along which the field functions f and g are preserved. The pressure[7] can be written as:

$$p = f(x - z) + g(x + z),$$

(1.13)
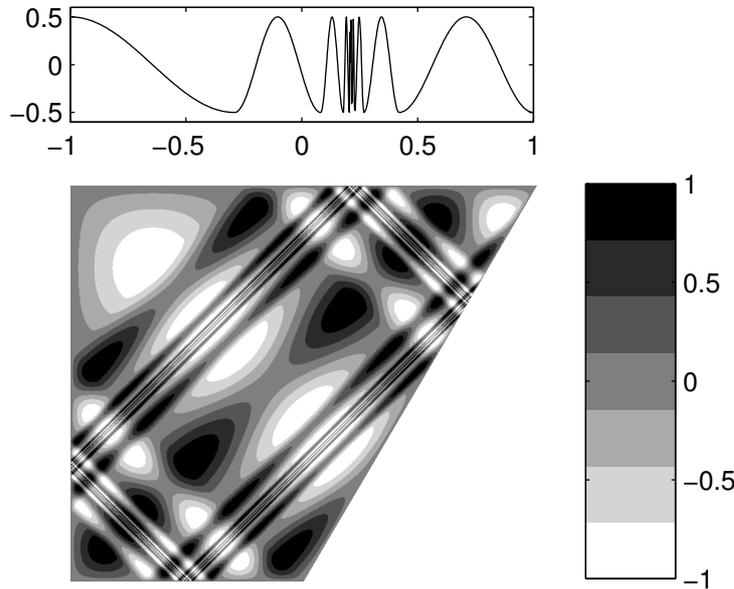
Figure 1.20: See figure C.6 for a full colour version. Example of standing wave solution $\psi(x,z)$ for a surface pressure $p_a(x) = 2f(x)$ that is prescribed within the two fundamental intervals and from which the whole pressure distribution along the surface, as indicated in the top panel, can be inferred. Values for ψ are coded with the greyscale as shown in the legend on the right.

which allows us to interpret f and g individually as *partial pressure*.

From the surface boundary condition ($\psi = 0$ at $z = 0$) it follows that $f = g$ in (1.12) and (1.13), so that at the surface: $p(x) = 2f(x)$. However, as explained in Maas and Lam (1995), this boundary condition at the surface can only be prescribed in specified, so-called *fundamental intervals*. This restriction needs to be made in order to prevent conflicts in assigning values of f at later reflections. Note that all characteristics and their reflections are present at the same instant, as time t is no longer present in equations (1.11), (1.12) and (1.13) upon considering a monochromatic wave. The definition of the largest fundamental intervals (called *primary interval*) for the basin with one sloping sidewall is illustrated in figure 1.18b. The repetitive character of the boundary condition can easily be recognized in figure 1.20 (top).

The solution for real ψ represents a standing wave solution for Ψ. Thus, with (1.10), it follows that this solution, as in figure 1.20, is *blinking* in time. This limita-

---

[6]Maas and Lam (1995) present an analytical solution for a semi-elliptic topography, using a transformation of co-ordinates.

[7]The reduced pressure p_* (that is, $p_* \equiv P + \rho_0 gz$, where P is the original pressure, and ρ_0 is the constant reference density) is written as $p_* = i\omega\rho_0 p$, so that p has the same dimension as the stream function ψ: m^2/s.

tion, as well as the artificial nature of the boundary condition, will be addressed in chapter 4.

1.4.5   Laboratory experiments and shortfalls

For two reasons we expect that in real fluids (including viscosity) only simple, low-order attractors are observable. First, since shear will be large in the direct vicinity of any periodic orbit that constitutes the attractor, the presence of more convoluted attractors will imply that shear regions fill the entire fluid domain. Second, attractors of lower period have higher convergence in terms of the Lyapunov exponents. Both reasons make a low-period attractor more likely to be found in a real fluid.

It appeared that the existence of such an attractor was not easy to demonstrate with a local wave generator, as in figure 1.16. Here the viscosity of the fluid prevented the internal wave beams from surviving multiple reflections. However, global forcing of the fluid, by vertical oscillation of the entire tank *(shaken, not stirred!)*, clearly demonstrated the existence of the internal wave attractor at the expected positions (Maas et al. 1997). The oscillation of the fluid tank (frequency 2ω) causes effectively a modulation of gravity. Internal waves of subharmonic frequency ω are generated by *parametric excitation*, similar to how a child's swing is brought into motion, by pushing it downward when it is at its extreme upward position. The forcing is most effective when done at *both* extreme upward positions, rendering the pendulum's period as half that of the forcing period, whence the *subharmonic* nature of the response.

The most prominent results from this experiment are presented (in black-and-white) in figure 1.21, visualized by following the vertical displacement of dye bands in the stratified fluid. This is done by subtracting the (intensities of the) original image of the tank at rest. The attractor shows up in the fluid at exactly the expected position for this forcing frequency and (salinity) stratification N, see Maas et al. (1997). It takes about five minutes for the fluid to respond to the forcing. The attractor then gradually shows up as a standing wave for about 4 minutes, with all observed displacements in the fluid occurring at the same time. Several minutes later this is replaced by propagating displacements, as illustrated in the subsequent images of figure 1.21 (bottom). As indicated by arrows, this phase propagation is in line with the typical properties for internal waves. Notably, for energy propagating clockwise along the attractor, phase lines travel downward and to the right for this branch of the attractor, as in the figure.

The initially calculated solution of the stream function field, as in figure 1.20, provides a good reference for predicting the high energy distribution along the attractor, as in figure 1.21. However, there are important remaining issues that can not be fully understood by this solution alone. The start-up time, as well as the evolution of the attractor's appearance (from standing or blinking to travelling) can not be explained with the standing wave solution of figure 1.20. In relation to this, the detailed forcing mechanism, of the parametric excitation needs to be understood more thoroughly. Moreover, not every spatial detail of figure 1.20 is reproduced in the
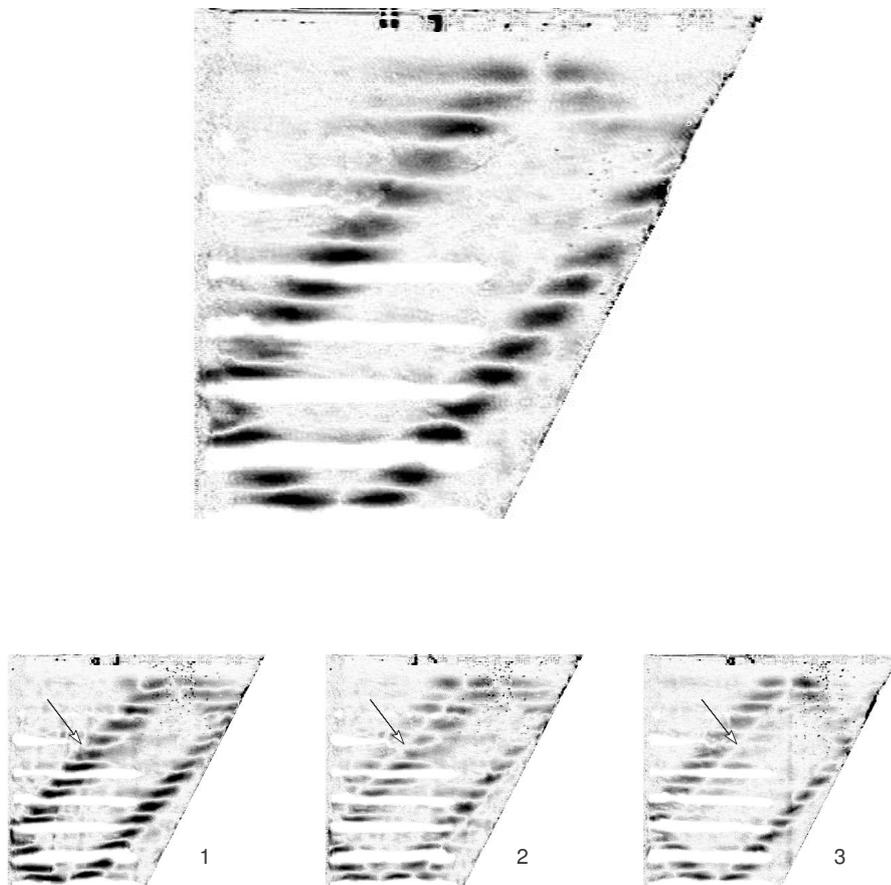
Figure 1.21: Black-and-white version of figure 4 of Maas et al. (1997). Here the attractor is visualized by highlighting the absolute difference (compared to some reference image) of the intensity of the video image. In this way, large displacements in the fluid (with originally horizontal dye bands) are visible. Here, $\tau = 1.71$ and a forcing amplitude of 10 cm was used. Pictures during growth phase taken 9 minutes after start of oscillations (top) and during permanent stage after 10 minutes, showing images at 3 instances $t/T = n/12$ labelled by integer n=1,2,3 (bottom).

laboratory experiment. It is clear that in the experiment it is not the stream function field itself that is observed directly.

While previous work has thus demonstrated the existence and physical relevance of the wave attractor, there are still a number of questions that need to be resolved, particularly when comparing the experimental results with the theoretical predictions. For example, while the location of the wave attractor is well predicted, there is

no full understanding why the intricate fine structure of the theoretical stream function field, particular in the attractor's vicinity, is not visible experimentally. One reason may be that we forget to 'translate' the predicted stream function field, when we try to compare this with observed dye displacements. But, surely the adopted theoretical model is also too simple, lacking a proper description of the way in which the waves are forced and how this is accomplished by means of oscillation of the table.

For these reasons, chapter 4 addresses the following issues:

- analysis of the detailed structure of the attractor and its evolution in the laboratory experiment;

- the forcing mechanism and the waves that these generate;

- the boundary condition and the generalization of the solution procedure to *propagating* waves;

- the calculated displacements associated to propagating waves and their comparison to those observed.

1.5 Overview

For the convenience of the reader, table 1.1 provides an overview of the topics addressed in the chapters that follow, and that have been introduced in this chapter.

	chapter 2	chapter 3	chapter 4
Area	Greenland	Biscay	Laboratory
Topic	Continental shelf waves	Internal tide (+ residual currents)	Internal wave focusing
Forcing	Topographic resonance at tidal period	Barotropic flow over topography	Parametric excitation
Scale	1000 km	100 km	100 cm

Table 1.1: Overview of chapters of this thesis.

Chapter 2

Shelf Waves with Diurnal Tidal Frequency at the Greenland Shelf Edge [1]

Tidal analysis was carried out on current measurements at a "cross-shelf" transect off Greenland at $71°N$. The diurnal tides manifest themselves mainly as a barotropic continental shelf wave, travelling southward along the shelf slope. This follows from the amplitude distribution of the diurnal tidal components and from the rotation sense of the tidal ellipses at different cross-slope locations, as calculated with simple two-dimensional models. The well organized cross-slope pattern of the velocity amplitudes is absent in observations further north near $75°N$. These observations suggest that the local vanishing of the group velocity, which is caused by topography, is of importance for the existence and local amplification of these continental shelf waves with diurnal tidal frequency.

2.1   Introduction

Since their discovery (Hamon 1962; 1963) continental shelf waves (CSWs) have become a well-known manifestation of topographic Rossby or topographic planetary waves. They have a period typically on the order of 1 week; see for example LeBlond and Mysak (1978, §25) and Mysak (1980). Cartwright was the first to discover CSWs with *tidal* frequency near the Hebrides (Cartwright 1969; Cartwright et al. 1980), while the dominating diurnal motion in this region had already been reported in 1665 by Moray. Numerous other observations of CSWs with tidal frequency have been reported since: over Rockall Bank (Huthnance 1974), near Bear Island, Norwegian Sea/Barents Sea (Huthnance 1981a), west of Vancouver Island (Crawford and Thomson 1982; 1984), near New Zealand (Heath 1983), near Yermak Plateau in the

---

[1]This chapter is previously published as Lam (1999)

Arctic Ocean (Hunkins 1986; Padman et al. 1992) and in the Weddell Sea (Middleton et al. 1987).

Continental shelf waves with diurnal (tidal) frequency are thus a common feature at high latitudes. The trapped nature of these sub-inertial vorticity waves distinguishes them from freely propagating superinertial gravity waves, such as the semidiurnal tides, and they are therefore more sensitive to off-shore (i.e. shelf break) depth differences. This can lead to problems in implementing the boundary conditions at the coast in numerical models for diurnal tidal constituents (see for example Gjevik and Straume (1989), comparing their tables 2 and 7 for M_2 and K_1 amplitudes respectively). It was also stated in Cartwright et al. (1980) that, because of insufficient resolution of incorporated bathymetry, measured tidal elevations at the coast cannot be used as boundary conditions for numerical models of diurnal tides. Understanding the dynamics (and generation) of CSWs with tidal frequency is therefore of importance for global tide modelling, and its applications, e.g. in satellite altimetry (Cartwright 1991; Andersen et al. 1995). Moreover, continental shelf waves are characterized by relatively large cross-shelfbreak currents, leading also to vertical transport of water particles, which are important for the exchange of water masses between coastal and deep-sea regions, the eventual generation of internal waves and for biological processes. Thus far, however, little is known about the origin of the spatial distribution of shelf waves in these high latitude regions. However, Kowalik and Proshutinsky (1993) recently found with a numerical model a number of high energy regions for diurnal currents in the Nordic Seas, while Maslowski (1996) found periodic motion with relatively high frequency (17.3 h) locally in the Greenland Sea at $75°N$ employing an OGCM (Ocean General Circulation Model) driven only by constant monthly-mean January wind stress.

The present paper reports observational evidence for the local amplification of diurnal (tidal) currents indicating the existence of a CSW travelling along the Greenland shelf edge in the northern Iceland Sea, at $71°N$. Together with the results of the abovementioned numerical study of Kowalik and Proshutinsky (1993), the apparent non-existence of CSWs in the observations further north in the Greenland Sea (at $75°N$) does raise questions about the generation of CSWs in relation to local topography.

After a brief description of the available data and a presentation of the most striking results in sections 2.2 and 2.3, some simple two-dimensional models, using flat shelf and deep-sea regions, are discussed in section 2.4, and the chapter ends with a discussion and conclusions in sections 2.5 and 2.6.

2.2   Description of data

In September 1988 and 1989 two joint Danish–Icelandic cruises took off for an extensive hydrographic program (Kristmannsson et al. 1991) and to deploy and recover 8 moorings with 26 self recording current meters: 3 moorings were located in the Denmark Strait and 5 at $71°N$ over the continental shelf break between Greenland
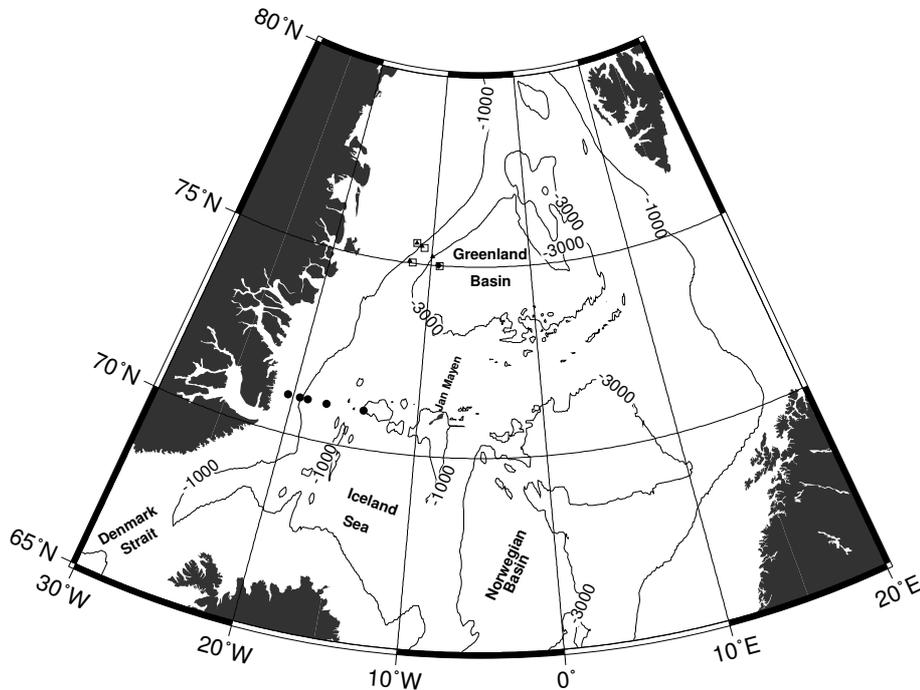
Figure 2.1: Greenland-Iceland-Norwegian (GIN) Seas with 1000 m and 3000 m isobaths (from ETOPO-5 database, NOAA (1988)). The following moorings are indicated: moorings at $71°N$ transect 1988-1989 (●), moorings near $75°N$ 1987-1988 (▲), 1988-1989 (□) and 1989-1990 (♦)

and the isle Jan Mayen (figure 2.1); see van Aken et al. (1992) for an overview of these current measurements, technical details about the moorings and current meter specifications. Details about the bathymetry and hydrography of this region can be found in Hopkins (1991).

From June 1987 to Jan.–May 1989 four moorings were situated near the shelf edge at $75°00'$–$75°30'N$, with 11 current meters deployed and replaced by 15 current meters after one year by German researchers from the Alfred Wegener Institute, Bremerhaven (Sellmann et al. 1992). One of these moorings (4 current meters) was deployed for another 6 months from May till December 1989. The results of the recorded low frequency currents and variability of these measured currents are reported in Strass et al. (1993).
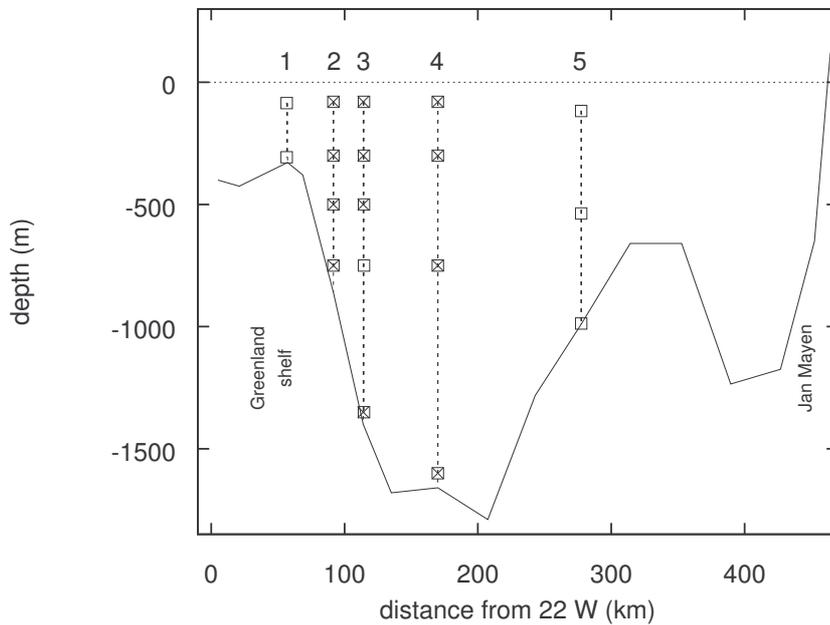
Figure 2.2: Cross section east of Greenland at $71°N$ with moorings numbered 1–5. Current meters (denoted as squares) are of type NBA, model DNC-2M (⊠, sample time 30 min) or Aanderaa, model RCM4, RCM5 or RCM7 (□, sample time 60 minutes). The two deepest meters of mooring 5 did not operate satisfactory, and are not used. In this sketch approximate depths are taken from CTD-casts (Kristmannsson et al. 1991).

Both of these programs were part of the *Greenland Sea Project* (GSP-Group 1990). We will focus mainly on the data from the transect between Greenland and Jan Mayen at $71°N$. A cross-section is given in figure 2.2, which shows that moorings numbered 1–4 are centered on the Greenland shelf slope, while mooring 5 is more remote and on the slope of a seamount. In section 2.4 the continental slope will be regarded as a straight two-dimensional extended feature, while the seamount has a more localized appearance, as can be verified from figure 2.1.

An example of the observed across-slope velocity component is given in figure 2.3, and their corresponding power spectra in figure 2.4. For this mooring the largest diurnal currents were recorded and were of the same order, or even dominating the semi-diurnal currents. Diurnal tidal currents appear to be relatively important near the shelf edge. Their nature is mainly barotropic (and even enhanced near the bottom), while the semidiurnal currents are more baroclinic, as is clear from analysis of all current meters (Lam 1992). In the next section we will take a closer look at the spatial distribution over the shelf slope for tidal amplitudes at specific tidal frequencies.
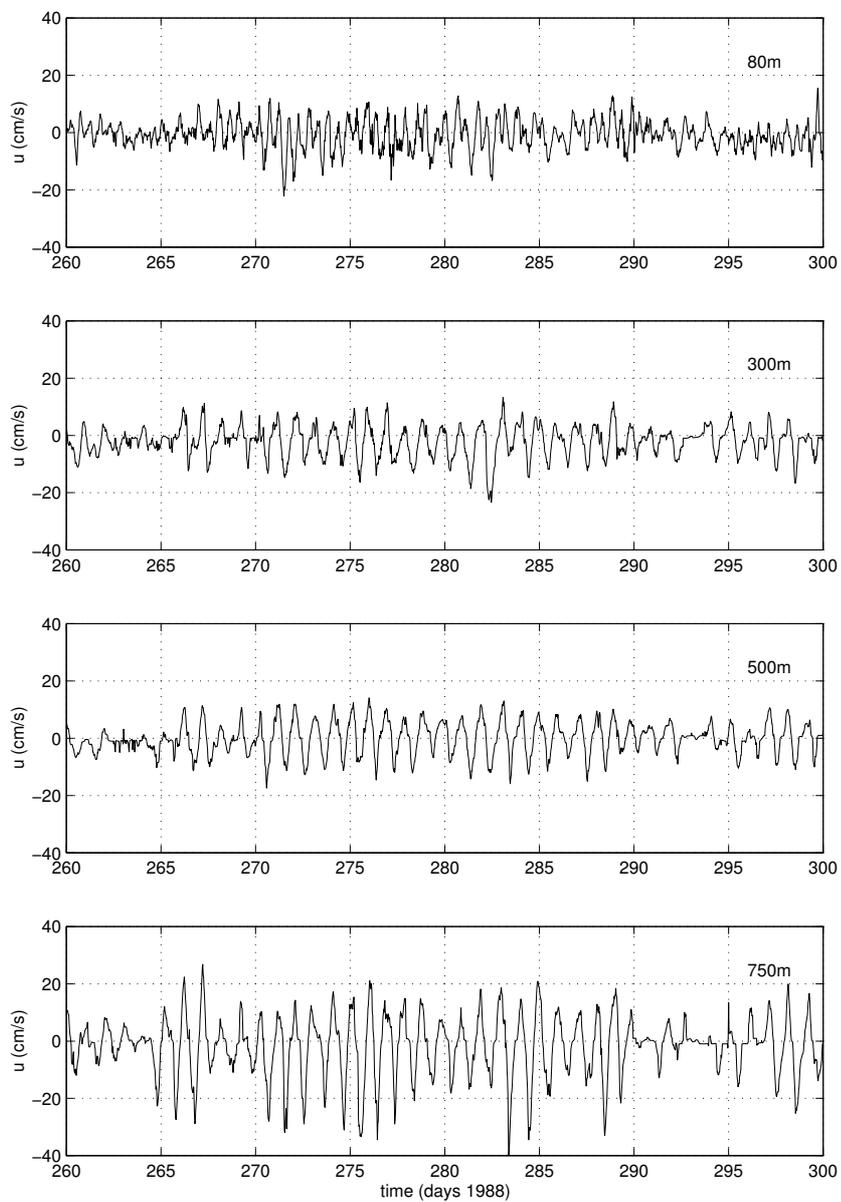
Figure 2.3: Part of measured time series of raw across-slope velocity component (105° True North positive) of mooring 2.
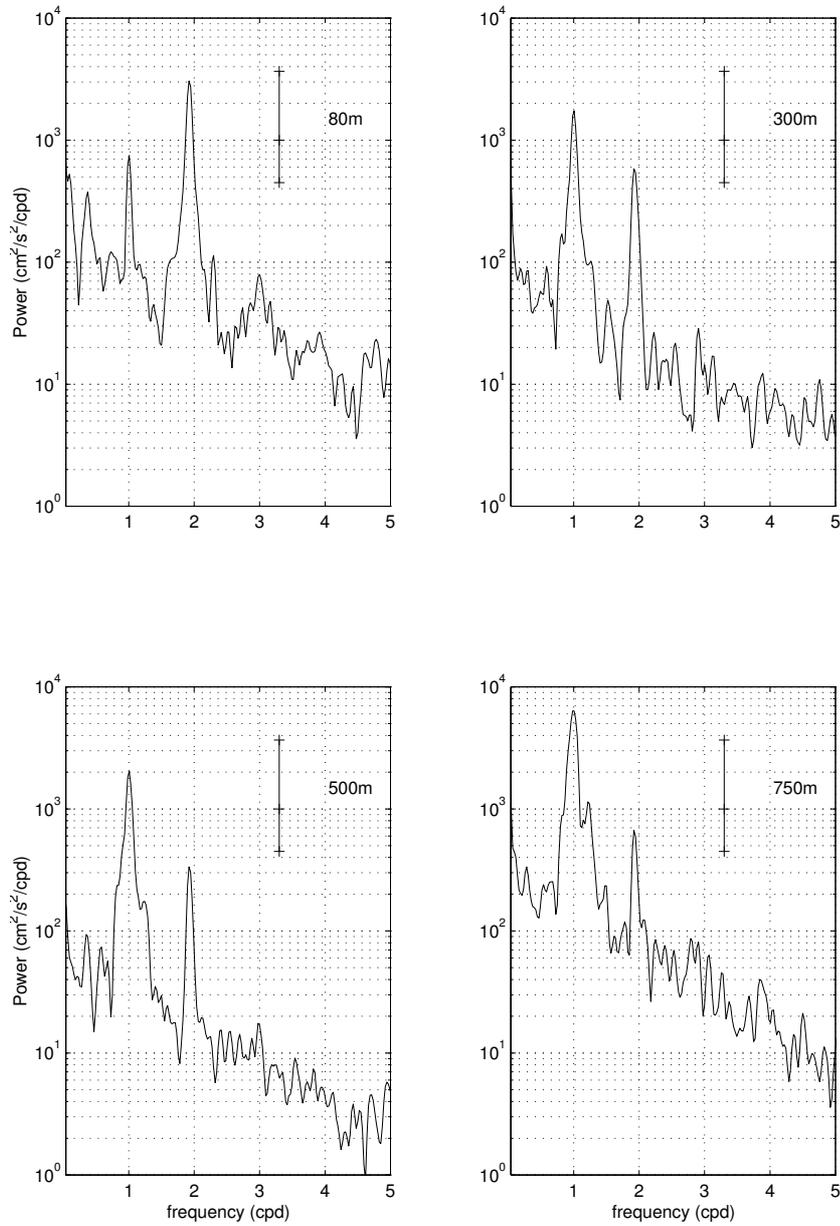
Figure 2.4: Power spectra for time series of figure 2.3. Length of all time series taken here is 142.77 days (6853 points). Window length is 2048 points (1024 h) here, semi-overlapping. 95% confidence limits are indicated in the upper right corner of each figure, together with the deployment depths of the current meters. Frequency units here are cycles per day (cpd).

2.3 Analysis of data / results

Amplitudes and phases for each tidal constituent were calculated with harmonic analysis, described by Dronkers (1964) and Godin (1972), for all current meter time series. This has been done for the 7 tidal frequencies O_1, P_1, K_1, N_2, M_2, S_2, K_2, while the higher harmonics M_4, S_4, M_6 were included as an indication of nonlinearity. The inertial frequency f at $71°N$ (1.379×10^{-4} rad/s; period 12.66 h) could not be separated from N_2 with the actual length of the time series (143 days). Errors (Δu) in the velocity component amplitudes (U), as estimated with the standard deviation (std) of the difference of the composed 'harmonic' time series (u_{ha}) with the measured time series (u): $\Delta u = \text{std}(u - u_{ha})/\sqrt{M}$, with M being half the number of data points (Godin 1972), were in the range 0.5–1.0 mm/s. Absolute error ($\Delta \phi$) in the phase (ϕ, chosen at Jan. 1 1988, 00:00 UTC) is then the same as the relative error in relating velocity component amplitude for each tidal constituent/frequency: $\Delta \phi = \Delta u / U$ in radians.

Results of harmonic analysis for K_1 and M_2 constituents at $71°N$ are shown in figures 2.5 and 2.6. The difference between the spatial distribution of M_2 and K_1 amplitudes and phases is striking. The semidiurnal M_2 constituent shows higher amplitudes near the surface, and a change in rotation sense for these upper meters. The diurnal K_1 constituent shows only a small change in amplitude and phase in the vertical direction indicative of dominantly barotropic motion. The currents are larger near the shelf break, especially the across-slope component, and show a clear change in rotation at the break: the current vector rotates clockwise on the shelf and anticlockwise in the ocean. Influence of the Greenland coastline is visible in the enhanced along-slope velocity for the western most mooring (no. 1 in figure 2.6). Mooring 5 is more remote from the shelf/slope system and is by contrast more affected by the nearby seamount.

The spatial distribution of amplitudes for the O_1-frequency (not shown) is comparable with the pattern for K_1, except for the absolute magnitude of the amplitudes, which is smaller by a factor 2.5. Especially the rotation sense of the O_1 velocity vector shows the same sign-reversal over the shelf–slope region. The same holds for the P_1-frequency, showing again somewhat smaller amplitudes, except at the deepest meter of mooring 2.

For the shelf edge at $75°N$, one might expect similar behaviour for the diurnal currents as given in figure 2.6, but this is not the case as the observations from moorings deployed there showed (see figure 2.7). Apart from some coastal influence for the shallowest mooring (mostly along-slope currents of comparable magnitude as mooring 1 of figure 2.6), currents for K_1 now are about 4–10 times weaker than at $71°N$, and do not show any amplification of the across-slope currents over the shelf-break. In section 2.4, we will try to find an explanation of the overall current pattern given in figure 2.6, while we will address the fact that, at the same time, this behaviour is not observed further north in section 2.5.
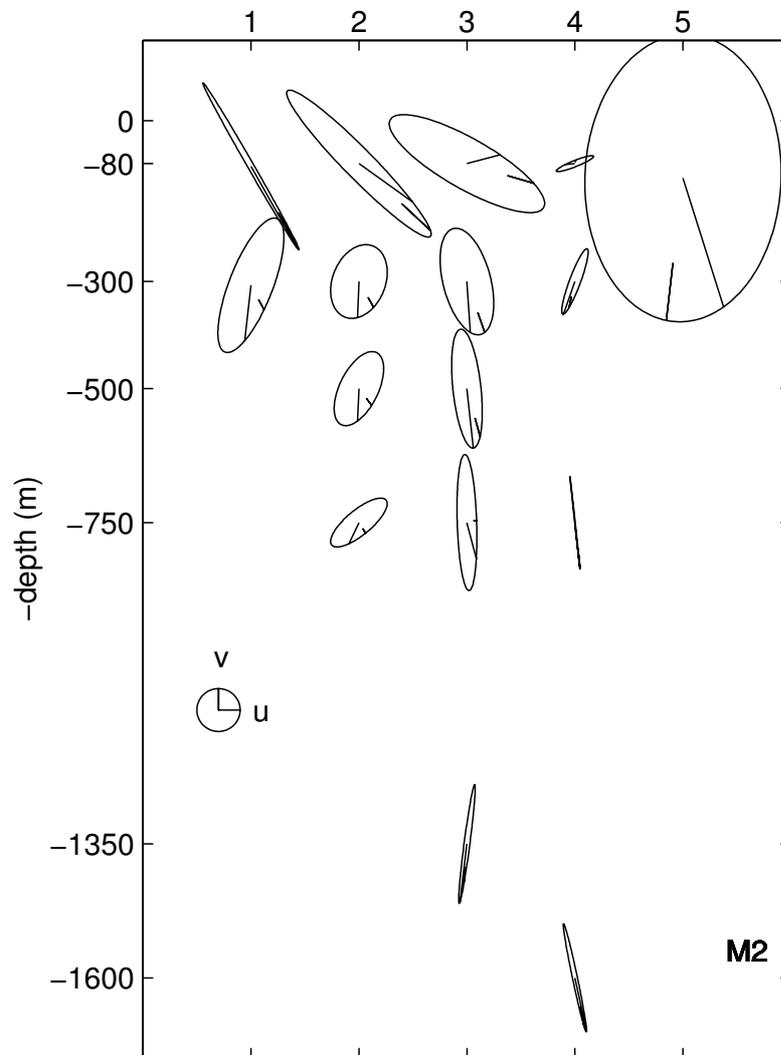
Figure 2.5: Tidal harmonic ellipses for M_2 frequency at Jan Mayen transect. Centres of the ellipses are equidistant and correspond more or less to the positions of the current meters in the xz–plane as in figure 2.2. Horizontal and vertical sizes of the ellipses correspond with across-slope (u) and along-slope (v) velocity amplitudes, respectively. These amplitudes can be compared with the reference circle in the lower left corner, which has a radius of 1 cm/s. For each ellipse the combined phase (at time 00:00 UTC, Jan 01 1988) of both velocity components is given with the line from the centre of the ellipse. Rotation sense is from this line towards the smaller tick mark. It thus follows here that all upper current meters (depth 80m) show a clockwise rotation sense, while all deeper meters recorded anticlockwise water motion for this (M_2) frequency.
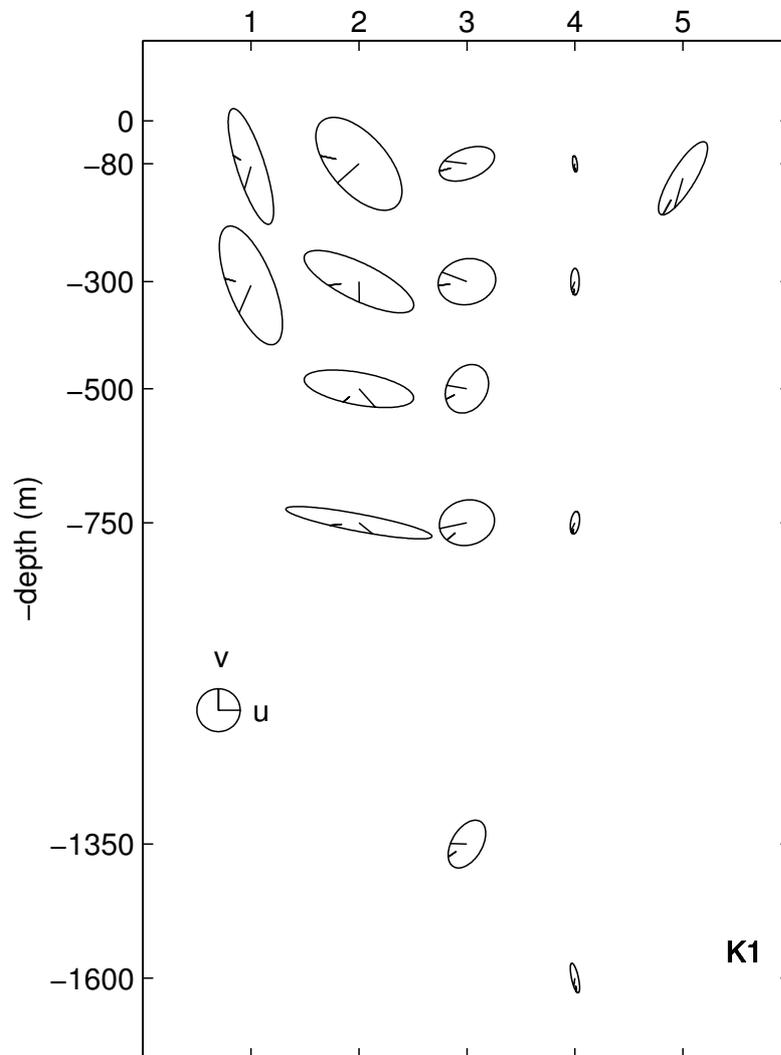
Figure 2.6: Tidal harmonic ellipses for K_1 frequency at Jan Mayen transect. Same conventions hold for definitions of ellipses as given in figure 2.5. For this diurnal frequency there is no change with depth in rotation sense, and most (barotropic) motion is in-phase vertically. Moorings 1 and 2 (on shelf and near shelf break) show clockwise rotation sense, while for moorings 3 and 4 in deeper water this is anticlockwise. Mooring 5, which is more remote and near the seamount, recorded clockwise motion again. Amplitudes are relatively large, as can be seen by comparison with figure 2.5. Especially current meters near the shelf break (mooring 2) show large across-slope currents, somewhat enhanced closer to the seafloor.
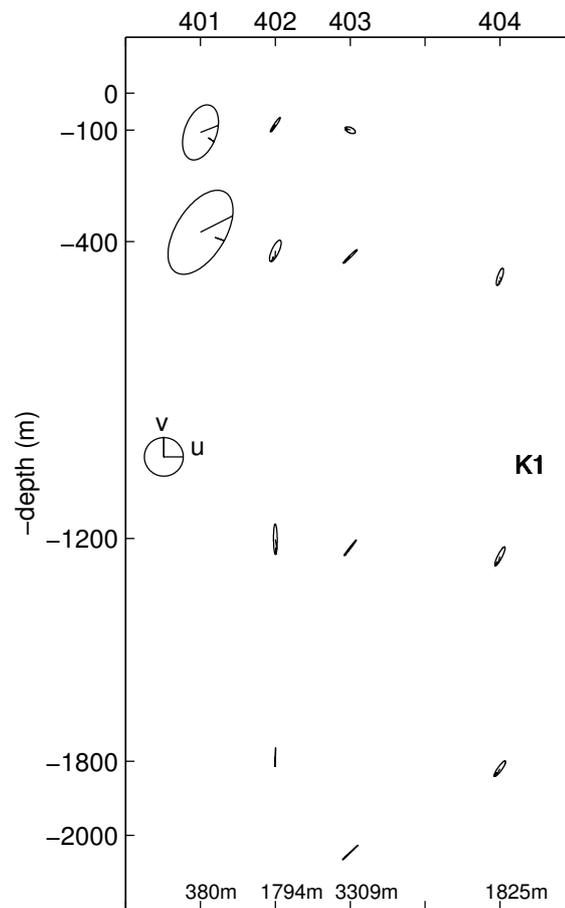
Figure 2.7: Tidal harmonic ellipses for K_1 frequency of moorings near $75°N$. Same scale and definitions for the ellipses are used as figures 2.5 and 2.6. In this example the measurements of 1988/1989 are used, depicted by open squares (□) in figure 2.1. Bottom depths of the mooring-sites are given at the bottom of the panel. Mooring numbers are given on top of the panel and correspond with the notation used in the data report (Sellmann et al. 1992).

2.4 Modelling

2.4.1 Equations

To explain the observed (mainly barotropic) behaviour of diurnal motion at $71°N$, the linearized shallow water equations for a homogeneous fluid, together with the

continuity equation will be used:

$$\frac{\partial u}{\partial t} - fv = -g\frac{\partial \eta}{\partial x} \tag{2.1}$$

$$\frac{\partial v}{\partial t} + fu = -g\frac{\partial \eta}{\partial y} \tag{2.2}$$

$$\frac{\partial \eta}{\partial t} + \frac{\partial(hu)}{\partial x} + \frac{\partial(hv)}{\partial y} = 0 \tag{2.3}$$

Here u and v are velocity components in x and y directions, respectively; t denotes time, g the acceleration due to gravity and η the surface elevation. We assume depth differences to exist just in the *cross-slope* x–direction: $h = h(x)$, which seems reasonable for the Greenland shelf edge (see figure 2.1), with y rotated $15°$ clockwise from the North direction near $71°N$.

Local vertical velocities in (2.3) (first term) can be neglected when the divergence parameter ϵ, defined as

$$\epsilon \equiv \Lambda^2 \frac{f^2}{gh_0} \tag{2.4}$$

is small. Here Λ is a length scale for the width of the *shelf slope*, typically 50 km. The square of this length scale is apparently much smaller than the squared barotropic Rossby radius of deformation (gh_0/f^2): when a typical overall depth scale h_0 at the slope is taken to be 1 km, and a Coriolis parameter $f = O(10^{-4})s^{-1}$, we find $\epsilon = O(10^{-3})$. Therefore a rigid-lid approximation (neglecting the first term in (2.3)) seems to be justified, and we can define a non-divergent transport stream function Ψ:

$$hu = -\frac{\partial \Psi}{\partial y}, \qquad hv = \frac{\partial \Psi}{\partial x}. \tag{2.5}$$

By assuming plane waves travelling in the y-direction, according to:

$$\Psi = \psi(x)e^{i(ky-\omega t)} \tag{2.6}$$

with frequency ω and along-slope wave number $k = 2\pi/\lambda$ (with wavelength λ), we get the following equation for ψ by eliminating η in (2.1) and (2.2):

$$\left(\frac{1}{h}\psi'\right)' - \left[\frac{k^2}{h} + \frac{fk}{\omega}\frac{h'}{h^2}\right]\psi = 0 \tag{2.7}$$

(primes denote x-derivatives).

2.4.2   Previous models with simplified 2D topography

Several different topographical shapes $h(x)$ have been chosen in trying to solve (2.7) explicitly. The first of these models is from Robinson (1964), with which he tries to explain the low frequency ($\omega^2 \ll f^2$) motion reported by Hamon (1962). His topography had a linearly sloping shelf and an abrupt depth change at the place were the depth drops to a constant deep ocean value. Here the name "continental shelf wave" was introduced, and this type of topography was extended later on by Mysak (1967) to model baroclinic waves in a two layer model, and to add a mean (along-slope) deep-sea current as well.

Continental shelf waves owe their existence to the influence of the Earth's rotation coupled to the presence of a depth difference between shelf and ocean, and not to the width of the shelf itself (i.e. to the presence of a topographic potential vorticity gradient). This is more clear from inspection of the step topography studied by Longuet-Higgins (1968a) for all subinertial frequencies ($|\omega/f| < 1$), including the more general divergent case. In that paper there is a jump in depth between shelf and ocean, which themselves are of infinite width. Solutions of (2.7), supposed to vanish infinitely far from the step, are two piecewise exponential functions, matched at the step by continuity of surface elevation and mass transport. These solutions were named "double Kelvin waves"(Longuet-Higgins 1968a), and basic properties will be discussed in the next subsection and compared qualitatively with the observations. As long as we restrict ourselves to two-dimensional models, there are two reasons to expect the step topography model to fail in giving a complete description of the waves. The first one is the absence of a coastline, which influences the fluid motion on a narrow shelf. The second reason is the lack of a proper length scale Λ for the width of the *shelf slope*, and therefore the along-slope wavelength can not be estimated.[2]

Larsen (1969) eliminated the first problem by simply introducing a vertical wall as a coast, with no normal flow at this boundary as condition instead of vanishing velocity infinitely far away. This, however, does not solve the second disadvantage of the step model, because the length scale introduced by this wall (the width of the shelf L) is not the same as the length-scale we were looking for: the width of the shelf slope, which for a step can be regarded as equal to zero.

Saint-Guily (1976) on the other hand did solve (2.7) analytically (and also for the more general divergent case) for a single two-parameter family of continuous depth profiles $h(x)$. The defining parameters were slope width and the (normalized) depth difference of shelf and deep-sea. Dependency on the width of the slope is clear now, but the shape of the (parameterized) depth profile is fixed, and a coastline can not easily be implemented, so in this case we are still left with an infinitely wide shelf (and ocean). Buchwald and Adams (1968) also used two-parameter families of piecewise topography (with essentially the same parameters). In their topography the slope had exponential behaviour (of width Λ), with flat shelf and ocean on either

---

[2]In the divergent case (Longuet-Higgins 1968a) the Rossby radius of deformation is the only length scale available, which gives rise to very long wavelengths.

side. They solved two cases: one for zero shelf width L, and the other one for infinite shelf width (leading to the solution of Longuet-Higgins (1968a) for the limit of zero slope width as well).

In order to maintain both length scales for shelf and slope we have extended the model of Buchwald and Adams (1968) to an exponentially shaped slope between a finite shelf and infinite ocean, both of constant depths. In all three domains (flat shelf, exponential slope and flat ocean) simple piecewise analytical solutions of (2.7) are matched again by continuity of surface elevation and mass transport, and with vanishing stream function assumed in the far ocean and no normal flow at the coast as boundary conditions. In this way dispersion relations for the continental shelf waves can be found. They will be presented in subsection 2.4.5, together with corresponding velocity profiles, to get a more quantitative comparison with the observations east of Greenland near $71°N$ and $75°N$.

A more numerical approach is of course also possible (Longuet-Higgins 1968b; Huthnance 1975), but we prefer (piecewise) analytical models here to study the parameter's dependency. All topography discussed here is essentially two-dimensional, which of course is a rigorous simplification of real depth distributions in the ocean. Moreover, no stratification is included, because the observations suggest the diurnal tide to be predominantly barotropic.

2.4.3   Step topography

The simplest topography to model the shelf-ocean system is a step topography:

$$h(x) = \left\{ \begin{array}{ll} h_1 & x < 0 \\ h_2 & x > 0 \end{array} \right. , \tag{2.8}$$

where h_1 is the water depth on the shelf, h_2 is the ocean depth ($h_2 > h_1$), and infinite width of shelf and deep-sea is assumed ($-\infty < x < \infty$). Now depth is piecewise constant, and a "trapped" general solution of (2.7), bounded for $|x| \to \infty$, simply looks like:

$$\psi(x) = \left\{ \begin{array}{ll} A_1 e^{kx} & x < 0 \\ A_2 e^{-kx} & x > 0 \end{array} \right. , \tag{2.9}$$

where we define the along-slope wave number k to be positive.

With this solution the continuity of across-slope mass transport ($uh \sim ik\psi$) is guaranteed for $A_1 = A_2$. A second matching condition comes from assuming continuity of surface elevation η at $x = 0$. Integrating (2.2), multiplied with h, over the step, and assuming η to have the same form as in (2.6), so $\partial\eta/\partial y = ik\eta$, gives:

$$\left[\frac{1}{h} \frac{d\psi}{dx} \right]_{-\varepsilon}^{\varepsilon} = -\psi(0) \frac{fk}{\omega} \left[\frac{1}{h} \right]_{-\varepsilon}^{\varepsilon} , \tag{2.10}$$

where $\pm\varepsilon$ is a small distance left and right of the step, and the square brackets define that the difference (at $x = \pm\varepsilon$) should be taken for the quantities inside these brackets.

From (2.9) with $A_1 = A_2$ the limit $\varepsilon \downarrow 0$ yields the dispersion relation (Longuet-Higgins 1968a):

$$\frac{\omega}{f} = -\frac{h_2 - h_1}{h_2 + h_1} \quad . \tag{2.11}$$

In other words, there is just one specific frequency for such a double Kelvin wave. As defined in (2.6), this wave will travel along the negative y-axis, because $\omega < 0$ in the northern hemisphere ($f > 0$). For the Greenland shelf edge this means southward phase propagation. For any non-zero depth difference ($h_2 > h_1$) the magnitude of the frequency ω of this wave will be smaller than the inertial frequency ($|\omega/f| < 1$). This confirms the "sub-inertial" nature of motion related to topographic Rossby waves.

Equation (2.11) for the step topography holds for every wave number k, so the group velocity $c_g = \mathrm{d}\omega/\mathrm{d}k$ is always zero: no energy can be transported. This is due to the lack of a proper length scale. By introducing a coastal wall at $x = -L$ we do get a dependency of frequency on wave number $\omega(k)$. Larsen (1969) found the dispersion relation for this situation:

$$\frac{\omega}{f} = -\frac{h_2 - h_1}{h_1 + h_2 \coth(kL)} \quad . \tag{2.12}$$

Now the available length scale is the shelf width L. Dropping the rigid-lid approximation, which was done by Longuet-Higgins (1968a) and Larsen (1969) without and with coast respectively, gives the Rossby radius of deformation ($\sqrt{gh_0}/f$) as (extra) length scale. In this case it is no longer possible to give the dispersion relation in analytic form, but only in terms of a transcendental relation. However, it turns out (Longuet-Higgins 1968a) that the qualitative dispersive behaviour of the waves is similar as in (2.12), with shelf width L replaced by Rossby radius $\sqrt{gh_0}/f$. This qualitative behaviour means that in both cases we get $\omega \to 0$ for $k \to 0$, and the limit for ω/f as in (2.11) for large wave numbers. The group velocity then always has the *same* sign as the phase velocity for long waves, tending to zero for "short" waves, i.e. short in relation to shelf width L and Rossby radius.

When we consider the Greenland shelf-ocean transition at $71°N$, we find approximately: $h_1 = 400m$ and $h_2 = 1600m$ (figure 2.2). Then the scaled frequency according to (2.11) gives $|\omega/f| = 0.6$, which is close to the diurnal frequency band; $\omega(K_1)/f(71°N) = 0.53$. Moreover, when we take a closer look at the polarization of the velocity vector with (2.9), (2.6) and (2.5), we observe that the polarization changes over the step (figure 2.8) are in qualitative agreement with the observations in figure 2.6 for moorings 1–4. Also the horizontal amplification of velocity, measured by moorings 2 and 3, is confirmed this way. The discontinuous change in phase over the step, related to the along-slope shear along the (discontinuous) step, can also be seen in the observations, and this phase information over the slope will be used in the next subsection. It is amazing how much of the qualitative behaviour of the observed CSW can already be explained by a simple step topography.

2.4.4 Estimation of wavelength

As is pointed out in the previous subsection, it is not possible to model the wavelength of the CSW above the step with the present assumptions of a rigid lid, zero slope width and no coast, because the dispersion relation (2.11) holds for every along-slope wave number k. With the plane wave assumption (2.6) however (and the change in rotation sense across the step/break, figure 2.8), it is possible to estimate the wavelength using the horizontal phase differences of the tidal constituents.
 Use is then made of the small angle that the wavecrests make with the latitude at which the moorings are deployed, assuming the wavecrests to be oriented in cross-isobath direction (figure 2.9). We assume that the isobaths are oriented $15°$ True North (figure 2.1). From the phase differences for the diurnal frequencies K_1 (figure 2.10) and O_1 (not shown), we then find an estimated wavelength λ of 88 ± 13 and 58 ± 24 km respectively. This estimated wavelength is critically dependent on the chosen angle between wavecrests and transect: $\lambda \sim \sin \alpha$, where we have chosen $\alpha = 15°$.
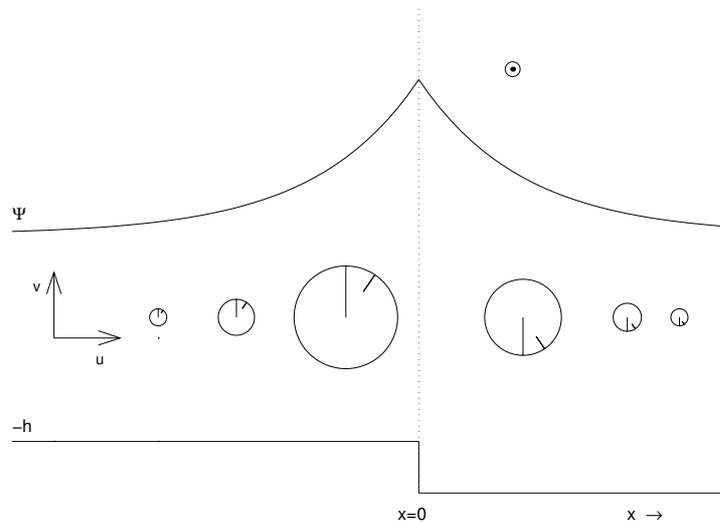

Figure 2.8: Polarization of currents for double Kelvin wave at phase $ky - \omega t = 0$, derived from (2.9), (2.6) and (2.5). Phase propagation of the wave is towards the reader. Notation for the velocities in the uv–plane is the same as in figure 2.5 and figure 2.6: the motion is circular; clockwise on the shelf and anticlockwise in the deep ocean.
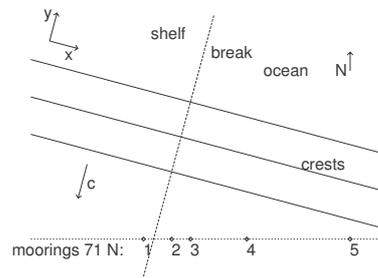
Figure 2.9: Plan view of a plane CSW approaching the moorings located at $71°N$. The angle that the phase lines and crests make with the latitudes should account for the leading phases observed further away from the shelf break, taking into account rotation sense and shear in along-slope velocity sketched in figure 2.8. This angle is about $15°$ for the moorings deployed near $71°N$, but is sketched here in an exaggerated way to show the effect more clearly. Direction of phase propagation in the along-slope y-direction (denoted as "break") is depicted as "c".
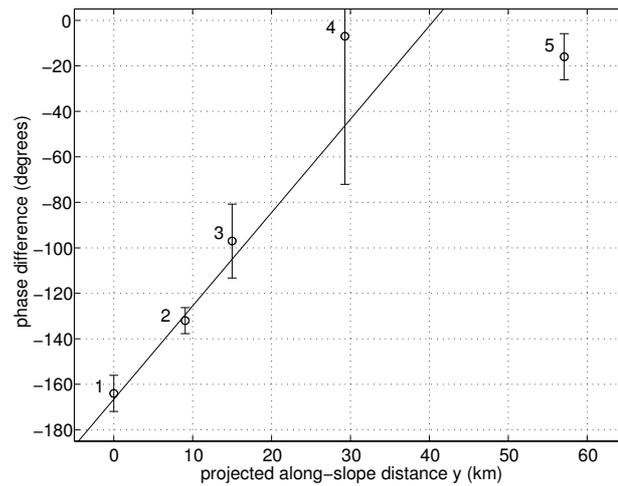
Figure 2.10: Phase differences for K_1 for top meters of moorings deployed at $71°N$. Phase difference defined as difference between phase of velocity vector (u, v) in xy–plane at Jan. 1, 1988 from figure 2.6 and the phase of maximum stream function, as sketched in figure 2.8. Distance of moorings is projected on the along-slope y-axis, and taken zero for mooring 1. A least squares fit for moorings 1–4 gives a progression of phase of $7.3°$/km for O_1 (not shown), and $5.5°$/km for K_1. This corresponds to wavelengths of 58 ± 24 and 88 ± 13 km respectively (and phase speeds of 0.53 and 0.76 m/s in southward direction). Mooring 5 is not taken into account because it is too far away from the slope, and apparently influenced by the nearby seamount (figures 2.1 and 2.2).

2.4.5 Exponential slopes

In order to obtain better insight in the motion on the shelf slope (of non-zero width Λ) and dispersion characteristics we introduce an exponential depth profile in between a flat shelf and ocean (figure 2.11):

$$
h(x) = \begin{cases}
h_1 & -L < x < 0 \\
h_1 e^{2bx} & 0 < x < \Lambda \\
h_2 \quad (\equiv h_1 e^{2b\Lambda}) & \Lambda < x < \infty \,.
\end{cases}
\tag{2.13}
$$

This depth profile is based on the study by Buchwald and Adams (1968), who treated the two cases $L = 0$ and $L \to \infty$, the solutions of which they called "shelf waves" and "interior shelf waves" respectively. Requiring no normal flow at the coast ($x = -L$) and vanishing motion in the far deep ocean gives as boundary conditions:

$$
\begin{aligned}
\psi(-L) &= 0 \\
\psi &\to 0 \qquad \text{for} \quad x \to \infty \,,
\end{aligned}
\tag{2.14}
$$
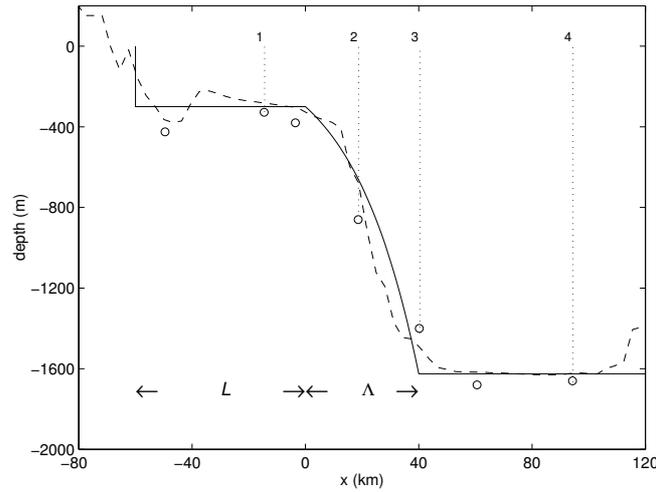
Figure 2.11: Fit of realistic topography and modelled exponential slope (2.13). Here the following parameters are used: $b\Lambda = 0.875$, $\Lambda = 40$ km, $L = 60$ km, $h_1 = 300$ m, $h_2 = 1625$ m. Distance x is in the across-slope direction ($105°$ True North), and the intersection at $x = 0$ with $71°N$ here is at $20°W$. Dashed line is ETOPO-5 data (with a resolution of 5 minutes, which is 5.6 km in East–West direction at $71°N$; depths are interpolated from two neighbouring points lying northward and southward from each point on the rotated x–axis). Dotted vertical lines are positions of first 4 moorings projected on this cross-section. Circles denote depths as measured at CTD–stations, also projected on this cross-section.

which give the following general solution of (2.7):

$$\psi(x) = \begin{cases} B_1 \sinh(k(x + L)) & -L < x < 0 \\ e^{bx}(B_2 \sin(mx) + B_3 \cos(mx)) & 0 < x < \Lambda \\ B_4 e^{-k(x-\Lambda)} & \Lambda < x < \infty . \end{cases} \qquad (2.15)$$

Again at $x = 0$ and $x = \Lambda$ we will assume continuity in across-slope mass transport ($uh \sim \psi$) and surface elevation. Because the depth according to (2.13) is continuous now, the latter with (2.10) simply implies continuity of ψ' at $x = 0$ and $x = \Lambda$. These four conditions give the relations (given in appendix A) between the constants B_1 to B_4, and a transcendental relation which determines m:

$$\tan(\Lambda m) = F(m) \quad , \qquad (2.16)$$

with:

$$F(m) = \frac{mk(\sinh(kL) + \cosh(kL))}{(b^2 + kb + m^2)\sinh(kL) - (kb + k^2)\cosh(kL)} \quad . \qquad (2.17)$$

See appendix A for the derivation of this relation. The intersections of both functions in (2.16) have to be calculated for given values of k, b, Λ and L. Each intersection $(m_0, m_1, m_2, ..)$ of $F(m)$ with a branch of $\tan(\Lambda m)$ represents a mode of the CSW.

When a value of m is found, the corresponding frequency is given by:

$$\frac{\omega}{f} = \frac{-2bk}{m(k)^2 + k^2 + b^2} \quad , \qquad (2.18)$$

which follows from substitution of (2.15) in (2.7) for $0 < x < \Lambda$.

So for given topographic parameters (b, Λ and L) values for m_i have to be found by (2.16) for each along-slope wave number k, and this defines by (2.18) the frequency ω corresponding to that wave number. A typical and relevant example of the resulting dispersion relation is given in figure 2.12, for the parameters also given in figure 2.11 near $71°N$. A typical feature of this dispersion relation is that $\omega \to 0$ for $k \to 0$, as well as for $k \to \infty$. It can be shown (Huthnance 1975) that this is generally true for the divergent case if h'/h is bounded, which was not the case for the step profile in section 2.4.3. This means that there has to be some extremum of $|\omega/f|$, which is theoretically bounded by the value found in equation (2.11). [3] For diurnal tidal frequencies only the zeroth mode is of importance; at $71°N$ we find: $|\omega(K_1)/f| = 0.53$, higher mode frequencies being too small. For small wave numbers k (to the left of the extremum of ω in figure 2.12) group velocity will have the

---

[3]Note that in the rigid lid approximation Buchwald and Adams (1968) found this limiting value for $k \to 0$ for the case $L \to \infty$. Then $|\omega/f| \to \tanh(\Lambda b) = (h_2 - h_1)/(h_2 + h_1)$. So the qualitative difference in behaviour for small k with Saint-Guily (1976), who found $\omega(k = 0) = 0$ in agreement with the earlier mentioned theorem of Huthnance (1975), is explained by the rigid lid approximation, which is not valid for small k. See also Djurfeldt (1984) for a clear example of the different behaviour for wide shelves with and without rigid lid approximation.
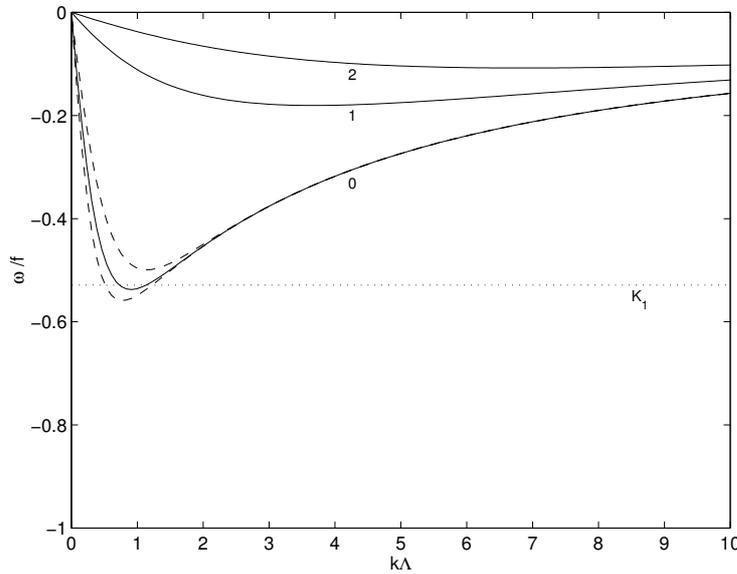
Figure 2.12: Dispersion relations for first three modes of CSWs with exponential topography (flat shelf and ocean, exponential slope). Along-slope wave number $k\Lambda$ is non-dimensional, and therefore corresponding wavelength ($\lambda = 2\pi/k$) has to be multiplied by slope width Λ (40 km in this case). Frequency ω is scaled by the Coriolis parameter f; negative values are interpreted as phase propagation in negative along-slope y–direction. Topographic parameters are the same as in figure 2.11. The full lines are for $L = 1.5\Lambda$. For mode 0 upper (lower) dashed line is for $L = \Lambda$ ($L = 2\Lambda$). Tidal K_1 frequency at $71°N$ ($\omega/f = 0.53$) is given as a horizontal dotted line.

same sign as phase velocity, which is southward for the Greenland slope situation, but for higher wave number the group velocity will be northward. Near the extremum the group velocity c_g equals zero, and energy then cannot be transported and is thus trapped, indicating a mechanism for resonance.

From the observations the choice between the short or long wavelength solution for given diurnal frequencies is not made yet using theoretical arguments. With the dispersion relations of figure 2.12, however, we see that the long wave solution ($k\Lambda = 0.5 - 1$, with $\Lambda = 40$km) corresponds with a wavelength of $250 - 500$ km, while on the other hand the short wave node ($k\Lambda \lesssim 2$) gives a wavelength of about 125 km. Both theoretical possibilities do not agree with the observed "plane wave based" wavelength of 58 ± 24 and 88 ± 13 km (subsection 2.4.4), though it is tempting to conclude that the short wavelength solution is the one observed. This also agrees with an estimate of the slope of the dispersion curve from the observations: we found shorter wavelength (58 km) for tidal constituent O_1 (period 25.8 h) than for K_1 (period 23.9 h), where we estimated a wavelength of about 88 km. In other
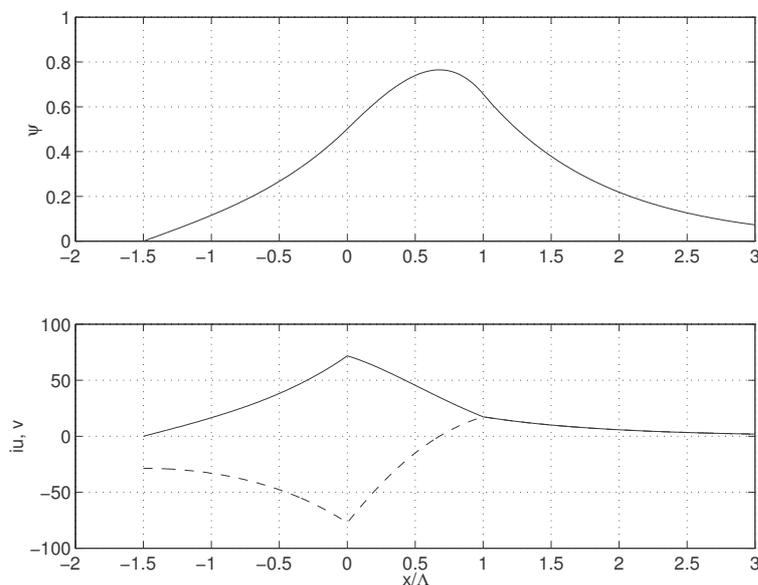
Figure 2.13: Stream function amplitude $\psi(x)$ (upper panel), as given in (2.15) (together with (A.1) to (A.3) of appendix A), for scaled along-slope wavelength $k\Lambda = 1.1$ and $B_1 = 0.2$. Topographic parameters are as in figure 2.11. These parameters give, using (2.16): $m = 1.26$ and frequency $\omega/f = -0.530$. The horizontal axis is across-slope distance x, scaled with slope width Λ (40 km in this case). Corresponding velocity distributions (arbitrary units) are given in the lower panel: across-slope velocity amplitude $iu(x)$ and along-slope velocity amplitude $v(x)$ (dashed), where iu means that u has a $90°$ phase-lag with respect to v and ψ.

words: $|\omega(K_1)| > |\omega(O_1)|$, and $k(K_1) < k(O_1)$, and the wave number of the wave then has to be on the right of the minimum of the dispersion curve of figure 2.12, which is the "short wave branch".

An example of the stream function distribution ψ for $k\Lambda = 1.1$ as given by (2.15) is depicted in figure 2.13 for the topographic parameters given in the caption of figure 2.11, and with $m = 1.26$ and $\omega/f = -0.530$ obtained from the transcendental relation (2.16) and (2.18). Corresponding distributions for the velocity components are given in the lower panel of figure 2.13. Note especially the difference with step topography (figure 2.8) in the along-slope velocity component v, which is continuous in x now, because ψ' and h are continuous. This might also be clear when we take a closer look at the polarization (v/iu, the imaginary unit i standing for the $90°$ phase difference) of the current over the slope (see figure 2.14). Observed polarization at 300 m depth at $71°N$ for the K_1 tidal frequency (figure 2.6) is compared with the calculated ratio of amplitudes of both velocity components for the topography of figure 2.11 and again $k\Lambda = 1.1$. We see that the observed (anticlockwise) rotation sense in the deep ocean (mooring 4) is not circular, as expected, but the ocean is not
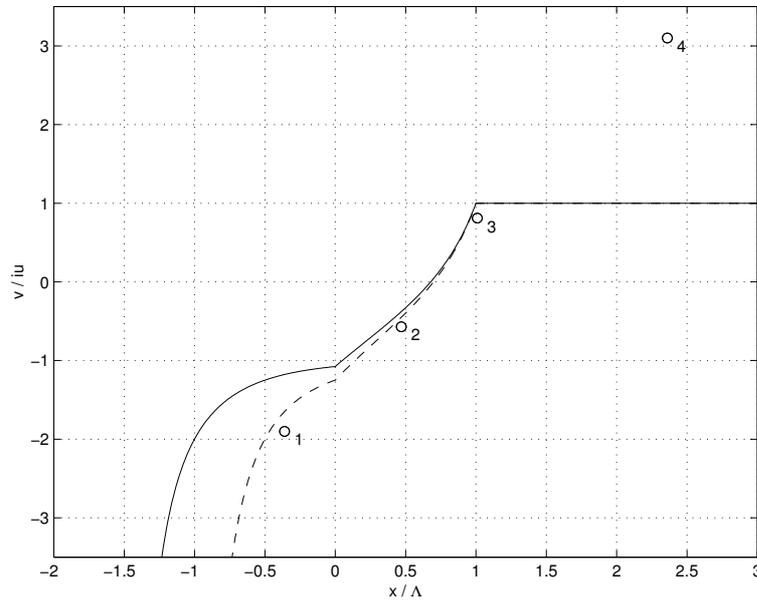
Figure 2.14: Polarization of currents $v(x)/iu(x)$ for topographic parameters as in figure 2.11 and scaled wave number $k\Lambda = 1.1$. Dashed line is for a smaller shelf width: $L = \Lambda$ instead of $L = 1.5\Lambda$. Horizontal distance scaled again with slope width Λ, and negative values for polarization denotes clockwise rotation sense of current velocity vector. Polarization of observed currents at 300 m depth for moorings 1–4 at $71°N$ is depicted with circles. Across-slope position of moorings follows from projection on section shown in figure 2.11.

flat either. The transition over the slope to rectilinear across-slope polarization, and to clockwise circular motion near the break is in fair agreement with the observations, but on the shelf ($x \sim -0.4\Lambda$) the motion is aligned more along-slope than can be explained by the modelled flat shelf and coastal wall at $x = -1.5\Lambda$.

2.5 Discussion

As noted in the introduction, this is not the first time CSWs with tidal frequency have been reported. Until now fewer than ten locations seem to have been reported with observational evidence, and one might wonder why its occurrence is apparently so limited, because near most continental shelf edges at high latitudes topography might be steep enough for first mode CSWs to exist with a tidal frequency (with a theoretical upper bound of the (absolute) frequency given by (2.11)). One reason for this might be that in most cases it is not easy to deploy moorings to obtain time series long enough at high latitudes, e.g. due to ice cover. This, however, can-
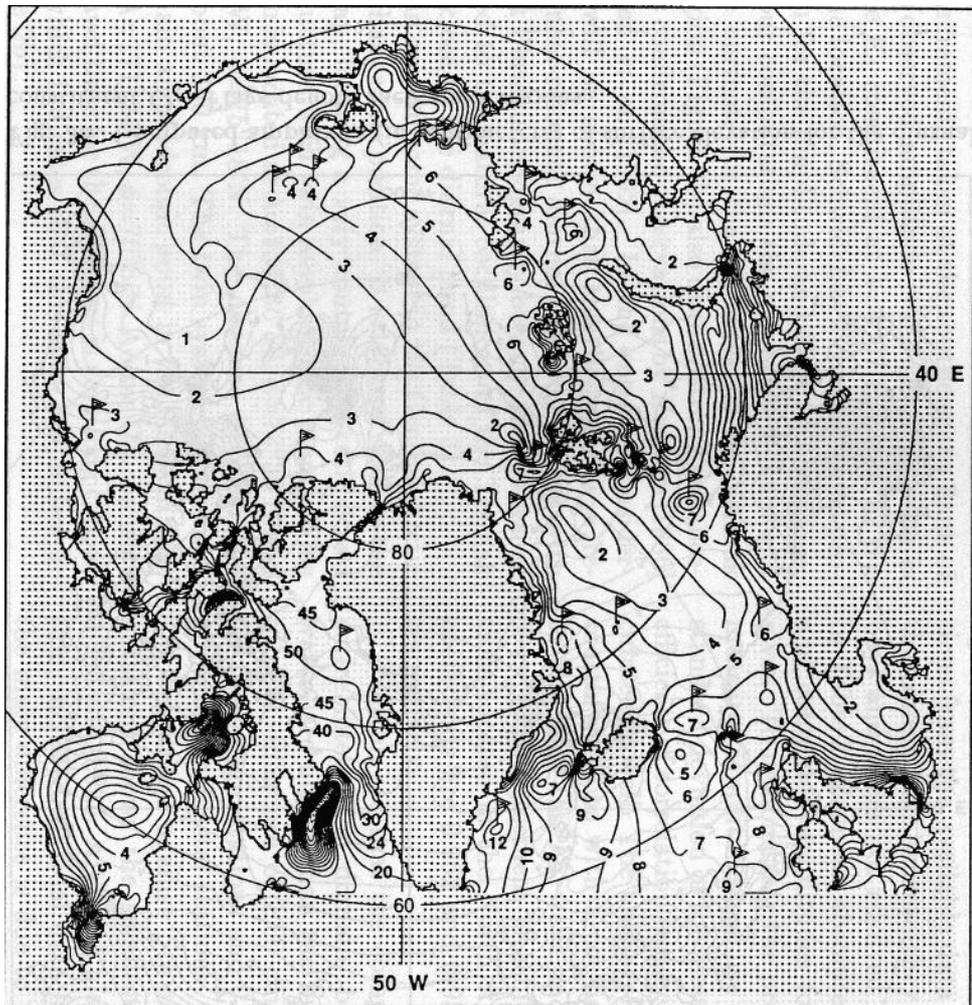
Figure 2.15: Surface elevation amplitude (in cm) of the diurnal constituent K_1, as given by the numerical model of Kowalik and Proshutinsky (1993). Flags denote shelf wave regions. Note the flag nearby the coast of Greenland and just north of the moorings at $71°N$. Picture from Kowalik and Proshutinsky (1993).

not be the only reason, as for example the observations at the shelf slope near $75°N$ (figure 2.7) showed: there was no clear amplification of diurnal currents there. The localized nature of the enhancement of diurnal tides by continental shelf waves was also found numerically by Kowalik and Proshutinsky (1993), see figure 2.15. So we have to look for better arguments in explaining the local occurrence of this diurnal current enhancement.

One simple argument might be that the spatial sampling with the moorings near $75°N$ is worse than that at $71°N$. This seems not to be the case: resolution on the slope might even be better there.

A second possible difference of importance between the two described locations might be the different distance of the shelf break to the coast, or in our model, the (flat) shelf width (L). Thomson and Crawford (1982) presented a model for tidal generation, based on the paper by Gill and Schumann (1974) discussing CSWs generated by wind. In these papers the coastline is of crucial importance for the transfer of momentum from the generating mechanism (bottom stress by the tides and surface stress by the wind) towards the CSWs via blocked Ekman transport leading to (barotropic) pressure gradients able to initiate the CSWs by input of vorticity. Gill (1982, p.412) states this in more general terms as: "The essential property of the ocean that permits continental shelf waves to exist is the variation in depth. A coastal boundary is not necessary. However, a coastal boundary *is* important for the *generation* of shelf waves by the wind (Gill and Schumann 1974)." For CSWs with diurnal tidal frequency, as treated by Thomson and Crawford (1982), *wind* should be replaced by *"background" barotropic tides*. We estimate $L = 60$ km and $L = 220$ km respectively for across-slope transects near $71°N$ and $75°N$, so it is tempting to conclude that shelf waves are more difficult to generate near $75°N$, because the coast is more remote.

Unfortunately, in the only explicit example of topography in Thomson and Crawford (1982) no discrimination is made between shelf and slope width. In this example they use the original Buchwald and Adams (1968) topography ($L = 0$) of exponential slope without shelf (or, in other words: a more gradual transition from shelf to slope). Secondly, only the coastal along-slope velocity component of the generated shelf wave is tabulated for this calculation, while the across-slope velocities on the slope are more characteristic for CSWs. Anyway, they find at the coast an energetically rather low response (a few percent at most) of CSWs for the prescribed lowest order velocity field, which is a large scale barotropic deep-sea Kelvin wave. They assumed, however, that the water motion of this Kelvin wave is oriented completely along-slope, which does not present a proper solution for the lowest order equation: Munk et al. (1970) and Miles (1972), for example, showed that the across-slope component of the currents of a large scale deep-sea Kelvin wave near a coastal region of nonuniform depth typically even exceeds the along-slope current component on the shallower shelf, while at the same time the phase speed of the Kelvin wave is decreased (a few percent typically) by the presence of the shelf region. This across-slope component of the currents of the large scale ("background") Kelvin wave might supply a significant and more direct contribution to the indirect ("blocked Ekman transport") generation of the CSWs, and should be investigated more thoroughly.

The third and last striking difference between the two locations is the magnitude of the extremum of the dispersion relation $\omega(k)$ (figure 2.12) in relation with the diurnal tidal frequency, both scaled by the Coriolis parameter f. This difference can be seen in a somewhat wider context in figure 2.16, where these minima have been calculated for the Greenland shelf and slope from estimates of topographic parameters
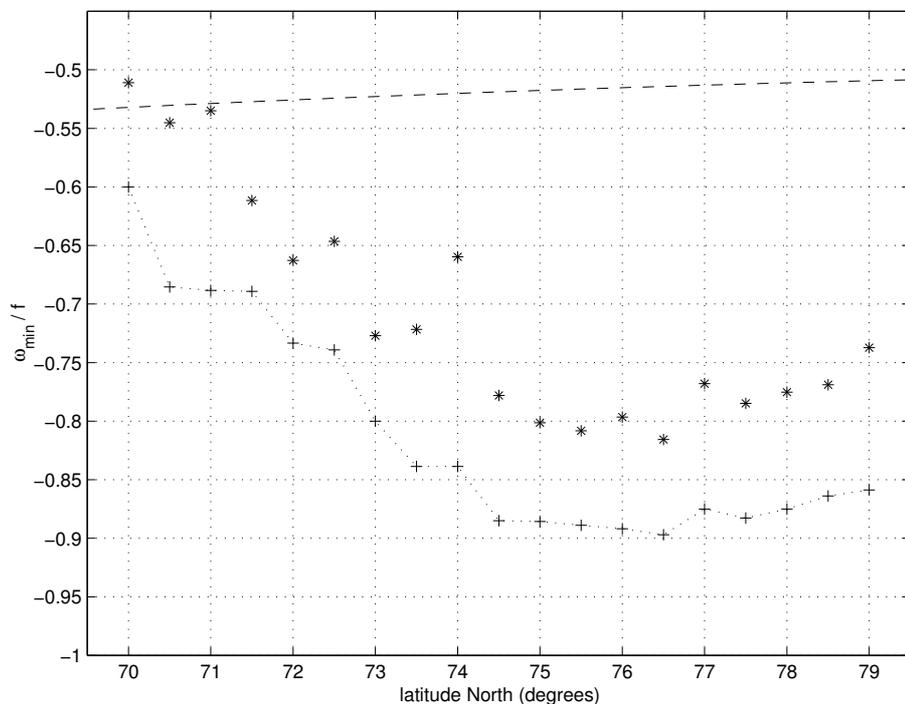
Figure 2.16: Minimum frequencies (ω_{min}) of dispersion relations, depicted by asterisks (*), for depth profiles fitted to exponential profiles at every $0.5°$ at latitudes between $70°N$ and $79°N$. Depth profiles are taken perpendicular to the 1000m isobath locally; values interpolated from the ETOPO 5 minute grid (NOAA 1988). For each exponential fit of this profile (figure 2.11) the zero mode dispersion relation is calculated, and the minimum frequency (ω_{min}), scaled with f, is thus obtained at each latitude. The scaled diurnal K_1/f frequency is given by the dashed line. The dotted line with plus marked symbols (+) gives the theoretical lowerbound of the scaled frequency, given by (2.11), for each estimated shelf depth (h_1) and ocean depth (h_2).

h_1, h_2, Λ and L at every half degree in latitude between $70°N$ and $79°N$. As an example: for an exponential slope, according to (2.13) and fitted to depths near $75°N$, we found the following parameters: $h_1 = 200$ m, $h_2 = 3400$ m (leading to $b\Lambda = 1.42$) and length scales $\Lambda = 70$ km (slope width) and $L = 3.1\Lambda = 217$ km (shelf width). This parameter fit is based on ETOPO–5 data (NOAA 1988), supplying $h(x)$, with an across-slope x–axis oriented $133°$ True North, and crossing the 1000m isobath at $75°30'N$ and $11°15'W$. With these parameters we find an extremum in the dispersion relation of $|\omega/f| \sim 0.8$ at $k\Lambda \sim 0.6$, while the tidal frequency $\omega(K_1)/f \sim 0.52$ is much lower. In subsection 2.4.5 we found that at $71°N$ the diurnal tidal frequency

($\omega(K_1)/f \sim 0.529$) is much closer to the calculated extremum ($|\omega/f| \sim 0.535$ near $k\Lambda \sim 0.92$, see figure 2.12) in the dispersion relation for the topographic parameters fitted to the depth profile given in figure 2.11.

The extremum in the dispersion relation $\omega(k)$ corresponds to a zero group velocity, so energy cannot escape the region. A kind of resonance therefore takes place; a mechanism already recognized by Cartwright (1969). From figure 2.16 it is suggested that this type of resonance does not occur for diurnal frequencies north of $73°N$, mainly because of the relatively deeper Greenland Basin (see figure 2.1), represented by the parameter h_2 in the exponential-slope fit for topography. An interesting consequence to mention here is that there are still two theoretical solutions for CSWs with diurnal frequency and with *non-zero* group velocity. The longer wave solution of these two is transporting energy southward, and will be slowed down further south by changed topography, and even be blocked at $71°N$, where topography is related to zero group velocity for diurnal frequencies. So, besides the local resonance at $71°N$, there is also the theoretical possibility that the high-energy region for diurnal motion there is caused by the trapping of less energetic (that is, for example, within the "noise of the measurements at $75°N$; figure 2.7) long CSWs further north which transport energy southward. Similarly, short CSWs, south of our observation site, will transport energy northward, which again may explain enhanced diurnal tides at $71°N$. This would be in agreement with the suggestion of the observed waves as being of short wavelength type (subsection 2.4.4), and with the calculations of Kowalik and Proshutinsky (1993) in figure 2.15 where the center of maximum diurnal tidal energy is just north of our observations at $71°N$.

We would like to stress, however, that the result of figure 2.16 is obtained by using essentially two-dimensional dynamics, which are fitted separately to local topography. This can also be seen from the somewhat scattered pattern of figure 2.16, mainly caused by the irregular coastline of Greenland (compared with the rather smoothly varying slope).

Smit (1975) related the appearance of CSWs to second-order turning problems in general. From his study however, it remains unclear whether the observed enhanced diurnal currents are a result of resonance by a second-order or a first-order turning point, as in the earlier described mechanism for energy trapping. In our example east off Greenland we can not distinguish a local minimum in the absolute values for the minimum (cut-off) frequencies (ω_{min}, figure 2.16), because the presumed resonance occurs "in the corner" of the Iceland Sea, near Iceland and Denmark Strait (figure 2.1). It is for this reason that the parameter dependency on latitude (figure 2.16) could not be extended southward any further. In the example of CSW enhancement Smit (1975) himself treated, near St. Kilda (Cartwright 1969), he concluded that topography is not slowly varying, as needed for the WKB–approximation.

Additional three-dimensional insights about the generation of CSWs with diurnal tidal frequency have to be obtained by addressing the problem numerically. This approach is followed by Flather (1988) for the diurnal tides along Vancouver Island, and by Kowalik (1994) for the CSWs near Yermak Plateau.

The discussed analysis of the observations in this paper, however, did give a clue

to the understanding to the generation and existence or non-existence of CSWs with diurnal tidal frequency. One would like to demonstrate the discussed mechanisms by incorporation of the correct forcing terms in our model equations (2.1) – (2.2), but we lack the observations of the forcing terms presently.

2.6   Conclusions

This paper presents a tidal analysis of current observations at the East Greenland shelf and slope. A striking feature of these observations at $71°N$ is the relatively strong diurnal component, comparable with or even dominating the semi-diurnal currents on the slope of the continental shelf edge. This strong amplification of diurnal currents is almost absent further north, near $75°N$. With very simple models with two-dimensional topography it is shown that most diurnal (e.g. K_1) current characteristics of the shelf–slope region near $71°N$ can be explained by a topographic Rossby- or continental shelf wave (CSW) travelling southward along the Greenland shelf edge. The same simple models also suggest that the existence of these CSWs with diurnal tidal frequencies at $71°N$ is caused by local resonance. This resonance frequency can be found with the help of the obtained dispersion relation, which shows a minimum, and zero group velocity, for the diurnal tidal frequencies. For topography near $75°N$ this minimum is related to frequencies higher than the diurnal tides, and no resonance is therefore to be expected.

   The main qualitative characteristics of the observations at $71°N$ can be explained with a simple step-topography (Longuet-Higgins 1968a), while more details on the slope can be covered in a model with a finite exponential slope in between a flat shelf and ocean, based on Buchwald and Adams (1968). Their two cases of flat shelves with zero and infinite width is here generalized to a finite shelf of arbitrary width. With the plane wave assumption (together with presumed two-dimensionality) the wavelength of the continental shelf wave near $71°N$ has been estimated as 58 ± 24 and 88 ± 13 km for O_1 and K_1 frequencies, respectively, which turns out to be too short as compared with the expected wavelength of about 125 km based on the dispersion characteristics of the simple model with exponential slope fitted to the local topography for these frequencies. This is theoretically the shortest possible wavelength, corresponding with group velocity opposite to phase velocity, leading to northward energy transport (along the isobaths).

   The spatial amplitude distribution of the observed CSW matches the theoretical expectations (figures 2.13 and 2.14), based on the finite exponential slope, surprisingly well in terms of the rotation sense and ratios of the amplitudes of the along- and across-slope components of horizontal velocity. Details of near-coastal and on-shelf motion appear not to be modelled very accurately by assuming a flat shelf and vertical coastal wall (figures 2.14 and 2.11), but extension of the model seems not to make much sense in the present study due to the rather poor spatial resolution of the observations, and will lead to more topographic parameters and unnecessary complexity.

acknowledgements

Chapter 3

Spatial Structure of Tidal and Residual Currents as Observed over the Shelf Break in the Bay of Biscay [1]

Theoretical and laboratory models show that internal-wave energy in continuously stratified fluids propagates in the vertical plane, at an angle set by the wave, buoyancy and Coriolis frequencies. Repeated Acoustic Doppler Current Profiler observations on three transects, crossing the shelf edge, now directly reveal this beam-wise propagation of internal tides in the Bay of Biscay. This confirms previous suggestions based on observations sampled more sparsely in space. The present observation is made by bin-wise harmonic analysis of horizontal currents, leading to the spatial resolution of barotropic and baroclinic semi-diurnal tidal and (time-averaged) residual flows.

The observed barotropic tide has a cross-slope mass flux that is roughly constant. Its fast along-slope phase variations can only in part be explained by the spring-neap tidal cycle. The observed baroclinic tide compares favourably to that produced by a two-dimensional numerical model. The observations reveal details of the internal tidal beam, including its spatial amplitude distribution, presence of amphidromes and direction of phase propagation. The cross-isobath structure of the along-slope barotropic mean flow shows a localized maximum near the shelf break. Over two transects it agrees in sign and magnitude with a theoretical tidally rectified flow. The baroclinic, cross-isobath mean flow shows a strong near-bottom downwelling flow, compensated by an on-shelf-directed flow in the upper part. The along-shelf mean flow displays subsurface intensification attributed here to frictional modification of a tidally rectified flow that is bottom-trapped due to stratification.

---

[1]This chapter is previously published as Lam, Maas, and Gerkema (2004)

3.1   Introduction

In the oceanographic literature on internal waves in continuously stratified seas there has been an emphasis on their vertical modal structure. This approach entails two problems. Usually only a few modes are taken into account; thus a description of a narrow beam arising from a localized source (deWitt et al. 1986), with its typical phase and energy propagation, becomes impossible. A more fundamental problem occurs when the bottom is sloping, in which case internal wave propagation cannot be described by vertical modes (despite the fact that at each location a decomposition is possible). In a beam-like description of internal waves these problems are circumvented; it reveals the quite peculiar dispersion characteristics of these waves, which distinguish them from interfacial and surface waves. Internal waves in a continuously stratified fluid propagate obliquely, under some specific angle with gravity, defined by wave frequency ω and local buoyancy frequency $N(z)$, and when the fluid is rotating also by the Coriolis frequency $f < N$. Phase velocity is perpendicular to group velocity and they have opposing vertical components. The group velocity is in the direction in which energy propagates, and is parallel to the main axis of the alternating fluid motion. We expect the internal wave beam to be observable and test its oblique propagation on observations from the Bay of Biscay.

The peculiar dispersion characteristics of internal waves have been demonstrated lucidly in laboratory experiments (Görtler 1943; Mowbray and Rarity 1967; Dalziel et al. 1998; Sutherland et al. 1999; Sutherland et al. 2000). A tank in a laboratory is of course much simpler than the ocean: it is non-rotating, has uniform stratification, simple topography and no steady currents. However, we intend to show here, by again making use of relatively recent technology (i.e. a towed Acoustic Doppler Current Profiler — ADCP) that, despite these differences, one is able to recognize the beam-wise propagation of internal waves, alluded to above, also in the ocean: a 'tank' about a million times larger as the one for example shown in Sutherland et al. (1999, fig.3). Moreover, the measurements will provide us with estimates of the barotropic and tidally averaged barotropic and baroclinic fields in the vicinity of the shelf edge, which will be discussed separately.

The region of observation is a part of the Bay of Biscay, well-known for its strong internal tides. Baines (1982) estimates the northwest European shelf (taken roughly from Biscay to the Hebrides, west of Scotland) to be one of the highest contributors to the global internal tidal energy flux. Strong, localized internal tides (internal waves of tidal frequency) in the Bay of Biscay result from a combination of favourable stratification, steep topography and strong barotropic tidal currents directed cross-isobath. (Cartwright et al. 1980; Baines 1982; Le Cann 1990). Away from the shelf edge, on the shelf and in the deep sea, these can give rise to internal solitary waves with thermocline depressions down to 50 m, especially in late summer (Pingree and Mardell 1985). In Pingree et al. (1986) the internal tidal wave, travelling away from the shelf break in both directions, was explored with a well designed observational program at sea. They found that the coastward travelling internal tide, if corrected for strong barotropic tidal advection, could be well explained by a so-

called first mode (linear) description. Therefore a two-layer description is adequate on the continental shelf for the phase propagation. For the oceanward travelling internal tide a first mode did not suffice to describe the observed isotherm displacements and higher modes were needed to explain the observed spatial structure. In fact the third mode is dominant (Pingree and New 1991).

Pingree and New (1989) found evidence for downward propagation of internal tidal energy into the ocean along characteristics. After a subsequent bottom reflection (Pingree and New 1991), the beam forms even a second source of internal solitary waves, approximately 140 km away from the shelf edge, where it reaches the thermocline (New and Pingree 1992; New and Da Silva 2002). Ray and Mitchum (1997) suggest that the higher mode behaviour of the internal tide in the Bay of Biscay (and thus its beam-like nature) makes it more susceptible to changes in stratification, thus preventing the internal tide from being observed coherently at the surface with altimetry measurements. Therefore, in line with theoretical and laboratory findings (Maas and Lam 1995; Maas et al. 1997), field observations too require a ray description of internal tides (Leont'yeva et al. 1992; Vlasenko and Morozov 1993). Here, we present direct field observations in support of this ray or beam-like interpretation of the deep internal tide, in and near its generation area.

In laboratory experiments (e.g. Mowbray and Rarity (1967)), the forcing is simply an oscillating body. Near the shelf break the forcing is defined by vertical motion due to tidal flow over the continental slope. Also, unlike in any laboratory experiment, there is no 'camera' available to get the whole region into scope. Yet, by measuring with a towed ADCP one can obtain a quasi-synoptic image in a two-dimensional (vertical) xz-plane of the barotropic and baroclinic structure of tidal and residual fields in the vicinity of the shelf edge.

In section 3.2 we will discuss ADCP-sampling, the employed observational strategy. Emphasis in this study is on resolving the baroclinic tides and residual flow along and near the shelf break. Aiming to capture these, we sailed up and down a cross-slope track as fast as possible, sampling each of the three 13 km long, cross-slope tracks for some 10 times during two tidal cycles. Fitting a semi-diurnal tide to the 10 observations that we obtain for each bin in the (approximately two-dimensional) vertical observational plane allows us to estimate tidal amplitude, phase and time-average (residual) of each current component, yielding a high spatial resolution of the barotropic and baroclinic tidal and residual fields.

In section 3.3 the observed tidal data are presented, as well as some related simple theoretical and numerical models. Barotropic (depth-independent) tidal currents, section 3.3.1, are discussed. We use the observed barotropic tide and stratification to evaluate the theoretical, internal-tide forcing term (as adopted in the model), which tells us how the forcing is distributed spatially. Baroclinic tides, section 3.3.2, computed from this forcing, will be compared with those observed.

In section 3.4 the offset of the estimated periodic motion in each bin is interpreted as the approximate stationary (residual) motion over the duration of the observation. Finding a reliable residual current is, however, more difficult than obtaining the tidal part: we are trying to extract a relatively small (time) mean from a signal that is

dominated by the periodic motion, where the latter is itself complicated and subject to large errorbars. The resulting mean values might therefore be questionable, but, comparison with theoretical values match surprisingly well, and are within the right order of magnitude. Finally, in section 3.5 the results are discussed and conclusions are drawn.

3.2   Sampling strategy

3.2.1   Towed ADCP measurements

Observations with a moving downward looking acoustic Doppler current profiler (ADCP), towed or ship-mounted, have been reported quite a lot in recent oceanographic literature. Spectacular improvements have been achieved in the quality of current measurements due to the use of differential global positioning systems (dGPS), on-line corrections for ship's motion (bottom tracking) and more available computer power (memory and storage capacities) in general. Subsequent data analysis is different from standard treatment of time series (like e.g. that of a moored current meter): the observations are *space-time series*. At this stage several different approaches are available to deal with measurements at different times and positions, and, more specifically, to split off tidal variability from lower frequency variability.

First, one can adjust the observational strategy to the (possibly dominating) tidal time and length scales. As a result, ship's tracks are repeated, so that every vertical bin of each interval of the track (horizontal bin) can be treated as a traditional mooring. In general, this delivers shorter time series, but with a much higher spatial resolution. An impressive example of this method is given by Geyer and Signell (1990), who used a number of repeated tracks in an extensive campaign to produce maps of amplitude and phase for M_2, M_4, M_6 frequencies, as well as residual currents (eddies) for Vinyard Sound, near Cape Cod. Simpson et al. (1990) used a repeated track to estimate tidal amplitudes and phases, as well as residual throughflow in the channel between the outer Hebrides and the westcoast of Scotland (the Minch). Lwiza et al. (1991) used the same strategy to resolve the spatial structure of two cross-sections of a front in the North Sea. Two cruises of a repeated track, one week apart, could be combined to estimate amplitudes and phases for both M_2 and S_2 frequencies. In Simpson et al. (1990) a fixed ratio between M_2 and S_2 amplitudes was presumed to obtain a spring-neap cycle. In general, the inability to resolve motion of M_2 and S_2 frequencies is a problem in the (mostly short) time series of the mentioned repeated tracks.

Second, the horizontal structure of the tidal velocity field can also be obtained from arbitrary ship's tracks (Candela et al. 1992). By appealing to continuity, the vertical tide was inferred. The vertical structure in the measured (tidal) horizontal velocity field was, however, not discussed.

The data set described below is obtained by following the first strategy of repeated tracks, which allows determination of both the horizontal and vertical struc-

ture of the tidal and residual fields. The observations show that by repeating tracks several times within about two tidal cycles, sufficient information is gathered to obtain coherent information on the vertical structure of the tidal (and residual) field.

3.2.2   Sampling strategy in Bay of Biscay

From June 4 to June 8 1993 three transects over the shelf break in the Bay of Biscay were monitored for about 24 hours each, as part of the *Triple B '93* project (van Aken 2000).

The transects 1, 2 and 3 (approximately in cross-isobath direction) had a length of about 13 km each, and were about 35 km apart along the shelf break (figure 3.1, table 3.1). The ship was towing a downward looking narrowband (75 kHz, *RD Instruments*) ADCP, measuring the three-dimensional current speed from 10 m below the water surface to the sea floor in 'bins' with thickness of 8 m. When the bottom is deeper than 800 m, the bottom could not be detected anymore, and correction for the ship's speed then had to be based on dGPS information, thereby deteriorating the measurement of the water velocity. While sailing up and down along transects 1, 2 and 3, the tracks were repeated 10, 14 and 11 times respectively. Deviations from the track in the along-slope direction were small: well within 250 m most of the time. Any bin thus has at least 10 measurements of each of the velocity components in it. For the present purpose —the resolution of internal tidal and tidally rectified currents— bins are taken 250 m long, and measurements have been averaged within each bin. These are subsequently used to estimate the amplitude and phase of the semi-diurnal lunar (M_2) tide and the time-averaged (residual) flow in that bin. The remaining 7 degrees of freedom were used to improve statistical reliability of these estimates, and together determine the level of the 'unexplained' variance in the remainder of the signal.

Size and duration of the experiments were chosen in order to resolve, within the limits set by available ship time, ship's speed, etc., the tidal temporal scales near the shelf break as well as possible. But, we cannot also *spatially* resolve the large-scale barotropic tide in the observed quantities. From an observational point of view, it is

transect	1	2	3
latitude	$47.4186°N$	$47.2356°N$	$47.1010°N$
longitude	$6.5881°W$	$6.1814°W$	$5.7106°W$
α (True North)	$34.2°$	$32.7°$	$34.7°$
start date 1993	June 4	June 6	June 8
duration (hours)	22.7	27.6	25.7
# repeated tracks	10	14	11

Table 3.1: Positions, orientation, dates and duration of ADCP-transects. Positions correspond to the most southward visited point, and is defined in all following figures as $x = 0$.
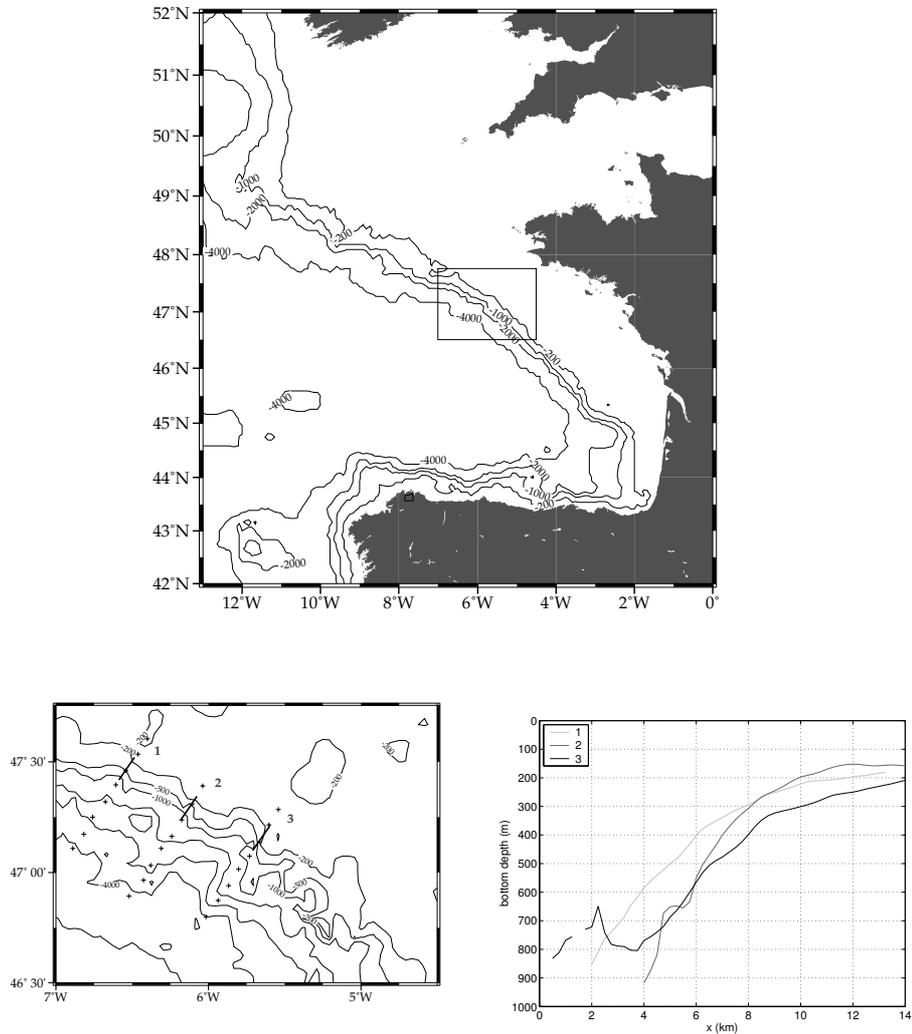
Figure 3.1: Bay of Biscay bathymetry (top), with an enlargement of the sampling area (lower left) and the ADCP-measured bottom depth for the 3 transects (lower right). In the lower left panel, towed ADCP-transects 1, 2 and 3 are depicted from left to right (straight solid lines). CTD-stations are marked with +. The bathymetry is from the ETOPO-5, 5-minute database (large area), and the enlargement with improved 2-minute NOAA database (Smith and Sandwell 1997). The position of each local origin (most south-western point of each transect) and the orientation of the x–axis in the lower right panel and all subsequent figures is given in table 3.1. As a reference in the enlargement, note that two tick labels (30 minutes) in the north-southward direction corresponds to 30 nautical miles, or approximately 56 km.

not so easy to split barotropic and baroclinic motion in the measurements for three reasons. First, bottom friction leads to variations of the barotropic current in the vertical (Prandle 1982; Maas and van Haren 1987), significant especially in shallow water; second, ADCP measurements always lack reliable data from the top and bottom layers; finally, tidal advection of geostrophic fronts falsely suggest free internal tides (van Haren and Maas 1987; Loder et al. 1992). However, for pragmatic reasons we will adopt standard practice and treat the vertical average as the barotropic, and the remainder as the baroclinic part. Note that all values with a depth deeper than 85% of the bottom depth have been disregarded in this vertical mean, because below that depth the acoustic beams of the ADCP are known to be suffering from interference with bottom reflected sidelobes.

3.2.3 Modelling the barotropic forcing of the baroclinic tide

The barotropic tide thus obtained will be used in the forcing term of an internal tide generation model, discussed in section 3.3.2, which also needs a topography and stratification.

Small-scale structures in the topography (like canyons) lead to strong local variations in the barotropic tide. This leads to local variations in the strength of the internal-tide generating terms which is perhaps responsible for the surface impression of radially diverging internal tides, seen on satellite (SAR) pictures (New 1988, his figure 3). This may also explain strong spatial variations in observations of currents (Holt and Thorpe 1997). These three-dimensional features can unfortunately not be captured in the present approach.

An approximate density profile for the region under study, as presented in the next section, is obtained with the CTD-casts from the simultaneous hydrographic program; see e.g. van Aken (2000). Along each transect, eight CTD-stations were located oceanward and across the shelf break, as depicted in figure 3.1. We will idealize these aspects in the internal tide generation model by neglecting depth variations along the shelf, and by calculating a forcing term from an ensemble average stratification and a typical cross-isobath bathymetry.

3.3 Tidal currents: observations and model results

3.3.1 Barotropic tide

An example of the method of estimating barotropic tidal amplitudes from repeated tracks is given in figure 3.2, where we display the barotropic current velocities (open circles) as determined and approximated by depth averaging. The currents, u and v, are in cross-slope (x) and along-slope (y) directions, respectively (see table 3.1). For each of the transects, the most south-westward point visited was taken as the local origin of this coordinate frame. The position at $x = 10$ km on transect 1 shown here is passed 10 times, and the least-squares fit to M_2-periodicity (frequency ω) gives
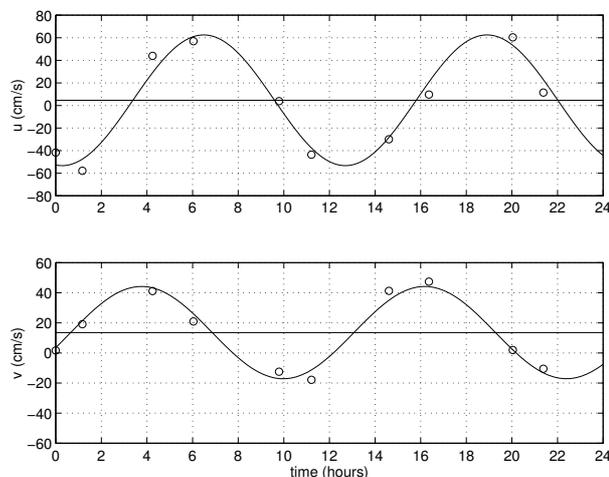
Figure 3.2: Example of a fit to the bin-wise observed velocity data in cross-slope (u) and along-slope (v) direction. In this example, time is measured in hours from the first crossing. The observations are marked with circles (o) and are fitted by a cosine and an offset (horizontal lines).

amplitudes of 58 and 31 cm/s for cross-slope and along-slope velocity components respectively. The velocity components are approximately 90 degrees out of phase, with v leading u, implying anticyclonic (clockwise, for $f > 0$) polarized motion, and the offset supplies an estimate of the residual currents, which we will deal with later on. We obtain these figures by assuming that at each position the velocity components can be written (e.g. for the cross-slope component) as

$$u = U_0 + U_2 \cos(\omega t + \phi_u) + u_\epsilon(t). \tag{3.1}$$

Here ϕ_u, U_0 and U_2 are constants, defining tidal phase, and the residual and tidal velocity amplitudes respectively. These are determined by a least-squares fit of this model to the data, which minimizes the error $u_\epsilon(t)$. Here $t = 0$ is defined as 00:00 UTC, January 1, 1993.

A spatial overview of the observed features of the barotropic semi-diurnal tides along the three transects is given in figure 3.3. We find high cross-slope velocities, up to 80 cm/s, which are about twice as large as the along-slope velocities. The amplitudes are roughly inversely proportional with depth (see the lower panels depicting mass transports uh and vh), so the cross-isobath flux is approximately constant (to within 30 %), especially for $x > 7$ km. Transect 1 was measured near spring tides, while transect 3, taken approximately 3.5 days later, was closer to neap tides. Because we could not resolve separate tidal constituents, like M_2 and S_2, it is hard to compare these values with values of M_2 from harmonic analysis of other observations of longer duration. Nearby, at a water depth of 310 m, Pérenne (1997) resolved
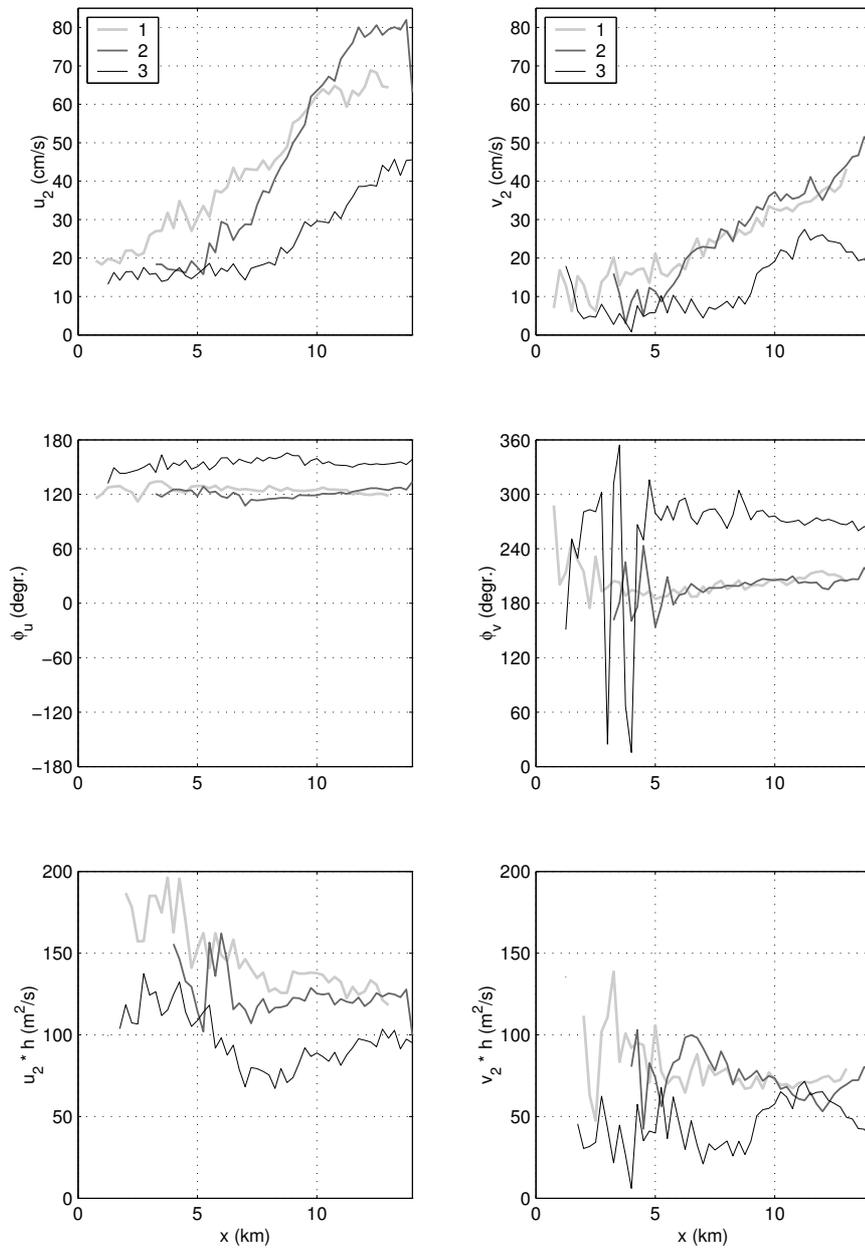
Figure 3.3: Observed barotropic velocity and transport. Cross-slope (left) and along-slope (right) velocity amplitudes (top), phase (middle) and transport (bottom). Transect 1, 2 and 3 are depicted as indicated in the legends in the top frames. The topography used is the same as shown in figure 3.1.

several tidal components (M_2, N_2, S_2 and K_2) with a bottom-moored ADCP which together lead to transports of comparable magnitude. Also the ellipticities are comparable: the cross-slope amplitudes are roughly twice as large as the along-slope amplitudes and the circulation is anti-cyclonic or clock-wise.

Phases of the velocity components (middle-left and middle-right panels of figure 3.3) are fairly constant over cross-slope distance x, but they differ quite a lot in magnitude: differences of about $50°$ for cross-slope phase (ϕ_u) and $70°$ for along-slope phase (ϕ_v) can be seen between subsequent transects. These differences are much too large to be explained by a monochromatic, barotropic deep-sea Kelvin wave, with phase speed $c = \sqrt{gh} \approx 200$ m/s, which, for the semi-diurnal tide, has a wavelength of about 9000 km. The transects are only about 35 km apart in the along-slope direction, so this would give an approximate phase difference of about $2.8°$. If the deep-sea Kelvin wave is somewhat "delayed" by the presence of the shallow shelf edge, its phase speed (wavelength) will be a little less (shorter), but for the actual situation differs always less then 10% (Miles 1972). It can be shown (by using the same method as in Simpson et al. (1990)) that inclusion of the S_2 component can explain additional differences (in the combined or mixed signal) of up to 15–20°, with perhaps additional phase differences due to other tidal components. But, this will not be sufficient to explain the observed large phase difference. More observations are needed to resolve this aspect.

3.3.2 Internal tide

Forcing

As already mentioned in section 3.2, in the forcing of internal tides three elements are essential: topography, a (cross-slope) barotropic tidal flow, and stratification. In estimating the strength of the forcing, we shall assume (as is usual, see e.g. Baines (1973)) that the cross-slope barotropic tidal flux is constant in space. In reality, the amplitude of the cross-slope barotropic flux will decrease oceanward on the scale of the (barotropic) Rossby radius of deformation, as well as coastward on the scale of the shelf-width (see, e.g., the discussion in Le Cann (1990), Sect. 4.3); however, since both scales are large compared to the width of the shelf break region, where the main generation of internal tides takes place, the assumption of a constant flux can be considered justifiable. This is corroborated by the observations described in the previous subsection.

The forcing F is thus constructed by prescribing a cross-isobath barotropic tidal flow $U_2(t,x) = Q \sin \omega t / h(x)$; here Q is the amplitude of the barotropic flux, ω the tidal frequency, h the local depth, and x the cross-slope direction. Continuity requires that the vertical barotropic component be

$$W = z \frac{Q \sin \omega t}{h^2} \frac{\mathrm{d}h}{\mathrm{d}x} \tag{3.2}$$

where the boundary condition $W = 0$ at $z = 0$ (upper surface, rigid lid) is satisfied.

Hence the forcing term to be included in the buoyancy equation becomes

$$F = N^2 W = z N^2 \frac{Q \sin \omega t}{h^2} \frac{\mathrm{d}h}{\mathrm{d}x} \equiv \hat{F} Q \sin \omega t \,. \tag{3.3}$$

The spatially depending factor $\hat{F}$ is depicted in figure 3.5a and depends only on topography and stratification. The latter requires the spatial distribution of potential density to be known. The complete forcing term F differs slightly from the forcing term in Baines (1982), which was included in the momentum equations instead; for the end results this makes no difference.

   Preceding the repeated tracks of every ADCP-transect, 8 CTD-stations were visited along the same tracks, extending further into the deep sea. Unfortunately, as is clear from figure 3.1, only a few of the CTD-stations lie on transects sampled with the towed ADCP afterwards. It is known that a banded structure, or shelf break front, exists along the 200 m isobath approximately, see e.g. Serpette and Mazé (1989) and Pingree and New (1995, their figure 10); with the given measurements, this structure is not adequately resolved. Moreover, the CTD-observations are snapshots of the density profile in an expectedly energetic internal tide/wave field. For example, in a nearby observation at a 'deeper extension' of transect 2, not shown here, over a water depth of approximately 1300 m, CTD-yoyoing revealed the presence of isothermal elevations of the order of 300 m on time scales from 1 hour to the tidal period (van Aken, personal communication). Ideally, each position should have been sampled for several tidal periods. Since this was not done, we have to estimate the mean density field by appropriate averaging.

   All in all, the density field $\rho(x, z, t)$ is not known in much detail with the given measurements, and hence neither is the buoyancy frequency N. To obtain the average stratification, $N(z)$, the 24 CTD casts were ensemble averaged and subsequently smoothed in the vertical by applying a running mean over distances of 101 metres (figure 3.4, left panel). In the model below this is again approximated (smooth line), retaining the sharp seasonal thermocline and deeper permanent thermocline typically found in this area (Pingree and New 1991). This figure also displays $-z N^2(z)$ (dotted line), which represents the vertical dependence of the forcing term, (3.3). It is seen that, although $N(z)$ itself is much larger in the seasonal thermocline, the deeper regions (especially in and around the permanent pycnocline) can be expected to be of importance in the generation of internal tides. Furthermore, high variability in the estimate of $N(z)$ is clearly visible, despite the vertical smoothing used.

   For the calculation of the horizontally varying part of the forcing (3.3), we used the topography observed on a transect traversed in a 1995 cruise. This transect was identical to transect 2, but extended farther coastward from the break. Figure 3.4 (right panel) displays $\mathrm{d}/\mathrm{d}x(1/h)$. The buoyancy frequency N is taken as in figure 3.4 (left panel, smooth line), which is regarded as an average stratification. The spatial part of the internal-tide forcing (multiplied by a factor 10^9) is shown in figure 3.5a. The figure clearly shows that there are *two* main generation areas: one in or close to the seasonal thermocline, near the shelf break, the other at deeper positions in the permanent thermocline. Compared to figure 3.4, the seasonal thermocline has
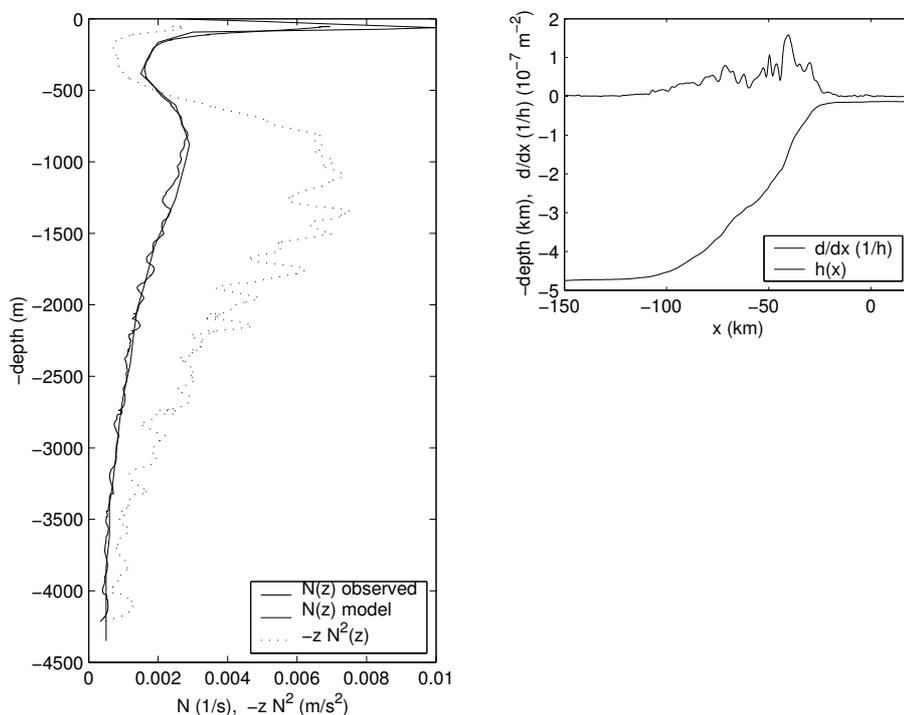
Figure 3.4: Left panel: averaged Brunt-Väisälä frequency profile $N(z)$, smoothed over 100 metres (full line) and $-zN^2(z)$ profiles (dotted line) in s^{-1} and m/s^2 respectively. All 24 different CTD-stations (see figure 3.1) are horizontally averaged. The smoother line is the profile used for the linear model calculations, see section 3.3.2. The right panel contains information about the depth profile used for the linear model calculation (based on the depth profile corresponding to that of transect 2, see figure 3.1). Also depicted in the right panel is the effect of the topography, $d/dx(1/h)$ (units: $10^{-7}m^{-2}$).

gained in relative importance thanks to its being present over shallower depths. It should be mentioned that the estimated body force given here involves some uncertainties in view of the only partly known density field as well as possible three-dimensional effects.

Though not as strong as in our observations, a second, deeper generation region was also found by Sherwin and Taylor (1990) further north in the Rockall Trough, northwest of Ireland. In figure 3.5a we find a maximum value in the forcing in the thermocline that is about 2.5 times higher than that in Sherwin and Taylor (1990) (who present $\hat{F}\rho Q/\omega$ in their Fig. 4). This is due to a combination of a larger cross-shelf mass transport, steeper topography and possibly stronger stratification locally. In the deep generation area the forcing can be up to 10 times as big. If N were constant, such as one often assumes in (semi-)analytical models (e.g. in Baines (1982)),
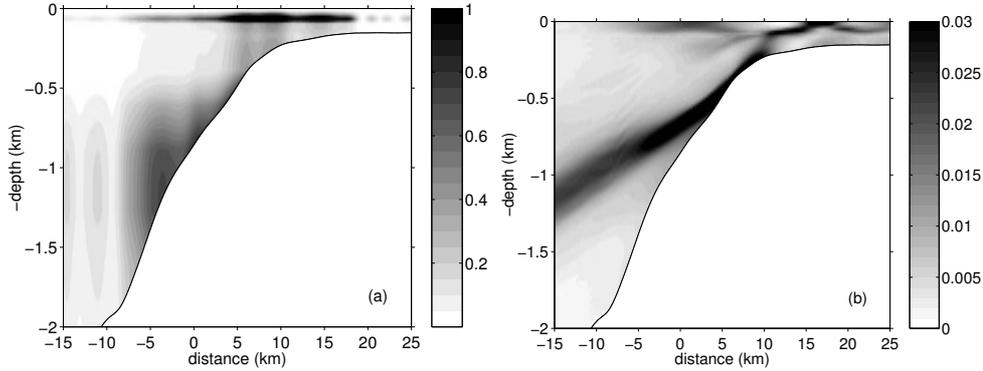
Figure 3.5: See figure C.7 for a full colour version. (a) Spatial structure of forcing term $\hat{F}$ (m^{-1}s^{-2}) multiplied by 10^9, as defined by (3.3). (b) same figure, but for internal tidal energy (m^{2}s^{-2}), as defined in (3.8).

only a single, near-bottom generation region exists. Furthermore, due to the smooth topography, the generation regions are much more blurred in figure 3.5a than in for example Baines (1982), where (due to the piecewise linear topography) point-sources occur, giving rise to singularities in the velocity field (Gerkema 2001, App. A).

Linear model results

The observed spatial structure of amplitude and phase (to be presented in the next subsection) can be compared with the outcome of a linear, hydrostatic internal-tide generation model (including Coriolis effects), which was previously described and used in Gerkema (2002). Here along-slope uniformity is assumed (i.e. $\partial/\partial y = 0$); we can therefore introduce a stream function ψ (expressing the baroclinic current speeds as $u = \psi_z$ and $w = -\psi_x$), and reduce the linear long-wave equations to

$$\psi_{zzt} - f v_z - \rho_x = 0 \tag{3.4}$$
$$v_t + f\psi_z = 0 \tag{3.5}$$
$$\rho_t + N^2 \psi_x = N^2 W = F \tag{3.6}$$

in which f is the Coriolis parameter, v transverse velocity component, and ρ the potential-density perturbation with respect to its local static value (multiplied by g/ρ_*, for convenience, where g is the acceleration due to gravity, and ρ_* the mean density). F, given by (3.3), represents the forcing due to the barotropic tidal flow over the topography.

Before we turn to the forced problem, it is useful (in view of the considerations put forward below) to recapitulate first some known theoretical results concerning internal-wave propagation, which follow from the unforced version ($F = 0$) of the model equations (3.4)–(3.6) if we assume that N is nearly constant. One finds, by

assuming that all fields can be written as a constant times $\exp(i(kx + mz - \omega t))$, the dispersion relation

$$\omega^2 = N^2 \cot^2 \theta + f^2 \,, \tag{3.7}$$

where $\tan \theta \equiv m/k = \sqrt{N^2/(\omega^2 - f^2)}$. The dispersion relation depends only on the direction of the wave vector $\vec{k} = (k, m)$, which implies that the group-velocity vector $\vec{c}_g$ must be perpendicular to it: $\vec{k} \perp \vec{c}_g \parallel \vec{u}$ (the latter follows from the continuity equation, $\nabla \cdot \vec{u} = 0$). Hence the wave-energy propagates along lines of equal phase, being given by $dx/dz = \tan \theta$. Furthermore, $\vec{c}_g$, being a gradient in wave number space, points (by definition) in the direction of increasing ω; in this case $f < \omega \ll N$, which implies that the vertical components of $\vec{k}$ and $\vec{c}_g$ must be opposite. Hence, where phase-propagation is upward, energy propagates downward (and vice versa). In the next subsection we shall check these results against the observations.

The input values for the topography and stratification are as described in the previous subsection. Based on figure 3.3, the barotropic cross-slope flux is taken to be $Q = 100$ m^2/s, corresponding with current speeds of about 2 cm/s in the deep ocean —being comparable to values found by Pingree and New (1991, their table 1). Notice that the value of Q is immaterial to the *structure* of the solution since the equations are linear.

As discussed in Gerkema (2002), the equations are solved by first transforming the xz–domain to a rectangular shape, which allows the application of a pseudo-spectral method in the vertical, involving here 64 Chebyshev polynomials. The boundary condition is $\psi = 0$ at bottom and surface. In the horizontal and in time centered differences are used (steps of 400 m in x, 360 time steps per tidal period). At the outer ends of the domain sponge layers are used to absorb the incoming waves. The fluid is initially at rest; after about 40 tidal periods the transients have left the region of interest, and the signal has become periodic in time.

The tidally averaged energy density $\langle E \rangle$, E being here defined as

$$E = \frac{1}{2} \left(u^2 + v^2 + \rho^2/N^2 \right) , \tag{3.8}$$

is shown in figure 3.5b. Surprisingly perhaps, in its details there is no strong similarity with the forcing term (shown in figure 3.5a); in particular, the main beam emanates from the topography (shelf break) rather than from the thermocline, despite the fact that the actual forcing term is stronger in the latter. This is because the generation is most efficient on those locations where the barotropic pair of components (U, W) is (literally) in line with the baroclinic tidal components (u, w), the direction of which is fixed by the stratification and Coriolis parameter; see (3.7). This condition is satisfied precisely at critical locations at the slope, i.e. where the steepness of the beam equals that of the slope.

On the whole, one can discern three regions in figure 3.5b of internal tide activity: a clear beam directed downward into the deep ocean, a weaker beam directed on-shelf, and a relatively high-energy region near the surface at the deep side of the
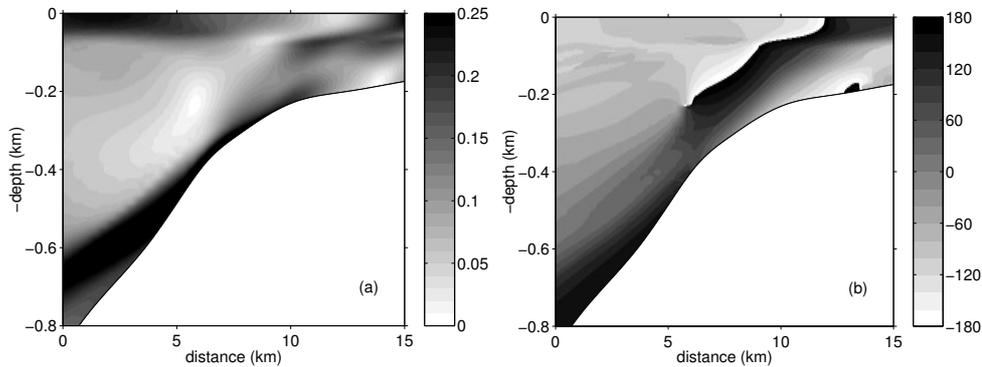
Figure 3.6: See figure C.8 for a full colour version. Linear model results of cross-slope baroclinic motion. Left panel (a) depicts amplitude distribution (m/s). Right panel (b) shows phases in degrees.

shelf break (near $x = 0$). This region starts in the thermocline and does not emanate as a beam from the shelf break; such a beam is predicted for piecewise linear topography (point source, see Baines (1982), New (1988)), but is absent here because of smooth topography. As the on-shelf propagating beam and the strong near-surface currents at the deep side of the break emanate from the seasonal thermocline, one may expect that they will be absent during winter. Further numerical results confirm this (Gerkema et al. 2004): during winter only the downward–oceanward beam is present. In Gerkema et al. (2004) the seasonal differences in the overall energetics of the internal tide is discussed as well.

The cross-slope baroclinic component u can be written as

$$u(t, x, z) = A(x, z) \sin(\omega t + \phi(x, z)) . \tag{3.9}$$

The spatial structure of amplitude A and phase ϕ is shown in figure 3.6; (3.9) implies that the lines of equal phase propagate in the direction of decreasing ϕ. Thus figure 3.6b divides almost perfectly into two parts, the division lying near $x \approx 6$ km: to its right phases propagate downward (except in the lower right corner), to its left upward. The latter does not hold in the region near the surface around $x = 5$ km, where phases propagate downward. Notice that this region coincides with that of the beam directed up– and oceanward in figure 3.5b.

A striking feature connected with this is what we may call an 'amphidromic' point, which lies near $x = 6$ km, just below 200m depth. Unlike the common amphidromes occurring in barotropic tides, this one appears in the *vertical* plane; such an amphidrome was previously found in numerical (deWitt et al. 1986) and analytical (Gerkema 2001) internal-tide solutions, but not, to our knowledge, in observations (but see the next subsection). Also remarkable is the diagonal band (blue) in which the amplitudes are very small. In the next subsection figure 3.6 will be compared with the observed data.
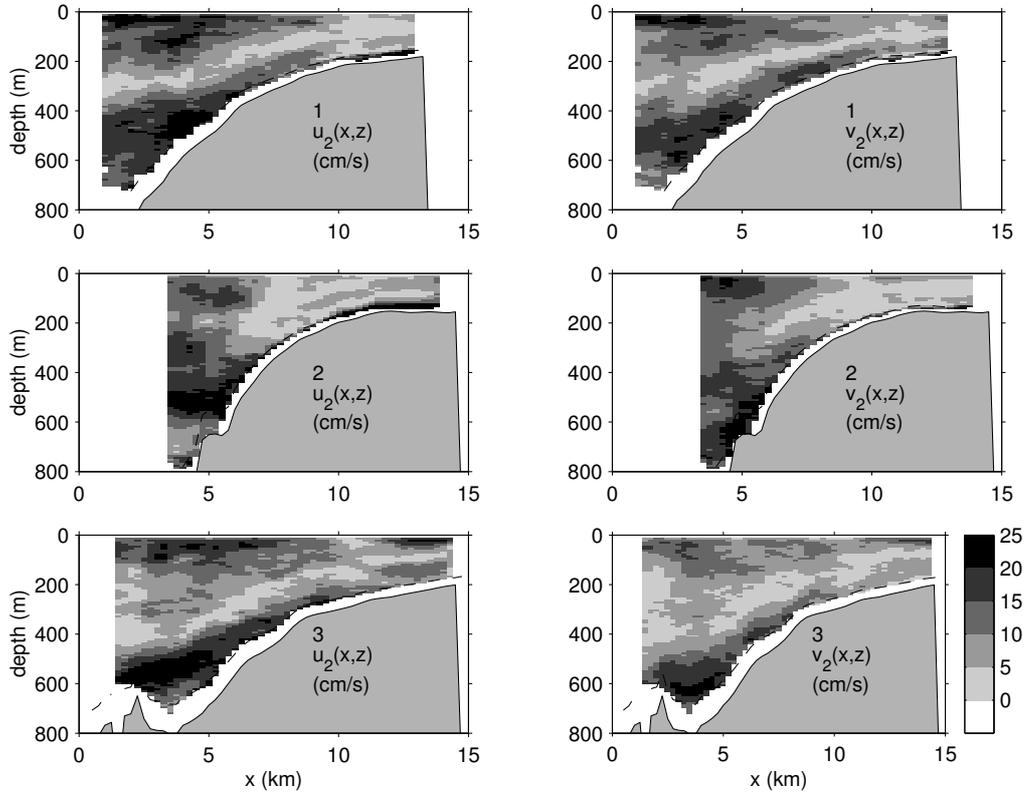
Figure 3.7: See figure C.9 for a full colour version. Internal tidal amplitudes (in cm/s), in cross-slope (left) and along-slope (right) direction at transects 1 (top), 2 (middle) and 3 (bottom). Dashed lines depicts 85% of the water depth. Measurements below these lines should be disregarded, as explained in subsection 3.2.2.

Observed internal tide

In subsection 3.3.1 the barotropic tide was assumed to be represented by the vertical mean of the estimated tidal motion, and so the internal (baroclinic) tide will consequently be assumed to be that part of the tidal motion that deviates from this vertical mean. The internal-tidal current thus defined is represented in terms of amplitude and phase distributions as indicated in (3.1).

The observed patterns of tidal amplitudes (u_2, v_2) and phases (ϕ_u, ϕ_v) are shown in figures 3.7 and 3.8. Qualitatively, one can distinguish three regions where strong currents occur: close to the slope, in the upper left-half, and in the upper right corner; they are separated by (blue) diagonal bands. This (rough) qualitative picture corresponds very well with the numerical results in figure 3.6a. Phase propagation
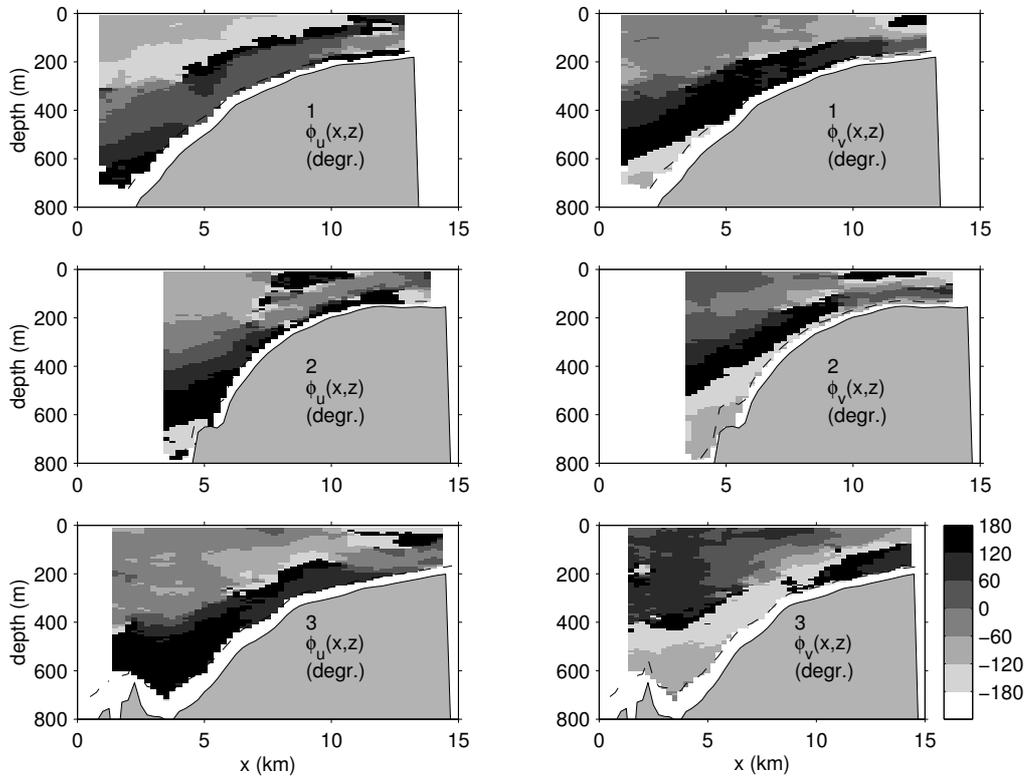
Figure 3.8: See figure C.10 for a full colour version. Internal tidal phases (in degrees) corresponding to figure 3.7, i.e. deviations from vertical mean. Dashed lines represent 85% of the water depth, as in figure 3.7.

is generally upward (i.e. in the direction of decreasing ϕ, see previous subsection) in the left-half of each figure, and (though less clearly) downward in the outer right part. Again, this is in qualitative agreement with the numerical result shown in figure 3.6b. Indeed one can discern the earlier mentioned amphidromes: for transect 1 near $x = 4.5$ km at 270 m depth; for transect 2 near $x = 7$ km at 250 m depth; for transect 3 near $x = 6.5$ km at 290 m depth.

Overall, one sees distinct diagonal bands of equal phase in figure 3.8, in qualitative agreement with results on internal-wave propagation established previously in laboratory experiments (e.g. Mowbray and Rarity (1967), Sutherland et al. (2000)), oceanic observations on internal tides (deWitt et al. 1986; Pingree and New 1989; Morozov 1995) and theory (LeBlond and Mysak 1978). Exact comparison with linear internal-wave theory is straightforward. First of all, phase- and energy propagation should have opposite vertical components (see previous subsection); this means that,
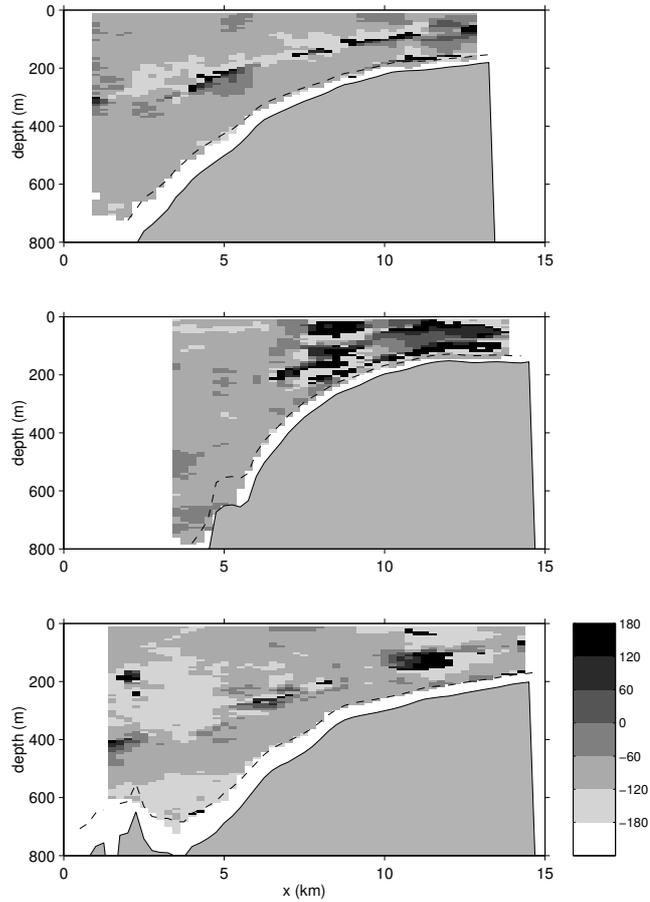
Figure 3.9: See figure C.11 for a full colour version. Phase differences, $\phi_u - \phi_v$, as derived from figure 3.8. Dashed lines represent 85% of the water depth, as in figure 3.7.

both in figure 3.6b and in figure 3.8, energy propagates generally down- and leftwards in the left-half of each figure, and up- and rightwards in the (outer) right-half; in other words, energy propagates away from the source (the shelf break), as one would indeed expect. Equation (3.5) implies that u and v should be out of phase by $90°$ if no along-slope variations were present; this seems indeed to be the case for all transects, as can be seen in figure 3.9, especially in those regions where the beam is intense. Finally, we consider the slope of the lines of equal phase. The observed (inverted) slope (see figures 3.7 and 3.8) is about 5 km/250 m, in agreement with that obtained from the numerical model (figure 3.6). This slope is for plane waves given by $\mathrm{d}x/\mathrm{d}z = \tan\theta$, (3.7), which yields the same slope taking $N = 2.0 \times 10^{-3}$, and $f = 1.0 \times 10^{-4}$ and $\omega = 1.4 \times 10^{-4}$ (all in units: s^{-1}).

3.4 Residual currents: theory and observations

3.4.1 Possible driving mechanisms of slope currents

The slope current, in the Northern Hemisphere having the shelf at its right when facing downstream, is a ubiquitous phenomenon along shelf edges. Clockwise mean-flows are (in the Northern Hemisphere) often found around isolated seamounts too (Eriksen 1991; Kunze and Toole 1997). The slope current is attributed to a number of causes, discussed in Pingree and Le Cann (1989, 1990) and Huthnance (1984, 1992). These include wind, a large-scale, along-shelf poleward density gradient, a shelf-slope frontal system (of which the slope current is the associated, geostrophic flow), rectification of continental shelf waves, tidal waves (Zimmerman 1978; Ou 1999), and internal waves (Thorpe 1999), or to a statistically forced flow (Kazantsev et al. 1998). Seasonality of current shear (weak in winter, strong in late summer) might reflect the geostrophic character of the flow, although Pingree and Le Cann (1990) estimate this geostrophic flow to be small for the present observation site (< 1 cm/s). Persistence of the mean flow and modulation at the spring-neap tidal time-scale, are often, particularly in shallower water, interpreted as pointing at a tidal origin of the flow (Butman et al. 1982).

Although tidal rectification may be important near Chapel Bank, where tides are particularly strong (about 70-80 cm/s, Pingree and Le Cann (1989)), this process is generally not seen as a significant contributor to the slope current over the shelf break, owing to the large depths (> 200 m). Huthnance (1992), discussing the observed spring-neap tide modulation of the slope current, advances another argument, by noting that the phase of this modulation *lags* that of the tidal fortnightly modulation, which is taken as signalling a modulation in the amount of friction of the barotropic tide, rather than as a clear indication of tidal rectification. Tidal rectification is therefore usually considered important in shallower areas, on continental shelves (with their increased tidal currents), like over Georges Bank (Butman et al. 1982), or the North Sea (Huthnance 1973; Zimmerman 1978; Howarth and Huthnance 1984). However, stratification may amplify the vortex stretching mechanism underlying the rectification process in deeper water too, by inhibiting vertical motions further away from the bottom, which may lead to a bottom-intensified, rectified flow (Maas and Zimmerman 1989b; Chen and Beardsley 1995). This is one of the reasons why tidal rectification may become important at and around seamounts, at several hundred metres depth (Eriksen 1991).

3.4.2 Cross-slope circulation

The along-isobath slope current is often accompanied by cross-isobath currents. Near the bottom these are downslope at the upper, and upslope at the deeper stretches of the slope. Several hypotheses have been formulated to explain the cross-slope circulation. It might be a secondary circulation of a rectified current system, whether of a frictional (Tee 1985; Wright and Loder 1985; Loder and Wright 1985) or strati-

fied origin (Ou and Maas 1986; Maas and Zimmerman 1989a,b; Chen and Beardsley 1995). It might also result as a secondary circulation of a frontal system (Garrett and Loder 1981), itself linked to the tide by tidal mixing. Indeed, the strongly nonlinear character of the external and internal tide, implying the presence of rectified flows and solitary waves, suggests that mixing may be particularly relevant in these areas too, which is indeed manifest in the consistent presence of a band of lower temperatures around the shelf edge, the "cold ribbon". This is a band (of width ~ 50 km) of relatively ($\sim 2°$) cooler surface temperatures along the shelf break of the Bay of Biscay, seen on numerous satellite infra-red images of the region (Pingree 1979; Pingree 1984, e.g.). Thus, strong tidal mixing will contribute to the shaping of (and be affected by) the shelf edge density front.

However, to settle which mechanism(s) is (are) responsible for the mean flow, it might be useful to find other observables that can distinguish between some of the proposed mechanisms. Contrasting the slope current as driven by a poleward buoyancy gradient with, for instance, a tidally rectified current, one might employ a predicted difference in cross-isobath structure of the residual flow to discriminate between the two. The along-slope, depth-mean flow

$$v = \frac{gH}{2r\bar{\rho}}\frac{\mathrm{d}\rho}{\mathrm{d}y}h(1 - h/H), \tag{3.10}$$

(with H the depth of the adjacent deep sea) is expected to extend over the whole sloping region (Huthnance 1984). This mean flow takes on its maximum approximately halfway over the slope (if we assume that on the shelf $h \ll H$ is satisfied). The tidally rectified current should be mainly concentrated over the top of the slope (Zhang et al. 1996):

$$v = -\frac{1}{2}\frac{fU^2H^2}{\omega^2h^3}\frac{\mathrm{d}h}{\mathrm{d}x}. \tag{3.11}$$

Here $\bar{\rho}$ and $\rho(y)$ denote the spatially constant and poleward y-varying part of the density field, f and ω the Coriolis and tidal frequency, U the tidal current speed on the shelf. Linearized friction is adopted in the former description, taking a velocity scale $r = 0.5$ cm/s. Note that this friction velocity is often parameterized as $r = C_D U$, where drag coefficient $C_D \approx 2.5 \times 10^{-3}$. Because cross-slope barotropic mass transport is nearly constant, an increase in depth leads to a decrease of U. The related decrease in friction velocity leads to a rapid increase of the slope current (3.10). Blaas et al. (2000), using a two-dimensional numerical model, identify regions along the North Western European shelf edge where either one of these processes dominates, and regions where the slope current is actually a (nonlinear) superposition of residual currents due to both processes. They note that when the density gradient were restricted to the upper part of the water column, rather than the whole column, then the position of maximum flow in (3.10) would shift from halfway the slope towards the shelf, and weaken (Blaas et al. 2000; Blaas 2002); however, we shall use (3.10) further on. In the following we will make such a comparison on the basis of the observed mean flow over the three transects.

3.4.3   Observed mean flow

The harmonic analysis of the towed ADCP-data offers us, apart from tidal informa-
tion, also a bin-wise estimate along each transect of the "residual" current as e.g. in
Loder et al. (1992). Due to the shortness of our "space-time" series, aliasing may
disturb the individually estimated residual currents. This is a greater source of noise
for the mean flow than for the tidal field because of the relative weakness of the
former. As this may lead to very erratic spatial patterns, we interpret any spatial co-
herence in the residual current patterns as indicative of a well-determined residual
field, although we recognize that the "residual" may, in this case, contain also other
low-frequency contributions, notably of a diurnal origin.

Rather than decomposing the mean flow into a (vertically averaged) barotropic
and a (remaining) baroclinic part, it turns out to be more useful to consider only the
barotropic and *total* mean flow patterns. Over the length of the transects this will
provide a detailed picture of the spatial structure of the residual current, which will
be compared with the theoretically predicted shape.

3.4.4   Observed barotropic currents

On transects 1 and 3 (figure 3.10) the vertically averaged, along-isobath residual
current has a localized, jet-like structure, with a maximum amplitude of some 10–
15 cm/s. The jet is centred near the shelf edge, over bottom depths of 200–300 m.
Transect 2 has a somewhat similar structure, although the mean flow seems to ex-
tend to deeper water (peaks at $x = 3$ and 4 km). It may well be that these peaks
result from the passage of what seems like a solitary wave, encountered during one
of the ten traverses. Solitary waves are, after all, not uncommon in this area (Pingree
and Mardell 1985; Pingree et al. 1986; New 1988; Pichon and Mazé 1990).

The mean flow jet is some 8 km wide, and is, over the shallower regions, accom-
panied by vertically averaged on– and off–shelf flows of some 5 cm/s (not shown).
The latter cross-isobath residual flows perhaps suggest an error in the local choice
of cross and along-isobath direction, which may be more influenced by local bathy-
metric features, instead of by the large-scale shape of the shelf edge on which our
present choice was based. The extent to which local canyons and shelf edge crevices
influence the actual barotropic-baroclinic conversion process and the resulting mean
flows, is currently a topic of research (Grimshaw et al. 1985; Holt and Thorpe 1997;
Petruncio et al. 1998).

Figure 3.10 also contains theoretical profiles, determined by (3.11) (solid) and
(3.10) (dotted). Except for transect 2, both the magnitude and the shape of the resid-
ual current seem well described by the barotropic, tidally rectified current of (3.11).
Since the slope stretches out over some 60 km, the slope current due to the joint ef-
fect of baroclinicity and relief (JEBAR, Huthnance (1984)), given by (3.10), should,
over the length of the transect, only increase in magnitude away from the shelf edge
(dotted line in figure 3.10; the calculated maximum of the slope current being almost
50 cm/s).
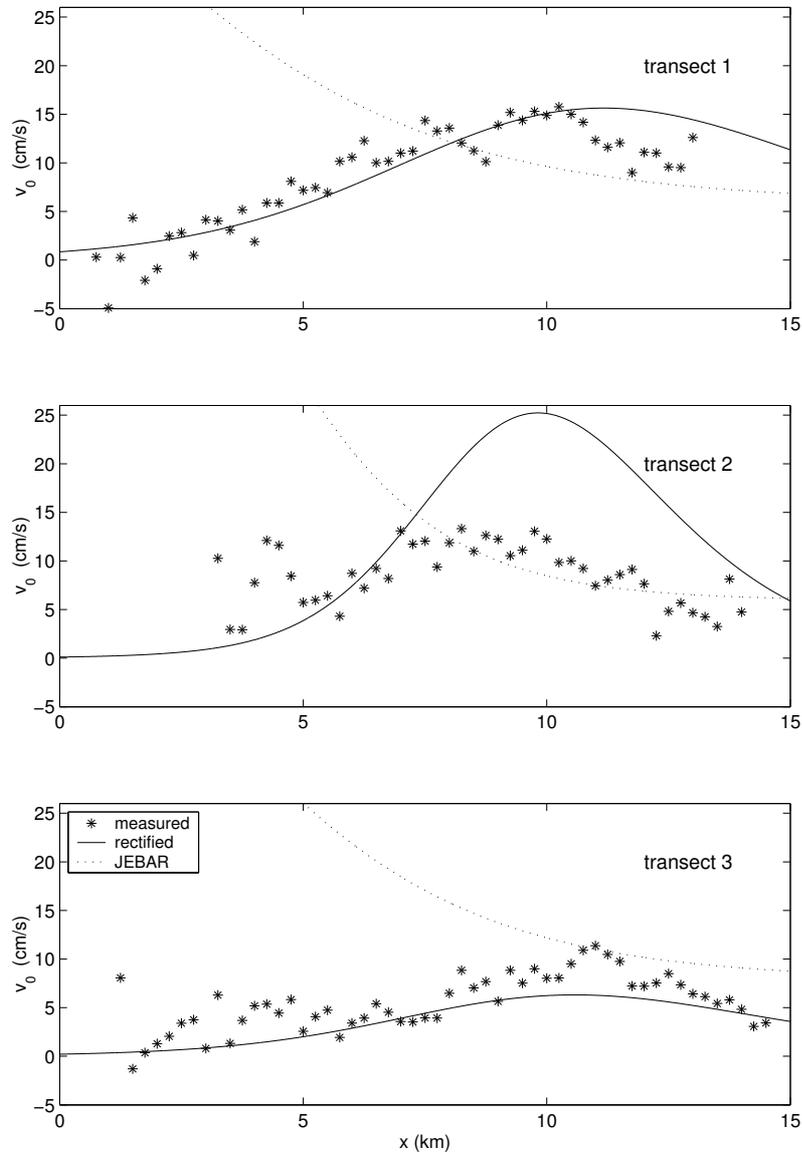
Figure 3.10: Observed vertically averaged along-slope currents as a function of cross-slope distance x. Observed values (for each bin) are given by stars (*). Calculated rectification, as given by (3.11), is given by smooth lines. Here the observed topography is fitted to a tanh-shape. Calculated slope current, as given by (3.10) (JEBAR), is represented by dotted lines. Here the following values have been used: $r = 0.005$ m/s and $1/\bar{\rho}\, \partial\rho/\partial y = 10^{-10}$ m^{-1}, the latter according to Blaas (2002).

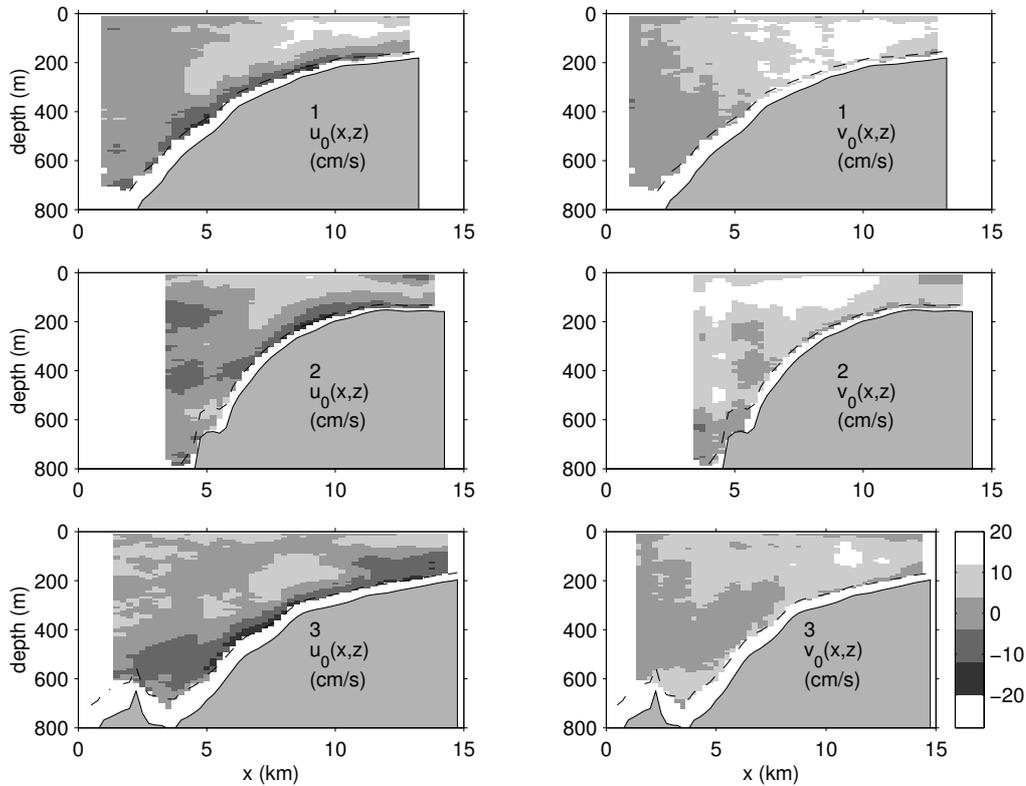**Figure 3.11:** See figure C.12 for a full colour version. Estimated total stationary currents cross-slope (left) and along-slope (right) in cm/s for transect 1 (top), transect 2 (middle) and transect 3 (bottom). Dashed lines represent 85% of the water depth, as in figure 3.7. Note that for these grey scales, both the maximum as well as the undefined numbers are labeled as white (see the legend).

3.4.5　Observed total currents

The bin-wise observed total residual currents are depicted in figure 3.11. The most remarkable features are a clear subsurface, along-isobath jet (red regions in right panels; recalling the comments with regards to the deeper parts of transect 2, made earlier) and the strong near-bottom, downslope cross-isobath currents (magnitudes of about 10-15 cm/s), over the shelf break region (blue regions in left panels).

　　The along-isobath current increases from the bottom upwards, reaching a maximum in the subsurface jet. The jet axis is at some 100 m depth and its width is similar to that of the barotropic part. Similar observations were made in this area by Pingree and Le Cann (1989), Pérenne (1997) and Pérenne and Pichon (1999). In models of tidal rectification (Maas and Zimmerman 1989b; Chen and Beardsley 1995;

Zhang et al. 1996) the along-isobath jet is surface-trapped in near-homogeneous conditions as the tidally rectified flow is impeded by friction close to the bottom. In principle this predicts its surface intensification. However, stratification inhibits the stretching and squeezing of vortex tubes further away from the bottom, limiting the rectification process to the near-bottom region. As a consequence, tidally rectified along-isobath flow in a stratified sea develops a subsurface maximum, as observed. Near the shelf break, and further on the shelf, observations with drifting buoys (Lagrangian measurements) support this Eulerian current pattern (Mazé 1987), and show that the rectified flow is not annihilated by the Stokes' drift. In the cross-isobath direction, however, New (1988) finds in a numerical model an *upslope* Stokes' drift which *does* annihilate the strong near-bottom Eulerian downslope current, so as to satisfy the requirement (Wunsch 1971) of zero net Lagrangian cross-isobath, isopycnal displacements.

The down-slope cross-isobath currents become up-slope from about a quarter of the water-column upwards. Further down the slope some near-bottom up-slope motion is observed. The cross-isobath currents seem to form part of a strong circulation cell (not very clearly visible along transect 3) that suggest an off-shelf upwelling area, near $x = 4$ km, over water-depths of some 500 to 600 m, and a downwelling higher up on the slope, beyond our most shallow, on-shelf measurement location. This suggestion is based on predictions from analytical and numerical models concerned with the cross-isobath structure of the cross-isobath, tidally rectified residual circulation (Maas and Zimmerman 1989b; Chen and Beardsley 1995).

3.5 Summary & Discussion

Elementary theory, supported by the results of earlier laboratory experiments, indicate that, in a continuously stratified fluid, internal waves propagate their energy obliquely through the fluid in beams, parallel to their phase lines. While this kind of propagation has previously been observed in the ocean, such observations were traditionally based on comparing velocity records of some isolated moored instruments with predictions from a two-dimensional numerical model. Here, we employed an alternative observational method that directly visualized the oceanic internal tidal beam emanating from the shelf edge of the Bay of Biscay. Comparison with the numerically predicted internal-tide field shows good correspondence even in the *details* of the current fields. Moreover, the observational method concurrently reveals spatial details of the barotropic tide and of the residual flow in the vicinity of the shelf edge.

The observed barotropic tide had a tendency to conserve its cross-isobath mass flux (as presupposed in many theoretical studies). While there was correspondence in the amplitude estimates, the phase of the barotropic tide varied rapidly over the three cross-isobath transects. To some extent this can be attributed to the fact that our estimates resolve only one semi-diurnal tide constituent, representing M_2. Contributions from other nearby frequencies, such as S_2, N_2 which are present in the region,

result in a larger phase change in the analysed (mixed) signal. But, this is insufficient to provide a full explanation. While we remain puzzled as to its immediate cause we speculate that it may reflect the barotropic tidal response to small-scale bathymetric features like canyons (Codiga et al. 1999).

The observed baroclinic tidal field showed phase lines (and corresponding amplitude lines) slanting downwards into the deep sea, under an angle that corresponds with that of the numerical model. A nodal point (amphidrome) in the vertical plane and the complex amplitude distribution find their counterparts in pictures computed with a linear two-dimensional hydrostatic model. These patterns to a large extent reflect 'complexities' in stratification and bathymetry: the deeper, continuous stratification, corresponding to the permanent thermocline, is capped by a stronger seasonal thermocline, while the bottom sometimes also shows sharp corners or bumps. This leads to the barotropic forcing term having multiple peaks over the vertical transect, one peak in the seasonal and one in the permanent thermocline, with further 'structure' due to bathymetric features. However, it was also shown that the forcing term, taken in isolation, does not necessarily indicate where the actual forcing is strongest; also important is the alignment of the barotropic current field with respect to the direction of internal-tide propagation, a fact that singles out near-critical slope regions as the dominant ones.

The slanting of phase lines is consistent with energy propagation into the deeper parts of the Bay of Biscay. While the present observations only reveal its initial generation and descent, this picture ties in with that sketched on the basis of previous observations from moorings that reveal the subsequent bottom reflection of this beam, upward propagation, and reflection from the seasonal thermocline, approximately 140 km away from the shelf edge (New and Pingree 1992). Gerkema (2001) shows that this beam can, under certain conditions on the stratification, lead to the local generation of large amplitude internal waves in this seasonal thermocline, consistent with observations in New and Pingree (1992) and New and Da Silva (2002). This means that the beam is weakened and becomes less recognizable. One may speculate that internal tides may also originate from the opposite site, the Iberian shelf, and then be amplified upon reflection at the slope. Indirect evidence of such a reflection is described by Gemmrich and van Haren (2001).

The structure of the observed residual current is fairly consistent with that of a tidally rectified current. It reveals both an along-isobath current having its shallow side at its right hand side (facing downstream) and a cross-isobath circulation dominated by down-slope flow just outside the bottom boundary layer (with a concurrent up-slope flow closer to the surface). Over the deeper parts of the slope this downslope bottom flow meets with an upslope bottom flow. The confluence leads to upwelling and may also be responsible for the 'cold ribbon' that is often encountered over the shelf edge.

While sunglint observations (Pingree and New 1995) suggest the shelf to act as a two-dimensional line source, one should realize that these surface manifestations reflect the properties of the internal tides only so far as they manifest themselves near the thermocline; the deeper (abyssal) internal tidal beams may have a differ-

ent character. Three-dimensionality may be expected because the shelf edge is after all filled with submarine canyons, some of which may be particularly effective in internal tide generation. Petruncio et al. (1998) reported detailed measurements of the internal tide in a specific submarine canyon on the Pacific coast, together with numerical investigations (Petruncio 1996). Ring-like structures suggest that such 'point-wise' generated internal tides also exist in the Bay of Biscay (Pingree et al. 1983; New 1988), and their phase propagation was observed at sea (Holt and Thorpe 1997) and in numerical models (Serpette and Mazé 1989). In our own measurements this may be evident in 'anomalous' waves near a local seamount, along section 3 (at $x = 2$ km), which were repeatedly encountered and gave rise to strong local current variations. It may well be that individual scatterers are also effective locally in converting barotropic to baroclinic tides, and are underestimated in two-dimensional theory.

Acknowledgements

Chapter 4

Internal wave focusing revisited; a reanalysis and new theoretical links [1]

An experiment which discussed the appearance of an internal wave attractor in a uniformly-stratified, free-surface fluid (Maas et al. 1997) is revisited. This is done in order to give a more detailed and more accurate description of the underlying focusing process. Evolution of the attractor can now be quantified. For the tank with one sloping sidewall, and for the parameter regime (density stratification, forcing frequency) studied, the inverse exponential growth rate determined at several locations in the fluid turns out to be 122 seconds always. Only the start and duration of the growth differs: away from the attractor region it appears later and is of shorter duration. Here, these features are interpreted by employing a new theoretical basis that incorporates an external forcing via a surface boundary condition (an infinitesimal barotropic seiche) and that describes the solution in terms of propagating waves.

4.1 Introduction: internal waves in a confined fluid domain

Internal waves in a continuously stratified fluid, represented by the stability frequency $N(z)$, have peculiar characteristics. We will only discuss the case of a non-rotating fluid with constant N, for which the internal wave frequency $\omega < N$ (Groen 1948). For monochromatic internal waves energy propagates obliquely through the fluid with a fixed angle, set by the ratio ω/N (see e.g. Turner (1973) or LeBlond and Mysak (1978)). The behaviour of propagating internal waves in such a stratified fluid is well suited for a description in terms of rays. As depicted for example in Turner (1973, fig.2.10), reflection of waves at solid boundaries of orientation other

---

[1] This chapter is submitted as Lam and Maas (2006)

than horizontal or vertical gives rise to divergence or convergence of wave energy. Maas and Lam (1995) demonstrate that in almost all confined fluid domains focusing dominates over defocusing. The result is that wave energy focuses at a limit cycle, called *wave attractor*. The existence of such an internal wave attractor was subsequently observed (Maas et al. 1997). It revealed this focusing of wave energy around the predicted location. The experiment qualitatively showed that the wave attractor occurred on a time scale large compared to the period of the waves that were excited. Interestingly, the wave field appeared to grow initially as a standing wave and evolved subsequently into a propagating wave as the final stationary state. Similar wave attractors arise in homogeneous rotating fluids and are reviewed in Maas (2005).

The aforementioned experimental study did not quantify the detailed evolution in terms of growth rate, transition, and spatial structure of the wave's amplitude and phase fields. Also, it lacked a quantitative description in terms of the applied forcing. This was due to the peculiar nature of the theoretical internal wave field, whose stream function field was given as a standing, free wave that appeared to be uniquely prescribed when the pressure was set in two specific boundary intervals only. However, this seems to contrast on the one hand with the propagating character of the observed asymptotic state of the wave field, and on the other hand with the intuitive notion that one should be free to apply pressure at the boundary in whatsoever interval one pleases. The aim of this paper is to bridge this gap between the theoretical description and the experimentally observed nature of the internal wave attractor by providing a quantification of the latter. For this reason, the phenomenon of geometric focusing, underlying the appearance of a wave attractor, will be recapitulated in the next section. Then, in section 4.3 the laboratory experiment will be revisited and the evolution of the wave field will be quantified better. The previously mentioned restriction on the prescription of the pressure at the boundary will be lifted in section 4.4, when propagating solutions to the forced problem are discussed. The paper ends with a summary and discussion.

4.2   Earlier theoretical results

4.2.1   Geometric focusing

Maas and Lam (1995) studied theoretically multiple reflections of internal wave rays (characteristics) in a confined two-dimensional fluid. Different geometrical basin shapes were explored: rectangular, parabolic, elliptic and trapezoidal. It was concluded that in almost all two-dimensional geometries internal waves are attracted to a limiting set of characteristics, including the geophysically relevant spherical shell. See also Rieutord and Noui (1999) for the latter. Exceptional boundary shapes are formed by rectangles and ellipses; that is, as long as these are not tilted with respect to the direction of gravity (Ogilvie 2005). The attracting set (limit-cycle or 'attractor') is classified by the number of surface reflections, called the *period* of the attractor,

which can be related to the rotation number (Manders et al. 2003). The period of the attractor remains the same over a finite interval of the lumped parameter τ, defined by stratification (density gradient), internal wave period and the basin's aspect ratio: $\tau = (N^2/\omega^2 - 1)^{1/2}D/L$, with $2L$ and D the width and the depth of the basin, respectively (Maas and Lam 1995). For a few basin shapes and for specific values of τ, a so-called global resonance can sometimes occur, when ray convergence is exactly balanced by divergence of the reflecting wave rays; all rays close upon themselves. In rectangular basins such a global resonance is known as an internal seiche, in which no convergence or divergence of reflected wave energy occurs at all. However, this global resonance is believed to be the exception rather than the rule for general topographic shapes, both in a laboratory as well as in a natural context. More generally, the attractor behaviour is found to be dominating the internal wave appearance. This conclusion, later experimentally confirmed in Maas et al. (1997), leads to a solution with more fine scale structure that opposes the belief in the dominance of large-scale modal behaviour.[2] See Thorpe (2003) for a recent discussion on this topic.

An example of an internal wave attractor is given in figure 1.18a. It is reached by the characteristic webs that are constructed by following two characteristics that start at the surface downwards. The wave energy propagates along these lines. The (half) webs are formed by these characteristic segments together with their subsequent boundary reflections (solid and dashed lines respectively) following the adage that the waves maintain their angle with respect to the direction of gravity. In this figure, the topography is the same as in Maas et al. (1997): a trapezoid with one sloping side wall. This geometry is defined by the lumped parameter τ that acts as 'virtual' depth: $z = -\tau$ for $(-1 \leq x \leq 0)$; $z = -\tau(1 - x)$ for $(0 < x \leq 1)$.

The parametric dependence of the attractor for this simple geometry is explained in Maas et al. (1997, fig.2). For example, for $1 < \tau < 2$ the attractor has only one surface reflection (called a period 1 periodic orbit). The location x_e of its surface reflection is: $x_e = \tau^2 - \tau - 1$, and $x_e = 0.2141$ for the example of figure 1.18 ($\tau = 1.71$).

4.2.2 Standing wave solution

In order to be able to relate the experimentally observed velocity field to the 'ray-web' that was found geometrically we will recall how its solution can be obtained from the web, see e.g. figure 1.18a. This procedure was referred to as the 'dressing of the web' (Maas 2005; Maas et al. 1997). In the basin, the ray-structure of the internal waves imposed by geometry, internal wave frequency and stratification is governed by a simple though peculiar kind of billiards, namely one which keeps the angle of reflection fixed with respect to the vertical (gravity). By stretching the vertical coordinate this fixed angle can for all monochromatic cases be made 45 degrees,

---

[2]We repeat that only waves in a continuously stratified fluid are addressed here; internal seiches explained in terms of interfacial waves are not considered here. For two layer systems with a stratified deep layer, the deep layer can be regarded as the basin shape; the interface then being the surface boundary of the basin. The scattering (trapping, reflection and transmission) of waves in dependence on the strength of the pycnocline is addressed e.g. in Gerkema (2001).

the stretching being present in the scaled depth τ. The velocity field is described in terms of the stream function $\Psi(x, z)$, with $u = -\partial\Psi/\partial z$ and $w = \partial\Psi/\partial x$. We study monochromatic waves: $\Psi(x, z, t) = Re[\psi(x, z)\exp(-i\omega t)]$. It can be shown that the spatial part of the stream function is governed by the hyperbolic equation: $\partial^2\psi/\partial x^2 - \partial^2\psi/\partial z^2 = 0$. This implies that the general solution for the stream function can be expressed as (Maas and Lam 1995, eq.2.8):

$$\psi = f(x - z) - g(x + z) \tag{4.1}$$

and similarly for the pressure

$$p = f(x - z) + g(x + z). \tag{4.2}$$

These solutions are given in terms of the partial pressures $f(x)$ and $g(x)$, which, in order to make the solutions unique, are prescribed along some specific parts of the surface of the basin only (Maas et al. 1997). For the unforced internal wave problem, the free surface is assumed to be quiescent and the union of the boundary segments at the surface ($z = 0$), the wall ($x = -1$), and the bottom ($z = -\tau h(x)$) is considered to be a streamline: $\psi = 0$. This leads to the requirement $g(x) = f(x)$, and the value of f is conserved along each web of characteristics. For real $f(x)$, this presents a standing wave solution and in this case the surface pressure is $p_a(x) = 2f(x)$, see section 4 of Maas and Lam (1995). However, because the partial pressure is preserved (instantaneously) along characteristics, the same values for f are passed to neighbouring surface intervals when following internal wave rays. This means that we are not free to specify the pressure along the whole boundary, but only within so–called fundamental intervals. The largest of these are called primary fundamental intervals. Prescribing the pressure in fundamental intervals defines the pressure over the whole surface. An example similar to that of Maas and Lam (1995) and Maas et al. (1997) is given in figure 1.20.[3] Note that the choice of $f(x)$ is similar, but slightly different from the example presented in Maas et al. (1997). For this basin (and for $1 < \tau < 2$) the primary fundamental intervals are found at the surface for $x \in [-1, \tau - 2]$ and $x \in [\tau - 1, 1]$. The boundaries of these surface intervals are obtained (see figure 1.18b) by connecting the corners of the basin with the surface along characteristics. For the basin of figure 1.18 this means: $x \in [-1, -0.29]$ and $x \in [0.71, 1]$.

Since ψ is real, the *standing wave* solution of figure 1.20 is oscillating synchronously or *blinking*. As mentioned in Maas and Lam (1995), this solution consists of *free waves*; it is unforced. To obtain a unique solution the pressure is prescribed at the surface within the aforementioned fundamental intervals, but still in an arbitrary manner. It is physically unsatisfactory that one is required to prescribe the pressure strictly on just two intervals. In section 4.4 we will lift this restriction by considering a possibly realistic forcing mechanism that allows a prescription of the pressure also beyond

---

[3]The example depicted in figure 1.20 is shown on an (arbitrary) xz-grid. However, it should be stressed that this solution is *not* a numerical approximation. For each element (x_i, z_j) on the grid, the corresponding (analytical) solution ψ_{ij} is *exact*.

these two intervals, leading to a propagating wave solution, similar to that observed. First, in the next section, we will have a closer look at the experimental results.

4.3 The internal wave attractor experiment revisited

4.3.1 Original analysis

Maas et al. (1997) verified the existence of an internal wave attractor in a laboratory experiment. The experiment was carried out in a uniformly stratified tank, with a sloping sidewall and free surface, see figure 1.18. The platform on which the tank was placed was oscillating vertically with angular frequency 2ω. The response in the fluid takes place by parametric excitation. This is a process where by vertical oscillation the restoring force of gravity is (slightly) modulated. Each fluid particle, seen as an individual oscillator, would then be subject to a buoyancy oscillation similar to a pendulum whose point of suspension is forced to oscillate vertically. The forcing is most effective when the suspension is forced to go down when the pendulum is in either of its extreme upward (leftward or rightward) positions, hence when the forcing has a frequency twice that of the pendulum. In a similar fashion, modulation of gravity at frequency 2ω excites subharmonic waves of frequency ω in the stratified fluid. Mathematically the modulation of gravity appears as an extra sinusoidal temporal perturbation in the restoring term of the harmonic oscillator. This extended oscillator equation is known as the Mathieu equation (Bender and Orszag 1978). See also Maas (2005) for a discussion.

Several frequencies inside and around the regime depicted in figure 1.18 have been explored in the experiment, and these confirmed the existence of the period-1 internal wave attractor in the interval $1 \leq \tau \leq 2$. This has been referred to as the $(m, n) = (1, 1)$–attractor, enumerating the number of reflections of the attractor at the surface (m) and the vertical side wall (n). In the experiment, at the edges of the $(1, 1)$–attractor frequency interval, somewhat higher forcing amplitudes (15 cm) were needed to excite the attractor than the threshold amplitude of 8 cm for central frequencies. Visualization was obtained by monitoring the position of eight layers of fluorescent dye that were stimulated by laser light.

The most prominent result was that in the experiment the predicted presence, shape and location of a $(1, 1)$ internal wave attractor are reproduced, see figure 1.21. Approximately five minutes ($\sim$ 70 wave periods) after the oscillation of the tank was started, localized fluid motion became visible. The attractor first showed up as a smooth *standing-wave pattern* (figure 1.21; top): the region around the attractor was oscillating synchronously or *blinking*. Later, the elevations of the dye layers showed propagating behaviour around the attractor (figure 1.21; bottom), in correspondence with the expected clockwise energy propagation along the attractor. This can be seen from the inwards (outwards) propagation of 'nodal' lines along the two long (short) branches of the attracting rectangle. During this phase the localization of the elevations around the attractor became less clear; the pattern smeared out, and lost

some of its coherency.

These two phases were called the growth and permanent phase respectively (Maas et al. 1997). The standing behaviour in the growth phase was explained qualitatively in terms of waves travelling in both directions along the characteristics. In the permanent phase, the internal waves are assumed to travel in their *final*, focusing direction only, which is the direction associated with energy travelling towards the attractor. This clockwise energy propagation around the attractor is perpendicular to the direction in which the phase propagates (as given by the behaviour of the nodal lines, referred to above). This perpendicular direction of group and phase velocity verifies the property inferred from the dispersion relation satisfied by plane, monochromatic internal waves (e.g. LeBlond and Mysak (1978, sec. 8)) and is due to the fact that frequency relates to wave number direction only, and not to wave number magnitude (Maas 2005).

In the next subsection the experiment will be examined in more detail with new digitized images from the video recording of the experiment. Typical elements of the previous findings can then be analysed in a more quantitative way. Especially, the growth rate of the amplitudes and the standing *versus* propagating nature of elevations are of interest. Moreover, limitations of the present experiment will become clear in more detail, so that previous conclusions drawn from this experiment can be fine-tuned, and future experiments can be improved.

4.3.2   Revisiting the wave-attractor experiment

The experiment as discussed in Maas et al. (1997) (see also figure 1.21) will be given a closer look. The forcing amplitude of the table oscillation was 10 cm and forcing frequency $2\omega = 2.88 \text{ s}^{-1}$. This leads to an internal wave period $T_w = 2\pi/\omega = 4.37$ s. The dimensionless lumped parameter for this experiment is: $\tau = 1.71$, see table 4.1.

The video recording of this experiment is digitized again, and translated to 25 images for each second, with a resolution of 256x224 pixels each. The experiment lasts for over 20 minutes, taking more than 31,000 images. With present computer power, it is not difficult anymore to analyse the evolution of the intensity of all pixels for all images during the experiment. As we will see later, it is more difficult to visualize the results of this kind of analysis. Below, step by step we will provide results of the analysis and details of the procedures that were followed.

Time series of greyscale intensity

As observed from some small fixed stains at the laboratory tank, individual images of the experiment appeared to be slightly shifted. The reason for this is not completely clear, but is probably either small camera movement, or inaccuracy of the digitizing device. We did not have a satisfactory explanation; the images are simply translated to a 'fixed stain' pixel-co-ordinate system. Shifts are typically only a few pixels, and are regarded to be irrelevant for all subsequent analysis.

The next step is to combine colour information of the images, for the combination of the three RGB-fields (Red-Green-Blue) contains more information than any of them independently. Images are translated to standard greyscale images with Matlab (Image Processing Toolbox, function: rgb2gray), with intensity on a scale from 0 to 255.

With the resulting greyscale intensities, time series can be retrieved for any position in the image. Some examples of two nearby pixels are shown in figure 4.1. Horizontal and vertical positions are labelled in pixel units, i_x and i_z respectively. Time is scaled here with $T = 4.36$ s, which is an integer number (109) of sampling periods (0.04 s) that is closest to the internal wave period of $T_w = 4.37$ s. Here time series are depicted for two positions in the image-pixel-frame: $(i_x, i_z) = (060, 115)$ and $(060, 120)$. Figure 4.1c,d shows that the second (lower) pixel resides close to the white band (near intensity 240; the lightest colour, before translating to greyscale, is originally yellow) and the first pixel lies close to the dye-less black band (near intensity 80). The two disruptions in light intensity in intervals $15 < t/T < 30$ and $65 < t/T < 75$ are due to external perturbations and are ignored here. Light intensity grows in time, but, despite the closeness of the two pixels, with different starting times and possibly different growth rates. Quantification of the growth rate will be given later. Eventually, light intensity oversaturates or undersaturates. This inhibits a correct estimate of the amplitude of the pixel intensity variation, see the enlargement in figure 4.1e, which shows this peak truncation. Another problem is that when displacements are large, dye from a second layer above or below may cause a renewed increase in pixel intensity. Superficially this suggests that the wave field develops a second harmonic, but this really bears testimony of the large wave amplitude, see figure 4.1f.

length	$2L$	261	mm
depth	D	261	mm
width	W	96	mm
amplitude	Z	80–150	mm
stratification	N	1.89	s^{-1}
corner point	d	0	–
experiment 4:			
amplitude	Z	100	mm
time scale	T; 109 images	4.36	s
period	T_w	4.37	s
frequency	$\omega = \frac{2\pi}{T_w}$	1.438	s^{-1}
scaled depth	$\tau = \frac{D}{L}\sqrt{\frac{N^2}{\omega^2} - 1}$	1.71	–

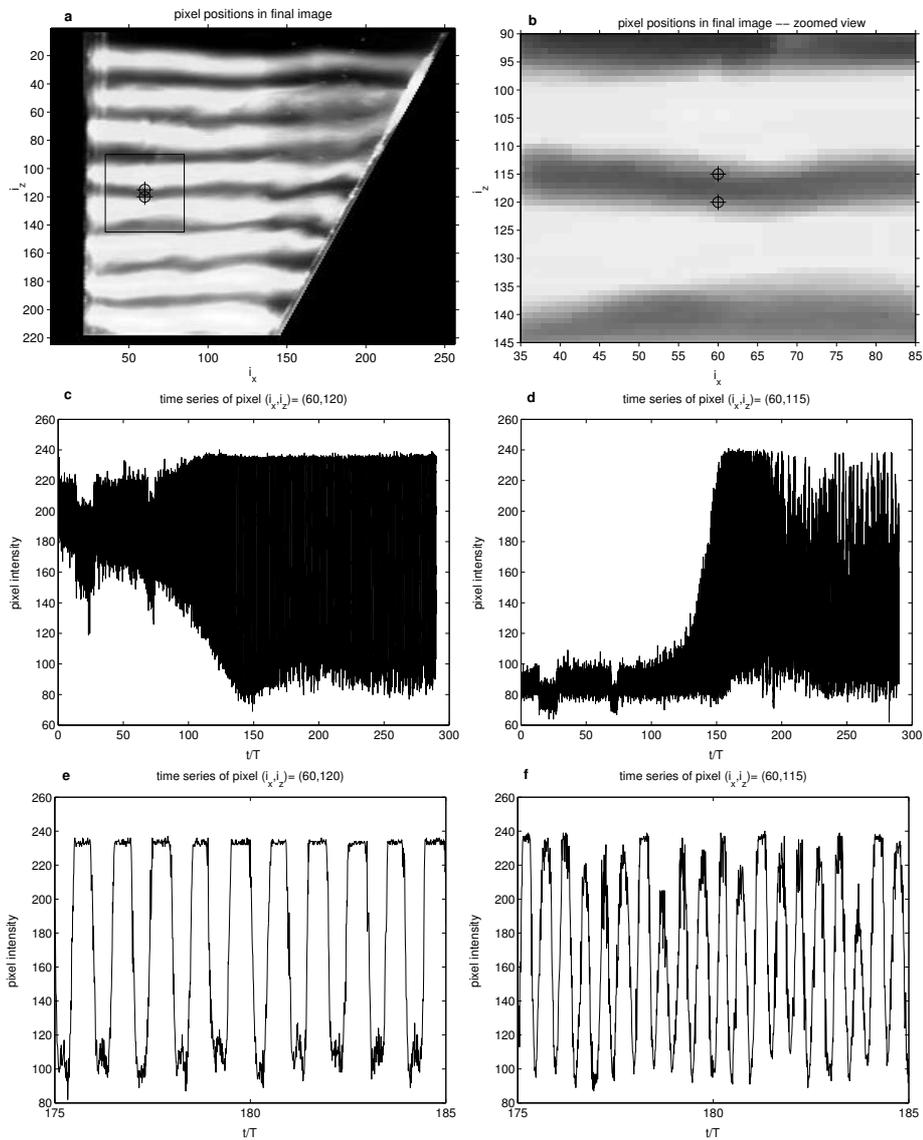**Table 4.1:** Parameters and scales used in Maas et al. (1997).

Figure 4.1: Example time series. Two positions (a, zoomed in b), time series (c,d) and zoomed view of time series (e,f).

Some 'waterfall plots' are shown for one column ($i_x = 60$; left), and for one row ($i_z = 120$; right) in figure 4.2, where pixel locations can be viewed in figure 4.1a,b. For waterfall plots, time is represented on the vertical axis and the vertical or horizontal
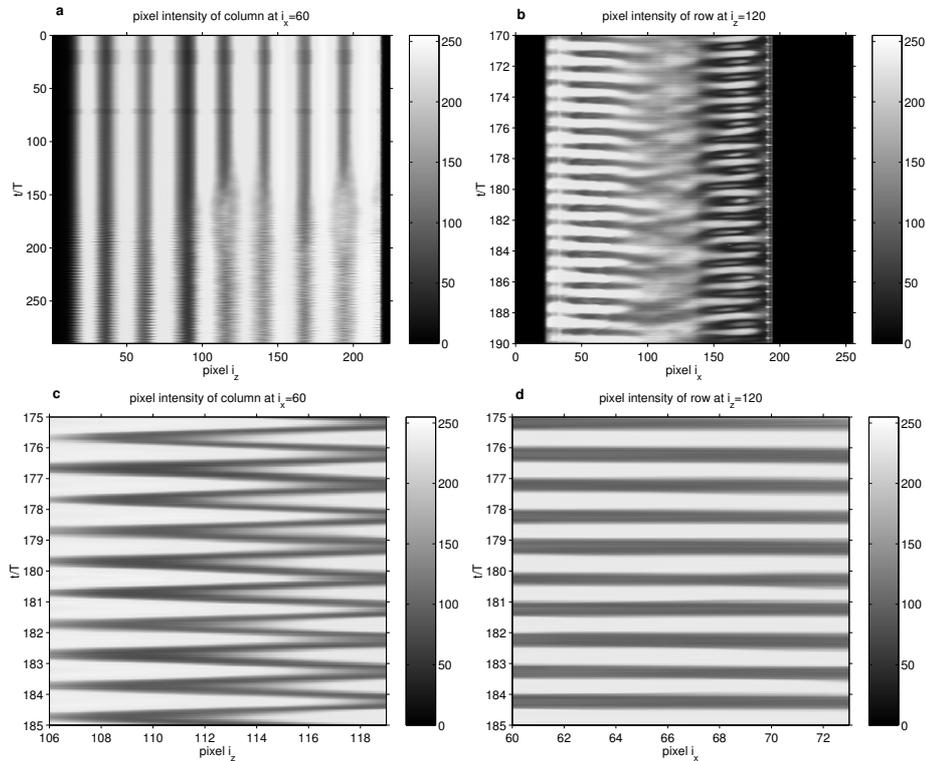
Figure 4.2: Example time series. Waterfall plots (time axis along vertical direction) of pixel intensity at a single line: for a column (left; a,c) and for a row (right; b,d). Figure b shows a selected time interval (t/T =170–190), because there are too many oscillations to be displayed in one single image. Bottom panels (c,d) are zoomed views. Greyscale intensity (0–255) is depicted in the legends.

pixel index is shown on the horizontal axis for the column and row waterfall plot respectively. Both waterfall plots are accompanied with a zoomed image. Figure 4.2a shows the eight dye bands along this vertical line and the perturbations (waves) that grow on them over time. Around $t/T = 150$ two intense wave manifestations are found near $i_z = 110$ and 190. These correspond with the intersections with two branches of the attractor, see figure 1.21. Figure 4.2b shows an intensity change near $i_x = 148$ above which the pixels are over the slope, which apparently reflects laser light differently on average. The sloping boundary is situated near pixel $i_x = 190$. Waves are evident here near $i_x = 60$ and 165, which represent the two intersections with the long branches of the attractor. Figure 4.2c,d represent two zooms, both in time as well as pixel range. The first of these again shows the appearance of the second harmonic near pixel i_z=115 due to the passage of two dye layers per period.

This clearly depends not only on the wave amplitude, but also on the pixel's vicinity to the edge of a dye layer.

Interface elevation versus pixel greyscale intensity

By looking at the time series and waterfall plots of figures 4.1 and 4.2, it is clear that the time evolution of the greyscale pixel intensity does not correspond to the elevation (or displacement) of the dyed lines as visible in the tank.[4] Particularly, when relating pixel intensity to local fluid displacement there is an ambiguity in the displacement direction. When the pixel gets darker, this can mean both an elevation as well as a depression of the neighbouring fluid parcels, depending on whether the pixel is originally in the dark or light layer. Another artifact of the time series of the pixel intensity was already mentioned and occurs when the amplitude of the interface elevation exceeds the thickness of the dyed bands of the fluid. This can be seen most clearly in figure 4.2c (and figure 4.1f). In this zoom of the waterfall plot for one column, it is as if the frequency of the oscillation has doubled around $i_z = 115$, where in reality this is caused by the high intensity bands from above and below that both reaches this vertical position.

Moreover, the waterfall plot of a complete row (figure 4.2; $i_z = 120$) also displays non-uniform light conditions (or excited fluorescence). As mentioned, especially the right half of the image is significantly darker due to a different reflection of the laser sheet over the sloping side wall.

In spite of these problems, the examples of figures 4.1 and 4.2 show that some useful information can still be obtained such as the location of the attractor as well as the exponential growth of the amplitude of the oscillation. In our subsequent analysis, and despite the artifacts mentioned above, we use pixel intensity to measure the (vertical component of the) oscillation of the fluid. In the next subsection we will introduce a method to summarize the periodic motion in the fluid, providing a better overview.

4.3.3   Harmonic analysis

In order to obtain the characteristics of the periodic motion of the fluid, we perform a harmonic analysis to the time series of the greyscale pixel intensity as described above. Harmonic analysis is used to obtain the amplitude and phase of a (sinusoidal) motion having a specific well-defined period. For long time series, motion with small frequency differences can be distinguished. However, harmonic analysis can be very useful also for relatively short time series (chapter 3). For the laboratory experiment, we will explore harmonic analysis output at every pixel position, so that the combined results can also give spatial information.

---

[4]Pixel intensity, determined at a fixed position, gives an (indirect) Eulerian description of fluid motion, while temporal evolution of dye displacement represents a Lagrangian description. See e.g. Batchelor (1967, sec.2.1) for definitions of Eulerian and Lagrangian descriptions of fluid motion.
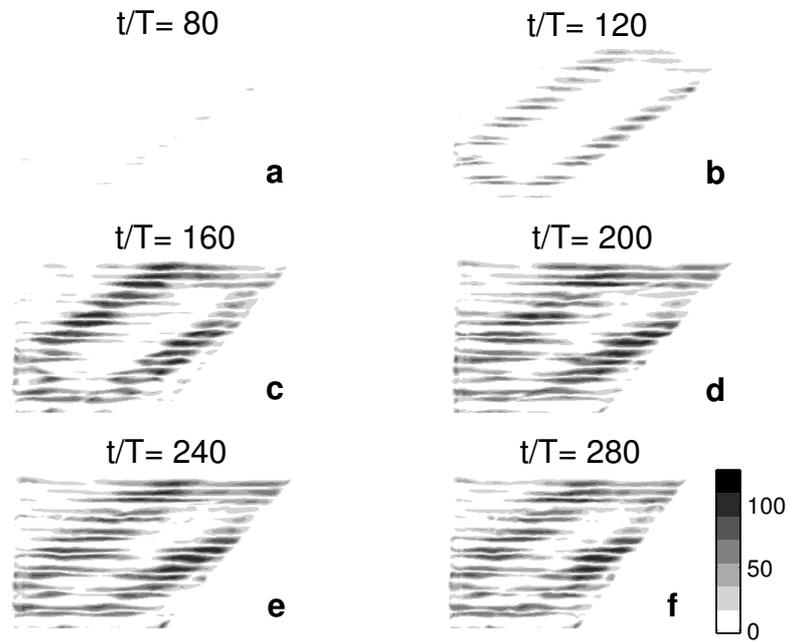
Figure 4.3: See figure C.13 for a full colour version. Evolution of harmonic amplitude of pixel intensity (colour coded, see legend). Scaled time t/T at the middle of time series is given above each image. These times correspond to the following dimensional times: $t =$347, 521, 695, 870, 1044 and 1219 s.

Here, we will perform short-term harmonic analysis over subsequent intervals ('sequences') of approximately one internal wave period ($T_w = 4.37$ s). Thus series of 290 times 109 images will be used. Recall that: $290T \equiv 290 \times 109 \times 0.04$ s $= 290 \times 4.36$ s. In figure 4.3 an overview is given over the total period consisting of 290 sequences. Harmonic analysis for these 290 sequences provides insight into the time evolution of the harmonic amplitude and phase as well as of the average pixel intensity. In all these figures, time is again scaled with approximate internal wave period T of 109 images, equal to 4.36 s. In the harmonic amplitude field, figure 4.3, we see that the rectangular shape of the internal wave attractor, consisting of four branches, becomes visible well before $t/T = 80$ (about 5 minutes). The attractor grows and gets more distinguished from $t/T = 100$ to 130 (7.3 to 9.4 minutes). After that, overall amplitudes (for this particular frequency) equilibrate, and the regions of higher amplitudes smear out somewhat over the image and also penetrate outside the attractor region. In particular, relatively high amplitudes become visible in the
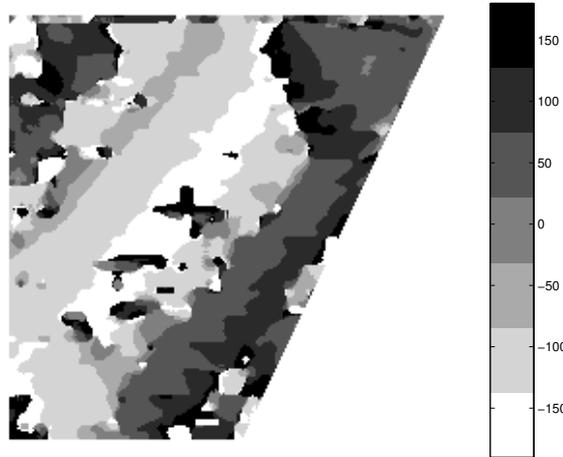
Figure 4.4: See figure B.2 for a full colour version. Example of harmonic phase (in degrees, see legend) of pixel intensity. Same time of image as in figure 4.3c: $t/T =$160. Here phase is corrected by checking for sudden jumps in vertical direction.

upper left corner of the image.

Figure 4.4 presents harmonic phase (see appendix B) at the moment the attractor is most clearly present, at $t/T = 160$ (11.6 minutes). It reveals the propagating character of the wave field around the attractor through the fact that phase lines are aligned with the attractor branches. Later in the experiment, images of mean pixel intensity demonstrate that mixing occurs along the attractor (not shown). The phase progression which this implies —e.g. inward, perpendicular to the attractor's two longest branches— is consistent with a clockwise energy propagation around the attractor. Especially the out-of-phase character of the two pairs of opposite attractor branches can be appreciated.

4.3.4   Composite harmonic results across the attractor

Because the oscillation has turned out to be in phase along the characteristics of the internal wave attractor (figure 4.4), it is possible to combine the information along a number of characteristics crossing the attractor. Doing so, we are able to fill the gaps (see e.g. figure 4.5a) that are caused by the finite width of the dye bands that were used to visualize the vertical elevations in the fluid. A sketch of this approach is given in figure 4.5b. In this sketch 27 (or 19) neighbouring characteristics are approximated by parallel lines of pixels, all crossing the long (or short) branches of the attractor. Maximum and median operations are used to remove the 'gaps' (located at the centre of the dye bands) from the 27 and 19 beams respectively. In order to remove irregularities, for example caused by non-smoothness of the estimated
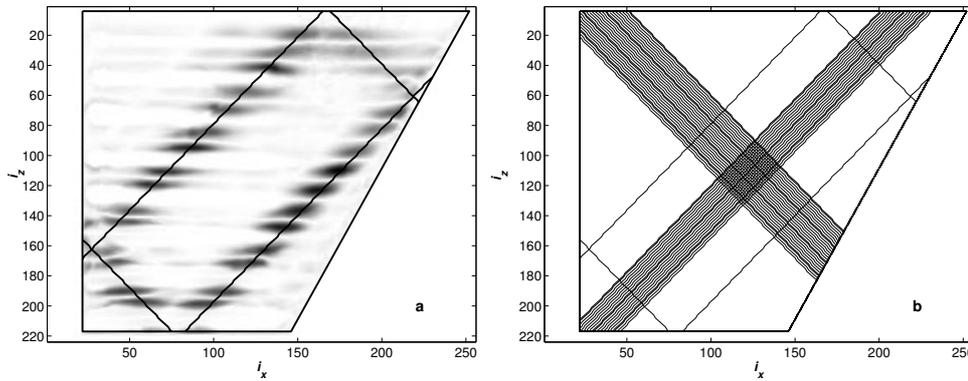
Figure 4.5: Overview of location of the attractor, based on a sample image (a, left) and selected lines used for composite waterfall plot (b, right). In subsequent figures (4.6 to 4.9) the horizontal pixel index i_x of the longest lines (starting at $i_x = 23$ in the upper and lower left corner of the tank) will be used as the co-ordinate (from left to right) along the beam.

(pixel-based) characteristics, the resulting images have been smoothed by taking the average over the central plus surrounding eight pixels. Note that by taking the maximum of the amplitudes (over all 27 or 19 beams), not only does the displacement amplitude around the attractor get a higher value, but also the (background) noise is amplified. The characteristics shown in these figures as black solid lines, were used as reference lines in the subsequent figures. They identify empirically the location of characteristics where the amplitude has its extrema and they approximate the location of the single periodic orbit constituting the attractor.

The slow-time evolution of the amplitude and phase fields is obtained by the composite short-term harmonic analysis and can be seen in figures 4.6 and 4.7 for the maximum of the harmonic amplitude (top panels), and the median of the harmonic phase (bottom panels; phase, modulo 180 degrees, similar as in figure B.1b).

The amplitudes observed across the long branches of the attractor (figure 4.6) are higher than those across the short branches (figure 4.7). The weakest amplitudes are found at the fourth and last attractor segment (counting clockwise from the sloping side wall). It is not clear why this happens. The characteristics are symmetric with respect to the vertical, and hence the projection of the true, oblique motion on the vertical direction is the same for both characteristic directions. Also, since both the bottom, left side wall and surface are all non-focusing it is not clear where the change in amplitude comes from. Clearly, the different stages can be recognized again; a growing attractor appears during $t/T = 100$–160 (growth phase), and finally the high amplitude motion smears out ($t/T > 170$, permanent phase).

The clear transition from the initial standing to final propagating wave behaviour, observed in Maas et al. (1997) in terms of the motion of a nodal line, is here seen to take place gradually. Figures 4.6 and 4.7 (bottom panels) show that in the initial
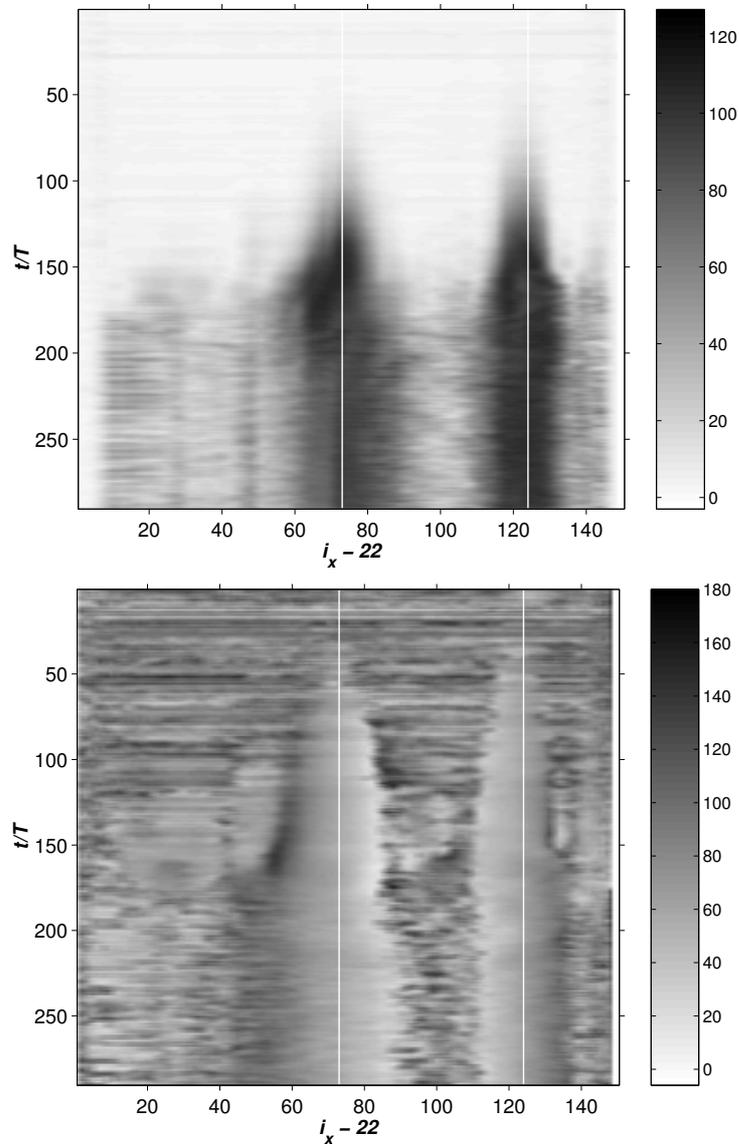
Figure 4.6: See figure C.14 for a full colour version. Composite waterfall plot of maximum of harmonic amplitude (top) and median of harmonic phase (bottom) along 27 characteristics crossing the long branches of the attractor, as depicted in figure 4.5. Phase, modulo 180 degrees, is similarly defined as in the appendix, figure B.1b. The theoretically predicted attractor crossings are depicted with vertical white lines at horizontal index numbers 73 and 124. Note that 22 pixels should be added to get the horizontal indices (95 resp. 146) of the attractor crossings of the longest characteristic, starting in the upper left corner in figure 4.5.
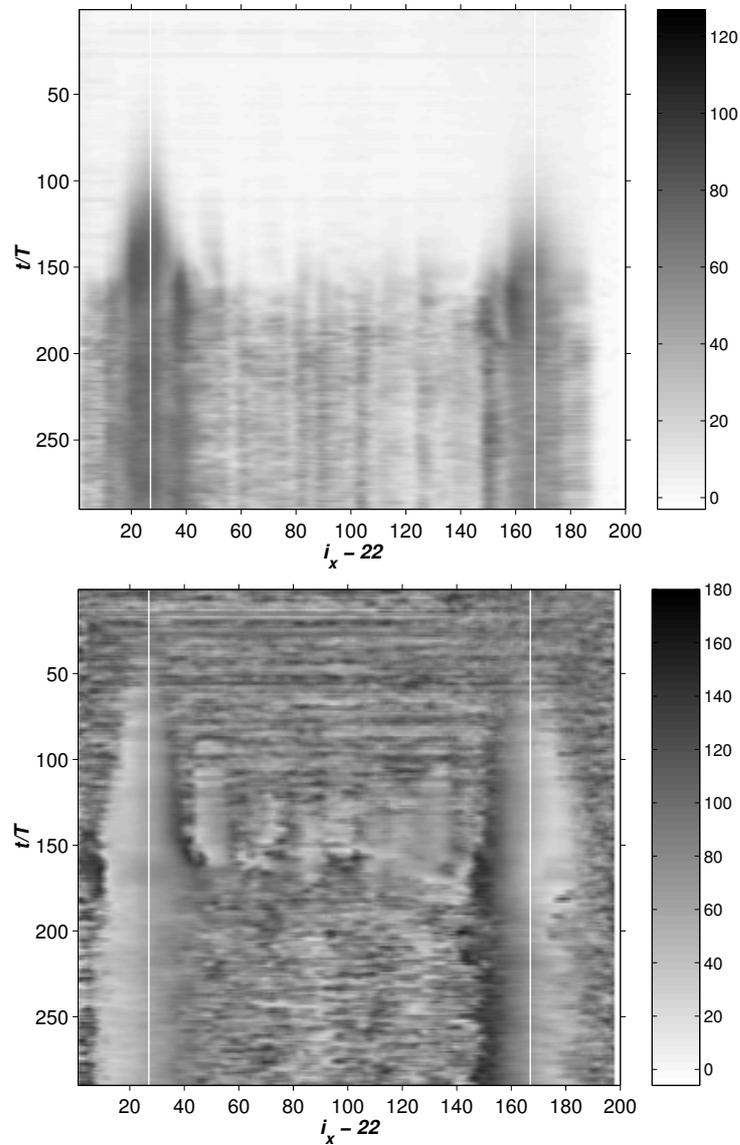
Figure 4.7: See figure C.15 for a full colour version. As figure 4.6 but for 19 characteristics crossing the short branches of the attractor (see figure 4.5). The original estimated attractor crossings are depicted with vertical white lines at horizontal index numbers 27 and 167. Note that 22 pixels should be added to get the horizontal indices (49 resp. 189) of the attractor crossings of the longest characteristic, starting in the lower left corner in figure 4.5.
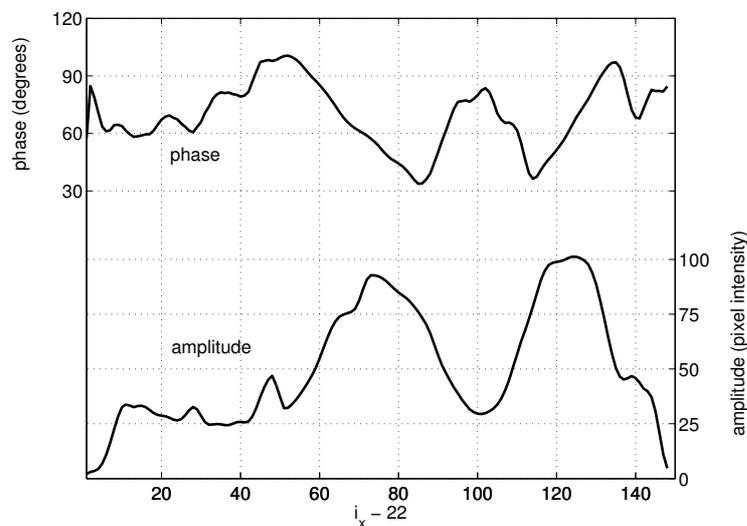
Figure 4.8: Mean phase and amplitude distributions across the long sides of the attractor for last 50 sequences ($t/T = 240$–290) of figure 4.6.

stages of the experiment the phase (modulo $180°$) is quite uniform around the attractor (characterized by the single green colour). Then the high-amplitude bands around the attractor beams amplify, and subsequently broaden until their width stays constant for $t/T > 180$. During the same transition period the phase develops a persistent phase gradient across the two branches of the attractor. This can be seen in figure 4.8, in pixel range $55 < i_x - 22 < 83$ and $115 < i_x - 22 < 135$. These gradients are consistent with the propagating phase observed in terms of the motion of a nodal line in Maas et al. (1997). This is indicative of the previously inferred clockwise energy propagation around the attractor. Surprisingly, the net observed phase variation (nearly 60 degrees, see figure 4.8) amounts to just part of the expected cross beam variation of 180 degrees valid for a stationary internal wave beam affected by linear dispersion and diffusion (Lighthill 1978). This difference is presumably limited by the range over which the amplitude stands out over the noisy background.

4.3.5 Second harmonic

Similar graphs as in figures 4.6 and 4.7 can be created for the second harmonic of the internal wave frequency. In figure 4.9, amplitude (top) and phase (bottom) are given as the maximum and median values of 27 (left) or 19 (right) neighbouring beams crossing the attractor, all for frequency 2ω. It is clear from figure 4.9 that for this frequency the amplitudes start growing around the attractor locations a little
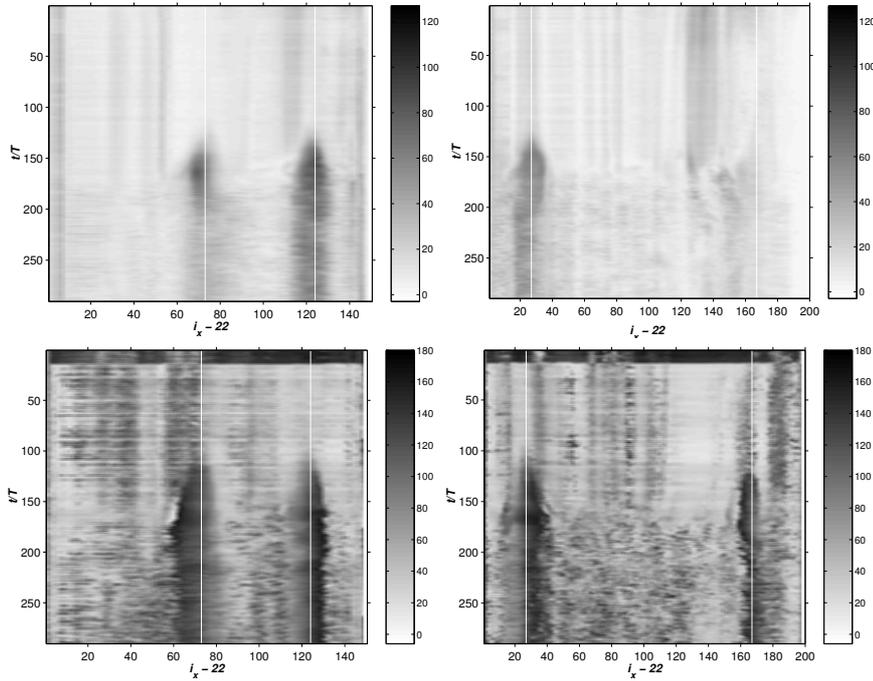
Figure 4.9: See figure C.16 for a full colour version. As figures 4.6 and 4.7, but for first harmonic frequency 2ω. Amplitude (top) and phase (bottom) are given for beams crossing the long branches of the attractor (left), and crossing the short branches of the attractor (right).

later (around $t/T = 135$; 9.8 minutes) than for the principal frequency. After having reached a maximum value around $t/T = 155$ (11.3 minutes), the amplitudes decrease again. Amplitudes for 2ω are always lower than for ω; phases show a larger gradient in the across-attractor direction.

This second harmonic can occur through a number of causes which we list here. Internal waves with frequency 2ω might first be directly forced, as a secondary instability of the Mathieu equation (Bender and Orszag 1978). Second, they may be generated due to nonlinear advection of overlapping internal wave beams (Peacock and Tabaei 2005; Gostiaux et al. 2006). However, in this experiment they are not expected to propagate away as free waves because they are above the buoyancy frequency ($2\omega > N$). Hence, when these second harmonics do show up, this could imply that they are forced locally. Their trapping, along the attractor that corresponds to frequency ω, suggests this to be a continuous process, occurring all along the attractor. Third, as shown in figure 4.2, double-frequency motion might also be simulated by artifacts. As we have seen, this is merely a problem of the tracer used in the experiment. In this case, the double-frequency amplitude would show up when the single frequency motion is saturated; the vertical component of fluid elevations
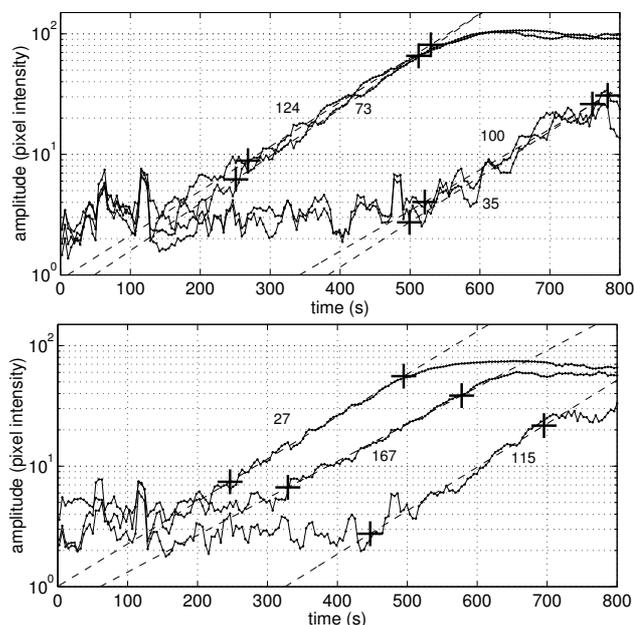
Figure 4.10: Analysis of exponential growth for signals shown in figures 4.6 and 4.7, top and bottom panels respectively. Numbers indicate four (left) and three (right) indices ($i_x - 22$) (including the vertical lines in figures 4.6 and 4.7). For all cases, the exponential factor τ_g is about 122 s, with pixel intensity growing as: $\exp((t - t_0)/\tau_g)$. This growth only occurs at a given time interval, and the growth rate is estimated between the plus (+) symbols above.

then equals or exceeds the width of the dye bands. While this certainly seems to be the case for certain pixel ranges, for instance pixels $112 < i_x < 117$ in figure 4.2, this does not seem to explain why the second harmonic is strong at every pixel along the attractor. Also, the expected associated decrease in the single-frequency amplitude is not clearly visible. Finally, the presence of second (and other) harmonics may reflect the nonlinear nature of the cross-beam structure that propagates in the cross-beam direction during each wave period (see e.g. figure 4.1e).

4.3.6 Exponential growth

In figure 4.10 the inverse exponential growth rate τ_g is estimated for some vertical cross sections of figures 4.6 and 4.7. This is obtained by modelling the evolution of the pixel intensity during a defined time interval as $e^{(t-t_0)/\tau_g}$, for some starting time t_0. For all (seven) cross sections examined, this inverse growth rate is estimated as 122 ± 5 s. Outside the attractor the pixel intensity starts to increase later (larger t_0) and the intensity saturates at a lower level (owing to a shorter growth duration), but it increases at exactly the same rate as within the attractor neighbourhood.

4.4   Travelling wave solution for sloshing surface forcing

4.4.1   Goal

In the previous section an extended, but still rather quantitative description is presented for the internal wave attractor experiment, first addressed in Maas et al. (1997). It became clear that the asymptotic state reached in the experiment is that of a propagating wave. It thus seems natural to search for a theoretical asymptotic description of the stream function field that captures this propagating feature which will be presented here.

Let us first list discrepancies between the present theoretical solutions (e.g. figure 1.20) and the experimental results which obstruct a direct, one-to-one, comparison:

i. The proposed solution is only allowed to have a 'standing-wave appearance'; the stream function field in figure 1.20 is supposed to be blinking, i.e. has a binary ($0°$ or $180°$) phase.

ii. It is difficult to associate the surface boundary condition for $f(x)$ that is needed to provide a unique solution and that is related to the surface pressure (Maas and Lam 1995, eq.(4.1)), to a realistic forcing, see for instance the upper frame of figure 1.20.

iii. It is hard to directly relate the stream function field $\psi(x,z)$ (or $\Psi(x,z,t)$ for that matter) to the observed (vertical) fluid displacement in the experiment presented in the previous section.

All three elements will be improved below. It could be objected that in the presence of wave attractors one may not expect the solution to be of a standing nature. The argument follows that employed in inferring the character of internal waves in a wedge. As Wunsch (1969) states, standing waves for a subcritical wedge (whose slope is less than that of the characteristics) are not likely to occur, for internal wave energy will not reflect back from the corner; all energy is transported in one direction, i.e. into the wedge, which acts as a point-attractor. There, these waves will amplify till the point of wave breaking and will locally mix fluid. Similar reasoning can be followed for most closed basins with supercritical slopes giving rise to wave attractors: all energy is supposedly transported just towards the attractor, without being reflected back from it. In Maas and Lam (1995) it is therefore suggested to employ propagating wave solutions. This will be performed in the following.

4.4.2   Travelling wave solution by allowing for complex $f(x), g(x)$: externally forced flow

Can we construct propagating solutions? Within the framework of free solutions, this question can be answered affirmatively by simply choosing the partial pressure

as a complex quantity. Taken literally, this solution is physically not very meaningful, as it implies that waves are generated at the wave attractor, propagate away from it against the focusing sense (anticlockwise in figure 1.18a), then pass through the bulk of the fluid and finally converge onto the attractor again, now approaching it in the focusing (clockwise) sense. But, can we use our knowledge on the existence of fundamental intervals and force waves such that they propagate away from these intervals only? This does indeed seem to be possible by supposing that some externally applied surface pressure field $p_a(x)$ is given there and by subsequently decomposing this into its Fourier components. Then in the fundamental intervals we decompose each such Fourier component further into complex 'rightward' and 'leftward' propagating components using the relation:

$$\cos(ax) = \frac{1}{2}e^{+iax} + \frac{1}{2}e^{-iax} \equiv f_R + f_L,\tag{4.3}$$

for arbitrary a, and similarly for $\sin(ax)$. The designation leftward and rightward for f_L and f_R refers to the horizontal direction into which phase and energy propagate when multiplying by $e^{-i\omega t}$ (or e^{-it} in non-dimensional form). It implies that, in contrast to the standing wave case, each web is no longer specified by a single invariant f. Instead, the quantities f_L and f_R are now invariant on two *semi-infinite* webs only (obtained by following characteristics leftwards or rightwards respectively from any starting point in the fundamental interval) and should be interpreted as the (complex) f and $-g$ in the original derivation, (4.1). As a consequence, within the fundamental intervals, the stream function ($\psi = f - g$) and its along boundary gradient ($w = \partial\psi/\partial x$) no longer vanish. This betrays that at that part of the boundary there is a periodic motion normal to the boundary which is in phase with the applied pressure ($p_a = f + g$) and hence represents a transfer of energy across the boundary.

In order to compute the stream function in any interior point from the given data at the boundary, some bookkeeping is needed for tracing back any characteristic to the fundamental interval where it originated, as well as the direction from which the fundamental interval is reached, as this clarifies to which of the two semi-infinite webs it belongs. This can easily be seen with the help of figure 4.11, where the original leftward (rightward) characteristics are represented by dotted (solid) lines. The only exception occurs when a characteristic is exactly part of the attractor, which remains undefined; both for the stream function, as well as for $f(x)$ and $g(x)$ at the surface. After this bookkeeping, for any point (x, z) the complex valued stream function $\psi(x, z)$ can be assigned by (4.1). The stream function at time t is then found with:

$$\Psi(x, z, t) = \text{Re}(\psi(x, z)e^{-i\omega t})\tag{4.4}$$

An example following this approach is given in figure 4.12. At the surface, the same boundary condition $p_a(x)$ is used as in figure 1.20. Here the stream function is given for six time steps; $t/T_w = n/12$, for $n = 1, .., 6$, showing half an internal wave period. It can be seen in this figure that outside the (primary) fundamental intervals the
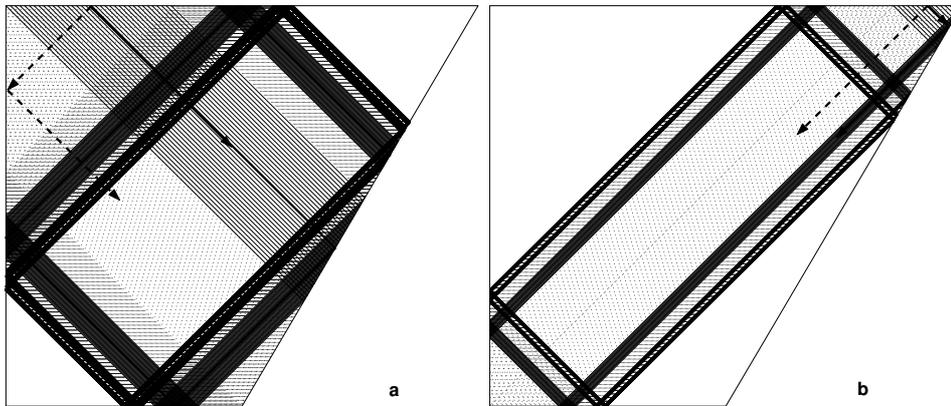
Figure 4.11: Leftward (dotted) and rightward (solid) characteristics, as originating from both fundamental intervals computed for $\tau = 1.71$. The fundamental intervals at the surface are $-1 \leq x \leq -0.29$ (a, left) and $0.71 \leq x \leq 1$ (b, right), see figure 1.18b. All characteristics emanating from the fundamental interval downward and to the right (along solid arrows), appear as a black band after one focusing reflection. The lighter, dashed band of characteristics are build up of dotted lines, travelling downward and leftward (along dashed arrows) from the fundamental intervals.

stream function remains zero at the surface as well as for all other rigid boundaries (uniformly dark grey colour); only reflection is taking place here. At the fundamental intervals however, the stream function is no longer zero at all times. This illustrates that the vertical velocity ψ_x is nonvanishing in these intervals which is in phase with the pressure perturbations so that work is done upon the fluid in these isolated intervals, similar to the action of two pistons.

In this 'movie', we can actually see internal wave energy transferring from the fundamental intervals towards the attractor. The direction of this transfer can be verified in figure 4.12: at the surface, phase moves 'out of' the fluid, which means that energy is entering 'into' the fluid.

4.4.3 Boundary forcing not restricted to two fundamental intervals

In the previous subsection the forcing of the travelling wave solution took place only at the (primary) fundamental intervals. This could be envisaged by two (flexible) pistons at the surface, which are exactly as wide as the fundamental intervals, and which are fully isolated from the remaining surface of the fluid. In natural systems the forcing is, of course, not restricted to such intervals. We therefore would like to prescribe e.g. a surface pressure over the entire surface domain; $x \in [-1, 1]$. Think of this as representing an infinitesimal-amplitude barotropic seiche, again generated by the modulation of gravity; nonresonant Faraday excitation (Faraday 1831; Drazin and Reid 1981).
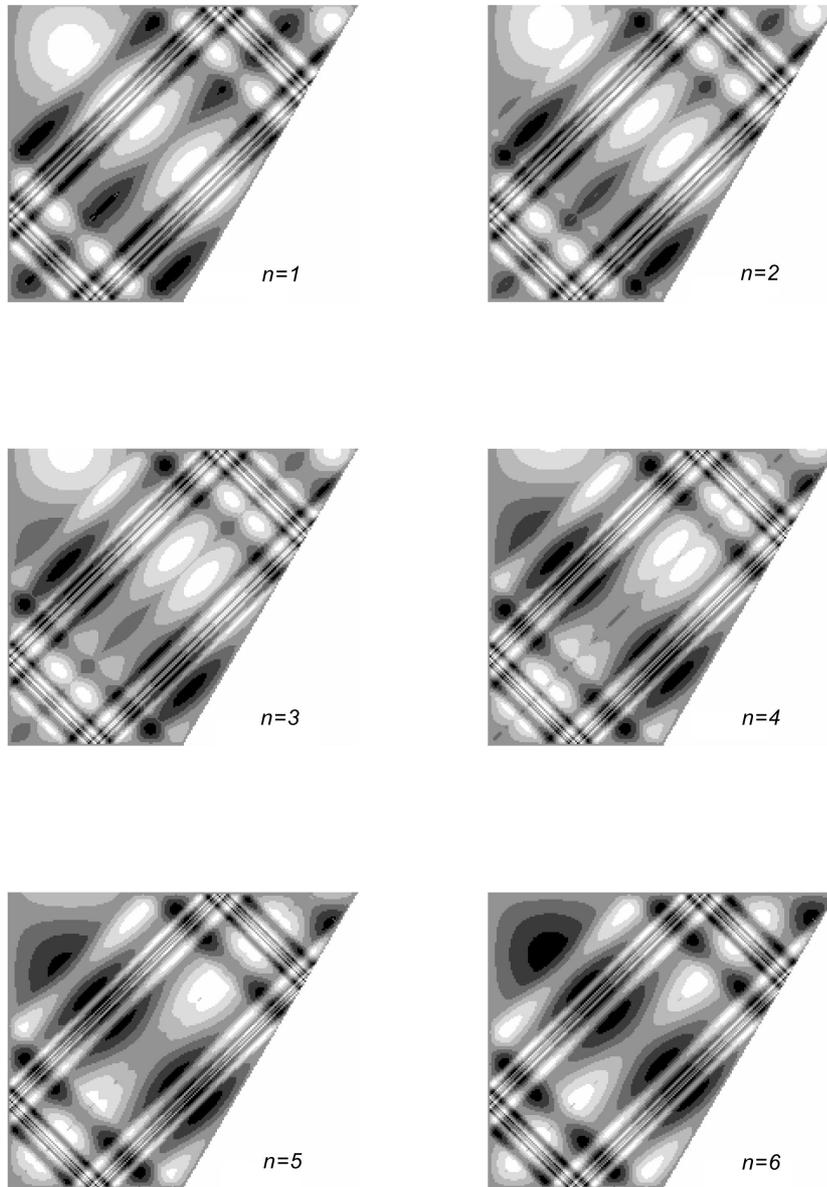
Figure 4.12: Example of travelling wave solution for $\tau = 1.71$. Shown are stream function fields at times $t/T_w = n/12$, for $n = 1, .., 6$. The same surface boundary pressure $p_a(x) = f(x) + g(x)$ is used as in figure 1.20 but is now understood as being composed of complex partial pressures $g(x) = f^*(x)$, where the asterisk denotes the complex conjugate. Also the same greyscale legend can be applied to these images (now for Ψ instead of ψ).

As explained in Maas and Lam (1995), this method is supposed to raise inconsistencies. For the partial pressure (values of f, g) that is passed along the characteristics, when prescribed over the complete surface, would generally define f, g multiple times along any characteristic (after two or more surface reflections). However, since the solution ψ is a (linear) solution to a linear problem this leaves open the possibility to construct a solution ψ by superposition of a number of partial solutions ψ_n:

$$\psi = \sum_{n=1}^{N} (\psi_n + \psi_{-n}). \tag{4.5}$$

Here, each successively ('reflected') fundamental interval is regarded as supplying an additional component ψ_n to the total solution. If we now want to impose the surface boundary condition over the complete surface, one more physical assumption needs to be made: we assume that anywhere at the surface, work is done only by the prescribed boundary value (surface pressure), not by the pressure variations induced at that location by forcing elsewhere on the boundary. Following the characteristics, the (complex) partial pressure that is thus set on each characteristic will simply be passed on upon successive boundary (surface) reflections. In other words: for each contribution ψ_n, the external boundary condition is applied once, and reflects from there on.

Physically, the above means that at the surface the boundary condition is imposed, while the surface's reflective nature is unaffected! Although this may apply only for small associated perturbations to the fluid, in general this is not an uncommon situation. This also happens when (resonantly) forcing a string that is fixed at one end and periodically shaking the other end (with infinitesimal amplitude). At this forced end of the string, energy both enters the system and is reflected there, enabling the build up of a standing wave.

In fact, due to the linear nature of ψ_n itself, also different (arbitrary) combinations of contributions of surface pressure $p_a = f + g$, as provided by (4.2), can be summed this way. Starting from any point (x, z) in the interior of the domain, we can therefore define the components of (4.5) as follows: ψ_1 is defined by the forcing on the first two surface reflections of the two upward characteristics that cross at (x, z); ψ_{-1} is similarly defined by the downward pair of characteristics crossing at (x, z) that reach the surface upon bottom and side-wall reflections. $\psi_{\pm n}$ for $n = 2, .., N$ are defined similarly, by following these characteristics further, until their next n surface reflections. The method converges (and the solution is bounded). When n is large, $\psi_{\pm n}$ does not contribute any more to ψ. For when the attractor is nearly reached, values of the prescribed surface pressure $f + g$ (assumed to be smooth) are nearly equal. So their difference as defined by (4.1) is zero. Only at the locations of the characteristics that describe the attractor, the solution and the boundary condition are undefined.

With the alternative algorithm, described above, also the previously constructed standing wave solution of figure 1.20 can be obtained. This solution, for which $g(x) = f(x)$, is found if $f(x)$ is now only being assigned, and taken real again, at the

primary intervals and is taken zero elsewhere. That is: $f(x) = 0$, at $\tau - 2 < x < \tau - 1$. See figure 1.18b for definitions of these intervals, and figure 1.20. Previously, by employing the invariance of $f(x)$ per web we constructed the partial pressure $f(x)$ over the whole surface (excluding the reflection point of the attractor) by iteration from the two fundamental intervals. The stream function was then read off at any point as the difference of the two invariants that were defined by their values at the first two upward surface intersections. Here, instead, from each field point one is supposed to iterate backwards until one arrives in a fundamental interval in order to determine the partial pressure.

This approach more naturally allows the partial pressure to be prescribed differently in different fundamental intervals, allowing for the description of propagating wave solutions, see Swart et al. (2006). In this process, now not only each of the four directions from which waves can reach the point of interest should be considered. But also at each surface reflection one should determine whether the leftward or rightward part f_L or f_R should be chosen. Doing so, we get a complete travelling wave solution for Ψ for an arbitrarily defined surface forcing! An example of this is given in figure 4.13. In this example, the applied surface pressure is chosen to be associated with: $p_a = \sin(x\pi/2)$; this is the lowest mode of a (surface) seiche (for a rectangular basin). We will refer to this choice as the 'surface sloshing' forcing. This could be thought of as the first Fourier component of a physically realistic surface sloshing mode. The only additional (physical) restriction for the surface boundary condition is that the derivative $\partial p_a/\partial x$ evaluated on $x = \pm 1$ is zero, because the corners are stagnation points, where $u(\pm 1) = 0$ at $z = 0$. This condition also prevents internal shear layers to appear, see figure 20a of Maas and Lam (1995) for an example of this effect.

4.4.4   Approximate fields for velocity and displacement

From the travelling wave solution (figure 4.13) we will now calculate the associated displacement in the fluid, in order to make a comparison with the displacement of the horizontal dye bands in the laboratory experiment, as described in section 4.3. This is done in a pragmatic way. From the stream function field Ψ, the fields for the velocity components u and w are derived, see vector fields in figure 4.13. In this example, the gradient of Ψ is computed numerically, although it should not be hard to derive this from the partial pressures f, g and their derivatives f', g'. After that, the displacement is approximated by a simple linear Taylor approximation: $x = x_0 + u(x_0)\Delta t$ and $z = z_0 + w(z_0)\Delta t$, for an arbitrary time increment Δt, and with original position (x_0, z_0). See figure 4.14 for an example, where the position of eight originally horizontal bands in the fluid are visualized (suppressing locations outside the domain in this linear approximation). This figure reveals that the waves get focused near the attractor. Large displacements arise in a band that is predominantly representing a projection of the primary fundamental intervals (figure 4.11).

Figure 4.15 shows there is good overall agreement between the laboratory experiment and the 'simulation'. The location of the attractor is clearly visualized and
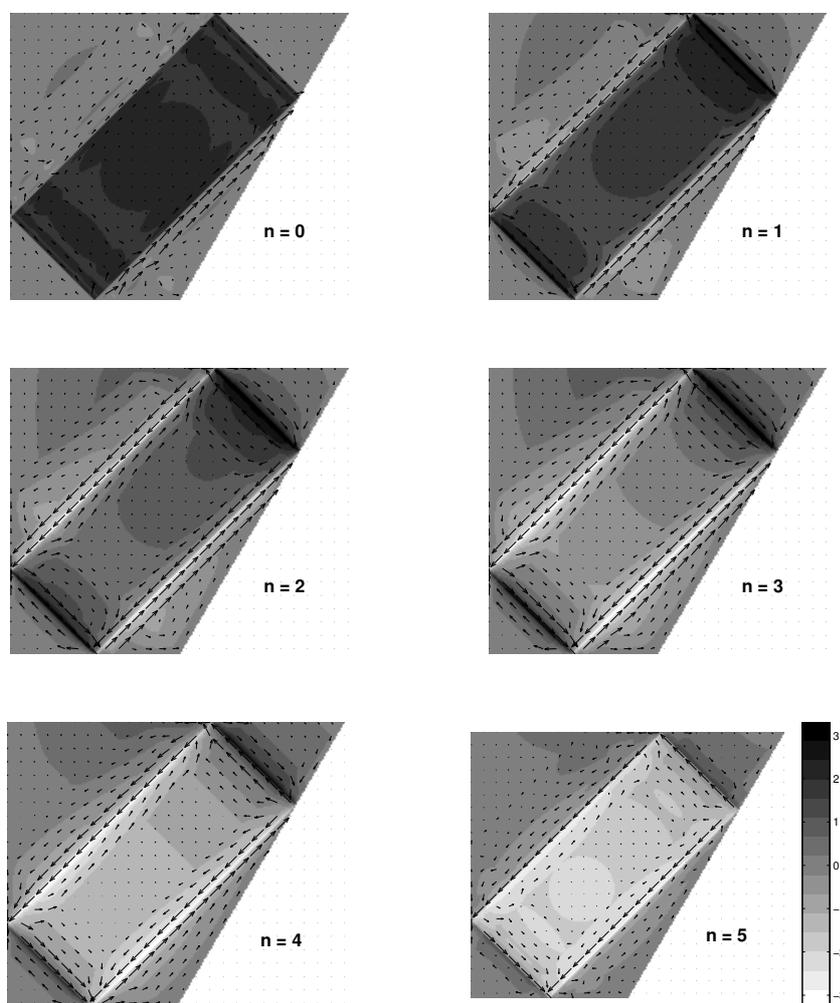
Figure 4.13: See figure C.17 for a full colour version. Example of iteratively defined travelling wave solution $\Psi(x, z, t)$ for 'surface sloshing' boundary condition; $p_a(x) = \sin(x\pi/2)$. Times shown are for $n = 0, .., 5$, with $t/T_w = n/12$. Stream function Ψ is colour-coded, as shown in the legend. Arrows represent the velocities as derived from numerically computed stream function gradients based on the algorithmically computed stream function field.

Figure 4.14: Example of iteratively defined travelling wave solution $\Psi(x, z, t)$ for 'surface sloshing' boundary condition; $p_a(x) = \sin(x\pi/2)$. Here the associated displacement is shown by artificial 'dye' bands for times $n = 0, .., 5$, with $t/T_w = n/12$.
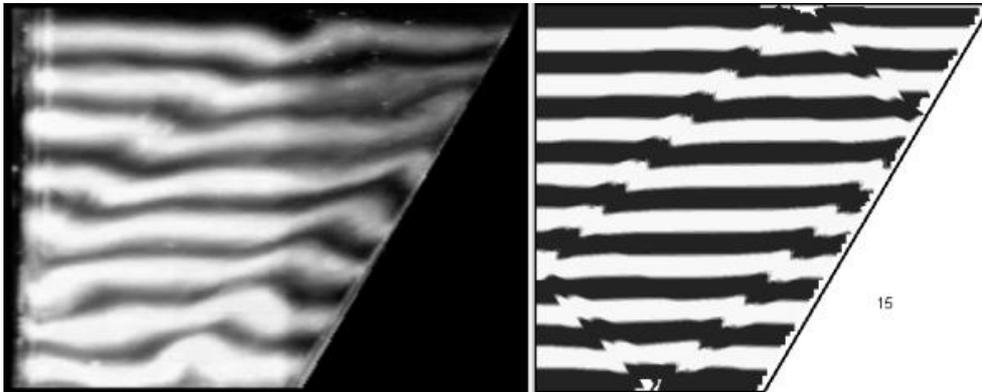
Figure 4.15: Comparison of observed (left) and computed dye displacement field (right). The computed image on the right is for time: $n = 15$, but now with $t/T_w = n/24$ (the opposite phase of the virtual image between $n = 1$ and $n = 2$ in figure 4.14).

its width is, geometrically speaking, to first order defined by the first surface reflection of the fundamental interval. This is visualized by the largest black band in figure 4.11. Also some finescale structure, with a scale defined by the next surface reflection of the fundamental interval, is visible in both cases. But in the experiment finer scales are suppressed, probably by viscosity.

Some other choices for the boundary condition are explored, especially the case $p_a = \cos(\pi x)$ is of interest, where the outer regions are in–phase at the surface, and contrary to the previous example. However, the first example has more resemblance with the laboratory experiment.

4.5 Summary and discussion

4.5.1 Brief summary of results

In section 4.3 the laboratory experiment as described in Maas et al. (1997) was reanalysed. More details in space and time about the amplitude and phase of the internal oscillations were revealed and quantified. Several limitations of the experimental setup were explored and mostly understood. The appearance and temporal and spatial development of the internal wave attractor were clearly visualized this way. The overall inverse exponential growth rate was found to be 122 seconds, starting later outside the attractor neighbourhood.

In section 4.4 the theoretical description of a monochromatic internal wave field of a stratified, confined, essentially two-dimensional free-surface fluid (Maas and Lam 1995; Maas et al. 1997) was extended to include travelling wave solutions. By

an iterative approach, also more generic (and more realistic) boundary conditions can be applied. Finally, visualization of displacement fields, as obtained by Taylor approximations of velocities obtained from numerical estimates of the gradients of the analytically predicted stream function field, made a better comparison to the actual experimental displacements possible. The closer resemblance between the two was based on assuming that the theoretical field was forced by a first order surface seiche.

4.5.2 Discussion

The reanalysis of the earlier observations reveal a number of new interesting facets regarding the formation of an internal wave attractor. Figure 4.10 showed that the wave field exhibits phenomena known from related studies on parametrically excited waves (Miles and Henderson 1990; Benielli and Sommeria 1998; Hill 2002): (1) slow growth above the noise level, (2) a rapid exponential growth phase, (3) a slight overshoot, and (4) saturation into a quasi-steady asymptotic state. These features are usually properties of the time-dependent amplitude field of a spatially fixed, standing wave structure. As a consequence, in such circumstances each field point exhibits these phenomena simultaneously (no spatial delay). The spatial structure of the field acts as a local weighting factor and determines the local saturation level. The amplitude equation is often a nonlinear Landau type of equation, whose steady state is obtained when nonlinearity together with dissipative and dispersive terms balance the parametric excitation. It can be used to infer the strength of interior and boundary damping processes.

However, the novel property encountered in the wave attractor is that there is no spatial eigenmode structure and that, indeed, the wave is not standing at all. Compared with the growing standing mode this distinctive property is visible in that different spatial positions exhibit (1) equal growth rates, (2) different delays, (3) different durations of growth periods. This is in consonance with expectations based on linear partial differential equations (PDEs), such as proposed to describe internal wave beams (Dauxois and Young 1999; Tabaei and Akylas 2003; Voisin 2003). These descriptions typically incorporate diffusive processes, balancing dispersive and dissipative effects, that may explain the observed delayed growth and reduced growth duration outside the direct vicinity of the wave attractor.[5] Such a PDE model is by itself not able to explain the appearance of a stationary state. This also requires a persistent internal wave source, e.g. an oscillating cylinder, as in experiments by Makarov et al. (1990). In the wave attractor case, geometric focusing acts as such a 'source' term. Its amplification balances the diffusive spreading that occurs along most of the attractor of the internal wave field. This was cleverly built into models

---

[5]Note that nonlinearity has not been discarded from these models, but the slow-time amplitude equation turns out to be linear, even though the nonlinear generation of the second harmonic and mean fields are necessary intermediaries. It is significant that the internal wave observations presented here also exhibit second harmonic (see figure 4.9) and mean (not shown) fields that are present around the location where the attractor of the primary harmonic is situated.

by Rieutord et al. (2002) and Ogilvie (2005). In the present experiment, however, it seems that wave diffusion is not the relevant process, but that damping is instead dominated by internal wave scattering upon reflection from the free surface. This suggestion is motivated by observing that the width and amplitude of the wave beam are nearly constant around the attractor, except suddenly on the final, fourth branch, where the amplitude drops significantly and where wave growth appears later in time. Compare e.g. the delayed exponential growth on this branch, evidenced in figure 4.10b by the curve labelled 167, to that on the other three branches (labels 124, 27 and 73, respectively).

As stated above, not all problems with the experimental setup could be overcome. Light conditions and instabilities of camera position or digitizing device appeared to be not optimal. The tracer that was used, namely fluorescine dye bands, inhibits a direct translation from colour intensity to actual (vertical) displacement of fluid particles. However, the analysis as presented in section 4.3 showed that harmonic analysis provided many valuable details of the experiment, even though harmonic fields did not show the passage of nodal lines, nor the transition from standing wave to travelling wave, as clearly as in Maas et al. (1997), see also bottom panels of figure 1.21. It seems that nonlinear processes (a non-sinusoidal response), or non-linear properties of the tracer that was used, may have enhanced these features in the original images over those displayed by the harmonic field. These processes are probably also the reason why the amplitude and phase fields of the second harmonic were most significant in the vicinity of the wave attractor whose location was set by the primary harmonic.

Nevertheless, the above results are an important step forward for a better understanding of the internal wave field in a confined, stratified and free-surface fluid. The limits for analysing the present experiment are reached, and lessons are learned for setting up new experiments. Moreover, the theoretical extensions provide better possibilities for comparison with present and future observations in the laboratory, in (pit) lakes and in the ocean like e.g. those discussed by Fricker and Nepf (2000), Thorpe (2003) and Boehrer and Stevens (2005).

References

Andersen, O. B., P. L. Woodworth, and R. A. Flather (1995). Intercomparison of recent ocean tide models. *Journal of Geophysical Research 100*, 25261–25282.

Apel, J. R. (1987). *Principles of ocean physics*, Volume 38 of *International Geophysics series*. London: Academic Press.

Baines, P. G. (1969). *Waves and stability in rotating or stratified fluids.* Ph. D. thesis, Cambridge University, Cambridge, UK.

Baines, P. G. (1971a). The reflexion of internal/inertial waves from bumpy surfaces. *Journal of Fluid Mechanics 46*, 273–291.

Baines, P. G. (1971b). The reflexion of internal/inertial waves from bumpy surfaces. Part 2. Split reflexion and diffraction. *Journal of Fluid Mechanics 49*, 113–131.

Baines, P. G. (1973). The generation of internal tides by flat-bump topography. *Deep-Sea Research 20*, 179–205.

Baines, P. G. (1974). The generation of internal tides over steep continental slopes. *Philosophical Transactions of the Royal Society of London A277*, 27–58.

Baines, P. G. (1982). On internal tide generation models. *Deep-Sea Research 29*, 307–388.

Batchelor, G. K. (1967). *An introduction to fluid dynamics*. Cambridge University Press.

Bender, C. M. and S. A. Orszag (1978). *Applied mathematical methods for scientists and engineers*. McGraw-Hill.

Benielli, D. and J. Sommeria (1998). Excitation and breaking of internal gravity waves by parametric instability. *Journal of Fluid Mechanics 374*, 117–144.

Berry, M. V. (1981). Regularity and chaos in classical mechanics, illustrated by three deformations of a circular 'billiard'. *Eur. J. Phys. 2*, 91–102.

Blaas, M. (2002). *Continental slope currents and shelf-sea circulation; dynamic effects of density forcing and tides*. Ph. D. thesis, Utrecht University.

Blaas, M., F.-P. A. Lam, T. Gerkema, and H. E. de Swart (2000). On slope currents forced by density gradients and tidal rectification. In T. Yanagi (Ed.), *Interactions between Estuaries, Coastal Seas and Shelf Seas*, Tokyo, pp. 233–250. Terra Scientific Publ. Comp.

Boehrer, B. and C. Stevens (2005). Ray waves in a pit lake. *Geophysical Research Letters 32*(24), L24608.

Buchwald, V. T. and J. K. Adams (1968). The propagation of continental shelf waves. *Proc.Roy.Soc.London A. 305*, 235–250.

Butman, B., R. C. Beardsley, B. Magnell, D. Frye, J. A. Vermersch, R. Schiltz, R. Limeburner, W. R. Wright, and M. A. Noble (1982). Recent observations on the mean circulation on Georges Bank. *Journal of Physical Oceanography 12*, 569–591.

Candela, J., R. C. Beardsley, and R. Limeburner (1992). Separation of tidal and sub-tidal currents in ship-mounted acoustic Doppler current profiler observations. *Journal of Geophysical Research 97*(C1), 769–788.

Cartwright, D. E. (1969). Extraordinary tidal currents near St Kilda. *Nature 223*, 928–932.

Cartwright, D. E. (1991). Detection of tides from artificial satellites (review). In B. B. Parker (Ed.), *Tidal hydrodynamics*, New York, pp. 547–567. John Wiley.

Cartwright, D. E. (1999). *Tides, a scientific history*. Cambridge University Press.

Cartwright, D. E., A. C. Edden, R. Spencer, and J. M. Vassie (1980). The tides of the northeast Atlantic Ocean. *Philosophical Transactions of the Royal Society of London A298*, 87–139.

Cartwright, D. E., J. M. Huthnance, R. Spencer, and J. M. Vassie (1980). On the St Kilda shelf tidal regime. *Deep-Sea Research 27*, 61–70.

Chen, C. and R. C. Beardsley (1995). A numerical study of stratified tidal rectification over finite-amplitude banks. Part I: symmetric banks. *Journal of Physical Oceanography 25*(9), 2090–2110.

Codiga, D. L., D. P. Renouard, and A. M. Fincham (1999). Experiments on waves trapped over the continental slope and shelf in a continuously stratified rotating ocean, and their incidence on a canyon. *Journal of Marine Research 57*(4), 585–612.

Crawford, W. R. and R. E. Thomson (1982). Continental shelf waves of diurnal period along Vancouver Island. *Journal of Geophysical Research 87*(C12), 9516–9522.

Crawford, W. R. and R. E. Thomson (1984). Diurnal-period continental shelf waves along Vancouver Island: a comparison with theoretical models. *Journal of Physical Oceanography 14*, 1629–1646.

Dalziel, S. B., G. O. Hughes, and B. R. Sutherland (1998). Synthetic schlieren. *Proc. 8th Int. Symp. Flow Visualization*.

Dauxois, T. and W. R. Young (1999). Near-critical reflection of internal waves. *Journal of Fluid Mechanics 390*, 271–295.

Defant, A. (1961). *Physical Oceanography*. Pergamon Press.

deWitt, L. M., M. D. Levine, C. A. Paulson, and W. V. Burt (1986). Semidiurnal internal tide in JASIN: observations and simulation. *Journal of Geophysical Research 91*(C2), 2581–2592.

Dietrich, G., K. Kalle, W. Krauss, and G. Siedler (1975). *Algemeine Meereskunde eine Einführung in die Ozeanografie* (3. ed.). Berlin: Gebrüder Borntraeger.

Djurfeldt, L. (1984). A unified derivation of divergent second-class topographic waves. *Tellus 36A*(3), 306–312.

Drazin, P. G. and W. H. Reid (1981). *Hydrodynamic stability*. Cambridge University Press.

Drijfhout, S. and L. R. M. Maas (2006). Impact of channel geometry and rotation on trapping of the internal tides. *Journal of Physical Oceanography*. submitted.

Dronkers, J. J. (1964). *Tidal computations in rivers and coastal waters*. Amsterdam: North-Holland Publishing company.

Eriksen, C. C. (1982). Observations of internal wave reflection off sloping bottoms. *Journal of Geophysical Research 87*, 525–538.

Eriksen, C. C. (1991). Observations of amplified flows atop a large seamount. *Journal of Geophysical Research 96*, 15227–15236.

Faraday, M. (1831). On a peculiar class of acoustical figures: and on certain forms assumed by groups of particles upon vibrating elastic surfaces. *Philosophical Transactions of the Royal Society of London 121*, 299–340.

Fjeldstad, J. E. (1933). Interne Wellen. *Geofysiske Publikasjoner 10*(6), 1–35.

Flather, R. A. (1988). A numerical model investigation of tides and diurnal-period continental shelf waves along Vancouver Island. *Journal of Physical Oceanography 18*(1), 115–139.

Fricker, P. D. and H. M. Nepf (2000). Bathymetry, stratification, and internal seiche structure. *Journal of Geophysical Research 105*(C6), 14237–14251.

Garrett, C. J. R. (2003). Mixing with latitude. *Nature 422*, 477–478.

Garrett, C. J. R. and J. W. Loder (1981). Dynamical aspects of shallow sea fronts. *Philosophical Transactions of the Royal Society of London A302*, 563–581.

Gemmrich, J. R. and H. van Haren (2001). Thermal fronts generated by internal waves propagating obliquely along the continental slope. *Journal of Physical Oceanography 31*(3), 649–655.

Gerkema, T. (1994). *Nonlinear dispersive internal tides: generation models for a rotating ocean.* Ph. D. thesis, Utrecht University, Utrecht, The Netherlands.

Gerkema, T. (1996). A unified model for the generation and fission of internal tides in a rotating ocean. *Journal of Marine Research 54*, 421–450.

Gerkema, T. (2001). Internal and interfacial tides: beam scattering and local generation of solitary waves. *Journal of Marine Research 59*, 227–255.

Gerkema, T. (2002). Application of an internal-tide generation model to baroclinic spring-neap cycles. *Journal of Geophysical Research 107*, 10.1029/2001JC001177.

Gerkema, T., F.-P. A. Lam, and L. R. M. Maas (2004). Internal tides in the Bay of Biscay: conversion rates and seasonal effects. *Deep-Sea Research II 51*, 2995–3008.

Geyer, W. R. and R. Signell (1990). Measurements of tidal flow around a headland with a shipboard acoustic Doppler current profiler. *Journal of Geophysical Research 95*(C3), 3189–3197.

Gill, A. E. (1982). *Atmosphere-Ocean dynamics*. Academic Press.

Gill, A. E. and E. H. Schumann (1974). The generation of long shelf waves by the wind. *Journal of Physical Oceanography 4*, 83–90.

Gjevik, B. and T. Straume (1989). Model simulations of the M2 and the K1 tide in the Nordic Seas and the Arctic Ocean. *Tellus 41A*, 73–96.

Godin, G. (1972). *The analysis of tides*. Liverpool University Press.

Görtler, H. (1943). Über eine Swingungserscheinung in Flüssigkeiten mit stabiler Dichteschichtung. *Z. angew. Math. Mech. 23*, 65–71.

Gostiaux, L., T. Dauxois, H. Didelle, J. Sommeria, and S. Viboux (2006). Quantitative laboratory observations of internal wave reflection on ascending slopes. *Physics of Fluids 18*(056602). doi: 10.10631/1.2197528.

Grimshaw, R. H. J., P. G. Baines, and R. C. Bell (1985). The reflection and diffraction of internal waves from the junction of a slit and a half-space, with applications to submarine canyons. *Dynamics of Atmosphere and Oceans 9*(2), 85–120.

Groen, P. (1948). Two fundamental theorems on gravity waves in the ocean. *Physica 14*, 294–300.

GSP-Group (1990). Greenland Sea Project; a venture toward improved understanding of the oceans' role in climate. *Eos Transactions of the American Geophysical Union 71*(24), 750–755.

Hamon, B. V. (1962). The spectrums of mean sea level at Sydney, Coff's Harbour, and Lord Howe Island. *Journal of Geophysical Research 67*, 5147–5155.

Hamon, B. V. (1963). Correction to ' the spectrums of mean sea level at Sydney, Coff's Harbour, and Lord Howe Island '. *Journal of Geophysical Research 68*, 4635.

Heath, R. A. (1983). Tidal currents in the southwestern Pacific Basin and Campbell Plateau, southeast of New Zealand. *Deep-Sea Research 30*, 393–409.

Hendershott, M. C. (1981). Long waves and ocean tides. In B. A. Warren and C. Wunsch (Eds.), *Evolution of physical oceanography*, Chapter 10, pp. 292–341. The Massachusetts Institute of Technology.

Hill, D. F. (2002). The Faraday resonance of interfacial waves in weakly viscous fluids. *Physics of Fluids 14*(1), 158–169.

Holt, J. T. and S. A. Thorpe (1997). The propagation of high frequency internal waves in the Celtic Sea. *Deep-Sea Research 44*(12), 2087–2116.

Hopkins, T. S. (1991). The GIN Sea — a synthesis of its physical oceanography and literature review 1972–1985. *Earth-Science Review 30*, 175–318.

Howarth, M. J. and J. M. Huthnance (1984). Tidal and residual currents around a Norfolk Sandbank. *Est. Coast. Shelf Sc. 19*, 105–117.

Hunkins, K. (1986). Anomalous diurnal tidal currents on the Yermak Plateau. *Journal of Marine Research 44*, 51–69.

Huthnance, J. M. (1973). Tidal current asymmetries over the Norfolk Sandbanks. *Estuarine Coastal Mar. Sci. 1*, 89–99.

Huthnance, J. M. (1974). On the diurnal tidal currents over Rockall Bank. *Deep-Sea Research 21*, 23–35.

Huthnance, J. M. (1975). On trapped waves over a continental shelf. *Journal of Fluid Mechanics 69*, 689–704.

Huthnance, J. M. (1981a). Large tidal currents near Bear Island and related tidal energy losses from the North Atlantic. *Deep-Sea Research 28*, 51–70.

Huthnance, J. M. (1981b). Waves and currents near the continental shelf edge. *Progress in Oceanography 10*, 193–226.

Huthnance, J. M. (1984). Slope currents and "JEBAR". *Journal of Physical Oceanography 14*(4), 795–810.

Huthnance, J. M. (1992). Extensive slope currents and the ocean-shelf boundary. *Progress in Oceanography 29*, 161–196.

Kazantsev, E., J. Sommeria, and J. Verron (1998). Subgrid-scale eddy parametrization by statistical mechanics in a barotropic ocean model. *Journal of Physical Oceanography 28*, 1017–1042.

Kowalik, Z. (1994). Modelling of topographically amplified diurnal tides in the Nordic Seas. *Journal of Physical Oceanography 24*, 1717–1731.

Kowalik, Z. and A. Y. Proshutinsky (1993). Diurnal tides in the Arctic Ocean. *Journal of Geophysical Research 98*(C9), 16449–16468.

Krauss, W. (1973). *Methods and results of theoretical oceanography*, Volume I: Dynamics of the homogeneous and the quasihomogeneous ocean. Berlin: Gebrüder Borntraeger.

Kristmannsson, S. S., S.-A. Malmberg, J. Briem, and E. Buch (1991). CTD data report joint Danish Icelandic cruise, September 1988. Data report Western Iceland Sea-Greenland Sea Project 23, Marine Research Institute, Reykjavik, Iceland.

Kunze, E. and J. M. Toole (1997). Tidally driven vorticity, diurnal shear, and turbulence atop Fieberling Seamount. *Journal of Physical Oceanography 27*, 2663–2693.

Lam, F.-P. A. (1992). Getij-analyse & interpretatie van stroommetergegevens uit de IJslandzee in de nabijheid van een shelfrand. Master's thesis, Utrecht University. IMAU, paper V 92-11.

Lam, F.-P. A. (1999). Shelf waves with diurnal tidal frequency at the Greenland shelf edge. *Deep-Sea Research 46*(5), 895–923.

Lam, F. P. A., T. Gerkema, and L. R. M. Maas (1999). Preliminary results from observations of internal tides and solitary waves in the Bay of Biscay. In T. F. Duda and D. M. Farmer (Eds.), *The 1998 WHOI/IOS/ONR Internal Solitary Wave Workshop: Contributed Papers*, pp. 203–208. WHOI-99-07. Technical Report, Woods Hole, MA.

Lam, F. P. A. and L. R. M. Maas (2006). Internal wave focusing revisited; reanalysis and new theoretical links. *Fluid Dynamics Research*. submitted.

Lam, F. P. A., L. R. M. Maas, and T. Gerkema (2004). Spatial structure of tidal and residual currents as observed over the shelf break in the Bay of Biscay. *Deep-Sea Research I 51*, 1075–1096.

Larsen, J. C. (1969). Long waves along a single-step topography in a semi-infinite uniformly rotating ocean. *Journal of Marine Research 27*(1), 1–6.

Le Cann, B. (1990). Barotropic tidal dynamics of the Bay of Biscay shelf: observations, numerical modelling and physical interpretation. *Continental Shelf Research 10*(8), 723–758.

LeBlond, P. H. and L. A. Mysak (1978). *Waves in the ocean*. Elsevier Oceanography Series. Elsevier.

Lek, D. L. (1938a). Interne wellen in den Niederländisch–Ostindischen gewässern. *Comptes rendus du Congres International de Geographie, Amsterdam 12*(section IIb), 69–76.

Lek, L. (1938b). Die Ergebnisse der Strom– und Serienmessungen. In P. M. van Riel (Ed.), *The Snellius-expedition in the eastern part of the Netherlands East-Indies 1929–1930*, Volume II, Oceanographic results, part 3. Leiden: E. J. Brill.

Leont'yeva, Y. A., K. D. Sabinin, V. A. Shulepov, and A. D. Yampol'skiy (1992). Experimental data on internal tides at the Mascarene Ridge and their ray tracing. *Oceanology 32*(6), 707–712.

Lighthill, S. J. (1978). *Waves in fluids*. Cambridge University Press.

Loder, J. W., D. Brickman, and E. P. W. Horne (1992). Detailed structure of currents and hydrography on the northern side of Georges Bank. *Journal of Geophysical Research 97*(C9), 14331–14351.

Loder, J. W. and D. G. Wright (1985). Tidal rectification and frontal circulation on the sides of Georges Bank. *Journal of Marine Research 43*, 581–604.

Longuet-Higgins, M. S. (1968a). On the trapping of waves along a discontinuity of depth in a rotating ocean. *Journal of Fluid Mechanics 31*, 417–434.

Longuet-Higgins, M. S. (1968b). Double kelvin waves with continuous depth profiles. *Journal of Fluid Mechanics 34*, 49–80.

Lwiza, K. M. M., D. G. Bowers, and J. H. Simpson (1991). Residual and tidal flow at a tidal mixing front in the North Sea. *Continental Shelf Research 11*(11), 1379–1395.

Maas, L. R. M. (2005). Wave attractors: linear yet nonlinear. *International Journal of Bifurcation and Chaos 15*(9), 2757–2782.

Maas, L. R. M., D. Benielli, J. Sommeria, and F.-P. A. Lam (1997). Observation of an internal wave attractor in a confined, stably stratified fluid. *Nature 388*(6642), 557–561.

Maas, L. R. M. and F.-P. A. Lam (1995). Geometric focusing of internal waves. *Journal of Fluid Mechanics 300*, 1–41.

Maas, L. R. M. and J. J. M. van Haren (1987). Observations on the vertical structure of tidal and inertial currents in the central North Sea. *Journal of Marine Research 45*, 293–318.

Maas, L. R. M. and J. T. F. Zimmerman (1989a). Tide-topography interactions in a stratified shelf sea I. Basic equations for quasi-nonlinear internal tides. *Geophysical and Astrophysical Fluid Dynamics 45*, 1–35.

Maas, L. R. M. and J. T. F. Zimmerman (1989b). Tide-topography interactions in a stratified shelf sea II. Bottom trapped internal tides and baroclinic residual currents. *Geophysical and Astrophysical Fluid Dynamics 45*, 37–69.

Magaard, L. (1962). Zur Berechnung interner Wellen in Meeresräumen mit nicht-ebenen Böden bei einer speciellen Dichteverteilung. *Kieler Meeresforschungen 18*, 161–183.

Magaard, L. (1968). Ein Beitrag zur Theorie der internen Wellen als Störungen geostrophischer Strömungen. *Deutsche Hydrographische Zeitschrift 21*, 241–278.

Makarov, S. A., V. I. Neklyudov, and Y. D. Chashechkin (1990). Spatial structure of two-dimensional monochromatic internal wave-beams in an exponentially stratified fluid. *Izvestiya 26*, 548–553.

Manders, A. M. M. (2003). *Internal wave patterns in enclosed density-stratified and rotating fluids*. Ph. D. thesis, Utrecht University.

Manders, A. M. M., J. J. Duistermaat, and L. R. M. Maas (2003). Wave attractors in a smooth convex enclosed geometry. *Physica D 186*(3-4), 109–132.

Maslowski, W. (1996). Numerical simulations of topographic Rossby waves along the East Greenland Front. *Journal of Geophysical Research 101*(C4), 8775–8787.

Mazé, R. (1987). Generation and propagation of non-linear internal waves induced by the tide over a continental slope. *Continental Shelf Research 7*, 1079–1104.

Middleton, J. H., T. D. Foster, and A. Foldvik (1987). Diurnal shelf waves in the Southern Weddell Sea. *Journal of Physical Oceanography 17*, 784–791.

Miles, J. and D. Henderson (1990). Parametrically forced surface waves. *Ann. Rev. Fluid Mech. 22*, 143–165.

Miles, J. W. (1972). Kelvin waves on oceanic boundaries. *Journal of Fluid Mechanics 55*, 113–127.

Moray, R. (1665). A relation of some extraordinary tydes in the West-Isles of Scotland. *Philosophical Transactions of the Royal Society of London 1*(4), 53–55.

Morozov, E. G. (1995). Semidiurnal internal wave global field. *Deep-Sea Research 42*(1), 135–148.

Mowbray, D. E. and B. S. H. Rarity (1967). A theoretical and experimental investigation of the phase configuration of internal waves of small amplitude in a density stratified liquid. *Journal of Fluid Mechanics 28*, 1–16.

Munk, W., F. Snodgrass, and M. Wimbush (1970). Tides off-shore: transition from California coastal to deep-sea waters. *Geophysical Fluid Dynamics 1*, 161–235.

Munk, W. and C. Wunsch (1998). Abyssal recipes II: energetics of tidal and wind mixing. *Deep-Sea Research I 45*, 1977–2010.

Münnich, M. (1996). The influence of bottom topography on internal seiches in stratified media. *Dynamics of Atmosphere and Oceans 23*, 257–266.

Mysak, L. A. (1967). On the theory of continental shelf waves. *Journal of Marine Research 25*(3), 205–227.

Mysak, L. A. (1980). Recent advances in shelf wave dynamics. *Reviews of Geophysics 18*, 211–241.

New, A. L. (1988). Internal tidal mixing in the Bay of Biscay. *Deep-Sea Research 35*(5), 691–709.

New, A. L. and J. C. B. Da Silva (2002). Remote-sensing evidence for the local generation of internal soliton packets in the central Bay of Biscay. *Deep-Sea Research 49*, 915–934.

New, A. L. and R. D. Pingree (1990). Large-amplitude internal soliton packets in the central Bay of Biscay. *Deep-Sea Research 37*, 513–524.

New, A. L. and R. D. Pingree (1992). Local generation of internal soliton packets in the central Bay of Biscay. *Deep-Sea Research 39*(9), 1521–1534.

NOAA (1988). Digital relief of the surface of the earth: ETOPO-5. Data Announcement 88-MGG-02, U.S. National Geophysical Data Center, Boulder, Colorado.

Ogilvie, G. I. (2005). Wave attractors and the asymptotic dissipation rate of tidal disturbances. *Journal of Fluid Mechanics 543*, 19–44.

Open University course team (1989). *The ocean basins: their structure and evolution*. Open University and Pergamon Press.

Ou, H. W. (1999). A model of tidal rectification by potential vorticity mixing. part I: Homogeneous ocean. *Journal of Physical Oceanography 29*, 821–827.

Ou, H. W. and L. R. M. Maas (1986). Tidal-induced buoyancy flux and mean transverse circulation. *Continental Shelf Research 5*(6), 611–628.

Padman, L., A. J. Plueddemann, R. D. Muench, and R. Pinkel (1992). Diurnal tides near the Yermak Plateau. *Journal of Geophysical Research 97*, 12639–12652.

Peacock, T. and A. Tabaei (2005). Visualization of nonlinear effects in reflecting internal wave beams. *Physics of Fluids 17*(6). article 061702 (4 pages).

Pedlosky, J. (1984). *Geophysical fluid dynamics* (2nd ed.). Springer.

Pérenne, N. (1997). *Etude expérimentale et numérique de la rectification topographique en milieu homogène ou stratifié*. Ph. D. thesis, Univ. Joseph Fourier-Grenoble 1, Grenoble, France.

Pérenne, N. and A. Pichon (1999). Effect of barotropic tidal rectification on low-frequency circulation near the shelf break in the northern Bay of Biscay. *Journal of Geophysical Research 104*(C6), 13489–13506.

Petruncio, E. T. (1996). *Observations and modeling of the internal tide in a submarine canyon*. Ph. D. thesis, Naval Postgraduate School, Monterey, CA.

Petruncio, E. T., L. K. Rosenfeld, and J. D. Paduan (1998). Observations of the internal tide in Monterey Canyon. *Journal of Physical Oceanography 28*(10), 1873–1903.

Pichon, A. and R. Mazé (1990). Internal tides over a shelf break: analytical model and observations. *Journal of Physical Oceanography 20*(5), 657–671.

Pingree, R. D. (1979). Baroclinic eddies bordering the Celtic Sea in late summer. *J. Mar. Biol. Ass. UK 59*, 689–698.

Pingree, R. D. (1984). Some applications of remote sensing to studies in the Bay of Biscay, Celtic Sea and English Channel. *Elsevier Oceanographic Series 38*, 287–315.

Pingree, R. D., D. K. Griffiths, and G. T. Mardell (1983). The structure of the internal tide at the Celtic Sea shelf break. *J. Mar. Biol. Ass. UK 64*, 99–113.

Pingree, R. D. and B. Le Cann (1989). Celtic and Armorican slope and shelf residual currents. *Progress in Oceanography 23*, 303–338.

Pingree, R. D. and B. Le Cann (1990). Structure, strength and seasonality of the slope currents in the Bay of Biscay region. *J. Mar. Biol. Ass. UK 70*, 857–885.

Pingree, R. D. and G. T. Mardell (1985). Solitary internal waves in the Celtic Sea. *Progress in Oceanography 14*, 413–441.

Pingree, R. D., G. T. Mardell, and A. L. New (1986). Propagation of internal tides from the upper slopes of the Bay of Biscay. *Nature 321*, 154–158.

Pingree, R. D. and A. L. New (1989). Downward propagation of internal tidal energy into the Bay of Biscay. *Deep-Sea Research 36*(5), 735–758.

Pingree, R. D. and A. L. New (1991). Abyssal penetration and bottom reflection of internal tidal energy into the Bay of Biscay. *Journal of Physical Oceanography 21*(1), 28–39.

Pingree, R. D. and A. L. New (1995). Structure, seasonal development and sunglint spatial coherence of the internal tide on the Celtic and Armorican shelves and in the Bay of Biscay. *Deep-Sea Research 42*(2), 245–284.

Pinke, F. (1938). The expeditionary ship and the naval personnel's share. In P. M. van Riel (Ed.), *The Snellius-expedition in the eastern part of the Netherlands East-Indies 1929–1930*, Volume I, Voyage, Chapter II, pp. 41–80. Leiden: E. J. Brill.

Platzman, G. W. (1968, July). The Rossby wave. *Quarterly Journal of the Royal Meteorological Society 94*(401), 225–248. Symons memorial lecture.

Prandle, D. (1982). The vertical structure of tidal currents and other oscillatory flows. *Continental Shelf Research 1*, 191–207.

Ray, R. D. and G. T. Mitchum (1997). Surface manifestation of internal tides in the deep ocean: observations from altimetry and island gauges. *Progress in Oceanography 40*, 135–162.

Rieutord, M. and K. Noui (1999). On the analogy between gravity modes and inertial modes in spherical geometry. *Eur. Phys. J. B 9*, 731–738.

Rieutord, M., L. Valdettaro, and B. Georgeot (2002). Analysis of singular inertial modes in a spherical shell: the slender toroidal shell model. *Journal of Fluid Mechanics 463*, 345–360.

Roberts, J. (1975). *Internal gravity waves in the ocean*. Marcel Dekker Inc.

Robinson, A. R. (1964). Continental shelf waves and the response of sea level to weather systems. *Journal of Geophysical Research 69*(2), 367–368.

Saint-Guily, B. (1976). Sur la propagation des ondes de seconde classe le long d'un talus continental. *C.R.Acad.Sc.Paris, Ser.B 282*, 141–144.

Sellmann, L., E. Fahrbach, G. Rohardt, V. H. Strass, and B. Bodungen (1992). Moored instruments oceanographic data from the Greenland Sea 1987–1989. Data report 27, Alfred Wegener Institut, Bremerhaven, Germany.

Serpette, A. and R. Mazé (1989). Internal tides in the Bay of Biscay: a two-dimensional model. *Continental Shelf Research 9*(9), 795–821.

Sherwin, T. J. and N. K. Taylor (1990). Numerical investigations of linear internal tide generation in the Rockall Trough. *Deep-Sea Research 37*(10), 1595–1618.

Siedler, G., J. Church, and J. Gould (2001). *Ocean circulation and climate: observation and modelling the global ocean*, Volume 22 of *International Geophysics series*. San Diego, CA: Academic Press.

Simpson, J. H., E. G. Mitchelson-Jacob, and A. E. Hill (1990). Flow structure in a channel from an acoustic Doppler current profiler. *Continental Shelf Research 10*(6), 589–603.

Smit, R. (1975). Second-order turning point problems in oceanography. *Deep-Sea Research 22*, 837–852.

Smith, W. H. F. and D. T. Sandwell (1997). Global sea floor topography from satellite altimetry and ship depth soundings. *Science 277*(5334), 1956–1962.

Strass, V. H., E. Fahrbach, U. Schauer, and L. Sellmann (1993). Formation of Denmark Strait overflow water by mixing in the east Greenland current. *Journal of Geophysical Research 98*, 6907–6919.

Sutherland, B. R., S. B. Dalziel, G. O. Hughes, and P. F. Linden (1999). Visualisation and measurement of internal waves by "synthetic schlieren". part 1: vertically oscillating cylinder. *Journal of Fluid Mechanics 390*, 93–126.

Sutherland, B. R., G. O. Hughes, S. B. Dalziel, and P. F. Linden (2000). Internal waves revisited. *Dynamics of Atmosphere and Oceans 31*, 209–232.

Swart, A. N., G. L. G. Sleijpen, L. R. M. Maas, and J. Brandts (2006). Numerical solution of the two dimensional Poincaré equation. *J. Comp. Appl. Math.*. in press.

Tabaei, A. and T. R. Akylas (2003). Nonlinear internal gravity wave beams. *Journal of Fluid Mechanics 482*, 141–161.

Talley, L. D. (2006). Vol.2: Pacific Ocean. In M. Sparrow, P. Chapman, and J. Gould (Eds.), *Hydrographic Atlas of the World Ocean Circulation Experiment (WOCE)*. Southampton: International WOCE Project office. In preparation.

Taylor, G. I. (1920). Tidal oscillations in gulfs and rectangular basins. *Proc. London Math. Soc. 20*, 148–181.

Tee, K. T. (1985). Depth-dependent studies of tidally induced residual currents on the sides of Georges Bank. *Journal of Physical Oceanography 15*, 1818–1846.

Thomson, R. E. and W. R. Crawford (1982). The generation of diurnal period shelf waves by tidal currents. *Journal of Physical Oceanography 12*, 635–643.

Thomson, W. (1879). On gravitational oscillations of rotating water. *Proceedings of the Royal Society Edinburgh 10*, 92–100.

Thorpe, S. A. (1999). The generation of alongslope currents by breaking internal waves. *Journal of Physical Oceanography 29*, 29–38.

Thorpe, S. A. (2003). A note on standing internal inertial gravity waves of finite amplitude. *Geophysical and Astrophysical Fluid Dynamics 97*(1), 59–74.

Turner, J. S. (1973). *Buoyancy effects in fluids*. Cambridge: Cambridge University Press.

Vallis, G. K. (2005). *Atmospheric and Oceanic Fluid Dynamics*. Available from: www.princeton.edu/gkv/aofd (To be published by Cambridge Univ. Press.).

van Aken, H. M. (2000). The hydrography of the mid–latitude Northeast Atlantic Ocean; II: the intermediate water masses. *Deep-Sea Research 47*, 789–824.

van Aken, H. M. (2005). Dutch oceanographic research in Indonesia in colonial times. *Oceanography 18*(4), 30–41.

van Aken, H. M., J. Briem, E. Buch, S. S. Kristmannsson, S.-A. Malmberg, and S. Ober (1992). Moored current meter data Greenland–Jan Mayen and Denmark Strait, sep.1988 to sep.1989. Data report Western Iceland Sea-Greenland Sea Project 30, Marine Research Institute, Reykjavik, Iceland.

van Haren, J. J. M. and L. R. M. Maas (1987). Temperature and current fluctuations due to tidal advection of a front. *Netherlands Journal of Sea Research 21*, 79–94.

van Riel, P. M. (1937). Programme of research and preparations. In P. M. van Riel (Ed.), *The Snellius-expedition in the eastern part of the Netherlands East-Indies 1929–1930*, Volume I, Voyage, Chapter I, pp. 1–40. Leiden: E. J. Brill.

van Riel, P. M. (1938). The voyage in the Netherlands East–Indies (with a list of stations, a large route chart and 16 detail charts). In P. M. van Riel (Ed.), *The Snellius-expedition in the eastern part of the Netherlands East-Indies 1929–1930*, Volume I, Voyage, Chapter III, pp. 81–164. Leiden: E. J. Brill.

Vlasenko, V. I. and Y. G. Morozov (1993). Generation of semidiurnal internal waves near a submarine ridge. *Oceanology 33*(3), 282–286.

Voisin, B. (2003). Limit states of internal wave beams. *Journal of Fluid Mechanics 496*, 243–293.

Wright, D. G. and J. W. Loder (1985). A depth-dependent study of topographic rectification of tidal currents. *Geophysical and Astrophysical Fluid Dynamics 31*, 169–220.

Wunsch, C. (1969). Progressive internal waves on slopes. *Journal of Fluid Mechanics 35*, 131–141.

Wunsch, C. (1971). Note on some Reynolds stress effects of internal waves on slopes. *Deep-Sea Research 18*, 583–591.

Wüst, G. and A. Defant (1936). *Deutsche Atlantische Expedition 1925–1927. Band VI, Atlas. Atlas zur Schichtung und Zirkulation des Atlantischen Ozeans*. Verlag von Walther de Gruyter & Co.

Zhang, X., D. L. Boyer, N. Pérenne, and D. P. Renouard (1996). Mean flow generation along a sloping region in a rotating homogeneous fluid. *Journal of Geophysical Research 101*(C12), 28597–28614.

Zimmerman, J. T. F. (1978). Topographic generation of residual circulation by oscillatory (tidal) currents. *Geophysical and Astrophysical Fluid Dynamics 11*, 35–47.

Appendix A

Derivation of transcendental relation

In subsection 2.4.5 it is stated that the transcendental relation, defined by (2.16) and (2.17), follows from the matching conditions at the top and the foot of the slope. These relations supply the value for m needed in the solution of the stream function above the sloping region (2.15), and also needed to construct the dispersion relation with (2.18) pointwise for each wave number k. In this appendix the derivation leading to this transcendental relation is given. For the first mode of the continental shelf wave problems for long waves (small wave number k) are discussed and an alternative transcendental relation is given in this case.

From continuity of ψ and ψ' at $x = 0$ we find:

$$B_3 = \sinh(kL)B_1 \tag{A.1}$$

$$B_2 = \frac{1}{m}\left(k\cosh(kL) - b\sinh(kL)\right)B_1 \tag{A.2}$$

From continuity of ψ at $x = \Lambda$:

$$B_4 = e^{b\Lambda}\left[\sin(m\Lambda)B_2 + \cos(m\Lambda)B_3\right] \tag{A.3}$$

So with (2.15) we have now found the solution of (2.7) for ψ up to a constant B_1 related to the arbitrary amplitude of the wave. The last condition, continuity of ψ' at $x = \Lambda$, still has to be satisfied, and leads to (2.16) and (2.17). One can verify that this expression indeed is the same as in the limits reported by Buchwald and Adams (1968): without shelf ($L = 0$) we get $F(m) = -m/(b + k)$, and for the infinitely wide shelf ($L \to \infty$) $F(m) = 2mk/(m^2 + b^2 - k^2)$.

As was the case for the infinitely wide shelf in Buchwald and Adams (1968), for small k the value of m becomes imaginary for the first mode:

$$m = in \qquad \text{for} \quad k \leq k_0 \quad (\text{mode } 0) \tag{A.4}$$

To see more clearly what happens in terms of asymptotes of $F(m)$, one might want to consider the infinitely wide shelf case: $L \to \infty$, see Buchwald and Adams (1968). With (A.4) the transcendental relation (2.16) and (2.17) now becomes:

$$\tanh(\Lambda n) = \frac{nk(\sinh(kL) + \cosh(kL))}{(b^2 + kb - n^2)\sinh(kL) - (kb + k^2)\cosh(kL)} \qquad \text{for} \quad k < k_0 \quad (\text{mode } 0)$$

$$\text{(A.5)}$$

A complication now for finite shelf-width L is to find the critical wave number k_0. This can be done by taking the derivative of (2.16) (with (2.17)) with respect to m and looking at $m = 0$. This is because the tangent of $F(m)$ at $m = 0$ defines when intersection with $\tan(\Lambda m)$ disappears for mode 0. (See also Buchwald and Adams (1968), their figure 10.) Now no regular expression for k_0 can be found, but a *second* transcendental relation has to be solved to find the critical wave number k_0:

$$\tanh(k_0 L) = \frac{k_0 + \Lambda(bk_0 + k_0^2)}{-k_0 + \Lambda(bk_0 + b^2)} \tag{A.6}$$

Again, one can verify that for $L = 0$ we find the same result as Buchwald and Adams (1968, p.245), $k_0\Lambda = -1 + \sqrt{1 + b^2\Lambda^2}$, which is thus the limiting case of (A.6).

Note that when m becomes imaginary, the solution (2.15) for the stream function will still be real. We use $\sin(mx) = i\sinh(nx)$ and $\cos(mx) = \cosh(nx)$, and terms with $i\sinh(nx)$ stay real because they are to be multiplied by B_2, given by (A.2): $B_2 \sim B_1/m = -iB_1/n$.

Appendix B

Phase ambiguity

The computation of the phase in the harmonic analysis in section 4.3.3 (figures 4.4 and B.2) proceeds in three steps. The first step computes the phase per pixel based on the pixel intensity. Figure B.1a shows an example of this harmonic phase which is taken at the same time, $t/T = 160$, as the amplitude displayed in figure 4.3c. Phase is defined relative to $t/T = 0.0$, at the beginning of the experiment. It appears (as expected) that pixel intensity around every dye interface in the fluid is in antiphase with the next interface. This means that the elevations along the attractor are in phase, so that intensity gets lighter at one interface (e.g. dark above light) and darker at the next interface (thus, light above dark), etc. Note that the pixel intensity is also in antiphase at the opposing branch of the attractor. This means that an in-phase elevation at the left side of the attractor is accompanied with an in-phase depression at the right side (and *vice versa*).

The second step consists in eliminating the former antiphase behaviour between bottom and top of each dye layer by simply using a double colourmap (modulo π instead of 2π). This is shown in figure B.1b. Now the regular shape of the attractor can be better appreciated, but the antiphase character of opposite attractor branches is no longer visible.

The third step repairs this deficiency by correcting the phase around all even interfaces, leaving the odd interfaces intact. In practice this is not easy to do, for the interfaces are not exactly at the same position for each analysed sequence of images. Figure B.2 shows the result of correcting phases around even interfaces, after having defined the interface position adaptively for each phase image (like e.g. figure B.1a). In order to get a coherent overview, figure 4.4 is smoothed by taking the median value of 25 neighbouring pixels for each pixel. This method of 'phase correction' is not always reliable, particularly not in the initial period (not shown here). Therefore, details need to be checked by comparing with the original phase image similar to figure B.1a. Due to practical considerations, the phase displayed in figures 4.6 to 4.9 is depicted as in figure B.1b.
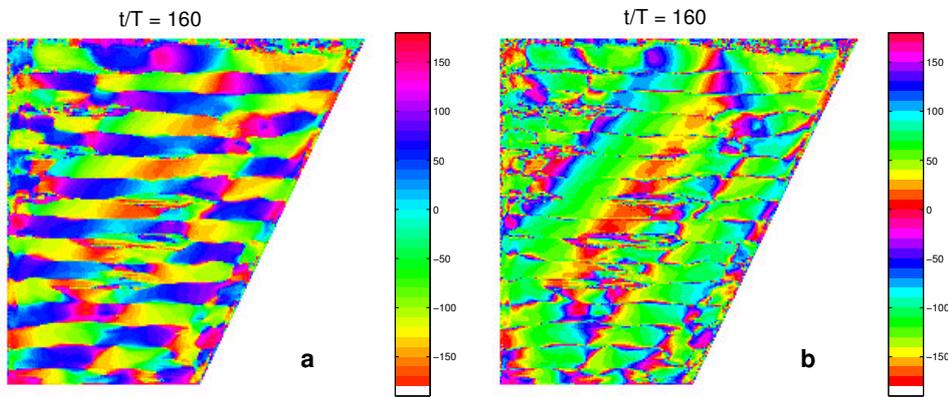
Figure B.1: (a) Evolution of harmonic phase of pixel intensity. Colour coded phase in degrees, see legend. Same time of images as in figure 4.3c: $t/T =$160. (b) Same as in (a), but now the (double) colourmap is modulo 180 degrees (see legend). This colourmap masks the elevation/depression ambiguity for the pixel intensity.
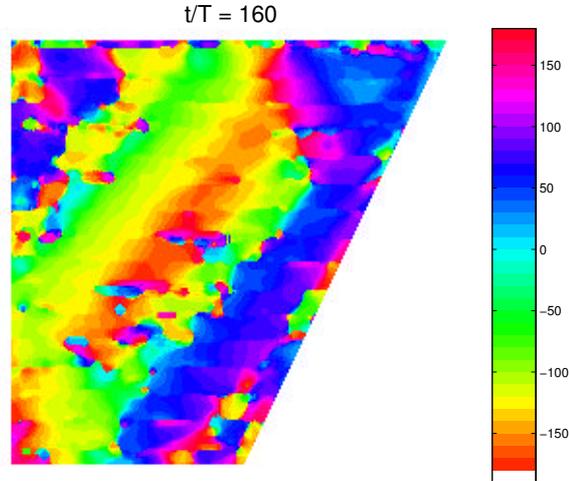

Figure B.2: Colour version of figure 4.4. Example of harmonic phase (in degrees, see legend) of pixel intensity. Same time of image as in figure 4.3c and figure C.13c: $t/T =$160. Here phase is corrected by checking for sudden jumps in vertical direction.

Appendix C

Colour figures
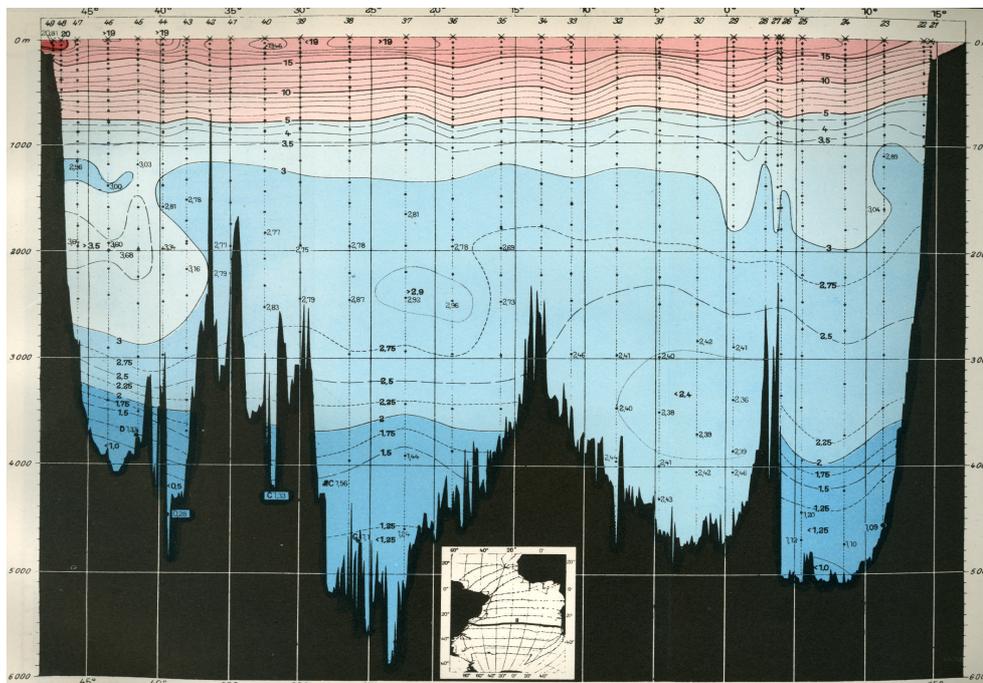
Figure C.1: Colour version of figure 1.1. Temperature cross section of the South Atlantic ocean ($\sim 30°S$), resulting from the Meteor expedition 1925-1927 (Wüst and Defant 1936). Temperatures are depicted by three tones of blue and red, for temperatures below 2°, 3°, 5° and above 5°, 10°, 15° C, respectively. Note the difference in scale between the vertical (6 km) and the horizontal (over 6000 km) directions.
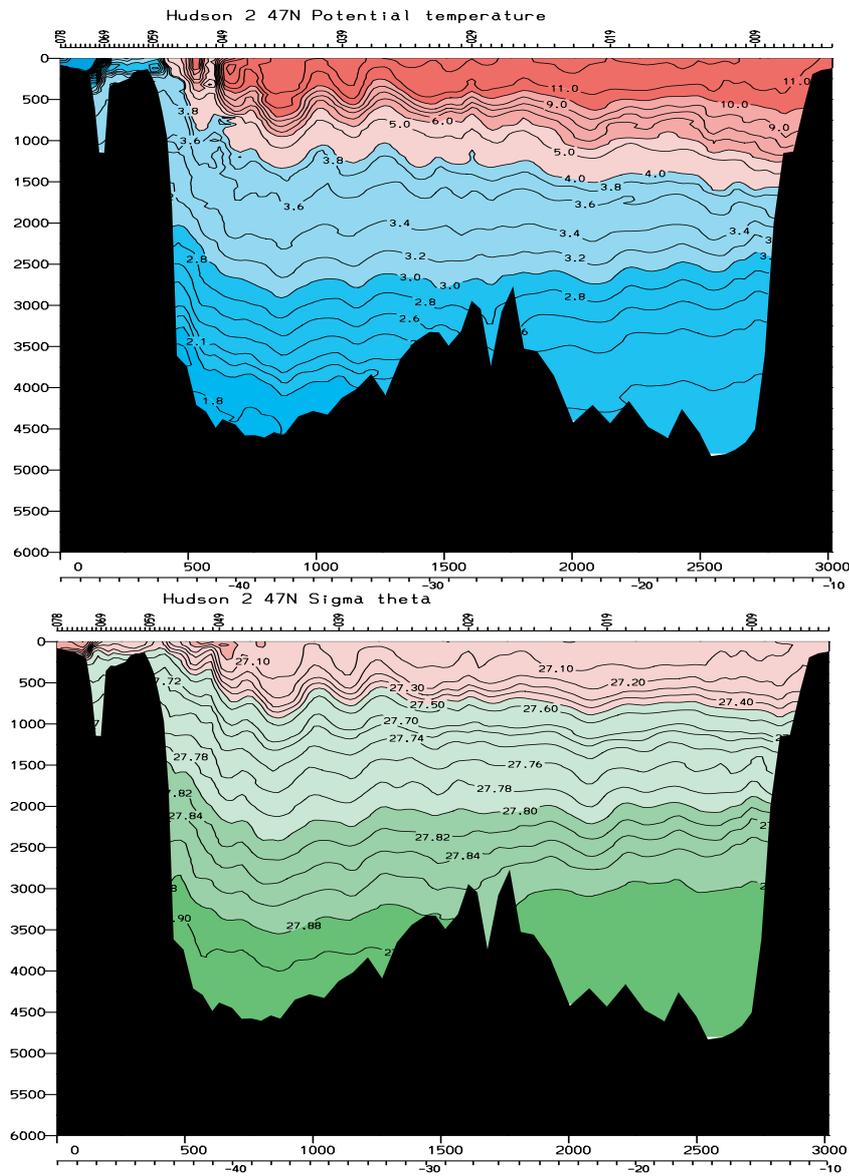
Figure C.2: Colour version of figure 1.7. Cross-sections of one of the many WOCE transects, (see e.g. Siedler et al. (2001)) along $\sim 47°$ N for potential temperature (top) and potential density anomaly (σ_θ, bottom) for a reference depth of 0 m. Potential density is σ_θ+1000 kg/m^3. Length of the transect is 3000 km, total depth 6000 m. A similar image (not shown) is available for salinity. Note that the deeper isopleths, roughly below 1000 m, have smaller increments: 0.2° instead of 1.0° below 4° Celsius. For potential density this is: 0.02 instead of 0.10 above 27.70 kg/m^3. Source: WOCE, see e.g. Talley (2006).
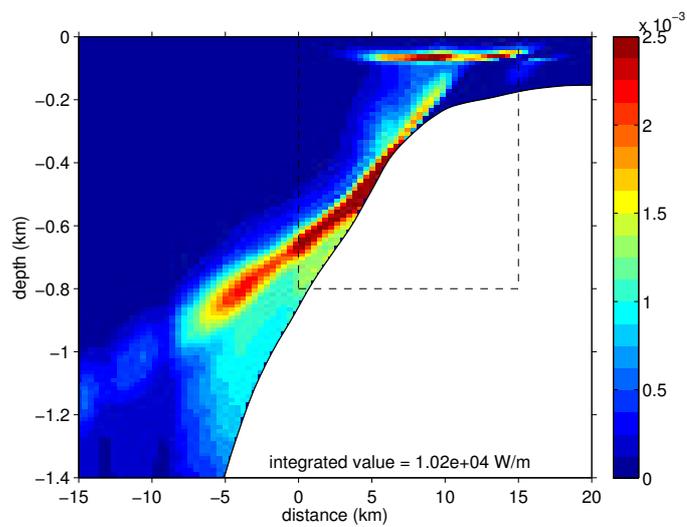
Figure C.3: Colour version of figure 1.12. Conversion rate (greyscale of legend in W m^{-3}) for transect in Bay of Biscay (summer stratification). Two major generation regions for internal tidal energy can be identified: the deep stratification region at the steep slope, and the seasonal pycnocline above the shelf break. The dashed box near the shelf break refers to the observation area of chapter 3. The integrated value in W/m, as indicated at the bottom of the image, is for the entire cross-section. Picture from Gerkema et al. (2004).
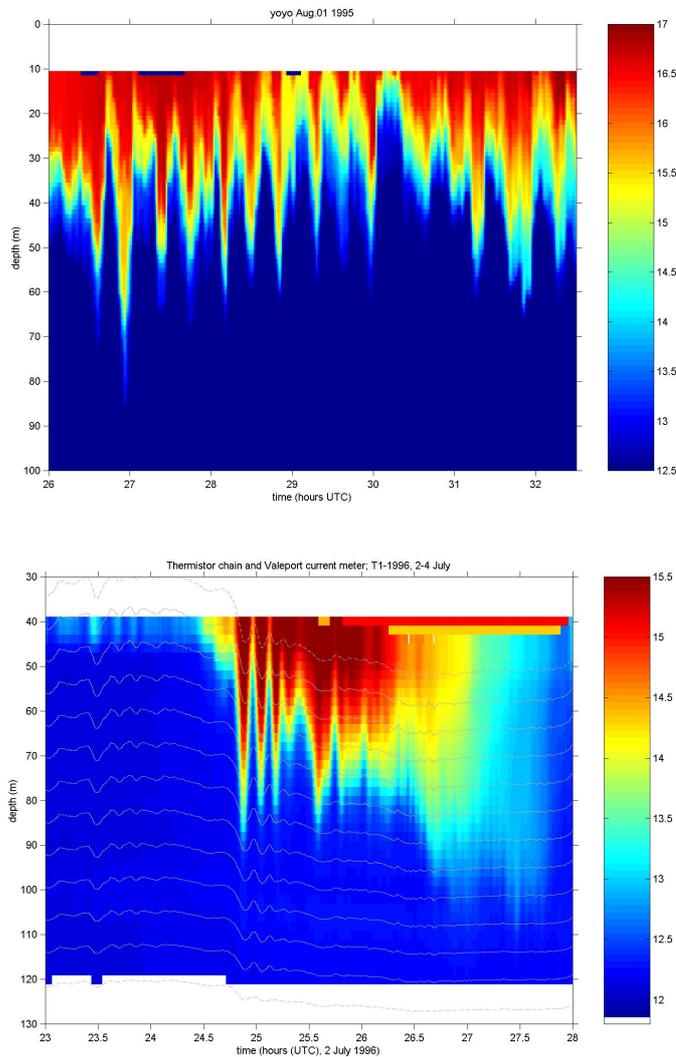
Figure C.4: Colour version of figure 1.15. Measured temperature profile halfway along the slope (top), and on the shelf (bottom) 32 km coastward. The temperature profile of the upper 100 m (130 m) is shown over 6.5 hours (5 hours) in the upper (lower) image. Temperature values (°C) are as indicated in the corresponding legends. The upper image is obtained by measuring temperature (and salinity, not shown) of the upper 100 m of the water column (CTD casts; 'yoyo-station') from the ship. The lower image is retrieved by correcting 'drifting depth' of thermistors along a partly broken mooring. Corrected thermistor depth vs. time (using interpolated values of pressure sensors on both ends of the thermistor chain) is visualized by white (light grey, hardly visible) lines. The horizontal bars at the upper right of the graph are artefacts of the interpolation algorithm used. Pictures taken from Lam et al. (1999)

Figure C.5: Colour version of figure 1.17. Internal wave experiment performed by the author in 1996 at DAMTP, Cambridge. The tank is about 380 mm high and 100 mm thick. The water is density stratified with a linear salt concentration ($N = 1.5$ rad/s). In this example, the cylinder (radius 22 mm) in the upper left corner is vertically oscillating with a frequency $\omega = 0.942$ rad/s, and an amplitude of 4 mm. In the figure at the right, the identified internal wave beams from the left image are shown. Lines not visible in the left image are dotted. The horizontal dash–dotted line near the surface is the pycnocline present in the tank. Energy propagates along the indicated arrows, similar to figure 1.11, with phase lines propagating perpendicular to the beam. Two regions of subsequent focusing reflections can be identified, regions A and B, respectively. The horizontal interruptions of the beam are caused by the *synthetic Schlieren* technique, that is used for visualization. This technique makes use of the changing refraction index in the fluid; the virtually displaced background (horizontal stripes) reveals the internal wave patterns (Dalziel et al. 1998; Sutherland et al. 2000).

Figure C.6: Colour version of figure 1.20. Example of standing wave solution $\psi(x, z)$ for a surface pressure $p_a(x) = 2f(x)$ that is prescribed within the two fundamental intervals and from which the whole pressure distribution along the surface, as indicated in the top panel, can be inferred. Values for ψ are coded with the colour scale as shown in the legend on the right.
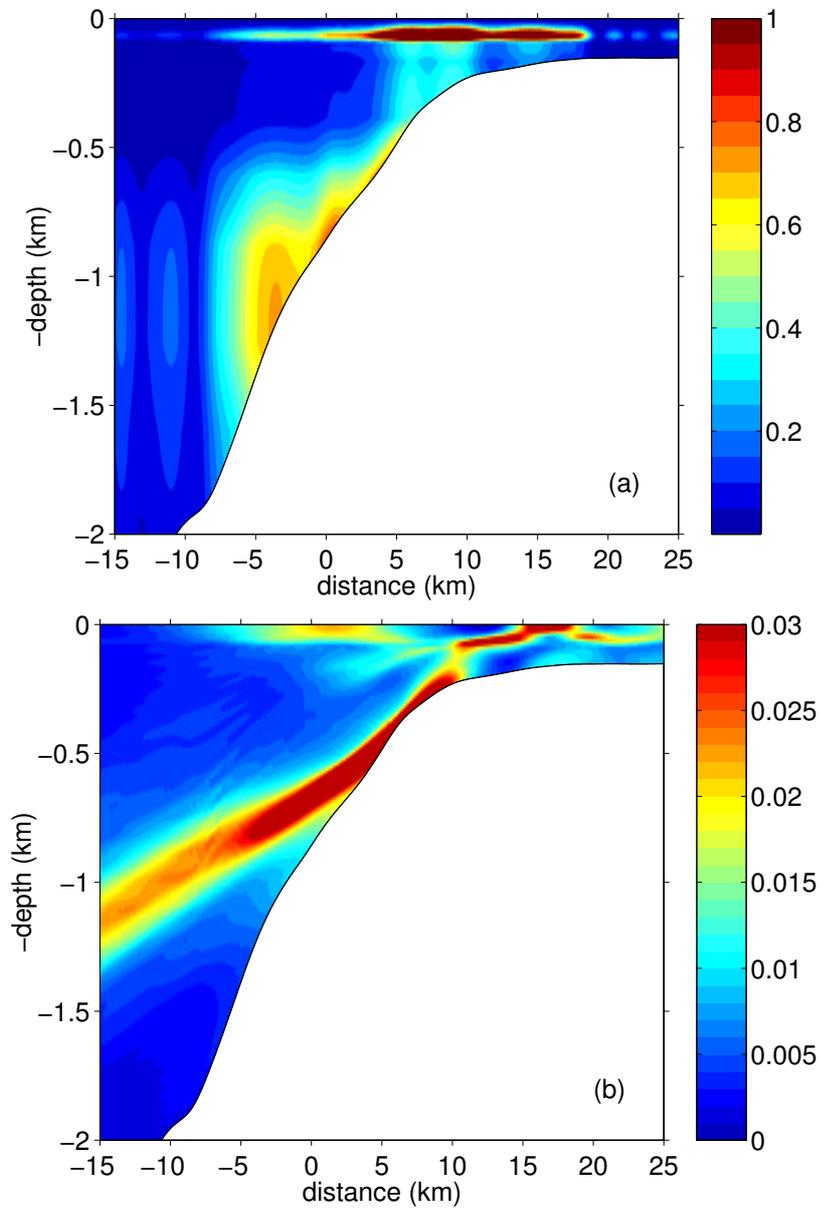
Figure C.7: Colour version of figure 3.5. (a) Spatial structure of forcing term $\hat{F}$ ($\mathrm{m}^{-1}\mathrm{s}^{-2}$) multiplied by 10^9, as defined by (3.3). (b) same figure, but for internal tidal energy ($\mathrm{m}^2\mathrm{s}^{-2}$), as defined in (3.8).
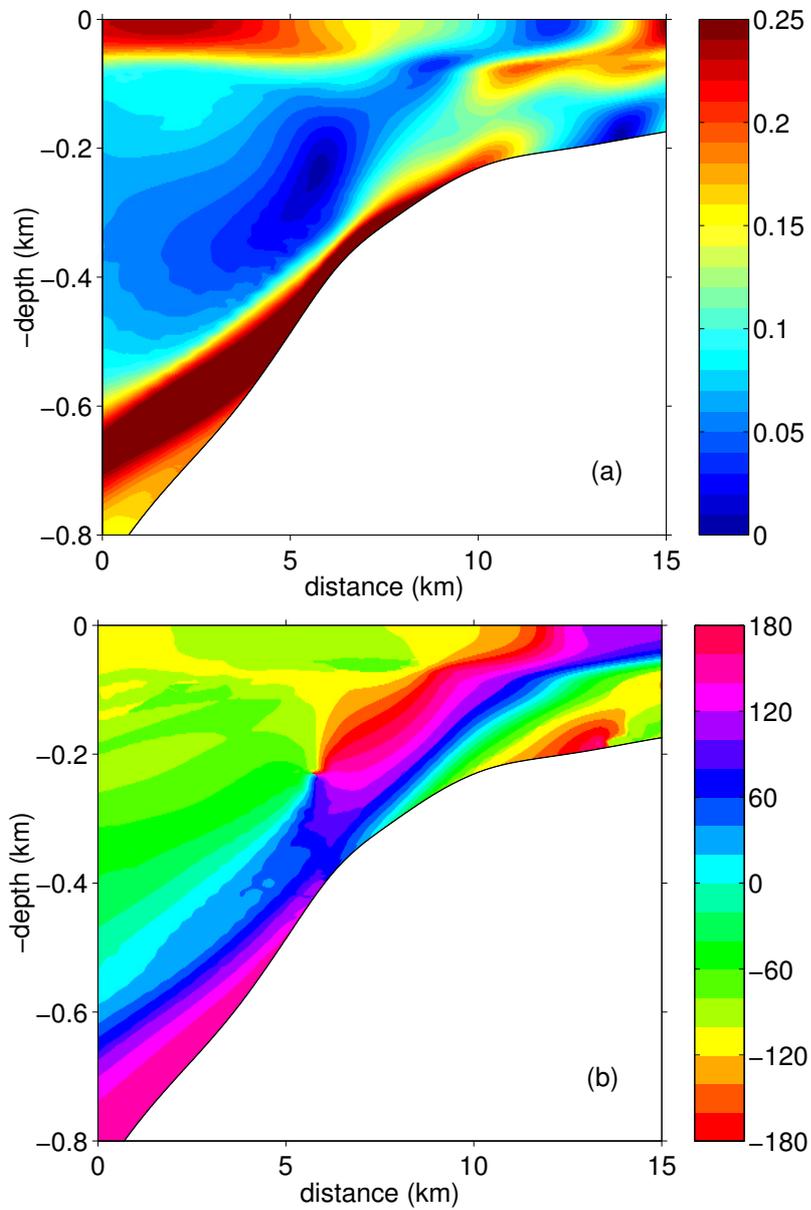
Figure C.8: Colour version of figure 3.6. Linear model results of cross-slope baroclinic motion. Top panel (a) depicts amplitude distribution (m/s). Bottom panel (b) shows phases in degrees.
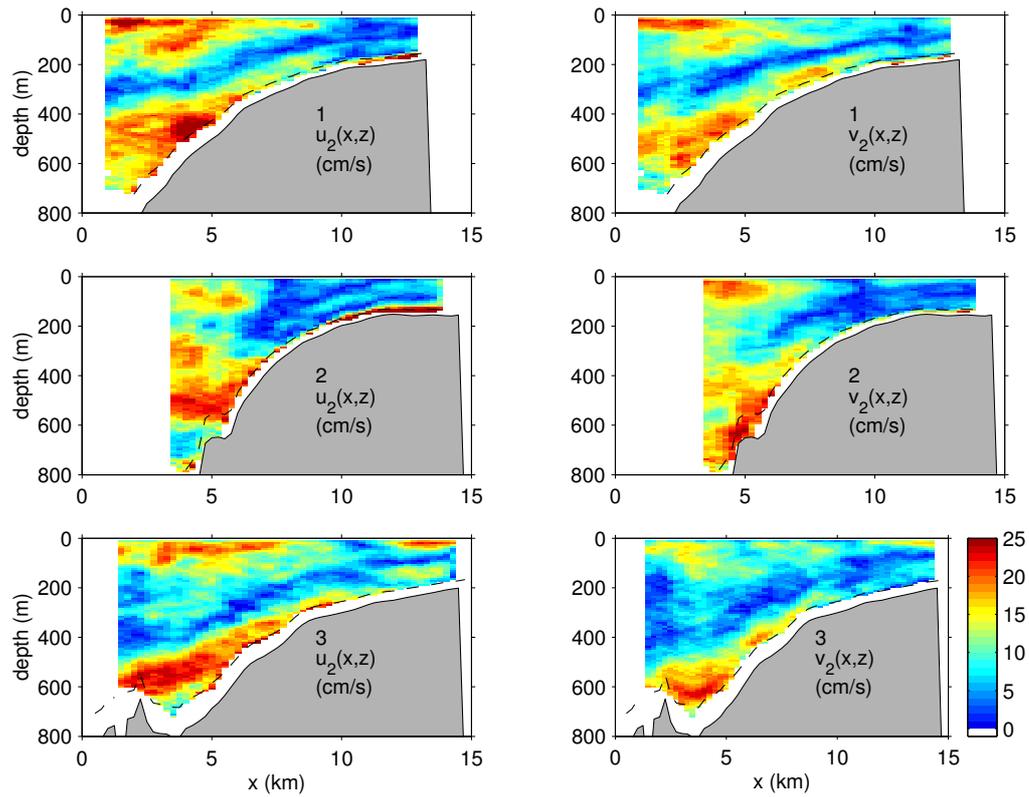
Figure C.9: Colour version of figure 3.7. Internal tidal amplitudes (in cm/s), in cross-slope (left) and along-slope (right) direction at transects 1 (top), 2 (middle) and 3 (bottom). Dashed lines depicts 85% of the water depth. Measurements below these lines should be disregarded, as explained in subsection 3.2.2.
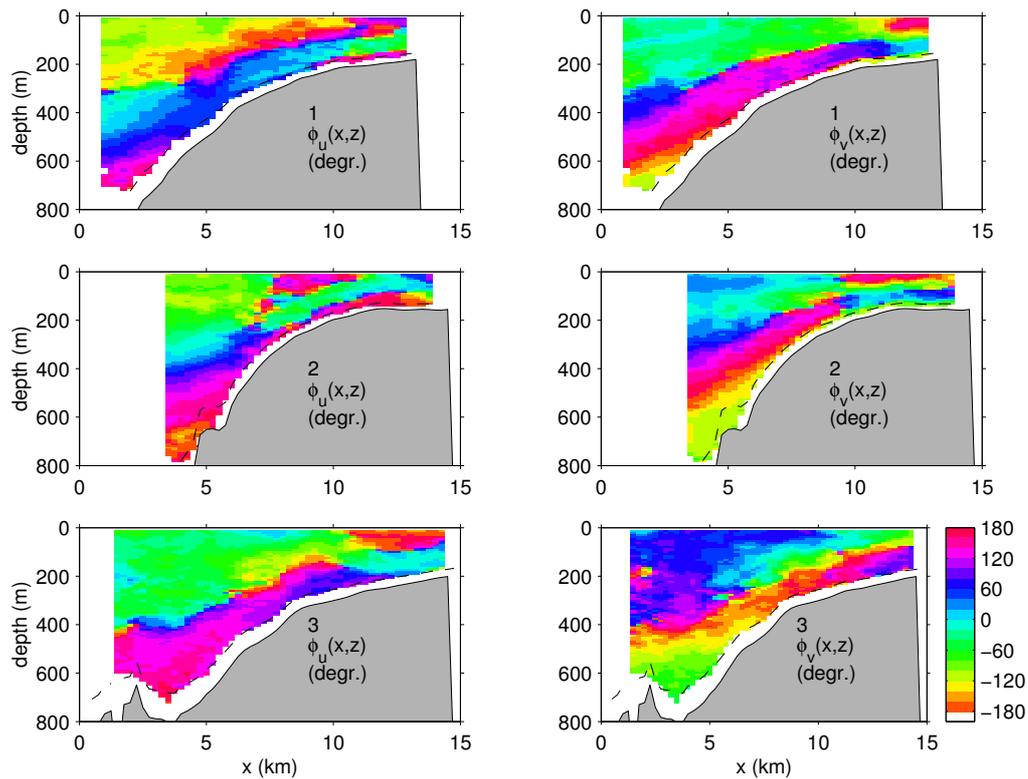
Figure C.10: Colour version of figure 3.8. Internal tidal phases (in degrees) corresponding to figure 3.7, i.e. deviations from vertical mean. Dashed lines represent 85% of the water depth, as in figures 3.7 and C.9.
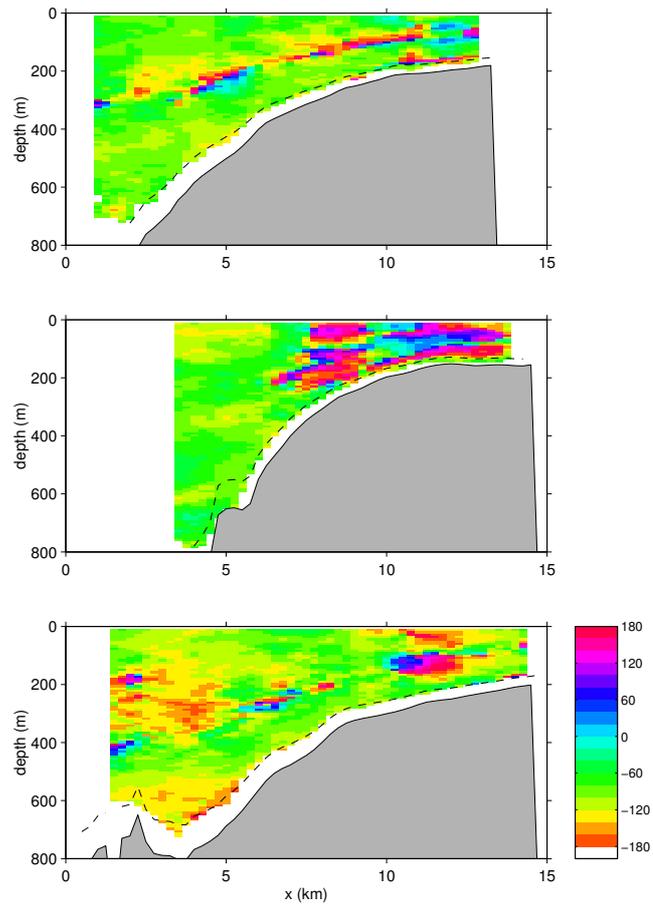
Figure C.11: Colour version of figure 3.9. Phase differences, $\phi_u - \phi_v$, as derived from figure 3.8. Dashed lines represent 85% of the water depth, as in figures 3.7 and C.9.
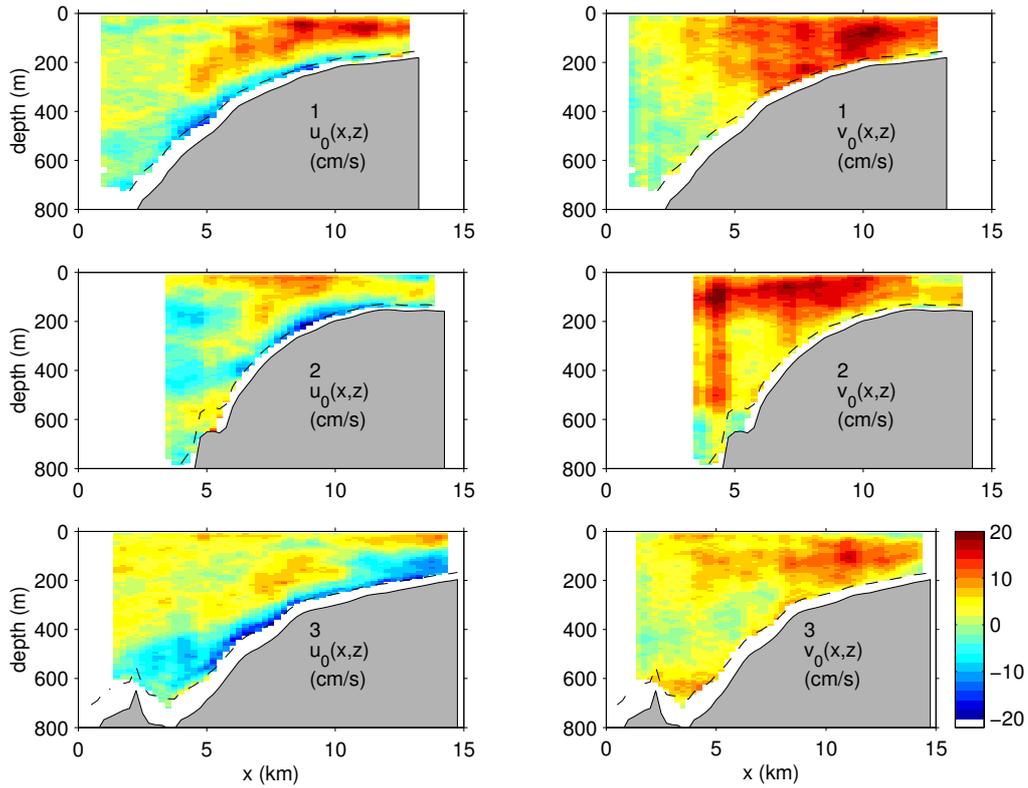
Figure C.12: Colour version of figure 3.11. Estimated total stationary currents cross-slope (left) and along-slope (right) in cm/s for transect 1 (top), transect 2 (middle) and transect 3 (bottom). Dashed lines represent 85% of the water depth, as in figures 3.7 and C.9.
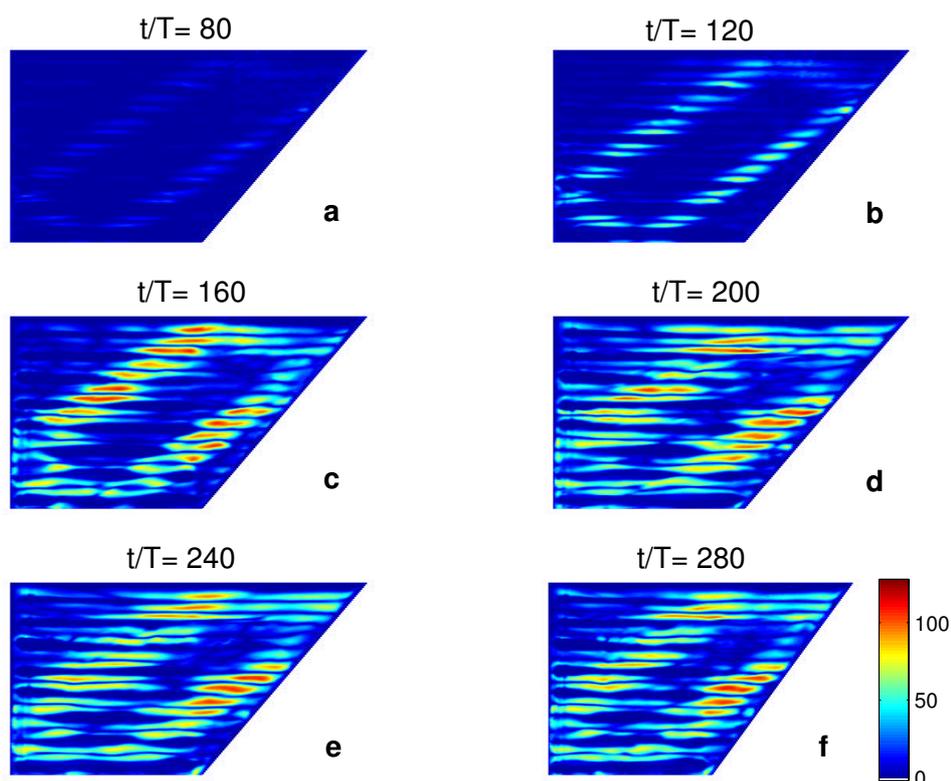
t/T= 80

t/T= 120

a

b

t/T= 160

t/T= 200

c

d

t/T= 240

t/T= 280

e

f

Figure C.13: Colour version of figure 4.3. Evolution of harmonic amplitude of pixel intensity (colour coded, see legend). Scaled time t/T at the middle of time series is given above each image. These times correspond to the following dimensional times: $t =347, 521, 695, 870, 1044$ and 1219 s.
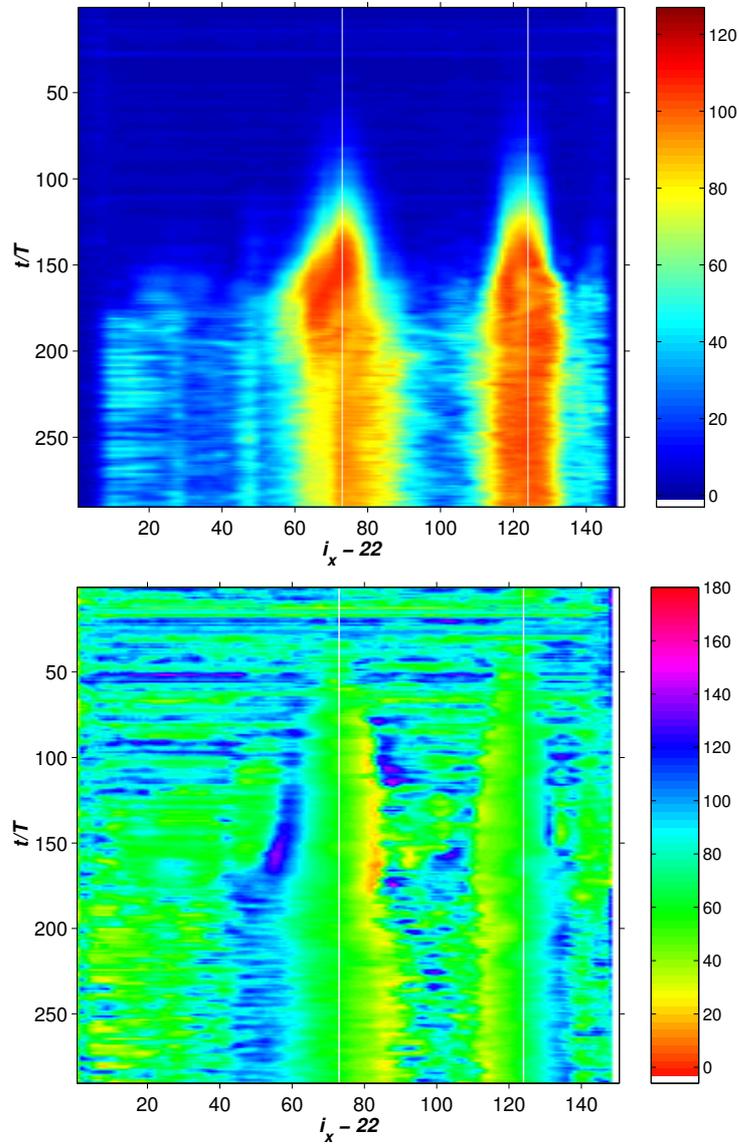
Figure C.14: Colour version of figure 4.6. Composite waterfall plot of maximum of harmonic amplitude (top) and median of harmonic phase (bottom) along 27 characteristics crossing the long branches of the attractor, as depicted in figure 4.5. Phase, modulo 180 degrees, is similarly defined as in the appendix, figure B.1b. The theoretically predicted attractor crossings are depicted with vertical white lines at horizontal index numbers 73 and 124. Note that 22 pixels should be added to get the horizontal indices (95 resp. 146) of the attractor crossings of the longest characteristic, starting in the upper left corner in figure 4.5.
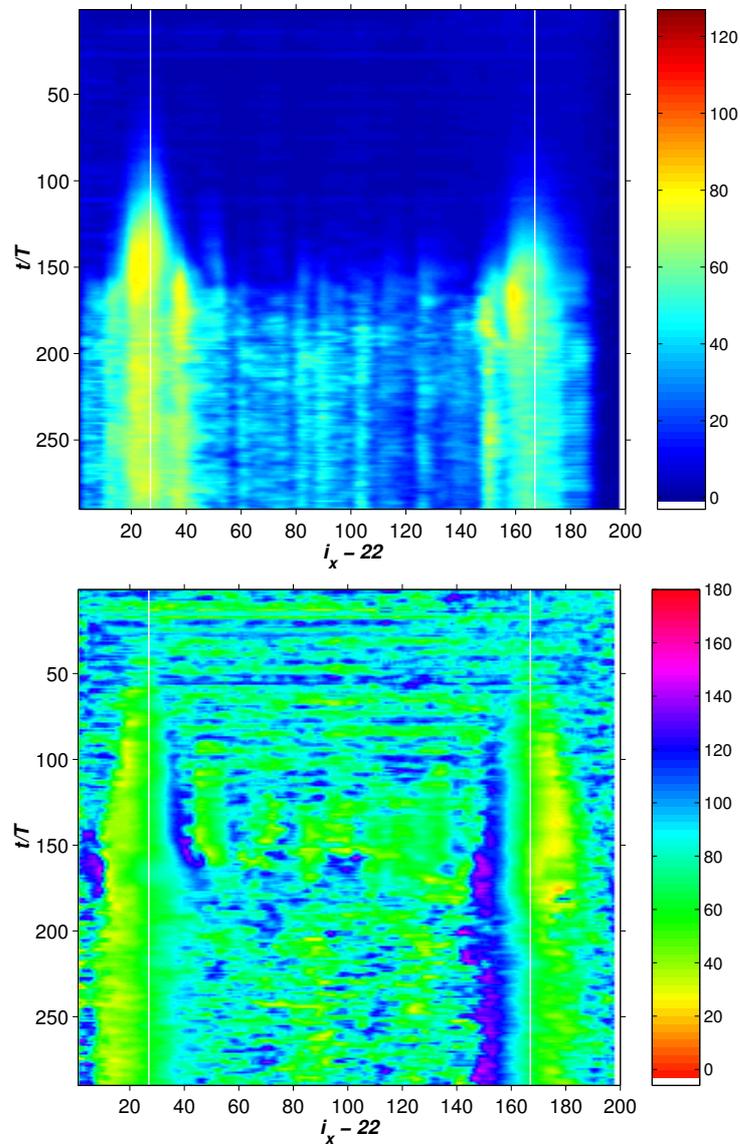
Figure C.15: Colour version of figure 4.7. As figures 4.6 and C.14 but for 19 characteristics crossing the short branches of the attractor (see figure 4.5). The original estimated attractor crossings are depicted with vertical white lines at horizontal index numbers 27 and 167. Note that 22 pixels should be added to get the horizontal indices (49 resp. 189) of the attractor crossings of the longest characteristic, starting in the lower left corner in figure 4.5.
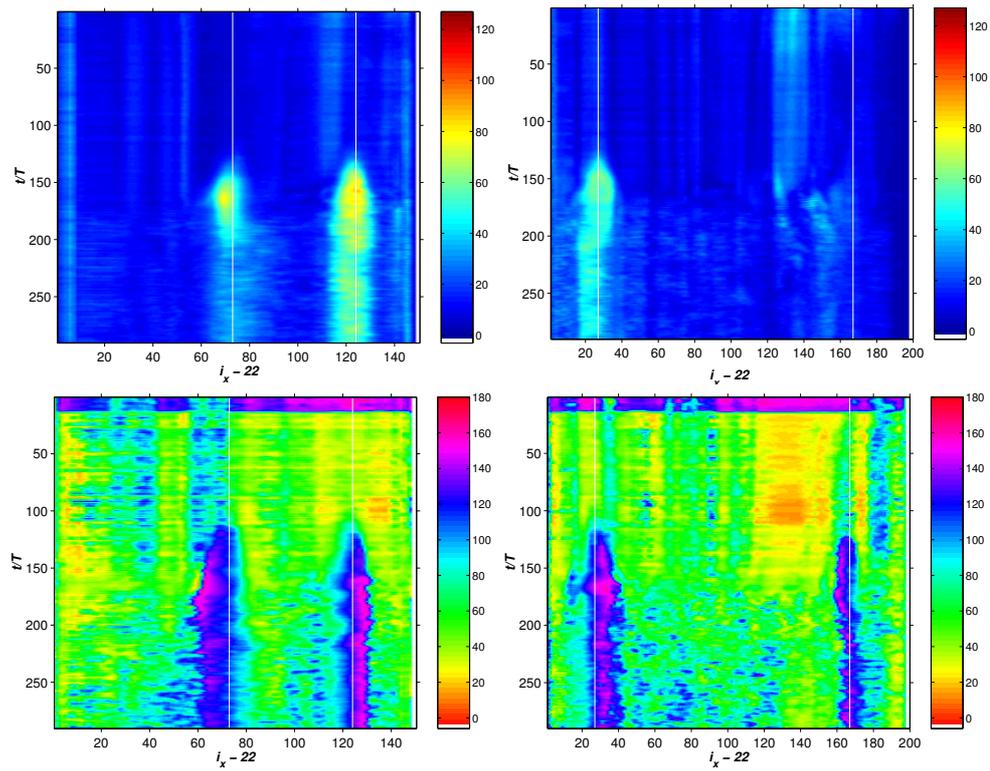
Figure C.16: Colour version of figure 4.9. As figures C.14 and C.15, but for first harmonic frequency 2ω. Amplitude (top) and phase (bottom) are given for beams crossing the long branches of the attractor (left), and crossing the short branches of the attractor (right).
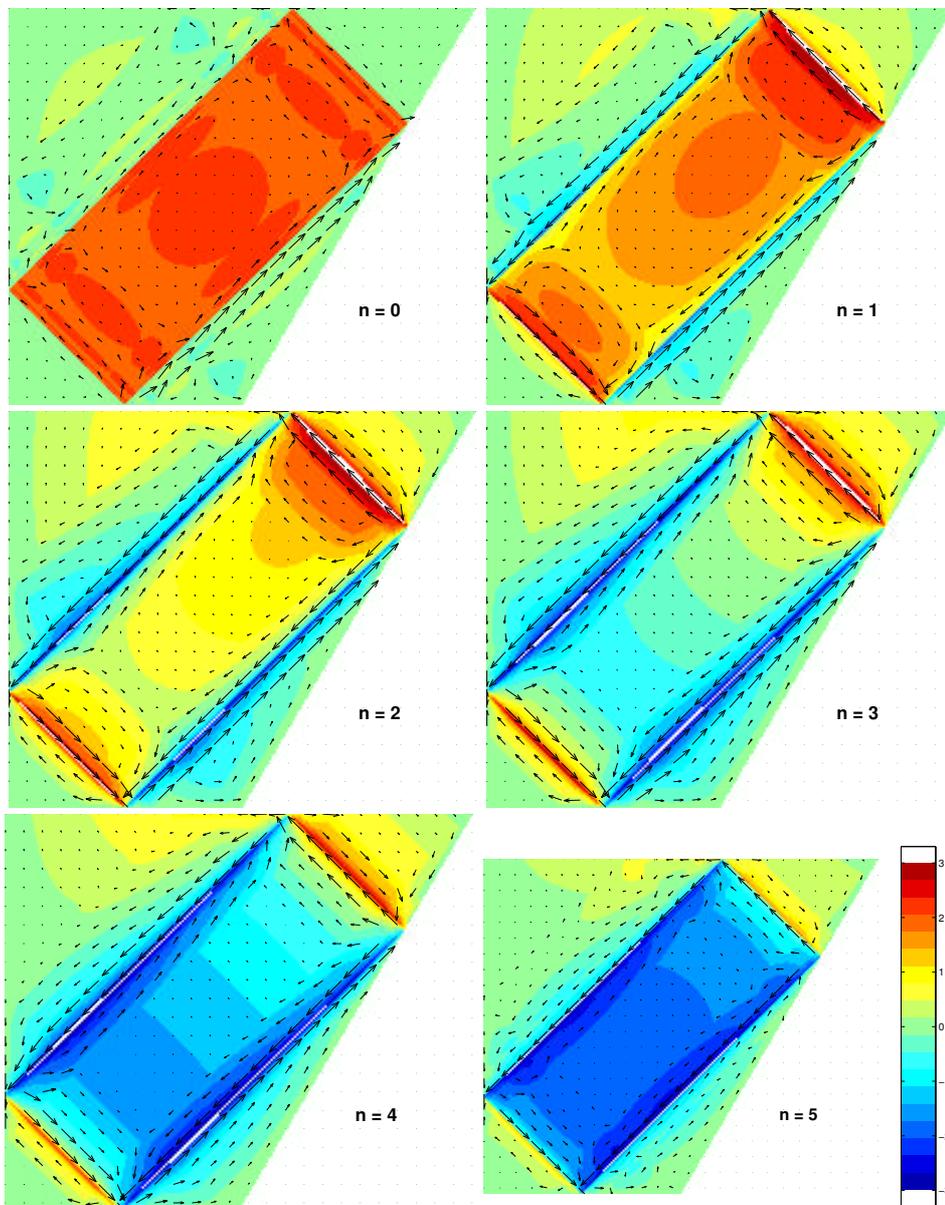
Figure C.17: Colour version of figure 4.13. Example of iteratively defined travelling wave solution $\Psi(x, z, t)$ for 'surface sloshing' boundary condition; $p_a(x) = \sin(x\pi/2)$. Times shown are for $n = 0, .., 5$, with $t/T_w = n/12$. Stream function Ψ is colour-coded, as shown in the legend. Arrows represent the velocities as derived from numerically computed stream function gradients based on the algorithmically computed stream function field.

Samenvatting

Waarnemingen, op zee en in het laboratorium, van golven boven een hellende bodem

Dit proefschrift gaat over de invloed van diepteverschillen op golven in de oceaan. Enerzijds wordt dit effect direct bestudeerd met behulp van metingen op zee. Anderzijds worden sommige eigenschappen van deze golven bestudeerd in het laboratorium. In dit proefschrift komen drie verschillende manieren aan bod waarop deze diepteverschillen golven beïnvloeden. Voordat daar op in wordt gegaan, volgt eerst een korte introductie van diepteverschillen in de oceaan (*topografie*), van waarnemingen op zee en van golven als zodanig.

Diepteverschillen en het waarnemen van golven in de oceaan

Continentale hellingen

De oceaan is gemiddeld circa 4000 meter diep. Echter, met name langs de randen van de continenten komen grote, bijna sprongsgewijze, diepteverschillen voor. Langs de kust steekt namelijk meestal nog een stuk continent onder water. Dit wordt het continentaal plat (Engels: *shelf*) genoemd en is relatief ondiep met een diepte van circa 100 tot 200 meter. De overgang van deze shelf- of randzeeën naar de oceaan is de continentale helling (Engels: *slope*). Deze steile overgang van diep naar ondiep water over een afstand van circa 50 km is een belangrijk gebied, waar allerlei fysische processen in de oceaan plaatsvinden. Deze zijn op hun beurt weer van belang voor biologische processen, waardoor er bijvoorbeeld veel visserij-activiteit voorkomt langs de continentale helling.

Waarnemingen op zee en in het laboratorium

Het doen van waarnemingen op en in de zee is niet eenvoudig. Het is moeilijk om voor langere tijd een heel gebied onder water te bemeten. Meestal kan men met een schip of een instrument de ontwikkeling in de tijd alleen op één plaats volgen. Als een groter gebied in kaart wordt gebracht, dan gebeurt dat in een veranderende omgeving, waardoor de gemeten processen niet of moeilijk te onderscheiden zijn als

165

veranderingen in tijd of in ruimte. Daarnaast is het een gegeven dat de natuur complex in elkaar steekt: veel verschillende processen lopen tegelijkertijd door elkaar. Dit zijn goede redenen om in het laboratorium processen in isolement te bestuderen. Meestal kan dan bovendien het vloeistofdomein volledig in beeld worden gebracht en bestudeerd. Dit kan bijvoorbeeld met videobeelden en gerelateerde analysetechnieken.

Golven

Golven zijn een fascinerend verschijnsel en komen in verschillende gedaantes voor, bijvoorbeeld in licht, geluid en aardbevingen als elektromagnetische, akoestische of seismologische golven. Golven op zee spreken in het bijzonder tot de verbeelding, omdat we ze van jongs af aan herkennen. Het karakteristieke aan golven is dat ze over een bepaalde afstand informatie ('energie') doorgeven, zonder dat materie zelf (hier: het water) over die afstand verplaatst wordt. Voor watergolven betekent dit dat een waterdeeltje nagenoeg alleen maar heen-en-weer en op-en-neer schommelt, waarbij alleen de informatie, de mate van schommeling, aan de buren wordt doorgegeven. Dit is vergelijkbaar met omvallende dominosteentjes die de beweging doorgeven, maar zelf (bijna) op hun plek blijven. Het verschil met een golf is dat bij een golf deze beweging periodiek is. Dit zou voor de dominosteentjes het geval zijn wanneer ze niet alleen om zouden vallen, maar ook weer terug zouden veren. Dit 'veertje' in de dominosteen levert dan de terugdrijvende kracht van de golf.

(Interne) golven in zee

Hoewel dit proefschrift gaat over golven in zee, zijn ze niet van het type dat wij normaal als golf zouden herkennen. Het betreft hier namelijk *interne golven* en *getijgolven*. Interne golven zijn golven die hun maximale uitwijking in het binnenste van de oceaan hebben. Ze zijn dus aan het oppervlak niet of nauwelijks zichtbaar. Daarnaast hebben zij ook andere eigenschappen dan golven aan het wateroppervlak. Dit blijkt onder meer uit de *focussering* die interne golven ondergaan wanneer zij simpelweg reflecteren aan een hellende bodem (Hoofdstuk 4). De interne golven die hier besproken worden hebben hun bestaan primair te danken aan dichtheidsverschillen in de oceaan. De gradueel met de diepte toenemende dichtheid wordt veroorzaakt door verschillen in temperatuur en zoutgehalte: hoe dieper, hoe kouder en zouter. Omdat kouder en zouter water een hogere dichtheid heeft wordt het water 'zwaarder'. Dit wordt de *stratificatie* of *gelaagdheid* van de oceaan genoemd. In het laboratorium wordt de dichtheidsgelaagdheid meestal met een geleidelijk veranderende zoutoplossing verkregen. Bij passage van een interne golf schommelen waterpakketjes om het evenwichtsniveau behorende bij hun eigen dichtheid.

Intern Getij

Ook het getij, dat we in de eerste plaats kennen als een lokale verandering van laag-naar hoogwater en terug, is op te vatten als golf. Hoogwater treedt namelijk niet op alle plaatsen gelijktijdig op, maar loopt als golftop langs de kust. In Scheveningen is het bijvoorbeeld eerder hoog water dan op Texel: de golf loopt in dit deel van

de Noordzee van zuid naar noord. Omdat de golf zo lang is, en een lange periode heeft, circa 12,4 uur voor het *dubbeldaagse* getij, wordt zij niet meteen als zodanig herkend.[1] In de oceaan kunnen ook interne golven voorkomen met de frequentie van het getij. Dit worden dan *interne getijden* genoemd. De generatie van interne getijden is door mijn collega's en mij bestudeerd met behulp van metingen uit de Golf van Biskaje (Hoofdstuk 3). Ook uit de kust van Groenland zijn getijstromen bestudeerd (Hoofdstuk 2). Met de metingen kon worden aangetoond dat deze getijgolven door de gecombineerde effecten van aardrotatie en diepteverschil als het ware *gevangen* (Engels: *trapped*) zaten aan de continentale helling.

Dit proefschrift
Het proefschrift gaat dus over golven die *of* gevangen *of* gegenereerd *of* gefocusseerd worden door diepteverschillen in de oceaan of in het laboratorium. Deze mechanismen worden achtereenvolgens behandeld in de verschillende hoofdstukken.

Hoofdstuk 2:
'Gevangen' hellinggolven met getijfrequentie bij Groenland

Dwars op de kust van Groenland, op 71 graden noorderbreedte, zijn op vijf locaties een jaar lang stromingen gemeten met een aantal instrumenten aan een verticale stalen kabel; een zogenaamde verankering. Deze metingen zijn gedaan met mechanische stroommeters, die gebruik maken van propeller en kompas om stroomsnelheid en richting te bepalen. Deze werden vervolgens een half jaar lang, twee keer per uur, op een cassettebandje vastgelegd. Deze waarnemingen lieten een interessant patroon zien voor het enkeldaagse getij; de beweging met een periode van circa 24 uur. Dit patroon bleek te verklaren als een continentale hellinggolf die langs de continentale helling van Groenland in zuidwaartse richting loopt. Deze golven worden ook aangeduid als: *topografische Rossbygolven* of *dubbele Kelvingolven*. Meer algemeen worden ze aangeduid als *vorticiteitsgolven*. Met vorticiteit wordt de hoeveelheid draaiing van de vloeistof aangeduid. Bij deze golven is niet de zwaartekracht de terugdrijvende kracht, maar een kracht die gerelateerd is aan het behoud van *impulsmoment*. Dit zal hier niet verder worden uitgelegd, maar komt er op neer dat bij waterbeweging over variabele diepte het water wordt teruggeduwd naar de oorspronkelijke positie. Hierbij speelt een rol op welke breedtegraad de golf zich bevindt op onze *draaiende* aarde.

Met een simpel wiskundig model, waarbij de diepte is benaderd door een sprongsgewijze overgang van diep naar ondiep water, kon worden berekend welke frequentie deze vorticiteitsgolf heeft. Voor de waarneming bij Groenland heb ik aangetoond dat de frequentie die dit type golf bij deze locatie en dieptesprong heeft precies past (En-

---

[1]De Engelse vertaling kan bovendien tot misverstand leiden: in het Engels heeft een *tsunami* (of 'vloed'golf) vaak de ongelukkige benaming *tidal wave*. Een tsunami wordt echter veroorzaakt door een aardbeving op zee ('zeebeving'), terwijl het getij haar oorsprong vindt in de aantrekkende krachten van zon en maan.

gels: *matches*) bij de golf met een enkeldaagse getijfrequentie. Vervolgens is gekeken hoe de vorm van de helling, en de nabijheid van de kust het gedrag van de golf kunnen beïnvloeden. Met dit model konden frequentie en stromingseigenschappen ter plaatse van de metingen nog beter worden verklaard. Tenslotte is de meetlocatie (71 graden noorderbreedte) vergeleken met andere locaties langs de continentale helling ten oosten van Groenland. Hierbij is aannemelijk gemaakt waarom de enkeldaagse getijbeweging zich juist op deze locatie zo sterk als een hellinggolf manifesteert. Het bijzondere gedrag van de getijstromen op deze locatie is inmiddels ook bevestigd met computermodellen voor deze regio.

Hoofdstuk 3:
Interne getijgeneratie in de Golf van Biskaje

In de Golf van Biskaje zijn stroommetingen gedaan vanaf het onderzoeksschip *Pelagia* van het Koninklijk NIOZ. Stromingen werden hier gemeten met een akoestisch instrument (ADCP), dat achter het schip werd gesleept. Dit instrument stuurt telkens geluidspulsen naar beneden, schuin in vier verschillende richtingen. Deze signalen weerkaatsen aan 'zwevend materiaal' dat met de lokale watersnelheid in de richting van de geluidsbundel beweegt. Dit leidt tot een verschoven frequentie van het terugverstrooide signaal (Doppler effect). Door combinatie van de informatie van de vier bundels kan hieruit, langs een verticale lijn van circa 800 meter, in stappen van 8 meter de driedimensionale stroming worden bepaald. Op drie posities is een traject van ongeveer 15 km gevaren, dwars op de continentale helling, precies van het punt waar de oceaanbodem 'de diepte ingaat' (Engels: *shelf break*). Hier is het getij weer overwegend dubbeldaags van aard. Door langs deze routes in telkens 24 uur, tien tot veertien keer heen en weer te varen, konden grootte, richting en fase van de getijstroming worden bepaald tot 800 meter diepte. Er zijn zo dus drie doorsnedes van een stukje oceaan gemaakt, langs het bovenste stuk van de continentale helling, 15 km lang en 800 meter diep.

Wat lieten deze doorsnedes zien? De locatie is zo gekozen, dat verwacht mag worden dat dit een generatiegebied is voor het interne getij. In de Golf van Biskaje bestaan over de hele waterkolom sterke, periodieke getijstromen die grotendeels dwars op de helling gericht zijn. Het water wordt dus twee keer per dag de steile helling op- en afgeduwd, waardoor een verticale beweging wordt veroorzaakt. Het gelaagde water komt van zijn plek, en een interne getijgolf loopt weg. Eerder was al vermeld dat interne golven bijzondere eigenschappen hebben: ze bewegen voornamelijk in een bundel vanaf de top van de helling, schuin de diepzee in. De hoek die deze *interne golfbundel* met de verticaal maakt wordt bepaald door de frequentie van de golf, de sterkte van de gelaagdheid en de aardrotatie (en daarmee de breedtegraad). Eigenschappen van deze interne golfbundel zijn goed inzichtelijk te maken met behulp van proeven die ik in 1996 in het laboratorium in Cambridge heb mogen doen. De interne getijbundel in de Golf van Biskaje is vanuit de theorie met een computermodel berekend en komt voor de omstandigheden en helling van

de Golf van Biskaje bijzonder goed overeen met de informatie die de waargenomen doorsnedes lieten zien. Het is voor de eerste keer dat de interne getijbundel in de oceaan met zoveel ruimtelijk detail in beeld is gebracht.

Hoofdstuk 4:
Focussering van interne golven; de interne golfaantrekker

De bijzondere aard van bovengenoemde interne golfbundel wordt nog versterkt wanneer deze aan een hellende bodem of zijwand reflecteert. Dit is hier bestudeerd aan de hand van een laboratoriumexperiment dat eerder was uitgevoerd in samenwerking met collega's in Lyon. Gekeken werd naar een bak met gelaagd water, waarvan één wand een helling heeft. Doordat de bak samen met het wateroppervlak een afgesloten domein vormde, kon de golfbundel als het ware door de bak kaatsen, zoals een biljartbal over het laken kan worden *rondgespeeld*.[2]

In de bak met gelaagd water gebeurde dit *rondkaatsen* van de interne golfbundel dus ook in het verticale vlak. Nu komt echter de bijzondere reflectie-eigenschap van interne golven voor de dag. De hoek wordt namelijk niet gespiegeld ten opzichte van de lijn loodrecht op de wand (zoals bij het biljart), maar ten opzichte van de *verticaal*. Deze hoek is namelijk een functie van de frequentie van de golf en de gelaagdheid van het water, maar deze veranderen niet bij reflectie. Dit betekent echter dat bij reflectie aan een hellende wand de randen van een bundel dichter bij elkaar komen, of juist verder van elkaar af komen; de bundel wordt smaller (intenser) of breder (zwakker). Dit wordt *focussering* respectievelijk *defocussering* genoemd.

In een afgesloten bak was eerder al aangetoond dat focussering meer voorkomt[3] dan defocussering: bij een groot aantal reflecties door het bassin (zoals in een wrijvingloos biljart) blijken de paden van de interne golven meestal te eindigen in een zogenaamde *limietcyclus*. Dit is de voorkeursbaan waarin alle interne golven eindigen voor de gegeven frequentie, gelaagdheid en geometrie. Deze voorkeursbaan wordt de interne *golfaantrekker* (Engels: *attractor*) genoemd. Nadat het bestaan van interne golfaantrekkers in 1995 op theoretische gronden werd voorspeld, werden deze in 1997 met bovengenoemde proeven in Lyon in een echte gelaagde vloeistof aangetoond.

In eerdergenoemde proeven in Cambridge kon slechts een klein aantal reflecties worden verkregen met de bundel die was ontstaan door een cylinder langzaam op en neer te bewegen; er was bij wijze van spreken teveel wrijving in het biljart. In Lyon werden de interne golven echter anders opgewekt: de hele bak werd periodiek op en neer geschud. Hierbij kwam na enige tijd 'schudden' het verwachte patroon van de aantrekker tevoorschijn. In dit proefschrift zijn deze experimenten opnieuw bestudeerd. Hierbij zijn details van de patronen van de aantrekker in de vloeistof in

---

[2]De benaming rondspelen is hier ongelukkig gekozen, omdat iedereen weet dat dit bepaald hoekig verloopt: door de randen van het biljart wordt de afgelegde weg van de biljartbal als (rechte) lijnstukken aan elkaar verbonden.

[3]Behalve wanneer de bak rechthoekig is en rechtop staat. Er zijn dan namelijk geen hellende wanden.

kaart gebracht, en ook hoe dit patroon zich in de tijd ontwikkelt. Hiermee is meer informatie verkregen om te kunnen verklaren hoe de interne golven in de bak precies worden opgewekt en uiteindelijk terecht komen in de aantrekker. Vooralsnog wordt nu aangenomen dat de beweging in gang wordt gezet door een periodieke beweging van het oppervlak: een staande golf, of 'seiche'.

Dankwoord (Acknowledgements)

Below, most acknowledgements are in Dutch. However, some people from abroad will be addressed in English (italicized text).

Lang geleden, op 1 december 1992, ben ik officieel begonnen aan mijn promotie-onderzoek als onderzoeker in opleiding bij het (inmiddels Koninklijke) Nederlands Instituut voor Onderzoek der Zee, NIOZ, op Texel. Inmiddels woon ik al weer bijna 9 jaar in Den Haag. Dit dankwoord is de plek om de mensen te bedanken voor hun hulp en steun tijdens mijn lange reis tot de promotie.

Hooggeleerde promotor, beste Sjef: je bent de beste docent die ik ken. Tijdens mijn studie waren jouw colleges het hoogtepunt van de week. In de afrondende fase van de promotie ben je in de procedure pal achter me gaan staan. Dit heb ik bijzonder gewaardeerd. Waar de promotor op afstand toekeek, was Leo de dagelijkse begeleider. In het eerste jaar ging dat gepaard met een intensieve en levendige e-mailuitwisseling vanuit Victoria BC, Canada. Leo, ik heb enorm veel respect voor je deskundige en creatieve benadering van het vak. Eigenlijk vind ik dat je hier veel te bescheiden in bent, want er is in deze wereld veel te weinig creativiteit. Ik heb enorm veel van je geleerd en ik heb altijd op je kunnen rekenen. Zo kon ik altijd in Den Burg logeren, waar ik gastvrij werd onthaald door Cathy en de kinderen. Ik kijk met heel veel plezier terug op onze samenwerking, met als hoogtepunt het samen ontdekken en ontrafelen van de interne golfaantrekker. Theo, je bent opgeschoven van collega promovendus tot co-promotor. Ook van jou heb ik veel geleerd. Je scherpe inzicht, en je heldere didactische uiteenzettingen hebben geholpen om in de eindfase van mijn promotie spijkers met koppen te slaan. De logeerpartijen op Texel waren altijd erg gezellig.

Na het bedanken van dit supertrio, wil ik ook de andere leden van de beoordelings-commissie danken voor hun bijdrage. Dit waren Will de Ruijter, Huib de Swart, Henk Dijkstra, Arjen Doelman, Stuart Dalziel en Adrian New. Hierin neemt Huib een speciale plaats in als oorspronkelijke begeleider en mentor vanuit Utrecht van mijn afstudeerwerk op Texel. *Stuart, thanks for all support at DAMTP in Cambridge. The fluid experiments in 1995 and 1996 were fun, and were highlights during my PhD track. Due to you and Paul I felt most welcome in the laboratory. Support from and discussions with Bruce and William proved very fruitful. Thanks to GertJan van*

Heijst some additional processing of the data could take place later at Eindhoven. All other people from both laboratories gave the feeling of a large geophysical family, including the warm hospitality of Claudia many years later in Falmouth and Woods Hole, USA.

Other international and inspiring contacts I would like to thank here are: Chris Garrett (lively discussions and a painful punting competition), Michael Ott, Peter Baines, Peter Craig, Steve Thorpe, Toby Sherwin, Mark Inall and Gus Jeans.

Dichter bij huis wil ik graag iedereen van het NIOZ bedanken. De sfeer op de afdeling was altijd erg goed. Herman, Hendrik, Kees, Hans: dank voor alles wat ik van jullie geleerd heb. De ochtend begon altijd goed als Rinus de krant voorlas, en Marcel hier het commentaar bij leverde. Ook Taco, Margriet, Ronald, Sven, Theo H. en Frans: allemaal bedankt voor jullie bijdragen en prettige samenwerking. De toenmalige collega-promovendi, waaronder Ramses en Gerard, zijn inmiddels allemaal uitgewaaid. Gerard heeft ook vanaf het KNMI nog input geleverd vanuit de klimaathoek, waarvoor dank. Astrid M. heeft in de eindfase LaTeX– en promotietips gegeven. Patrick Berkhout heeft als afstudeerder een belangrijke bijdrage geleverd aan dit proefschrift.

Veel bewondering en respect heb ik voor het zeegaande personeel. Tijdens mijn verblijf op Texel heb ik een aantal malen aan boord van de *Pelagia* kunnen zien hoe deskundig alle waarnemingen op zee door bemanning en technici werden uitgevoerd. Met name Hans Groot maakte veel indruk door zijn betrokkenheid afgewisseld met sterke verhalen van de grote vaart. Ook de mensen van de andere afdelingen van het NIOZ, inclusief de studio, werkplaats, bibliotheek en administratie, ben ik erkentelijk. Erwin Embsen heeft enorm goede Unix support gegeven. Door Potvisverblijf en de volleyballers van DGM kon worden kennisgemaakt met de andere zeedisciplines. Toen ik in Alkmaar woonde, kon met de carpoolclub leven en werk in bredere zin worden beschouwd op veerboot en in de auto. Dank hiervoor, Klaas, Cok, Susan, Hein en Chris. Ingeborg, jou wil ik apart bedanken voor de paar mooie jaren die we samen in Alkmaar gehad hebben.

Texel is een prachtig eiland. Dit is ook door de bijzondere mensen die hier wonen. Jeannette, ik ben je niet vergeten: dank voor alle warmte en gezelligheid. Een paar volleybalzomers waren heel bijzonder. Hiervoor ook dank aan alle andere teamgenoten.

Vanaf 1998 is TNO voor mij een prettige werkgever. Ik heb gelukkig voldoende verlof kunnen opnemen om dit proefschrift uiteindelijk toch nog af te kunnen ronden. Met name van Coen heb ik als groepsleider in dit traject veel steun en vertrouwen gekregen. Ook dank aan de vele overige TNO collega's. Dit zijn er teveel om hier te noemen. Pascal is al jaren mijn trouwe kamergenoot, en werkt toch onverstoorbaar door aan bijzonder krachtige tools. In de eindfase heb ik veel smart kunnen delen met Hans, Tilly en Jeroen. Michael heeft mij fantastisch geholpen door het Engelse taalgebruik in het gehele proefschrift te controleren. Jacqueline heeft mij uit de brand geholpen met enkele onwillige illustraties en Paul heeft vele versies van de

verschillende manuscripten bij mij in de brievenbus gestopt.

De afgelopen jaren heeft mijn oceanografische werk steeds meer relatie gekregen met mijn werk voor de Koninklijke Marine. Dit heb ik als zeer motiverend en inspirerend ervaren. In het bijzonder wil ik hier de laatste twee projectofficieren Frans Jansen en René Dekeling noemen. Naast de beroepsmatige belangen toonden zij zich zeer geïnteresseerd in de voortgang van mijn promotie.

Dank ook aan alle geïnteresseerde familieleden en vrienden. Fransje heeft mij in de beginfase ondersteund. Ronald, Edith, Edwin, Hedri, Ardis en iedereen die ik hier vergeet. Ik hoop jullie straks weer wat vaker te zien en te spreken. Andries heeft in de beginfase, nog tijdens de studie een belangrijke bijdrage geleverd in het inzicht van het fysisch experiment en het volleybal (met een volleybalbal). Lot heeft in drukke tijden de Nederlandse samenvatting helpen verbeteren. Ko en Anja, dank voor support en gezelligheid.

Nimfen, bedankt. Peter, vanaf het allereerste begin, op de Potvis, was het altijd gezellig. Ook bij TNO ben je een fijne collega. Bart, je bent mijn beste vriend. Dank voor alle steun, maar ook voor alle lol die we samen gehad hebben. Wordt vervolgd!

Mijn ouders wil ik bedanken voor de fijne jeugd, en het stimuleren tijdens school en studie. Hier ligt de basis van dit proefschrift. Dennis, daar hoor jij ook bij. Daarom is dit boekje ook eigenlijk aan jullie alle drie opgedragen.

Annemarie, vrouw van mijn leven, jij hebt me de laatste negen jaren met alles gesteund. Ik kan je hiervoor niet genoeg bedanken. Ik kijk uit naar de komende tijd, waarin we meer tijd hebben om samen leuke dingen te gaan doen. Met jou is alles veel leuker.

Het is klaar!

Frans-Peter
Den Haag, november 2006

AANKOMST

Na lange dagen door de storm geteisterd
En somtijds uit de kooi gesmakt te zijn,
Door 't leven van 't zacht Lisboa nog verbijsterd,
Vind ik mij zitten op het zonnig plein.

Geleund in de uithoek van een balustrade,
Zie ik als over hemelsbreed kozijn
't Beproefd schip dat stilligt aan de kade,
De gele stroom, de kleurge oeverlijn.

Beneden karren raatlen, kranen kreunen,
Hier is het stil, terwijl alleen gitaren
Een oude fado traag en droef opdreunen,
En of karveelen weer de Taag opvaren.

J. J. Slauerhoff

Curriculum vitae

Frans-Peter Lam is geboren op 12 april 1968 in Ede, Gelderland. Op 27 februari 1986 voltooide hij zijn eerste van twee elfstedentochten. In datzelfde jaar haalde hij zijn VWO-diploma aan het Christelijk Streeklyceum in Ede.

Daarna ging hij Natuurkunde studeren in Utrecht. Vanaf 1990 koos hij voor de bovenbouwstudie Meteorologie en Fysische Oceanografie aan diezelfde Universiteit Utrecht. In 1992 haalde hij zijn doctoraaldiploma, na een afstudeeronderzoek bij het Koninklijk Nederlands Instituut voor Onderzoek der Zee (NIOZ). Dit onderzoek werd begeleid door Leo Maas, Hendrik van Aken en Huib de Swart. Het afstudeerverslag had de titel *Getij-analyse & interpretatie van stroommetergegevens uit de IJslandzee in de nabijheid van een shelfrand* en vormt de basis voor hoofdstuk 2 van dit proefschrift.

Aansluitend werd een promotie-onderzoek aangevangen als onderzoeker in opleiding bij het Koninklijk NIOZ. Dit proefschrift is hier het resultaat van. Tijdens dit promotiewerk zijn daarnaast, tijdens twee korte stages, laboratoriumexperimenten uitgevoerd in Cambridge.

In de periode van 1990 tot heden is zeegaande ervaring opgedaan aan boord van verschillende schepen: *RV Tyro, RV Pelagia, RV Navicula, Hr.Ms. Tydeman, NRV Alliance, Hr.Ms. Mercuur, Hr.Ms. Luymes* en *RV Sverdrup II.*

Vanaf 1998 is hij in dienst bij de afdeling Onderwatertechnologie van TNO in Den Haag. Hier doet hij onderzoek aan onderwaterakoestiek (sonar) en operationele oceanografie, grotendeels in opdracht van de Koninklijke Marine.

Colophon